Characterization of Air Voids in Fresh Cement Paste through Ultrasonic Nondestructive Testing

A Thesis
Presented to
The Academic Faculty

by

Richard Kmack

In Partial Fulfillment
of the Requirements for the Degree
Master of Science in the
School of Civil and Environmental Engineering

Georgia Institute of Technology
August 2008

Characterization of Air Voids in Fresh Cement Paste through Ultrasonic Nondestructive Testing

Approved by:

Dr. Laurence J. Jacobs, Advisor
School of Civil and Environmental Engineering
Georgia Institute of Technology

Dr. Kimberly Kurtis, Co-Advisor
School of Civil and Environmental Engineering
Georgia Institute of Technology

Dr. Reginald DesRoches
School of Civil and Environmental Engineering
Georgia Institute of Technology

Date Approved: July 7, 2008

Acknowledgements

I would like to thank my advisor Dr. Laurence Jacobs and my co-advisor Dr. Kimberly Kurtis for their encouragement and belief in me these last few years; I am blessed to have two mentors who are both passionate about their work and devoted to the well-being and development of their students. I am grateful as well to Dr. Reginald DesRoches for his serving on my thesis committee and for putting up with my inquisitiveness during class. In addition, I am indebted to Dr. Jin-Yeon Kim for his expertise and tireless efforts in helping me overcome technical issues with waveform collection and analysis; his knowledge of ultrasonics leaves me in awe.

To Wonsiri "Bo" Punurai, I am especially thankful for her contributions and eagerness to share her knowledge during my earliest forays into research. Many thanks to Victor Garas and Amal Jayapalan for their technical assistance with autogenous strain tests. To my companions in lab, I am grateful for inspiring discussions, their sense of humor, and a friendly working atmosphere: Kritsakorn "Eak" Luangvilai, Chi Won In, Sebastian Kuechler, Christoph Prüll, Martin Treiber, Aline Zimmer, and Michael Braun.

I wish to recognize the generous support of the American Concrete Institute and the ACI Graduate Fellowship program, the Georgia Department of Transportation, the Georgia Tech Foundation and the President's Fellowship Program, and the Ira H. Hardin family. I would also like to thank Joe Wolfe of W.R. Grace and Terry Vines of Lafarge, both of whom provided materials and services essential to this project.

To my parents, thanks for always being there and believing in me. To my brothers and sister, thanks for looking out for me all these years.

Contents

List of Tables

List of Figures

Summary

The objective of this research is the pursuit of a better characterization method for the air voids - particularly air-entrained voids - in fresh cement-based materials through the use of ultrasonics. The use of air-entraining agents (AEA's) to incorporate a stable network of air voids into fresh cement paste is common practice in the concrete industry. These particular air voids significantly improve durability of hardened cement paste through mitigation of stresses associated with freezing and thawing cycles. It is understood that the performance of entrained air voids in cement paste is dependent on their size and distribution, or spacing factor. However, conventional methods for qualifying air content, such as the Pressure, Volume, and Gravimetric Methods, only measure total air volume and cannot assess size or spacing. In this investigation, using matched pairs of transducers, ultrasonic pulses were transmitted through fresh cement paste specimens (0.0% up to 0.6% AEA by weight of cement). The received signals were recorded every five minutes during the first six hours and then every fifteen minutes thereafter. Analysis shows strong distinctions between specimens with and those without the AEA. Further research is needed into the distinctions among specimens with the AEA. However, the data suggest correlations between Vicat setting times, heat of hydration, and autogenous strain and ultrasonic metrics such as pulse velocity and peak frequency of the signal. The findings of this research should be most appropriate as a foundation for an inversion process and improved air-entrainment detection methods.

CHAPTER 1

Introduction

1.1 Motivation

Standard practice in the concrete industry calls for the addition of chemical admixtures called air-entrainment admixtures (AEA) to cement mixtures in order to resist damage from frost action – freezing and thawing cycles. The American Concrete Institute's Document 201.2R-08 [1] provides guidance on the volume of air to be entrained based on environmental conditions. Through surfactant action, the AEA's ideally incorporate a stable system of air voids of 50 to 200 μm in diameter spaced less than 0.20 mm apart. This system of air voids accommodates the expansion of water during freezing cycles, relieving the matrix of otherwise damaging hydraulic stresses. Given the nature of frost action and the role of entrained air voids, proper size and dispersion of air voids is critical. However, conventional methods for characterizing air content fail to provide information beyond air volume. Du and Folliard [2] emphasize the challenge of quality control of air-entrainment in light of the complex relationship between the character of the air void system in cement paste and the variations of the additional components of concrete (e.g., cement fineness, water-to-cement ratio, curing temperature) as well as physical disturbances to fresh cement (e.g., transportation, compaction, finishing).

The use of ultrasonic wave measurements is an efficient and economical component to

structural health monitoring of civil infrastructure. As a non-destructive – and potentially in-situ – method, ultrasonic wave measurements of concrete structures provide an effective means of assessing member thicknesses and stiffness as well as cracking and delamination without incurring additional damage to a structure. However, ultrasonic monitoring in concrete practice is generally reserved for finished structures and hardened material. Research efforts in recent years have addressed the application of ultrasonic monitoring to fresh, hydrating cement pastes and mortars and could further expand the use of ultrasound in quality control during concrete casting. This new focus emphasizes the time-dependent nature of hydrating paste as opposed to the relatively static condition of hardened paste. This investigation proposes that ultrasonics may offer a valuable tool for quality assurance of plastic or early age air-entrained concretes. The objective of this research is the pursuit of a better characterization method for the air voids – particularly air-entrained voids – in fresh cement-based materials through the use of ultrasonics.

1.2 Previous research

Interest in the application of ultrasonics to plastic cement paste is relatively recent, and investigations into testing mechanisms and the potential for continous monitoring are limited to a handful of studies. There are currently no standards for the containment system and testing procedures for ultrasonic monitoring of fresh cement paste, but each new study generally utilizes a similar setup to the thru-transmission setup proposed by Reinhardt et al. [3– 4]. This involves paste containment between two acrylic sheets separated by an elastomeric spacer; transducers on the outside surfaces of the assembly transmit and receive signals. Less common is a pulse-echo system, such as that proposed by Öztürk et al. [5], in which a single transducer transmits through a barrier into the paste and records the resulting echos reflected off of the

opposite free surface of the paste.

Sayers and Grenfell [6], using ultrasonic thru-transmission of longitudinal and shear waves, considered the development of mechanic strength and stiffness in cementitious materials through initial and final sets. Adhering to American Petroleum Institute specifications for class G oil-well cements, tests focussed on the shear modulus and Poisson's ratio of four cement pastes: Neat (Cement and water), Accelerated (neat with $CaCl_2$ added), paste containing latex polymer particles, and surfactant paste. The tests reveal the critical development of the mechanical properties of cement within the first few hours of curing and emphasize time-dependent distinctions of the ultrasonic waveforms traveling through each slurry.

In further experiments of cement pastes with and without a chemical accelerator $CaCl_2$, Sayers and Dahlin [7] found wave propagation during the earliest hours after mixing to be sensitive to air inclusions in the paste. Pastes containing the accelerator transmitted relatively high-frequency wave components in the earliest hours after mixing compared to the lower-frequency spectra of pastes without the accelerator. By further monitoring $CaCl_2$ that were de-aerated, Sayer and Dahlin propose that the resonance of air voids resulting as a secondary effect of the addition of $CaCl_2$ superimposes the higher-frequency wave components.

Aggelis' and Philippidis' [8–10] investigations of quality control of water-content using fresh cement/mortar pastes and hardened cement paste specimens of various water-to-cement ratios distinguish the difference in material properties of hardened cement in which solid products provide the means for wave propagation versus fluidous paste in which water provides a means necessary for transmittal.

1.3 Thesis structure

Chapter 2 presents background to cement-based materials and the hydration process. Chapter 3 provides the theoretical background on wave propagation. Discussion of the experimental setup and procedures is given in Chapter 4. In general, experimental procedures and equipment were devised to allow for continuous ultrasonic monitoring of fresh cement paste specimens through the first 12 hours of hydration; paste specimens were cast within a sealed container coupled to transmitting and receiving transducers in a thru-transmission configuration. Additional tests of time of initial set, heat of hydration, and autogenous shrinkage of the cement pastes were also conducted. The results of the ultrasonic studies are discussed in Chapter 5 followed by conclusions and recommendations in Chapter 6. The waveform data collected during ultrasonic monitoring and the resulting frequency spectra are shown graphically in Appendices A and B, respectively.

CHAPTER 2

Cement-based materials

Portland cement concrete consists of a cement paste matrix (cement, water, air, and additives combined and hardened through chemical reaction) binding mineral aggregates into a solid, composite mass. The aggregate phase contains both fine particles, such as sand, as well as coarse particles, such as crushed gravel and stone, of various shapes and sizes. Air in the cement paste may be either entrapped due to mixing action or artificially entrained through use of chemical air-entraining agents. Additives to the cement paste can include supplementary cementitious materials (SCM's), chemical admixtures, as well as fibrous materials. SCM's, such as fly ash, ground granulated blast-furnace slag, and silica fume may be substituted into the cement prior to mixing in order to improve the properties of fresh and hardened cement. Chemical admixtures, such as air-entrainers, water-reducing agents, setting accelerators and retarders, shrinkage inhibitors, and even coloring agents added before and during mixing provide also provide improved performance characteristics to the cement paste. Table 2.1 summarizes the Portland Cement Association's recommendations for proportioning of the raw materials, not including admixtures or SCM's, in concrete mixes [11].

Table 2.1: Recommended material proportions (by volume) for Portland concrete[11]

Material	Non-air-entrained cement paste (%)	Air-entrained cement paste (%)
Cement	7-15	7-15
Water	16-21	14-18
Air	1-3	4-8
Fine agg.	25-30	24-28
Coarse agg.	31-51	31-51

2.1 Hydration of cement paste

The setting and hardening of cement paste results from hydration, the chemical reaction that occurs when water is mixed with cement. The resulting solids are called hydration products. Very early stages of the reactions are dominated by the through-solution hydration mechanism in which anhydrous compounds dissolute into their ionic constituents followed by precipitation of the newly formed hydrates. At later ages, ionic mobility in the hydrate solution is restricted, and the solid-state hydration mechanism proceeds. Further discussion of the hydration reaction is available in numerous texts [12–14].

2.1.1 Chemical components of Portland cement

Modern Portland cement prior to hydration consists essentially of calcium silicates and aluminates. The results of chemical analysis for cements are generally presented in terms of oxide contents; these oxides and their shorthand notation are listed in Table 2.2. A discussion of the main components of Portland cement clinker follows:

Calcium Silicates include tricalcium silicate (C_3S) and beta-dicalcium silicate (βC_2S), otherwise known as alite and belite, respectively. C_3S has an irregular crystal structure with large interstitial holes, resulting in high lattice energy

Table 2.2: Oxide shorthand for ordinary Portland cement[12]

Oxide	Shorthand	Example Compound	Shorthand
Calcium oxide (CaO)	C	$3CaO{\cdot}SiO_2$	C_3S
Silicon dioxide (SiO_2)	S	$2CaO{\cdot}Si_2$	C_2S
Aluminum oxide (Al_2O_3)	A	$3CaO{\cdot}Al_2O_3$	C_3A
Ferric oxide (Fe_2O_3)	F	$4CaO{\cdot}Al_2O_3{\cdot}Fe_2O_3$	C_4AF
Magnesium oxide (MgO)	M	$4CaO{\cdot}3Al_2O_3{\cdot}SO_3$	$C_4A_3\overline{S}$
Sulfer trioxide (SO_3)	$\overline{S}$	$3CaO{\cdot}2SiO_2{\cdot}3H_2O$	$C_3S_2H_3$
H_2O	H	$CaSO_4{\cdot}2H_2O$	$C\overline{S}H_2$

and reactivity. C_2S, also irregular in structure, has smaller interstitial holes and is less reactive than alite. Thus, C_3S accounts for the early strength gain in cement paste while C_2S contributes to later strength gain.

Calcium Aluminate and ferroaluminate. Tricalcium aluminate (C_3A) is the principle calcium aluminate in Portland cement, and tetracalcium aluminoferrite (C_4AF) is the most common calcium ferroaluminate. Both C_3A and C_4AF hydrate rapidly due to large holes in the crystal structures with the former accounting for considerable heat liberation during the first few days of cement hydration. There is little or no strength contribution to the cement paste due to this group of compounds.

Magnesium oxide and calcium oxide are generally undesirable in portland cement clinker and can cause unsoundness in the hydrated paste. Magnesium oxide (MgO) and calcium oxide (CaO) may be introduced to the clinker as impurities in the raw materials or as secondary effects of production conditions.

Sulfate compounds in the form of gypsum, are generally interground with the Portland cement clinker in order to suppress quick-setting of clinker otherwise brought on by the high reactivity of C_3A.

2.1.2 Setting and Hardening

During the hydration process, the formation of hydration products drive the stiffening, setting, and hardening of the paste. Stiffening simply refers to a loss of consistency associated with plasticity. Setting refers to the solidification of the paste, often referred to in practice in terms of *initial set* – when the paste becomes unworkable – and *final set* – the complete solidification of the paste. Workability qualitatively refers to the state during which the paste can be mixed, transported, placed, compacted, and finished. Final set is also considered the beginning of hardening of the matrix lasting for several weeks. Initial and final set are most commonly indicated based on the resistance of the cement paste to penetration by Vicat needle as instructed by ASTM C191 [15].

This last point demands further consideration regarding setting as the point where the paste undergoes transition from a fluid to a solid [16– 17]. As dictated by the Vicat test, initial and final set are marked as the points where a needle under constant load penetrates a paste specimen to exact depths of 25 mm and 0 mm, respectively. Interpretation of these points may be subjective, particularly regarding final set as the point when the Vicat needle fails to leave a "complete circular impression" on the specimen [15]. Further, the consequence of Vicat results is only an arbitrary set of points at which a paste specimen has achieved a particular shear resistance; Vicat tests fail to present the actual material property developments occuring during solidification.

A more precise definition of setting as the transition from fluid to solid may be understood through the percolation of solid particles in the paste. Initially, the paste is a suspension of particles only loosely connected in a flocculated pattern; without an interconnected matrix of solid particles, the system lacks rigidity. Percolation simply

refers to the presence of a continuous path within a phase from one side to another; in the case of cement paste, it refers to the bridging between hydration products, leading to interconnectivity on the larger scale and the development of a solid skeleton. Percolation may be further defined in terms of a percolation threshold, a volume fraction at which a phase transitions from isolated regions to the interconnected state; for calcium silicate hydrates – the primary strength-providing phase in hydrated cement – this volume fraction is approximately 17% to 18% [18]. Bentz confirmed through loss-on-ignition tests as well as through use of a CEMHYD3D computer hydration model that after only 4-8% of hydration, sufficient solidification occurs to begin providing shear resistance to Vicat needle [19].

The hydration of cement paste is an exothermic reaction and can be illustrated in terms of heat evolution. Fig. 2.1 shows an example of heat generation during the first 24 hours of hydration. A brief period of rapid heat evolution - region A - occurs when the cement is first mixed with water, attributable to dissolution of aluminates. The presence of sulfates in the hydration solution depresses the solubility of C_3A, resulting in a dormant period of low heat evolution at B. During this dormant period, the paste retains plasticity. At 2-4 hours after mixing, initial set occurs, and ettringite formation and hydration of C_3S into calcium silicate hydrates drive the acceleration of heat evolution along region C; the depletion of sulfate ions during ettringite formation also renews the hydration of aluminates. As the heat evolution peaks, the paste achieves final set and begins hardening. An additional peak at D may occur as hydration of the aluminates, is once again depressed by the aluminate-to-sulfate balance.

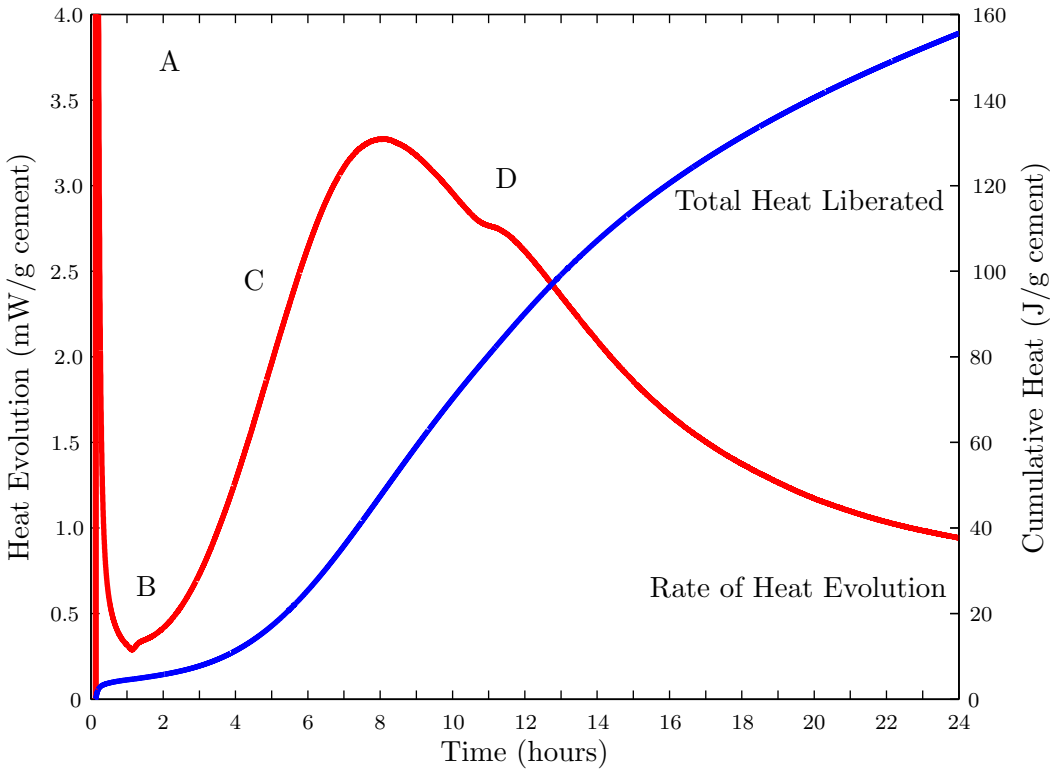

Figure 2.1: Heat of Hydration

2.2 Structure of hydrated cement paste

For the investigation discussed, cement paste refers to mixtures of Portland cement, deionized water, entrapped and entrained air, as well as varying degrees of air-entraining admixture. This section introduces the final components that make up hardened cement paste. A summary of these components follows and is illustrated in Fig. 2.2 from Mehta and Monteiro [12].

2.2.1 Solid components of hydrated cement paste

The four principle solid phases found in hydrated cement paste are as follows:

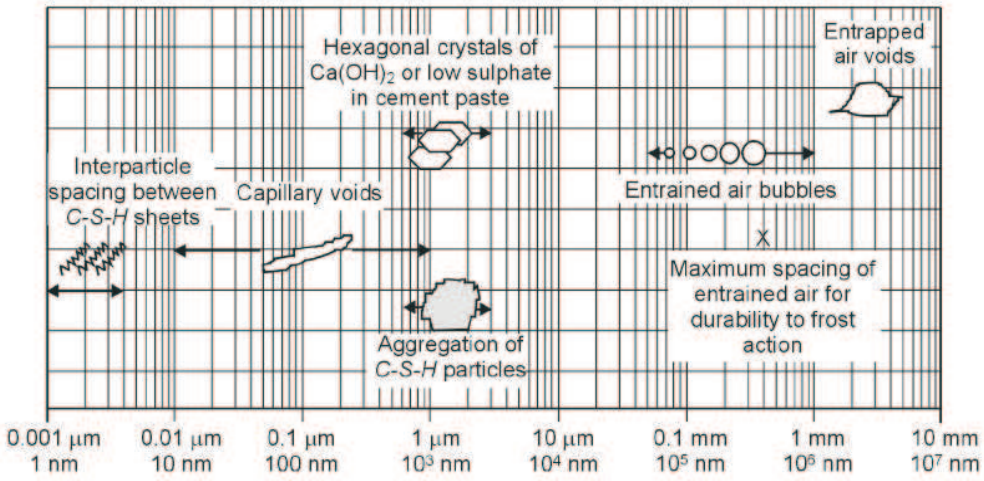

Figure 2.2: Dimensional range of solid and pore phases in hydrated cement paste [12]

Calcium silicate hydrate is the primary strength-giving component of hydrated cement paste and results from the hydration of the calcium silicates. Abbreviated as C-S-H (using oxide shorthand), this is the most important phase as to determining the properties of the paste and makes up 50 to 60 percent of the final volume of solids. The exact structure of C-S-H is not known, but may be best described in terms of poorly crystalline fibers or a rectilinear network. This phase is often referred to as C-S-H gel due to the unresolved internal crystal structure. Likewise, the dashes imply that the composition of C-S-H is not fixed, and the C/S often varies between 1.1 and 2.0. For purposes of stoichiometry, C-S-H is often approximated as $C_3S_2H_3$ as shown in the following expressions for the hydration of the C_3S and C_2S:

$$2C_3S + 6H \rightarrow C_3S_2H_3 + 3CH \tag{2.1}$$
$$2C_2S + 4H \rightarrow C_3S_2H_3 + CH$$

Calcium hydroxide possesses a definite stoichiometry, $Ca(OH)_2$, and forms large, hexagonal-prism crystals. This phase makes up 20 to 25 percent of the

final volume of solids. Due to lower surface area, calcium hydroxide does not provide as much strength to the hydrated cement paste as does C-S-H.

Calcium sulfoaluminates constitute 15 to 20 percent of the final volume of solids. They consists of needle-shaped prismatic crystals of trisulfate hydrate, also known as ettringite, as well as hexagonal-plate crystals of monosulfate hydrate.

Unhydrated cement grains may persist long after hydration has ceased even in well-hydrated pastes. During hydration, smaller cement grains on the scale of 1 μm dissolve first followed by larger particles, which may be as large as 50 μm. Given the degree of hydration and space limitations of other hydration products, these larger cement grains may only incur hydration on their outer surfaces.

2.2.2 Voids in hydrated cement paste

Four types of void spaces occur in cement paste. Depending on the size and type, these voids have important influence on the properties of the cement paste. Discussion of each void type is as follows:

Interlayer spacing of C-S-H, also known as gel pores, is an intrinsic part of the C-S-H structure and accounts for approximately 28% of the porosity of C-S-H. The voids range in size from 0.5 nm to 2.5 nm and the are generally too small to adversely affect the overall strength and permeability of hydrated cement paste. Gel porosity cannot be resolved through scanning electron microscopy.

Capillary voids represent the irregularly shaped spaces within the cement matrix not filled by solid hydration products or unhydrated cement particles. Capillary porosity is highly dependent on water/cement ratio as well as the degree

of hydration: pastes of high water/cement ratios at early stages of hydration can have pores as large as 3 to 5 μm; well-hydrated pastes with low water/cement ratios will have smaller capillary pores of 2.5 nm to 50 nm, otherwise referred to as micropores. Capillary voids larger than 50 nm are called macropores, and their presence can significantly affect strength and permeability.

Entrained air are spherical voids generally ranging in size from 50 to 200 μm in diameter. These voids are intentionally introduced into the cement paste during mixing through the use of synthetic air-entraining surfactant admixtures (AEA's). Successful inclusion of air-entrained voids produces exceptional durability to freeze-thaw cycles: as hydraulic pressures build due to the volume expansion of freezing water and ice formation, the entrained air voids offer open spaces for the pore water solution to expand. The size of the entrained voids is important as they must be large enough to accommodate the bulk expansion of water yet small enough to reduce the necessary travel distance, or spacing factor, for the expanding pore water to less than 0.20 mm [20]. Due to the resulting increase in porosity, air-entrained voids can likewise adversely affect the strength of the hydrated paste: for typical mixtures, a 1% increase in air-entrainment voids results in a 2% to 6% loss in compressive strength [21]. However, air-entraining admixtures also act as water-reducers, which when considered can partly or wholly offset the loss in strength due to entrained voids.

Entrapped air are larger, irregularly shaped voids upwards of 3 mm in diameter. These voids, which are incorporated through the mixing process can be removed through proper compaction. Otherwise, these voids increase porosity and permeability of the hydrated cement paste, adversely affecting the strength and durabilty. Unlike entrained air voids, these voids are too large and too widely spaced to offer any expansion, i.e., freeze-thaw, relief.

2.3 Curing considerations

The mixture ratio of water to cementitious materials (w/c), curing conditions, and stage of hydration are the primary factors controlling the character of the solid and void phases in the hydrated cement paste structure. As indicated in Fig. 2.3, Powers proposes a simple model for estimating the proportions of the components of cement paste before and after hydration [22– 23], supposing that 1 cm^3 of cement produces "little more" than 2 cm^3 of hydration products and assuming that the gross volume of the cement mixture changes *insignificantly* during the hydration of cement paste. Further, Powers' model neglects distinctions within paste components and only defines the paste in terms of three components: capillary pores, hydration products ("cement gel"), and unhydrated cement.

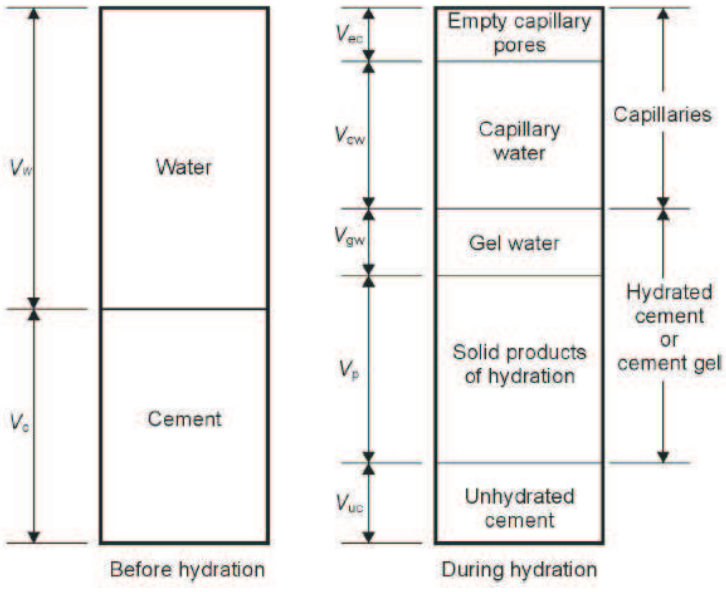

Figure 2.3: Powers' schematic representation of the volumetric proportions in cement paste before and during hydration [23]

In other words, the Powers model suggests that the initial volume of the system prior

to hydration – the sum of the volumes of mixed water and cement particles – approximates the volume of the resulting hydration products – the sum of the volume of unhydrated cement grains, hydrated solid products, and voids filled by water or by air. Solid hydration products fill the space once occupied by the unhydrated cement along with part of the surrounding space initially occupied by water.

It is important to note then, that the Powers model is only a simplification and neglects the volume changes that do occur during the earliest stages of hydration in the fresh paste and throughout the lifetime of the hardened paste.

Hydrating cement paste is subject to time-dependent deformations throughout the curing process, primarily plastic shrinkage, chemical shrinkage, as well as autogenous shrinkage. Plastic shrinkage occurs as a result of the loss of water through evaporation from the paste surface. The negative capillary pressure that results from the removal of water from between cement particles leads to contraction of the still-plastic matrix. Horizontal slab surfaces exposed to high wind velocities, high air temperatures, low relative humidity levels are most prone to plastic shrinkage. The effects of plastic shrinkage in fresh concrete can be alleviated in practice by: moistening subgrade surfaces and formwork; minimizing surface evaporation with wet burlap, fog curing, or curing compounds; reducing wind velocities with windbreaks; keeping concrete surfaces cool using sunshades [12].

Even in cases where no moisture is lost to surroundings, hydrating cement paste can indeed experience internal redistribution of moisture and subsequent internal stress as water is combined into products during the hydration reaction. For w/c less than 0.44, the paste will undergo the process of *self-dessication* during which time the capillary pores will become partially empty, resulting in significantly reduced relative

humidity within the pores and possible cessation of hydration [14]. This is because the volume required for C-S-H gel is less than that of the mix water, leaving additional empty space once available water is used up for the hydration reactions. Chemical shrinkage refers to the decreased absolute volume of the hydration products versus the initial volume of solids and water. If self-dessication causes the internal relative humidity to fall below 80%, the paste can undergo a bulk shrinkage known as *autogenous shrinkage* [13]. Sant, et al. [in review], show that chemical shrinkage and autogenous shrinkage appear similar prior to solidification; the contributions of these two sources of shrinkage diverge upon solidification as the rigid matrix resists autogenous shrinkage while chemical shrinkage proceeds with further hydration reactions. Cement pastes that are in a sealed environment, may therefore, only experience autogenous shrinkage during hydration [16– 17] [24].

During autogenous shrinkage, the external volume of the paste decreases. Prior to solidification, this decrease follows from the reduction in void space volume due to hydration. Following solidification, however, the paste develops a rigid structure to resist the internal collapse mechanism, resulting in the buildup of cavitation forces and negative capillary pressure in the empty vapor spaces, further driving autogenous shrinkage, though at a reduced rate. To alleviate the effects of autogenous shrinkage, it is therefore important to provide an adequate supply of externally or internally supplied moisture during curing.

Bentz proposes an improved model of cement hydration kinetics [25], which takes into consideration changes in the water-filled porosity, volume fraction of unhydrated cement, and effects of chemical shrinkage with respect to hydration time. Based on the Powers model, the volume fractions of the water-filled capillary porosity and total porosity ($\phi_W(t)$ and $\phi_T(t)$) and the unhydrated cement ($\gamma(t)$), as functions of time

are given by:

$$\phi_W(t) = \frac{\rho_{cem}(w/c) - (f_{exp} + \rho_{cem}CS)\alpha}{1 + \rho_{cem}(w/c)} \tag{2.2}$$

$$\phi_T(t) = \frac{\rho_{cem}(w/c) - f_{exp}\alpha}{1 + \rho_{cem}(w/c)} \tag{2.3}$$

$$\gamma(t) = \frac{1 - \alpha}{1 + \rho_{cem}(w/c)} \tag{2.4}$$

where ρ_{cem} is the specific gravity of cement (taken as 3.2), (w/c) is the water-to-cement ratio, f_{exp} is the volumetric expansion coefficient for the cement hydration products relative to the cement reacted (taken as 1.15), CS is chemical shrinkage per gram of cement (generally taken as 0.07 mL/g), and α is the degree of hydration of the cement at time t. Assuming the local hydration rate of the cement is linearly proportional to the volume fractions of available water-filled porosity and the available unhydrated cement at a given time, Bentz's model proposes:

$$\frac{\partial \alpha}{\partial t} = k_1 \phi_W(t) \gamma(t) \tag{2.5}$$

for a saturated system (CS=0) where k_1 represents a rate constant that varies with the curing conditions and cement composition. In the case of a sealed system, the model is modified to

$$\frac{\partial \alpha}{\partial t} = k_2 \phi_W(t) \gamma(t) \frac{\phi_W(t)}{\phi_T(t)} \tag{2.6}$$

to account for the inactivation of portions of the unhydrated cement due to creation of empty porosity and the reduction of the water-filled capillary porosity. This kinetic model does not distinguish between entrained and entrapped voids, and will not be quantitatively applied in this particular investigation.

2.4 Freeze-thaw action

Seasonal cycles of freezing and thawing subject concrete to internal stresses, which, if unmitigated, can deteriorate the cement matrix, aggregates, and the bond between these phases. This is primarily due to the hydraulic pressures associated with the freezing actions of pore water. As environmental temperatures decrease, the associated expansion of water near structural surfaces displaces warmer internal pore water; the permeability of cement paste can restrict this flow rate, resulting in the expansive buildup of internal stresses [26]. Additionally, freezing of capillary water out of the alkaline pore solution, which may become more concentrated when de-icing chemicals are applied to the concrete surface, sets up osmotic gradients within the remaining freezable liquid, inducing stresses associated with contraction of the matrix [27]. Other freeze-thaw mechanisms that attribute to internal stresses include ice crystal formation [28–30] and the gradients associated with free energy changes between gel water, ice within capillaries, and ice within much larger air voids [31].

To protect cement paste, mortar, and concrete from freeze-thaw damage, these mixtures incorporate air-entraining surfactant admixtures (AEA's). This results in a network of stable spherical air voids within the fresh paste. When properly sized and well-distributed, air voids serve as expansion chambers to relieve freeze-thaw stresses. Research suggests entrained voids should be ideally 10-100 μm in diameter and spaced at 0.16-0.20 mm [20]. As shown in Table 2.3, ACI [32] recommends an entrained air content of 3-8% by volume, depending upon the anticipated severity of the environment.

Table 2.3: Recommended air contents for frost-resistance concrete [32]

Nominal maximum aggregate size, in. (mm)	Average air content, (%)*	
	Severe exposure†	Moderate exposure‡
3/8 (9.5)	7-1/2	6
1/2 (12.5)	7	5-1/2
3/4 (19.0)	6	5
1 (25)	6	5
1-1/2 (37.5)	5-1/2 §	6 §
3 (75)	4-1/2 §	3-1/2 §
6(150)	4	3

* A reasonable tolerance for air content in field construction is $\pm\ 1 - 1/2\%$

† Outdoor exposure in a cold climate where the concrete maybe in almost continuous contact with moisture before freezing or where deicing salts are used. Examples are pavements, bridge decks, sidewalks and water tanks.

‡ Outdoor exposure in a cold climate where the concrete will be only occasionally exposed to moisture before freezing and where no deicing salts will be used. Examples are certain exterior walls, beams, girders, and slabs not in direct contact with soil.

§ These air contents apply to the whole as for the preceding aggregate sizes. When testing these concretes, however, aggregate larger than 1-1/2 in. (37.5 mm) is removed by hand-picking or sieving and the air content is determined on the minus 1-1/2 in. (37.5 mm) fraction of the mixture. (The field tolerance applies to this value.) From this, the air content of the whole mixture is computed.

Note: There is conflicting opinion on whether air contents lower than those given in the table should be permitted for high-strength (approximately 5500 psi)(37.8 MPa) concrete. The committee believes that where supporting experience and experimental data exist for particular combinations of materials, construction practices and exposure, the air contents can be reduced by approximately 1%. For nominal maximum aggregate sizes over 1-1/2 in. (37.5 mm), this reduction applies to the minus 1-1/2 in.(37.5 mm) fraction of the mixture.

2.5 Methods of characterization of air-voids in cement paste

Proper air-entraining of cement paste is contingent on ensuring appropriate air volume, typical sizes of air voids, and spacing between voids. A number of methods exist for measuring air volume, including the Pressure Method (ASTM C231), the Volumetric Method (ASTM C173), and the Gravimetric Method (ASTM C138) [33–35]. These methods are conducted using freshly mixed paste and, therefore, are commonly used in practice. The pressure method is based on observations of changes in volume with changes in pressure and assumes air is the only substantially compressible part of the cement paste. The volumetric method is based on the displacement by air of a calibrated volume of water. The gravimetric method extracts air volume given accurate knowledge of the relative densities, moisture contents, and proportions of the mixture ingredients.

Use of an air-void analyzer allows for determination of air volume and size distributions of voids in fresh mortar sieved from a concrete element. Small samples are submerged in a column of viscous liquid, in which the air voids from the paste rise and are collected by a submerged bouyancy recorder. As per Stokes' law, the larger air void bubbles rise fastest, and the change detected by the bouyancy recorder over time can be interpreted with relation to the number of air voids of a given size. There is no standard for this method at present, and it is likely that the small sample sizes used as well as the time duration needed to adequately collect the air bubbles do not establish this as a practical test in the field.

Further, following initial mixing, concrete is subject to a number of physical disturbances, which can cause differences in the measured air content and void system

of fresh material versus that of hardened material. These physical disturbances are associated with production processes of batching and mixing as well as construction-related activities such as transport, handling, pumping, placement, retempering, consolidation, and finishing procedures. Thus, in addition to the tests on fresh cement-based materials, hardened specimens can also be analyzed for air content using petrographic analysis on samples extracted from structural members, as per ASTM C457 [36]. In this test, polished specimens are scanned visually using a microscope, and number of voids, voids sizes, and spacing parameters are inferred based on observations of linearly traversing the surface. A technician should be able to determine average void size and even distinguish entrained air content and entrapped air content. However, this method must be done in a lab using hardened specimens extracted from the structural member.

As previously discussed, recent research investigates the use of ultrasonic waves to monitor the setting of fresh, hydrating cement pastes by thru-transmission methods [3– 4] [6] and pulse-echo methods [5]. Additional work shows ultrasonic monitoring as an effective method for analyzing water content [8–10] and Sayers and Dahlin demonstrate the possible effect of bubble resonance on ultrasonic waveforms as a result of air voids within the paste.

CHAPTER 3

Background on wave propagation

This chapter provides a brief introduction to the basic principles to the propagation of ultrasonic stress waves in solids. Further details are available in several books on wave propagation [37–39].

3.1 Propagation of stress wave in solids

In linear elasticity, the surface traction t_i on a plane within a solid $n_i x_i = d$ is given by the Cauchy stress formula

$$t_i = \sigma_{ij} n_j, \tag{3.1}$$

where σ_{ij} is the stress tensor.

The balance of linear momentum for a solid body with surface S and volume V subjected to surface traction t_i and body force f_i can be expressed as

$$\int_S \sigma_{kl} n_k dS + \int_V \rho f_l dV = \int_V \rho \ddot{u}_l dV \tag{3.2}$$

with ρ representing the material mass density. Gauss' theorem applied to Eq.(3.2) leads to

$$\int_V (\sigma_{kl,k} + \rho f_l - \rho \ddot{u}_l) dV = 0 \tag{3.3}$$

Eq.(3.3)has to be fulfilled for any arbitrary volume V of the solid body, and therefore the stress equations of motion becomes

$$\sigma_{kl,k} + \rho f_l = \rho \ddot{u}_l \tag{3.4}$$

Ultrasonic testing utilizes mechanical waves being composed of oscillations of particles in the material. It is more efficient to have the equations of motion given solely in terms of the displacement, u_i (as opposed to Eq.(3.4), which has terms of stress σ_{ij} and displacement u_i). This can be achieved by applying Hooke's law. For a homogeneous, isotropic and linear elastic solid, the generalized form of Hooke's law is given by

$$\sigma_{ij} = \lambda \epsilon_{kk} \delta_{ij} + 2\mu \epsilon_{ij}, \tag{3.5}$$

where ϵ_{ij} is the strain tensor, related to the displacement u_i by

$$\epsilon_{ij} = \frac{1}{2}(u_{i,j} + u_{j,i}), \tag{3.6}$$

and μ and λ are the Lamé constants. Plugging Eq.(3.6) into Eq.(3.5) and subsequently into Eq.(3.4) and neglecting body forces $\mathbf{f}$ leads to Navier's equations of motion

$$\begin{aligned} \mu u_{i,jj} + (\lambda + \mu) u_{j,ji} &= \rho \ddot{u}_i \\ \mu \nabla^2 \mathbf{u} + (\lambda + \mu) \nabla \nabla \cdot \mathbf{u} &= \rho \ddot{\mathbf{u}}. \end{aligned} \tag{3.7}$$

Solving Eq.(3.7) is somewhat difficult as it couples a partial differential equation (PDE). The Helmholtz decomposition

$$\mathbf{u} = \nabla \varphi + \nabla \times \psi, \tag{3.8}$$

provides a more convenient way to uncouple these equations. Eq.(3.8) represents the three components of displacement u with the four functions φ, ψ_1, ψ_2, and ψ_3. To guarantee the uniqueness of the solution, an additional constraint

$$\nabla \cdot \psi = 0 \tag{3.9}$$

is introduced. Substitution of Eq.(3.8) into Eq.(3.7) leads to the two uncoupled wave equations expressed in terms of the displacement potentials φ and ψ

$$\nabla^2 \varphi = \frac{1}{{c_L}^2} \ddot{\varphi}, \quad \nabla^2 \psi = \frac{1}{{c_T}^2} \ddot{\psi}, \tag{3.10}$$

whereas c_L represents the wave velocity of the longitudinal wave (P-wave) and c_T the wave velocity of the vertically and horizontally polarized shear waves (SV and SH waves),

$${c_L}^2 = \frac{\lambda + 2\mu}{\rho}, \quad {c_T}^2 = \frac{\mu}{\rho} \tag{3.11}$$

It is always true that $c_L > c_T$. Both wave velocities are expressed in terms of material properties density ρ and the Lamé constants μ and λ. The Lamé constants define the elastic behavior of isotropic solids. These two constants may also be conveniently expressed in terms of the 'material properties Young's modulus E and Poisson's ratio ν as given by

$$\lambda = \frac{E\nu}{(1+\nu)(1-2\nu)}, \tag{3.12}$$

$$\mu = \frac{E}{2(1+\nu)}. \tag{3.13}$$

Thus, the two wavespeeds can be rewritten as

$${c_L}^2 = \frac{E}{\rho} \cdot \frac{1-\mu}{(1+\mu)(1-2\mu)}, \quad {c_T}^2 = \frac{E}{\rho} \cdot \frac{1}{2(1+\mu)} \tag{3.14}$$

3.1.1 Plane wave phenomena

When an elastic wave encounters the interface of two media, that is half-spaces, the resulting stresses and displacements must be balanced through a combination of reflected and refracted waves. Assuming a wave with constant properties (ϵ, σ, u) on a plane perpendicular to its direction of propagation $\mathbf{p}$. Eq.(3.15) shows the mathematical representation of a plane wave,

$$\mathbf{u} = f(x \cdot \mathbf{p} - ct)\mathbf{d} \tag{3.15}$$

where $\mathbf{d}$ is the unit vector defining the direction of particle motion, and c is either the longitudinal wave velocity c_L or the transverse wave velocity c_T. By substituting Eq.(3.15) into Eq.(3.7), one obtains

$$(\mu - \rho c^2)\mathbf{d} + (\lambda + \mu)(\mathbf{p} \cdot \mathbf{d})\mathbf{p} = 0. \tag{3.16}$$

Since $\mathbf{p}$ are the two different unit vectors, it can immediately be seen that the two possible solutions that form the basis of wave propagation are either $\mathbf{d} = \pm\mathbf{p}$ or $\mathbf{p} \cdot \mathbf{d} = 0$:

1) $\mathbf{d} = \pm\mathbf{p}$ leads to $\mathbf{p} \cdot \mathbf{d} = \pm 1$ and yields with Eq.(3.16), $c = c_L$ (see Eq.3.14). Since $\mathbf{d}$ and $\mathbf{p}$ are linearly dependent, this represents a particle movement in the direction of propagation – a longitudinal or P-wave.

2) $\mathbf{p} \cdot \mathbf{d} = 0$ yields with Eq.(3.16), $c = c_T$ (see Eq.3.14). Now the direction of motion is normal to the direction of propagation, and the wave is called a transverse wave. If a two dimensional plane of propagation is considered (for example, the (x_1, x_2) plane), a wave with an in-plane displacement (in the (x_1, x_2) plane) is called an SV-wave (vertically polarized), while a wave with out-of-plane displacement (in the x_3 direction) is called an SH-wave(horizontally polarized).

In a homogeneous, isotropic material, longitudinal and transverse wave speeds are independent of frequency, or nondispersive.

3.1.2 Mode conversion

The wave types derived so far propagate independently in an infinite media. As soon as a finite media in the direction of propagation is considered, reflections and coupling will occur. An incident P-wave (or SV-wave) as described previously, is reflected at a stress free boundary ($\sigma_{21} = 0$ and $\sigma_{22} = 0$), resulting in reflection of both a P-wave and SV-wave. Figure (3.1) shows the reflections of an incident P and SV-wave.

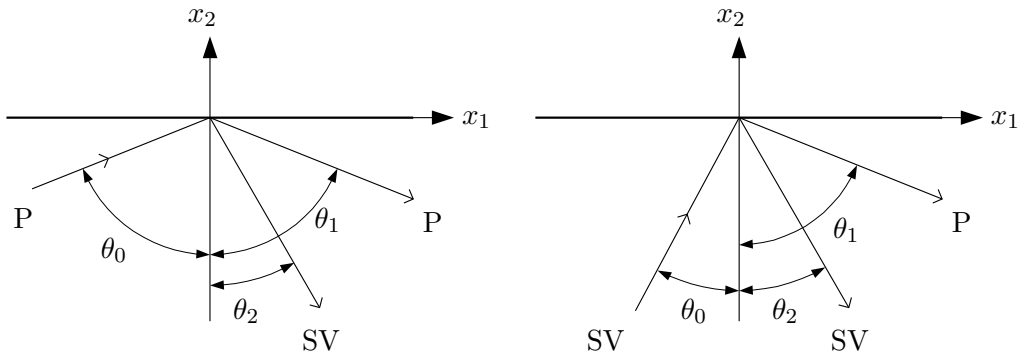

(a) Reflection of a P-wave (b) Reflection of a SV-wave

Figure 3.1: Reflection of waves

The effect of a single incident wave-type producing two different waves (after reflection from a boundary) is called mode conversion. The displacement field of a harmonic wave in the x_1, x_2 plane (propagating in an infinite media, plane strain case) can be expressed as,

$$\mathbf{u}^{(n)} = A_n \mathbf{d}^{(n)} e^{ik_n(x_1 p_1^{(n)} + x_2 p_2^{(n)} - c_n t)}, \tag{3.17}$$

whereas n denotes the wave (longitudinal or transverse), $k_n = \frac{\omega}{c_n}$ is called the wave number of wave n, and the respective wave velocities are c_n. Using these definitions, and noting that the angular frequency ω remains constant for the incident and reflected waves, it is possible to determine the relationship between the angle of the incident and the angles of the reflected waves. In order to obtain non-trivial amplitudes A_n, the angles of incident and reflected waves, θ_0, θ_1, and θ_2 as depicted in Fig. (3.1), must satisfy Snell's law:

$$k_0 \sin\theta_0 \;=\; k_1 \sin\theta_1 \;=\; k_2 \sin\theta_2. \tag{3.18}$$

Exceptions of mode conversion are the normal incidence with $\theta_0 = 0$, in which case the waves are reflected as themselves, and if the angle θ_0 is greater than a critical angle,

$$\theta_{cr} = \arcsin\frac{c_T}{c_L}; \tag{3.19}$$

then only a SV-wave is reflected. The P-wave portion of the reflected signal degenerates into a surface wave (Rayleigh wave), travelling along the surface and exponentially decreasing in amplitude with increasing depth.

3.2 Attenuation

3.2.1 Definition

In experimental setups, measured attenuation is the superposition of several attenuation mechanisms, which are introduced and briefly explained. Assuming the geometry is already known, geometric attenuation can be accounted for prior to testing. Generally, interest is mainly on intrinsic attenuation associated with material absorption

and scattering effects. Consider a plane stress wave that is attenuated as it propagates through the medium:

$$\sigma(x,t) = \sigma_0 e^{i(\omega t - kx)} \tag{3.20}$$

where ω denotes the angular frequency, and k is called the wave number. This expression is valid for an attenuated wave only if either the wave number k or the velocity c is complex. Thus, taking the wave number to be complex $k = k_1 - i\alpha$, one obtains the equation for a plane attenuated wave:

$$\sigma(x,t) = \sigma_0 e^{-\alpha x} e^{i(\omega t - k_1 x)} \tag{3.21}$$

The attenuation factor α is thus defined as the imaginary part of the complex wave number and the phase velocity is given by $c = \frac{\omega}{k_1}$. As it is understood that α causes an exponential decay in pressure amplitude, one can use

$$\sigma(x) = \sigma_0 \cdot e^{-\alpha x} \tag{3.22}$$

to specify the attenuation α, which is not dependent on x. Another way of expressing the same thing is to write

$$\log_e \sigma(x) = \log_e \sigma_0 - \alpha x \tag{3.23}$$

Then, for two different points x_1 and x_2 where $x_1 < x_2$, the difference of expressions at the two points is

$$\alpha = \frac{1}{x_2 - x_1} \log_e \frac{\sigma(x_1)}{\sigma(x_2)}, \tag{3.24}$$

and, since any ratio of two pressure amplitudes such as $\sigma(x_1)$ and $\sigma(x_2)$ must, in order to be expressed in decibels (dB) or in nepers (Np), be written, respectively, as

$$20 \log_{10} \frac{\sigma(x_1)}{\sigma(x_2)} \text{ dB} \quad \text{or} \quad \log_e \frac{\sigma(x_1)}{\sigma(x_2)} \text{ Np} \tag{3.25}$$

then

$$\alpha = \frac{1}{(x_2 - x_1)} 20 \log_{10} \frac{\sigma(x_1)}{\sigma(x_2)} \text{ dB/unit length,} \tag{3.26}$$

$$\alpha = \frac{1}{(x_2 - x_1)} \log_e \frac{\sigma(x_1)}{\sigma(x_2)} \text{ Np/unit length,} \tag{3.27}$$

$$\alpha \text{ (Np/unit length)} = 8.686 \; \alpha \text{ (dB/unit length)} \tag{3.28}$$

The ratio between pressures $\sigma(x_2)$ and $\sigma(x_1)$ at two different distances, due to the attenuation along the transducer axis, is shown in Fig.3.2 versus path difference $x_2 - x_1$. The coefficients of α vary between 0 and 50 dB/m.

3.2.2 The cause of attenuation

The cause of total attenuation may be divided into two classes: those "intrinsic" attenuations that are of physical interest, having to do with physical properties of the material (absorption and scattering), and those apparent or "extrinsic" attenuations arising as a result of the method by which the attenuation measurements are made (geometric).

Material absorption, α_a: General elasticity theory assumes that a material stores energy without dissipation during deformation. However, many materials (e.g. polymers, composites like cement-based materials) do dissipate part of the stored energy through absorption. Such materials are said to be viscoelastic – combining the properties of an elastic solid and a dissipative viscous liquid. Viscoelasticity occurs if the material stress and strain are not single-valued

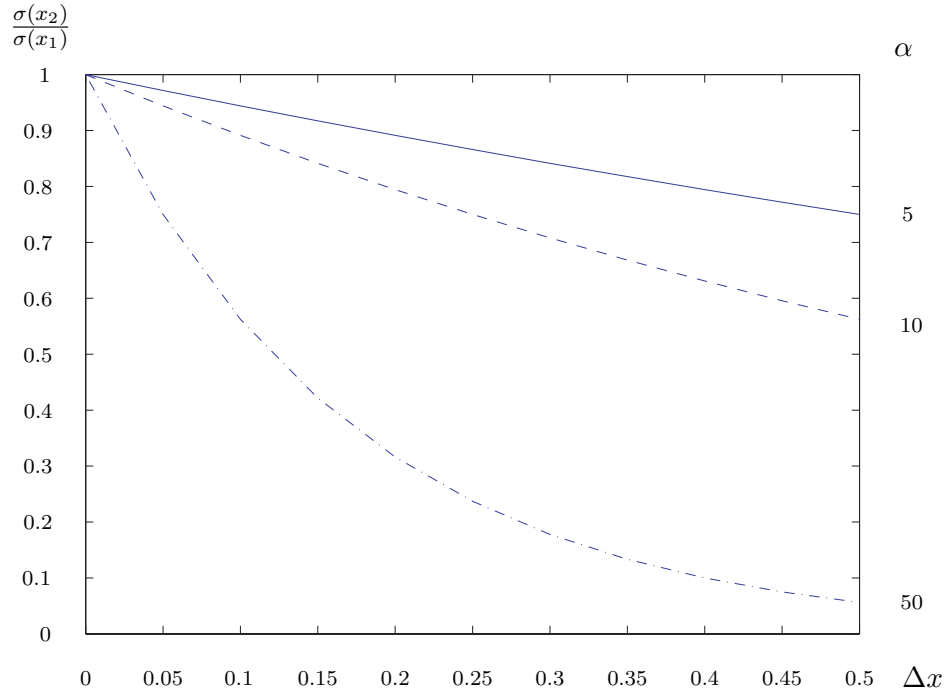

Figure 3.2: Relative pressure $\frac{\sigma(x_2)}{\sigma(x_1)}$ versus path difference Δx [m], due to attenuation α [dB/m]

functions of one another for a complete cycle of oscillatory stress; that is, stress is a function not only of strain but also the time derivative of strain. Even when the stress-strain part of the equation remains piecewise linear, the presence of time derivatives assures dissipation. The result is the hysteresis effect – the strain can not keep up with the alternation in stress. If the strain is not homogeneous, as for example, in the case of a longitudinal ultrasonic wave propagating through metals [40], temperature gradients will be set up between regions of compression and of rarefaction. This will lead to a flow of heat, accompanied by a production of entropy, and attenuation of the pressure wave amplitude. This type of attenuation is reportedly proportional to the square of frequency.

In some polymers, in the glassy state (above the rubber-glass transition), an absorption has been observed with attenuation coefficient, α_a proportional to the first power of the frequency [41]. This type of absorptionis called hysteresis absorption. Hysteresis absorption has also been observed in biological tissues [42]. A quantitative model was proposed for hysteresis absorption in polymers [41]. However, no quantitative model for hysteresis has been developed for any material in which this type of loss has been observed. It should be noted that hysteresis loss can be accounted for formally by assuming a relaxation mechanism with a very broad distribution of relaxation times extending over many decades of frequency [42].

Scattering, α_s: Scattering, which is the other part of the intrinsic attenuation, arises at the boundaries between materials, grains, or inclusions with different elastic properties. These differences are associated with the grain structure, multiple phases, precipitates, crystal defects from dislocations, etc. In short, any inhomogeneity can serve as scatterer. The general problem of expressing attenuation due to scattering through a medium containing scatterers with given size, shape, material property, and density of scatterers dates further back. When the scatterer density is low, the loss caused by a single scatterer is not affected by the presence of other scatterers and the total loss can be calculated from the so called *single scattering theory.*

The scattering from an individual can be treated independently [39], as anticipated in Fig. 3.3(a) and the combined scattering attenuating effect is simply the arithmetic addition of their individual contributions. When propagating waves experience many scattering events (high scatterer density), as one shown Fig 3.3(b)-(d), multiple scattering effects are present and the problem for obtaining scattering attenuation is much more complicated. The approach to multiple

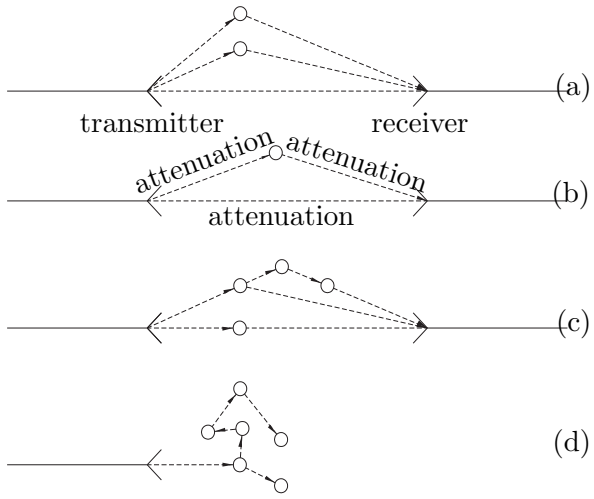

Figure 3.3: Scattering models (a) single scattering, (b) first order multiple scattering, (c) multiple scattering, and (d) diffusion approximation

scattering involves methods primarily due to Foldy [44], Waterman and Truell [45], who utilized the technique called configuration average and by Dainty and Toksoz [46], who modelled the scattered wavefield energy by a diffusion approximation (or *diffusive wave theory*).

Three scattering regions are usually defined on the basis of (single, or self similar) scatterer size a to the wavelength λ ratios [47] and the functional dependence of scattering losses on frequency can be often established without really solving the wave equation.

$$\begin{aligned} \alpha_s &\sim f^4 \cdot a^3 \quad - \text{ Rayleigh Domain}, 2\pi a/\lambda << 1 \\ \alpha_s &\sim f^2 \cdot a^3 \quad - \text{ Stochastic Domain}, 2\pi a/\lambda \approx 1 \\ \alpha_s &\sim a^{-1} \quad - \text{ Geometric Domain}, 2\pi a/\lambda > 1 \end{aligned} \tag{3.29}$$

Geometric spreading: Spreading of the ultrasonic wave attenuates the initial wave amplitude independent of frequency. Geometric attenuation is dependent on the wave mode and geometry of the elastic body under investigation. Plane longitudinal wave amplitudes are attentuated at $1/r$, where r is the distance to the (point) source.

CHAPTER 4

Experimental procedure

This section describes the experimental setup for performing ultrasonic measurements on hydrating cement pastes as well as additional tests on the cement pastes. The discussion covers necessary equipment, a description of specimens, and analysis techniques used on data collected.

4.1 Ultrasonic experimental setup

Figure 4.1 illustrates the experimental setup used for conducting ultrasonic measurements.

4.1.1 Ultrasound equipment

Pulser/Receiver: a Panametrics 5072PR pulse generator provides the source signals for the ultrasonic experiments. The transmission node on the pulser is connected to a piezoelectric transducer; when the pulser generates an electrical impulse, it excites the crystal within the transducer, which converts the signal to mechanical energy and generates and ultrasonic pulse. The use of impulse signals allows for a broadband performance of the transducer.

Piezoelectric transducers convert electrical energy into mechanical energy, such as ultrasonic pressure waves, based on the piezoelectric effect [48]. The

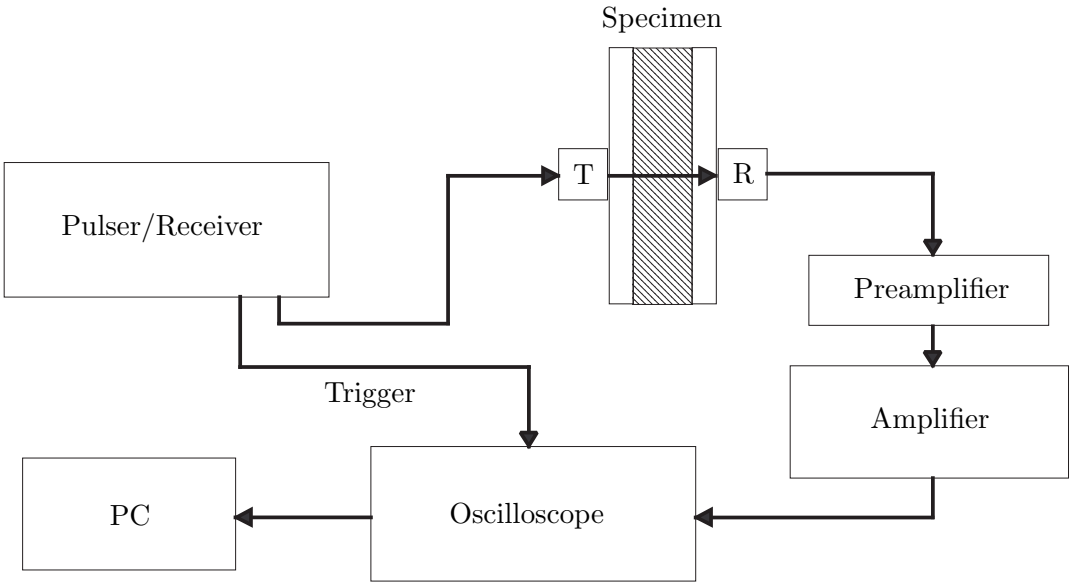

Figure 4.1: schematic diagram of the ultrasonic measurement system for hydrating cement pastes

conversion occurs in the piezoelectric active element of the transducer, in which electrical voltage across the element induces mechanical stress and vice versa. Active elements are generally made of certain crystals, such as quartz, or ceramics. For the experimental setup, a pair of broadband Panametrics V103 1.0/0.5" (1 MHz nominal center frequency) transducers were used in a through-transmission orientation – ultrasonic longitudinal pulse from the transmitting transducer (labelled as T in Figure 4.1) travels through the specimen to be received and converted to an electrical signal by the receiving transducer (labelled R in Figure 4.1).

Pre-amplifier and amplifier: the signal from the receiving transducer is subsequently processed by a Digital Wave PA2040G/A Preamplifier and a Digital Wave FTM4000 Amplifier. The preamplifier provides conditioning to the electrical signal by improving the signal-to-noise ratio; this particular preamplifier

allows for discrete amplification of the signal by -20 dB, 0 dB, 20 dB, and 40 dB. The preamplifier component is essential for monitoring the evolution of ultrasonic waveforms through hydrating paste; as the paste proceeds from a fluid matrix to a solid, hardening matrix, the magnitude of signal received can change by a factor of 100. Without the preamplifier to overcome signal-to-noise issues, the experiment would require much higher pulse energy during the earliest hours of hydration, which could potentially damage the transducers and overwhelm the circuitry of the oscilloscope. The amplifier can provide for an additional 21 dB of signal amplification - via a switch - as used for this set of experiments.

Oscilloscope: once processed by the preamplifier and amplifier, the signal is displayed and recorded by a Tektronix TDS5034 Digital Oscilloscope. The signal is displayed on the time-domain with amplitude representing the waveform voltage. The oscilloscope allows for the user to specify sampling frequency (resolution), sample size, and signal averaging for the waveform of interest before saving the data.

4.1.2 Specimen containment

In order to collect ultrasonic waveforms, a thru-transmission technique is used. However, unlike solid specimens, which allow for direct contact between the transducers and specimen surfaces, the fresh paste requires a means of containment that allows for measurements and interfaces that prevent contact between transducer and hydrating paste. In this case a closed-cell, silicon rubber gasket is sandwiched between two 2.0 mm thick acrylic glass sheets, which serve as interfaces for the transducers. The gasket is U-shaped to provide space for the paste. For the sake of holding the transducers in place throughout the measurements, two 20.0 mm acrylic glass sheets

drilled with holes fitted to the diameter of the transducers are placed on the outside surfaces of the thinner acrylic glass sheets. With one of two foam gaskets in place, the entire container is compressed by four threaded rods, providing a paste cavity of 12.0 mm or 16.0 mm in thickness; cavities thicker than 16.0 mm were found to be too attenuative to early hydration waveforms. The transducers are then coupled to the thinner acrylic surfaces using silicon grease. Signals generated at the transmitting transducer pass through the first 2.0 mm acrylic sheet, into the paste specimen, and finally through the second 2.0 mm acrylic sheet where the receiving transducer collects the signals.

Paste specimens are mixed and immediately placed in the containment vessel through an opening at the top. After consolidation of the paste through vibration or use of a metal rod, a silicon rubber stopper is inserted in the top opening. The gasket and stopper provide an effective moisture barrier, preventing evaporation and ensuring that shrinkage effects in the paste are attributable to autogenous and chemical shrinkage and not drying shrinkage. With this system, ultrasonic measurements can proceed within 20 minutes of first mixing.

4.1.2.1 Shrinkage effects on measurements

In designing the containment system, several necessary shrinkage considerations became apparent. Initially, thicker 25.0 mm acrylic barrier sheets were used for the transducer interfaces with the intent of isolating any echo effects in received waveforms and to prevent elastic deformations of this interface due to dimensional changes in the paste specimen. However, dimensional changes due to plastic shrinkage are practially unavoidable for fresh cement paste, and the paste has a tendency to "pull away" from the acrylic barriers after as little as 5 to 12 hours of hydration, completely cutting off signal transmission to the receiving transducer as seen in preliminary tests.

Further, preliminary tests suggested that the highly attenuative nature of fresh cement paste makes echoing effects negligible with any interface.

Surprisingly, previous research into ultrasonic monitoring of fresh cement paste does little to address the issue of interface decoupling due to shrinkage; several researchers do not address this issue at all despite using thicker, more rigid acrylic interfaces. Among the latter: the use of mortar – cement paste with sand aggregate – may have provided the dimensional stability to make such shrinkage effects negligible [8– 9] or monitoring times may be left limited to only those early times not visibly affected by decoupling [5]. Reinhardt and Grosse suggest maintaining a layer of free water at the top of the paste specimen such that it can percolate down to fill gaps formed as the paste separates from the 15.0 mm acrylic interfaces [3– 4]. This last solution brings up concerns that the introduction of additional free water will unintentionally increase the w/c ratio and porosity at exposed paste surfaces and possibly alter the original mix design during chemical hydration. Also, any chemical shrinkage that results in dilatation of internal pores will pull additional water into the specimen.

Shrinkage effects in this investigation are unavoidable without altering either the mix design or the container rigidity. In order to maintain a relatively consistent acrylic-paste interface, 2.0 mm acrylic glass sheets were selected such that they can undergo elastic plate deformation with the shrinkage of the paste while maintaining contact with the specimen. In addition, simply smearing a thin layer of silicon grease – chemically inert to the hydration process – on the interior surfaces of the acrylic glass does improve contact between the hydrating paste and the acrylic – while not completely eliminating the decoupling effect – and offers a practical form-release agent.

4.2 Cement paste specimens

Specimens were prepared for this investigation from an ASTM Type I Portland cement produced by Lafarge. Bogue potential composition for this particular cement is provided in Table 4.1 based on chemical oxide analysis.

Table 4.1: Specimen specifications

Oxide	Amount(%)	Compound	Amount(%)
SiO_2	20.06	C_3S	64.0
Al_2O_3	4.89	C_2S	9.21
Fe_2O_3	3.00	C_3A	7.88
CaO	64.22	C_4AF	9.13
SO_3	2.74		

Specimens vary in the amount of chemical air-entraining agent (Darex AEA provided by W.R. Grace) and specimen thickness as set by the acrylic glass spacing in the specimen container. Eight AEA and specimen thickness combinations exist; further, two separate samples were mixed and monitored for each combination. All specimens are of w/c equal to 0.35 – a relatively low ratio that is often seen in transportation structures. Table 4.2 summarizes the composition of each specimen.

Prior to mixing, the ingredients were measured to an accuracy of 0.1 mg. Once all ingredients were combined they were blended by hand for 30 seconds to wet the cement and then placed in a Hobart N-50 mixer set to the lowest speed for 30 seconds. Then, the sides and bottom of the mixing bowl were scraped before mixing for 60 seconds at medium speed. The prepared paste was immediately scooped to fill approximately half of the specimen container volume and was then rodded with a metal dowel 25 times. The remaining space in the container was filled with paste and rodded another 25 times. Paste was then removed from the top of the cavity to provide room for the silicon rubber stopper, which was snugly fit in place. This mixing procedure was

Table 4.2: Specimen specifications

Name	w/c	Darex entrained agent (% by cement mass)	Thickness (mm)	Entrained air fraction (% by volume)
SP01	0.35	-	12.0	-
SP02	0.35	-	12.0	-
SP03	0.35	0.2	12.0	-
SP04	0.35	0.2	12.0	-
SP05	0.35	0.4	12.0	-
SP06	0.35	0.4	12.0	-
SP07	0.35	0.6	12.0	-
SP08	0.35	0.6	12.0	-
SP09	0.35	-	16.0	-
SP10	0.35	-	16.0	1.2*
SP11	0.35	0.2	16.0	-
SP12	0.35	0.2	16.0	2.5*
SP13	0.35	0.4	16.0	-
SP14	0.35	0.4	16.0	3.7*
SP15	0.35	0.6	16.0	-
SP16	0.35	0.6	16.0	4.9*

*As examined by a petrographer at Lafarge according to ASTM C 457

consistently accomplished such that ultrasonic monitoring could begin at 20 minutes after the ingredients were combined. For each mixture, ultrasonic measurements were recorded every 5 minutes for the first six hours of hydration and then every 15 minutes thereafter until twelve hours of hydration.

In addition to ultrasonic tests, independent tests of setting time, heat of hydration, and autogenous shrinkage were conducted for each mix specification; these are explained as follows:

4.2.1 Vicat time of setting

Vicat tests were conducted according to ASTM C191 [15]. Specimens were batched and mixed as described for the ultrasonic tests and were placed into conical ring molds with approximate dimesions of 40 mm height, 60 mm inside diameter at the top of the ring, and 70 mm inside diameter at the bottom of the ring; glass sheets sealed the bottom opening of the mold. The specimens were smoothed at the top surface using a trowel, and care was taken to avoid compressing the paste during molding procedures. Each batch yielded two molded specimens to allow for verification of results. The specimens were kept in a sealed, moist container to provide a relative humidity greater than 50%.

The Vicat apparatus consists of a vertically-mounted 300 g metal rod holding a flat-tipped needle at the end; the rod moves freely up and down unless held in place by a set screw. A scale along the length of the rod measures its travel distance. Prior to each test, the rod location is adjusted such that the needle tip rests on the surface of the paste and the scale calibrated to an initial distance of 0 mm. When released by the set screw, the rod falls, plunging the needle into the paste specimen until it contacts the glass surface below – an approximate travel distance of 39 mm – or when it is stopped earlier by shear friction within the paste. Although the ASTM procedure suggests leaving them undisturbed for 30 minutes before initiating needle penetration tests, for the actual experiment specimens were left undisturbed for two full hours prior to penetration testing. Vicat Time of Initial Set is defined at the time at which the needle penetrates to 25 mm into the paste. For this reason, penetration tests were conducted every 5 minutes until the needle penetrated less than 25 mm into the paste in order to allow for more accurate interpolation. Tests were conducted every 15 minutes thereafter, each time on a location at least 5 mm from any previous test. Figure 4.2 illustrates an example Vicat Penetration reading for a specimen.

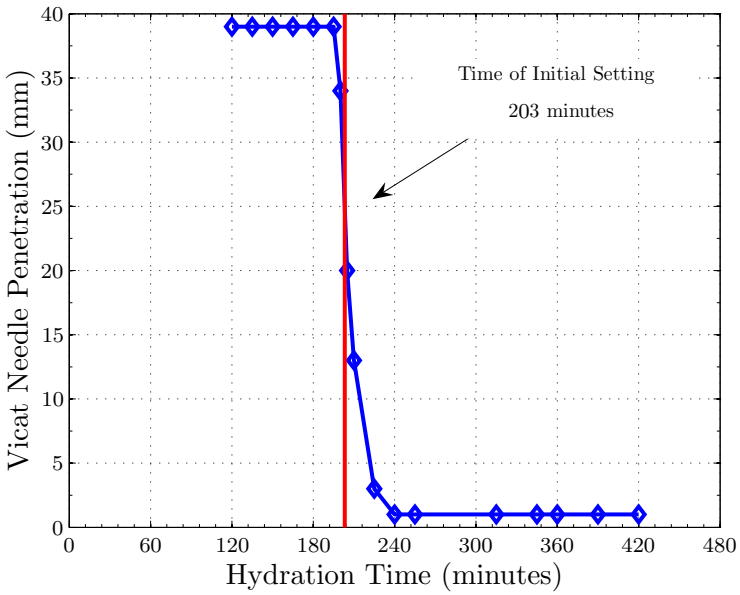

Figure 4.2: Sample result from Vicat Penetration Test

4.2.2 Calorimetry tests

Heat of hydration tests were conducted through use of isothermal calorimetry. Paste batches were prepared in proportion to the ultrasonic test specimens. Materials and equipment were allowed to reach consistent temperature of $23\,^{\circ}\mathrm{C} \pm 1$. Due to a smaller batch size (less than 150 g of paste), paste components were combined in a tumbler and mixed by hand with a metal tamping rod for 2 minutes. Plastic ampoules were filled with 4-7 g of the cement paste and the mass of each paste specimen was recorded prior to loading into a Thermometric 3114 TAM Air isothermal heat-conduction calorimeter. The calorimeter measured the heat flow from each specimen versus an inert reference ampoule and recorded the data every 5 seconds for 50000 data points. This method provides a means to measure the heat of hydration produced by the specimen and indirectly monitor the hydration process.

4.2.3 Autogenous shrinkage tests

Autogenous shrinkage tests were conducted for hydrating pastes based on a method developed by Jensen and Hansen [49]. Immediately following mixing, fresh pastes were placed into plastic, corrugated molds of approximately 300 mm long. Plastic plugs at the end were inserted and sealed using Parafilm, thus preventing moisture loss through evaporation. The specimens were vibrated for approximately 30 seconds on a vibration table to distribute any air pockets. Then, the specimens were mounted in a dilatometer frame fitted with a digital strain gauge, and the entire apparatus placed in an environmental chamber set to 23 °C and 50% relative humidity. Strain readings were read directly from the digital strain gauge every 15 minutes instead of being recorded automatically by a data logger. As these tests measure linear bulk deformation, they represent the effects of isothermal autogenous shrinkage.

4.3 Waveform acquisition

Digitization of analog signal is literally a form of information compression; when processing an analog waveform, such as electrical excitation, through a digital oscilloscope, one must consider appropriate sample parameters in order to preserve meaning and efficiency for future analysis. The sampling rate must be selected such that *aliasing* effects are avoided. For a periodic signal of period T, if the sampling interval Δt is greater than or equal to $\frac{T}{2}$, then frequency aliasing occurs, and the periodicity of the digitized signal appears deceptively greater than that of the true analog signal; in other words, the sampling frequency ($f_s = \frac{1}{\Delta t}$) should be greater than or equal to the *Nyquist* frequency ($f_{ny} = \frac{2}{T}$) [50].

Another important consideration during digitization is signal averaging. Due to the nature of electronic signal acquisition, noise and unpredictable variations are always

inherent in signals. Signal averaging over several waveform records can reduce the interference of these variations and improve the signal-to-noise ratio. Given that the specimens in this investigation are hydrating fresh paste samples and, therefore, undergoing continuous evolution of their viscoelastic structure, any signal averaging distorts the time-dependency of the waveforms. Thus, signal averaging should be substantial enough in number of waveforms averaged such that noise is effectively reduced while also representing a sufficiently short period of time during hydration.

For the ultrasonic tests conducted, waveforms consist of 50000 points at a sampling frequency of 50 MHz and a total window size of 1 ms. This proves sufficient both in avoiding aliasing and ensuring complete capture of the signals of interest. Each ultrasonic measurement in this investigation is averaged from 2000 waveforms consecutively obtained during 1 minute of hydration time.

4.4 Signal Processing

Ultrasonic waveforms are recorded by the oscilloscope in the time-domain. These measurements can provide immediate comparison of the changes in time duration and relative energy of transmission through the paste. Additional insight into the waveforms can be obtained through analysis in the frequency domain; changes in the frequency-response spectra may be more apparent than those in the time-domain.

4.4.1 Discrete Fourier Transform (DFT)

Conversion of a time-based signal to the frequency domain requires consideration of the waveform as a finite sequence of length N where the signal amplitudes are 0 outside of the domain $0 \leq n \leq N-1$. Discretization occurs as a result of digitization of the waveform into individual impulses spaced at regular time intervals $\triangle t$. The

Discrete Fourier Transform, or DFT, presumes that this signal representation can be described as a set of complex, sinusoidal functions, all harmonics of $(\frac{1}{N\triangle t})$. The following

$$V(f_n) = \triangle t \sum_{j=0}^{N-1} v(t_j) \exp[\ -i(\frac{2\pi}{N})jn] \quad (n = 0, 1, ..., N-1) \tag{4.1}$$

$$v(t_k) = \frac{1}{N\triangle t} \sum_{n=0}^{N-1} V(f_n) \exp[\ i(\frac{2\pi}{N})nk] \quad (k = 0, 1, ..., N-1)$$

represent the discrete values of a time signal and its Fourier transform, respectively, where $\triangle t = t_{k+1} - t_k$ is the sampling time interval, and N is the total number of sampled points.

It is important to recognize that the DFT presumes that aperiodic signals of N points are actually periodic with maximum period $T = N\triangle t$; this is illustrated in Fig. 4.3. Thus, $v(t_N) = v(N\triangle t)$ is equal to $v(t = 0)$ and the N length sample repeats from this point. This periodicity is also reflected in Fig. 4.4 for the frequency domain. The value of $V(f_N) = V(N\triangle t)$ is equal to $V(f = 0)$ and is known as the DC offset value. This value is nonzero in the frequency domain if a DC shift exists in the time domain signal.

4.4.2 Windowing

An additional consequence of the periodicity assumption of the DFT is the possibility of *leakage* of the frequency spectra into other frequencies. In the case of a periodic sinusoid, if the section of N points does not contain a whole number of periods, then the periodicity presumption will produce a discontinuity in the time domain input to the DFT function. This is demonstrated in Fig. 4.5. This lack of complete cycles leads to static displacements in the frequency spectra. The effects of spectral leakage can be mitigated by applying to the input signal an appropriate window function, such as

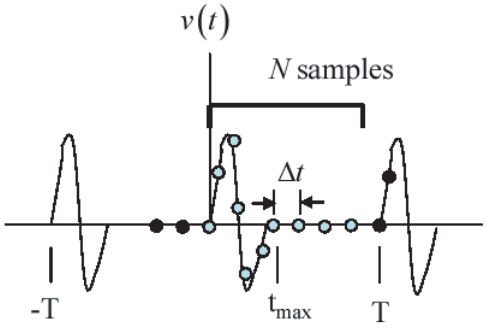

Figure 4.3: A sampled periodic time signal of N sampled values to be used in the DFT (light circles) and other sampled values (dark circles). The sampling interval is t, the time t_{max} is the time at which the transient signal ends and the time $T = N\triangle t$ is the period

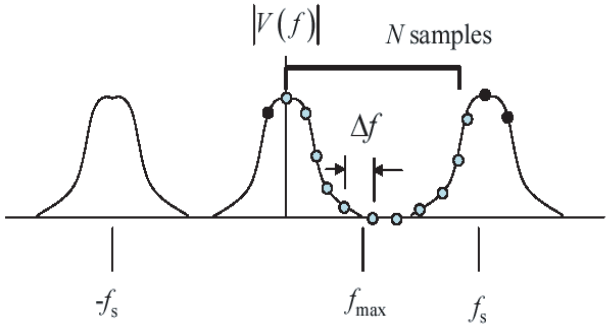

Figure 4.4: The magnitude $|V(f)|$ of a sampled periodic frequency domain function of N sampled values with sampling interval $\triangle f = \frac{1}{T}$. Note that the sampling frequency used to collect the time domain signal $f_s = \frac{1}{\triangle t}$ is twice that of the maximum frequency f_{max} contained in the time signal

a Hanning window as shown in Fig. 4.6. In this case, more of the signal energy is focussed in the main lobe, while the side lobes reduce the leakage of edge discontinuities.

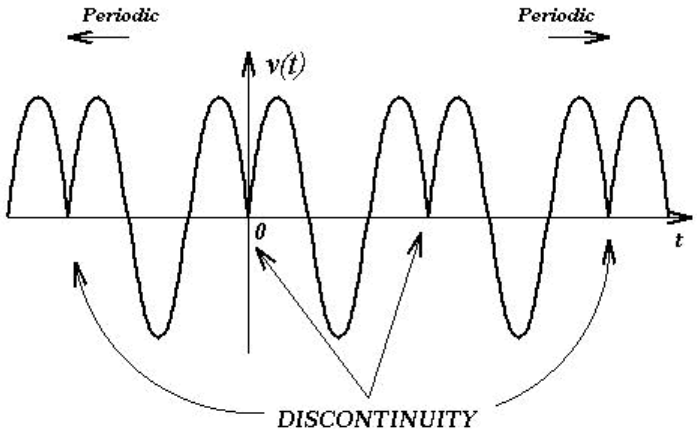

Figure 4.5: Spectral leakage in the DFT

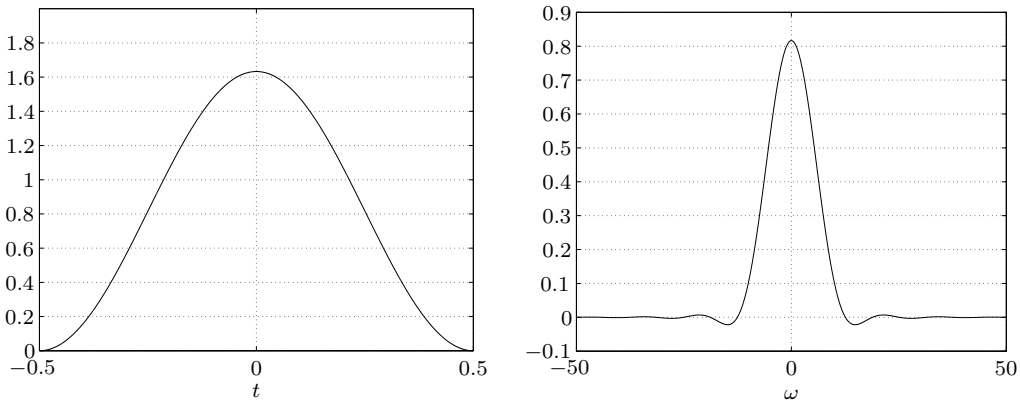

(a) normalized Hanning window

(b) Fourier transform of Hanning window

Figure 4.6: Hanning window

CHAPTER 5

Experimental Results

Results of the additional tests conducted concurrently with the ultrasound tests are described first.

5.1 Cement pastes

5.1.1 Vicat time of setting

Figure 5.1 shows the Vicat Time of Initial Setting for the paste mixes used based on the total air-entraining agent (AEA). Data were obtained from two separate specimens for each mix type. Vicat data are within acceptable standard deviations as stated by ASTM C191 [15]. These data suggest that the addition of the AEA delays the time of initial set by approximately 15-20 minutes for each 0.2% addition of the AEA by weight of cement. Again, these setting times as obtained through Vicat tests only explicitly represent the time at which the shear resistance of the paste can resist the needle at a depth of 25 mm; these tests alone do not provide insight into the process of solidification occuring.

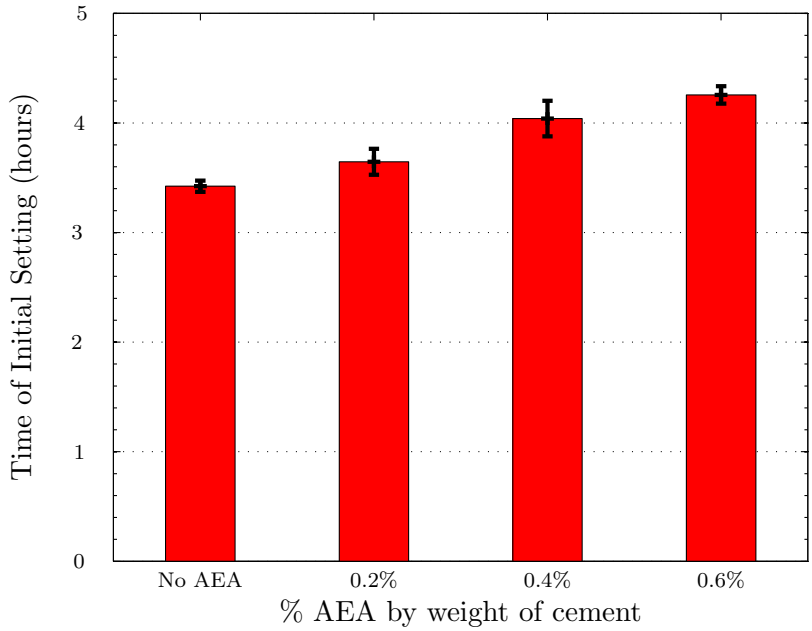

Figure 5.1: Vicat Time of Initial Setting for cement specimens

5.1.2 Calorimetry tests

Figure 5.2 shows the results of calorimetry tests for the paste mixes during the first 24 hours of hydration. As expected, each has an initial period of rapid heat evolution as the cement components dissolute. The Vicat initial set times for each mix occur during the period of high C_3S hydration between 2 and 8 hours of hydration. The specimens closely correspond in their heat evolutions with the exception of the 0.2% AEA specimen. The latter leads the other specimens by approximately 45-60 minutes throughout the first 24 hours, and has a shorter dormant period during the first 2 hours of hydration. Where the heat evolution peak for the other specimens is at 8 hours, the 0.2% AEA specimen peaks at 7 hours. Repeated calorimetry testing confirmed this phenomenon was genuine and consistent, although the time of set for this mixture was not accelerated, as shown in Figure 5.1. This may indicate that

flocculation of cement grains otherwise present in cement without AEA is alleviated with the addition of 0.2% AEA by weight of cement, and any depression of the chemical reaction between water and the cement grains due to the presence of the AEA is offset by an increase in contact between water and cement particle surfaces. However, any further addition of the AEA beyond 0.2% by weight of cement depresses the hydration reactions. Often, admixture producers will add other ingredients to offset ancillary effects. So, it may be that the AEA also contains an accelerator to offset any reduction in the reaction rate by the interaction between the cement and AEA. It may be that this effect is noticed when the admixture is used at lower-than-usual dosage rates.

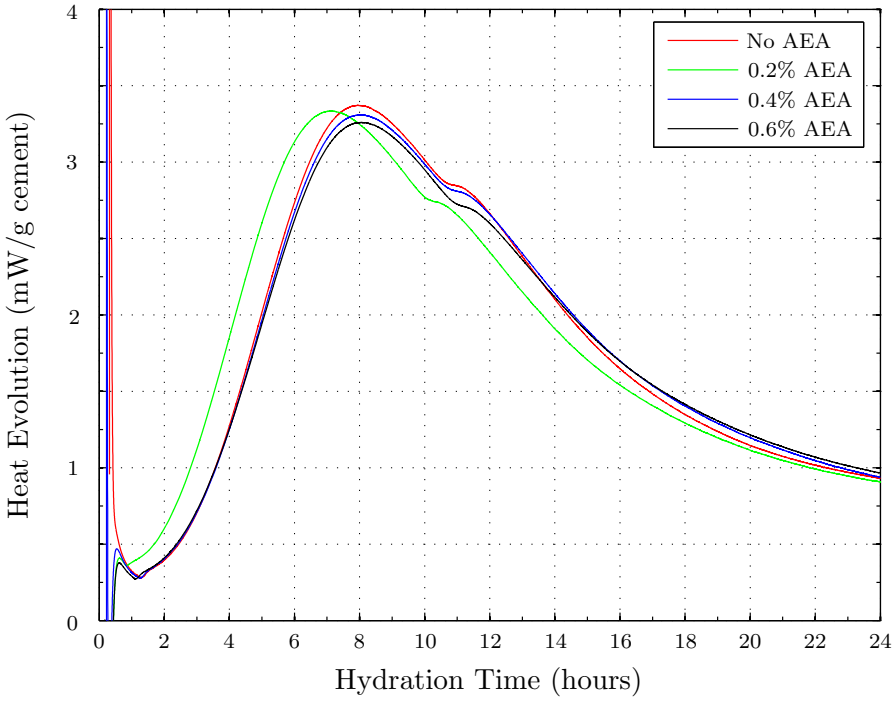

Figure 5.2: Heat of hydration for cement specimens

5.1.3 Autogenous shrinkage tests

Results of autogenous strain measurements on the fresh pastes are displayed in Figure 5.3. All the specimens show a dormant period for the first 30-60 minutes of hydration during which time measurements of bulk linear deformation are stable at zero. This is followed by a period of considerable shrinkage until roughly 4 hours of hydration. During these first 4 hours, the pastes maintain plasticity such that they allow for relatively uninhibited bulk shrinkage. However, the paste matrix undergoes the process of solidification as individual hydration products percolate. Once a sufficient degree of percolation occurs in the solid hydration products, the matrix establishes a rigidity that resists additional autogenous deformations. This resistance is apparent in all of the specimens at 4 hours of hydration when the strain measurements stabilize prior to beginning a period of expansion starting at 5 hours of hydration and proceeding through 12 hours of hydration. This last expansion stage is likely due to the formation of calcium aluminate trisulfate hydrate (ettringite); these components will destabilize and convert back to monosulfate hydrate as the hydration of C_3A and C_4AF renews. Normally, this expansion effect is more than compensated by plastic shrinkage brought on by environmental evaporation; since the specimens are sealed, however, no moisture can escape and plastic shrinkage due to evaporation is negligible.

As seen in the heat of hydration tests, the 0.2% AEA mix appears to be an exception to trends in the other mixes. For the other mixes, the presence of the AEA appears to reduce the autogenous strain at the 4 hour peak by approximately 100-120 μm/m for each additional 0.2% increase in AEA by weight of cement. As presumed from the discussion of the heat of hydration data, the 0.2% AEA mix may serve as an ideal case in which cement grain flocculations are dispersed, allowing greater contact between cement particles and water and resulting in greater reactivity than in the non air-entrained paste.

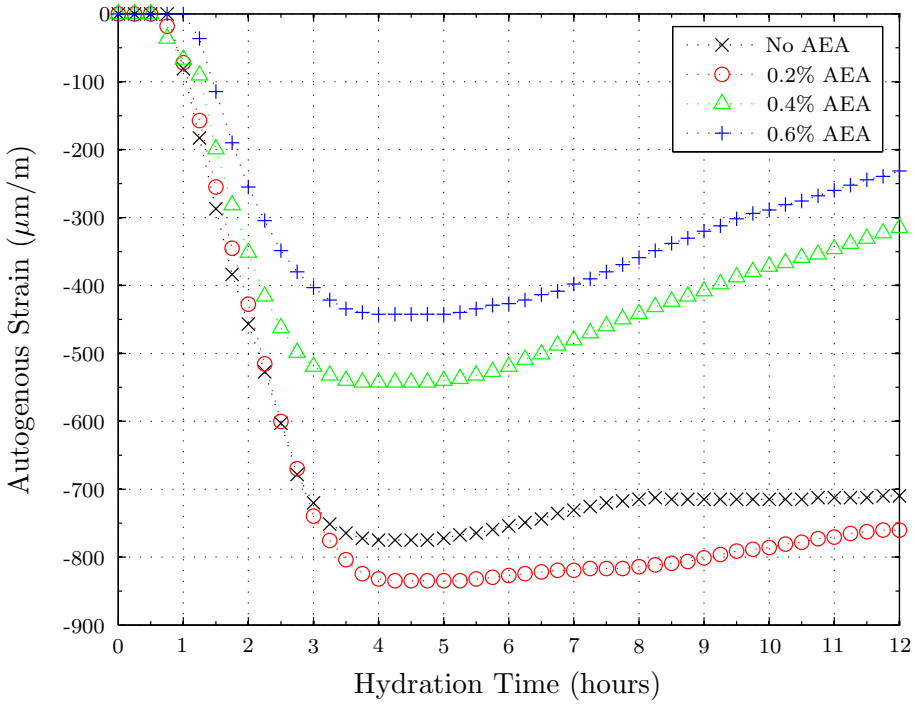

Figure 5.3: Autogenous Strain for cement specimens

5.2 Ultrasonic tests

Ultrasonic tests of the specimens were carried out as described in Chapter 4. Due to particularly high absorption attenuation during the earliest hours of hydration, the received thru-transmission signals were amplified as much as 61 db through a combination of the preamp and amplifier units. These amplification levels were reduced over the course of hydration as solidification decreased the degree of absorption by the paste. Later, the recorded data sets were corrected to factor out amplification. Plots of the time-domain waveforms recorded for all 16 specimens are provided in Appendix A. Each waveform is normalized by its maximum magnitude to allow visual comparison of the character of each waveform during the hydration process; visual inspection

reveals the evolution of each set of waveforms through the course of hydration.

Figure 5.4 shows a comparison of waveforms for a typical non-air-entrained (No AEA) specimen and an air-entrained specimen at three times during the early stages of hydration. The air-entrained specimen has a well-defined wave representing the signal through the paste phase. The non-air-entrained specimen contains a similar waveform with an additional higher-frequency component early in the signal; for the example shown, this higher-frequency component begins at approximately 10 μs. This effect appears universal and unique to the non-air-entrained specimens tested. Not only does this higher-frequency component arrive sooner than the "bulk" wave, but it also maintains a constant arrival time through the first 90 minutes. Further, while the "bulk" wave for both specimens tightens up over time and is clearly dispersive – the wavespeed is a function of frequency – the higher-frequency component in the non-air-entrained specimen shows no change to its general shape, suggesting a travel path through a stable material – most likely water. This is in sharp contrast to the findings of Sayers and Dahlin [7] who observed the opposite phenomenon in which a higher-frequency wave component occurs only in *air-entrained* specimens. In the latter case, the higher-frequency components were attributed to resonance of air-entrained voids.

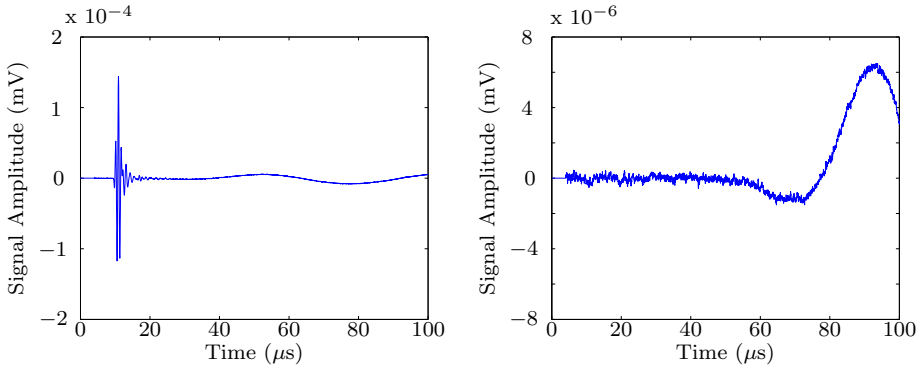

(a) SP01 30 Minutes

(b) SP03 30 Minutes

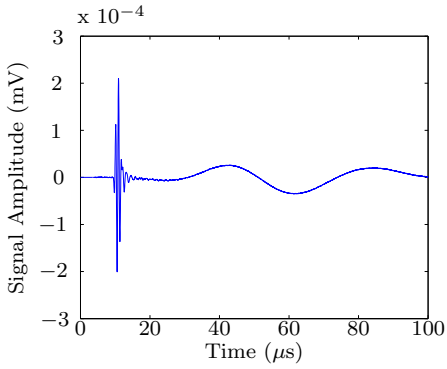

(c) SP01 60 Minutes

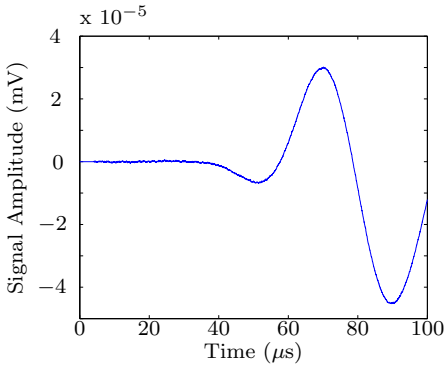

(d) SP03 60 Minutes

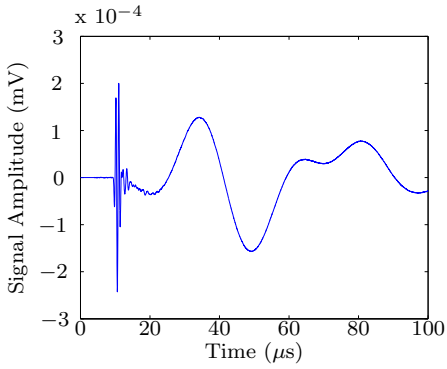

(e) SP01 90 Minutes

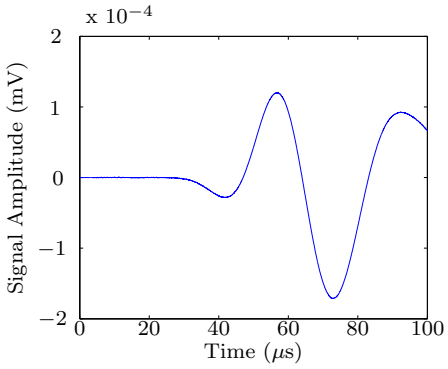

(f) SP03 90 Minutes

Figure 5.4: Comparison of waveforms from a non-air-entrained specimen on the left column (SP01, 12mm thick) and an air-entrained specimen on the right column (SP03, 12mm) each at 30, 60, and 90 minutes of age. Note the presence of a higher frequency component in the non-air-entrained waveform

5.2.1 Signal strength

Initially, a comparison was sought between the signal strengths for the various degrees of air-entrainment. A typical waveform is illustrated in Figure 5.5; the peak-to-peak distance between maximum and minimum values measures the signal strength through the cement paste at a given time.

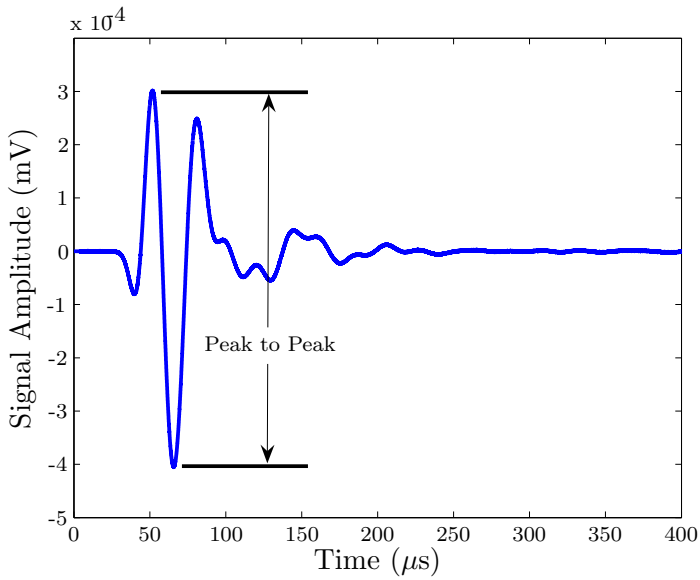

Figure 5.5: Typical waveform in time-domain

Figures 5.6, 5.7, 5.8, and 5.9 show the peak-to-peak magnitudes for each specimen mix type over the first 12 hours of hydration; peak-to-peak amplitudes are shown with linear and logarithmic scales to allow better visual comparison of specimens across the entire hydration timeframe. All specimens show the general trend of increasing peak-to-peak amplitude over the first 12 hours of hydration; this is consistent with expectations that the increasing stiffness of the hydrating paste improves transmission of compression waves. Indeed, through the means of specimen containment and signal amplification as discussed in Chapter 4, the setup is capable of monitoring and

discerning the continuous increase in the signal transmission strength over 4 or 5 magnitudes. As the plots show comparisons of peak-to-peak amplitudes for each specimen thickness monitored, the shorter thickness (12 mm) should also theoretically result in higher peak-to-peak amplitudes than the thicker 16 mm specimens throughout hydration, assuming that a longer travel distance simply results in greater absorption and scattering of signal. However, as shown in the plots, this is not necessarily true particularly after 5 or 6 hours of hydration. In Figures 5.6 and 5.9, both 12 mm specimens actually show peak-to-peak strength falling below that of the 16 mm specimens during the course of hydration.

There is also a severe dropoff in peak-to-peak amplitudes for the specimens at approximately 4-6 hours of hydration. While this dropoff may last for 30 minutes to an hour, the signal peak-to-peak readings eventually return to their prior rate of increase. This is analogous to slipping of grips during tensile tests of materials; load-displacement curves maintain a consistent or continuous slope due to stiffness with sudden decreases in load due to slipping. In the ultrasonic peak-to-peak case, this "slipping" of amplitude readings suggests a dramatic change to the specimens and/or the bond between the acrylic interface and the surfaces of the specimens. Referring again to Figure 5.3, the stabilization of autogenous strain at 4-5 hours and the drops in peak-to-peak amplitudes suggest a correlation between the rigidity of the paste matrix and the reliability of the ultrasonic transmission. In other words, despite efforts to account for hydration shrinkage and decoupling of the paste from the acrylic interfaces, the solidification of the paste eventually results in a material rigidity sufficient enough to resist plastic bonding to the interface. In light of the fact that preliminary tests resulted in complete loss of transmission at these thresholds, the use of the silicon coupling grease does appear to maintain a transmission medium between the paste and the acrylic even after slippage of the peak-to-peak curve, thus

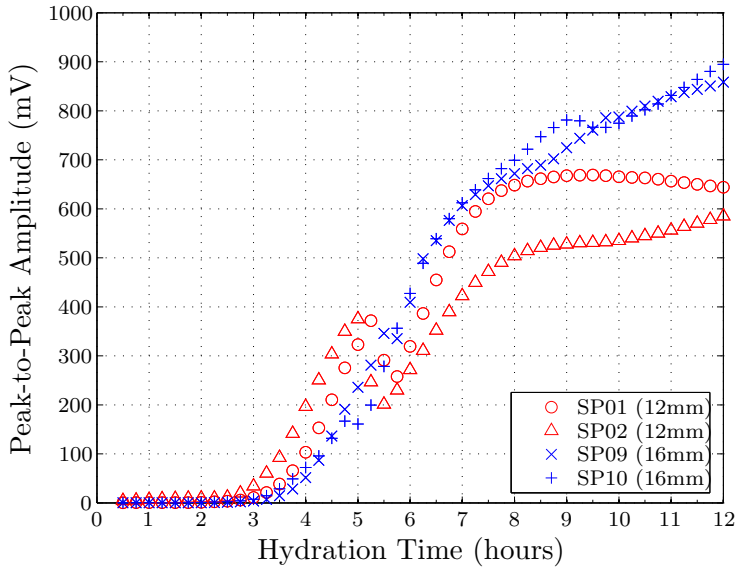

(a)

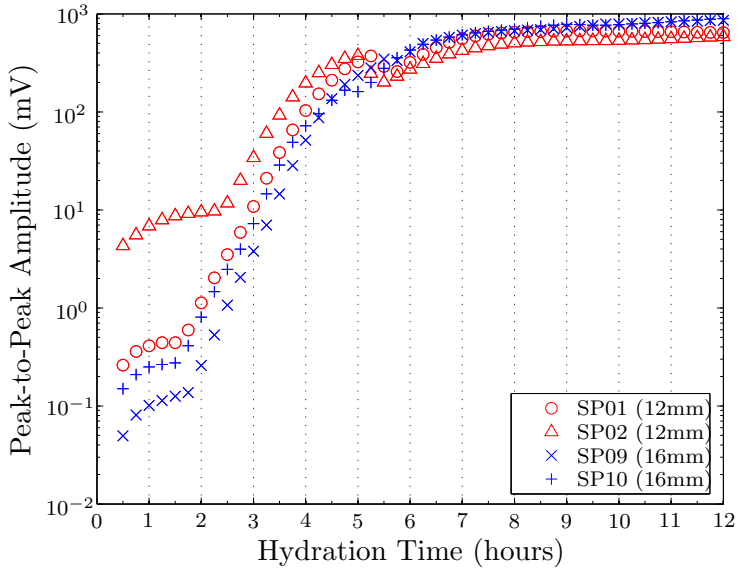

(b)

Figure 5.6: Non-air-entrained Peak-to-Peak comparisons (a) linear, (b) logarithmic

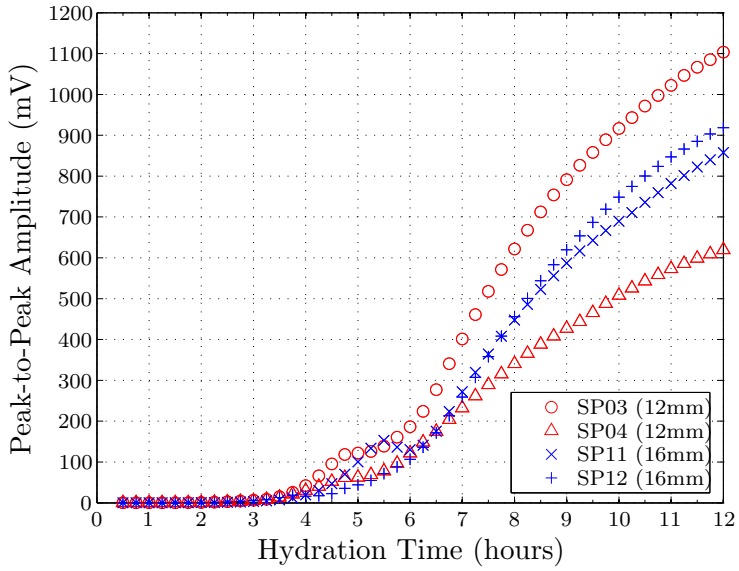

(a)

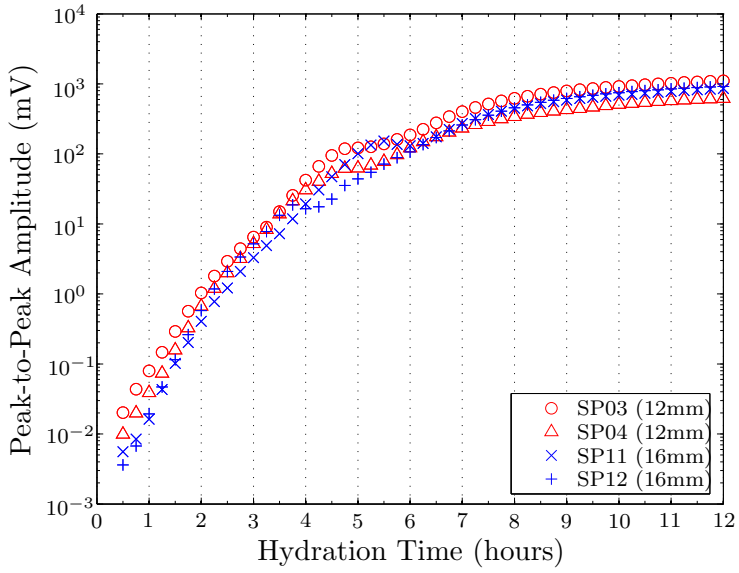

(b)

Figure 5.7: 0.2% AEA Peak-to-Peak comparisons (a) linear, (b) logarithmic

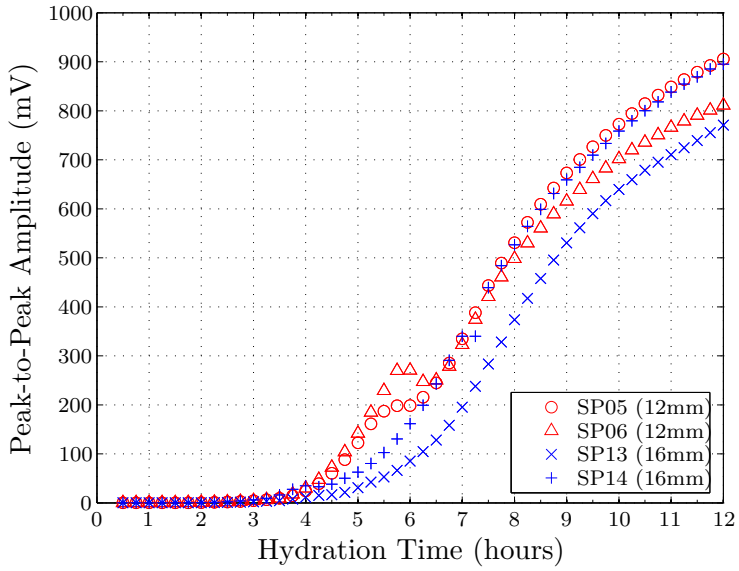

(a)

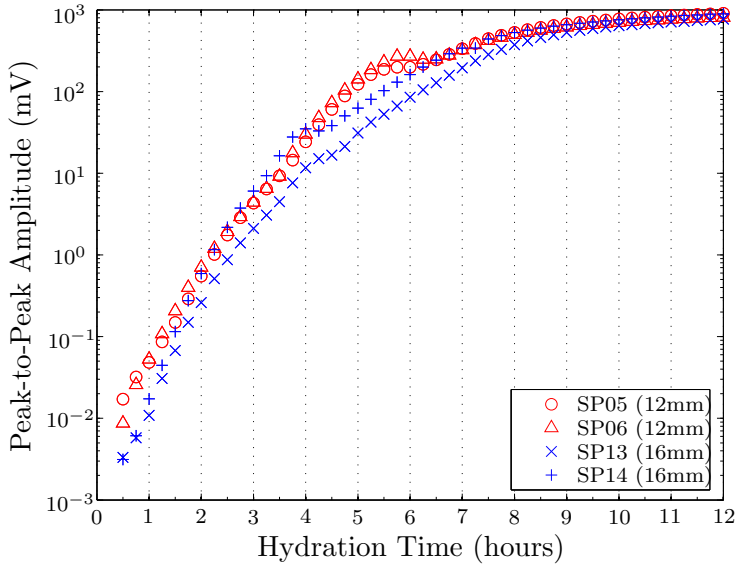

(b)

Figure 5.8: 0.4% AEA Peak-to-Peak comparisons (a) linear, (b) logarithmic

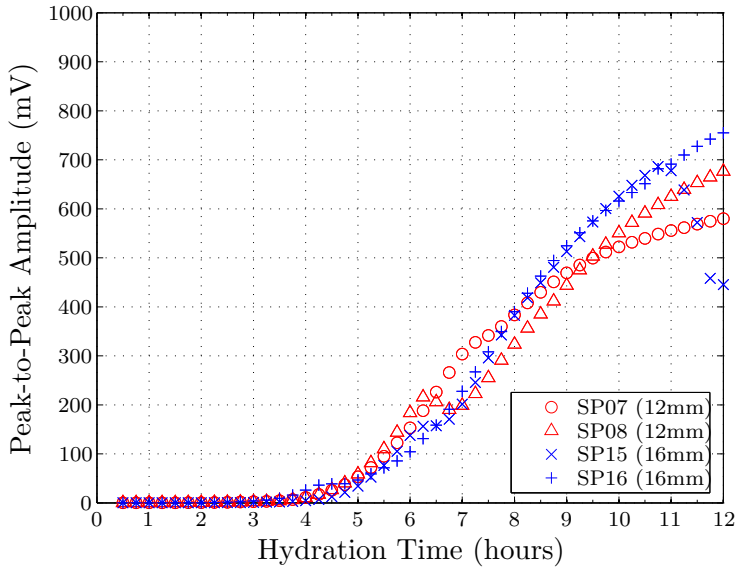

(a)

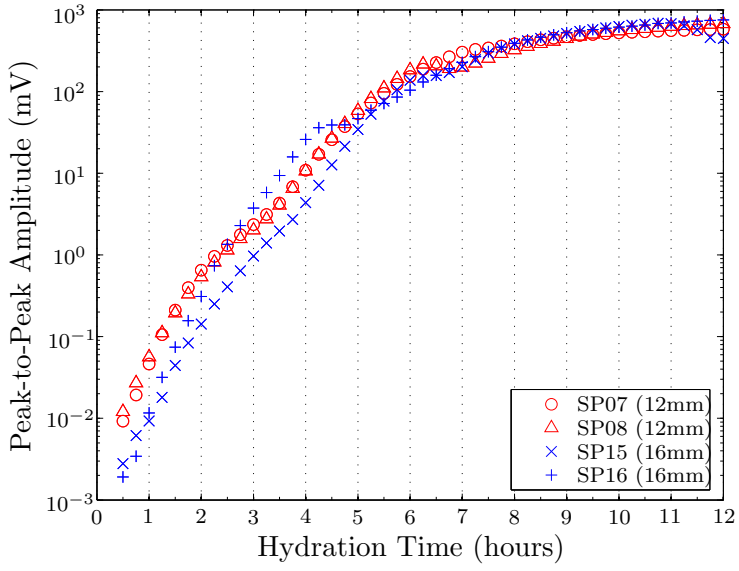

(b)

Figure 5.9: 0.6% AEA Peak-to-Peak comparisons (a) linear, (b) logarithmic

allowing continuous monitoring through the first 12 hours of hydration. Considering the various factors of material solidification, autogenous shrinkage, interface bond, and plate deformation in the acrylic sheets, the peak-to-peak measurements suggest that signal transmission strength through the material cannot be clearly interpreted with the present setup beyond 2-4 hours.

Comparison of Figures 5.6, 5.7, 5.8, and 5.9 with Figure 5.1 suggests correlation between the regions of greatest slope in the linear-scale peak-to-peak plots and the initial setting times as observed through Vicat tests. This rapid increase in peak-to-peak amplitudes through the specimens is indicative of the onset of percolation of hydration solids, which provide less attenuative paths than those of the plastic cement paste. Further, the regions of rapidly increasing peak-to-peak amplitude (linear-scale) show an incremental time-delay with respect to AEA content similar to the delay in initial setting observed in the Vicat tests.

Although direct inspection of peak-to-peak data past a threshold hydration time appears flawed, the method does appear relevant for the first 2 hours of hydration in each specimen as shown in Figures 5.10, 5.11, 5.12, and 5.13. From these plots, the assumption holds that the thinner specimens will have higher signal strengths than the thicker specimens. For the air-entrained specimens, the signal strength transmitted (as measured by peak-to-peak amplitude) appears to increase exponentially for each mix, and the mean peak-to-peak magnitudes transmitted through the 12 mm specimens are roughly 2-5 times those of their 16 mm counterparts.

Figure 5.14 shows the comparison of the mean peak-to-peak values for each mix type over the first 2 hours of hydration. The non-air-entrained specimens are represented by two sets of data: “Wave through water path” considers the entire signal including

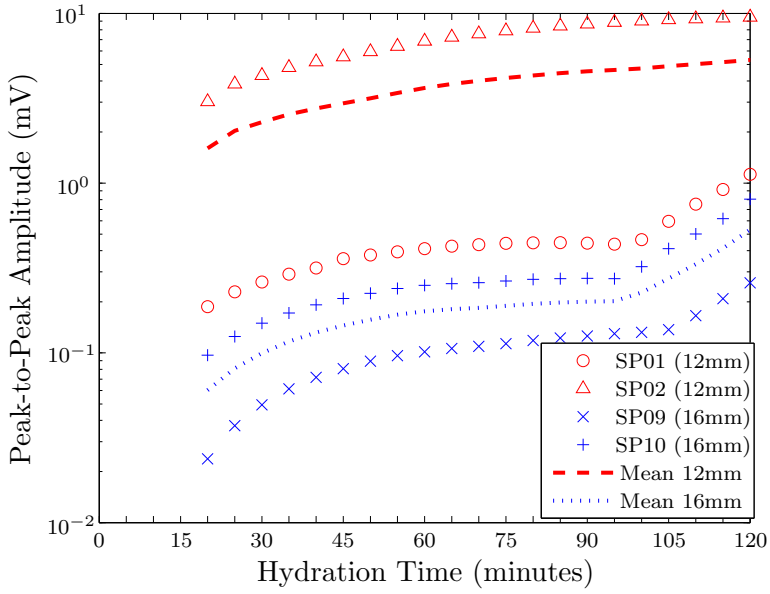

Figure 5.10: Non-air-entrained Peak-to-Peak at first 120 minutes of hydration

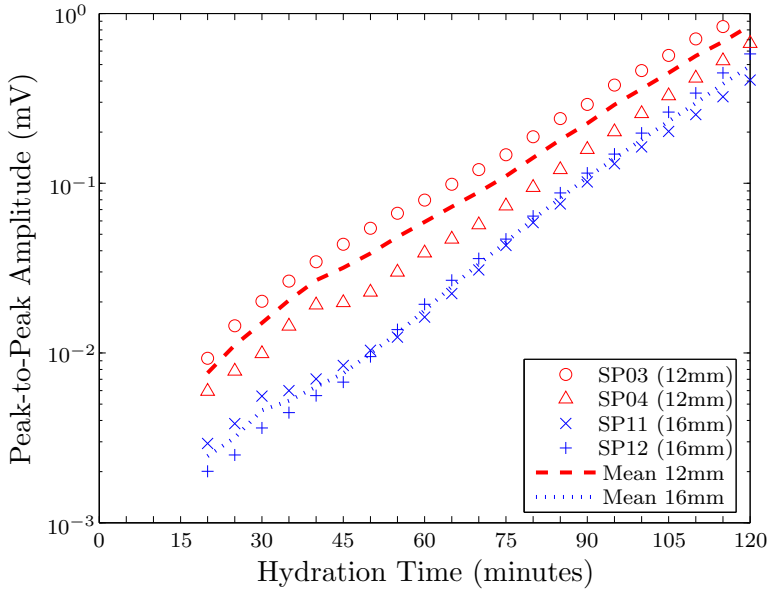

Figure 5.11: 0.2% AEA Peak-to-Peak at first 120 minutes of hydration

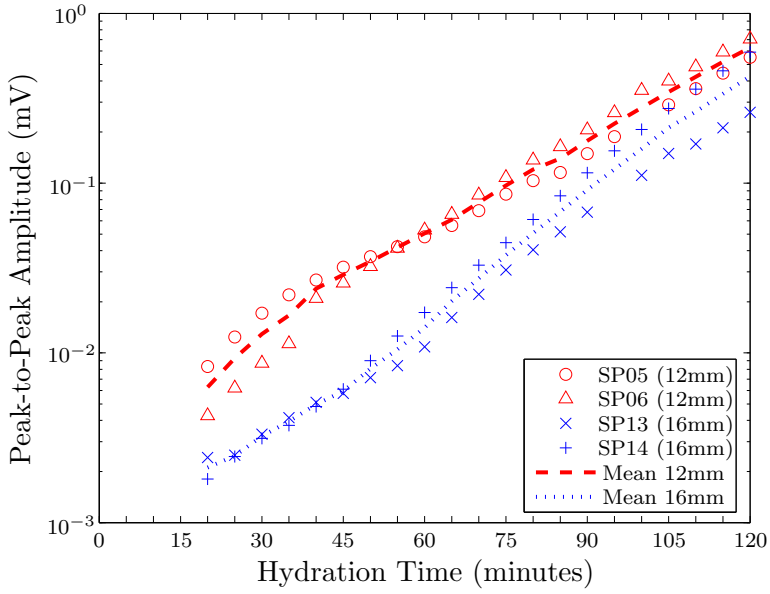

Figure 5.12: 0.4% AEA Peak-to-Peak at first 120 minutes of hydration

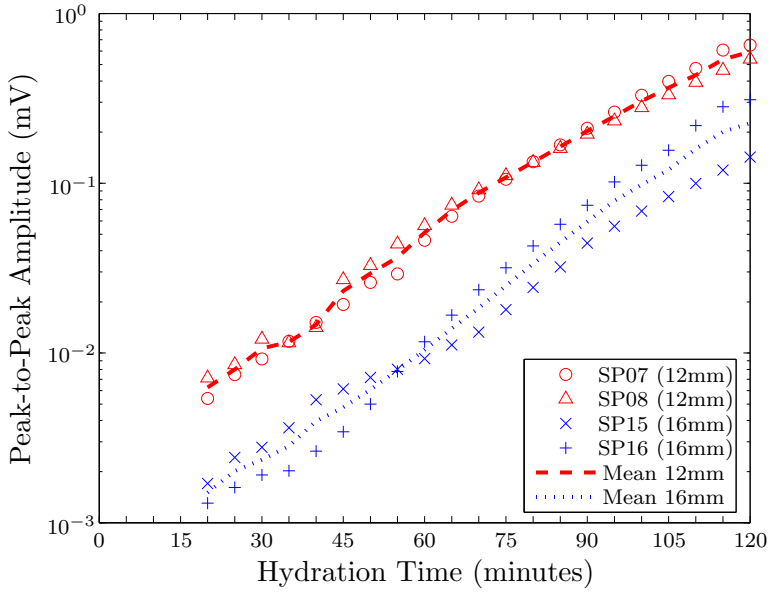

Figure 5.13: 0.6% AEA Peak-to-Peak at first 120 minutes of hydration

the higher-frequency wavelet at initial incidence while "wave through bulk paste" neglects this wavelet and focusses instead on the "bulk" wave. In the case of the entire wave form for the non-air-entrained specimens, the plots of the peak-to-peak magnitudes reveal a behavior slightly different from that of the air-entrained specimens: where the latter specimens increase exponentially in signal strength from approximately 0.0001-0.001 mV at 20 minutes, the non-air-entrained specimens have initial peak-to-peak signal strengths 1-2 magnitudes higher but do not increase at as great an exponential rate during the first two hours of hydration. This distinction is better pronounced in Figure 5.14. Most obvious is the shift in magnitude between the non-air-entrained and the air-entrained specimens. A possible reason for this dramatic difference is that the air-entrainer actually aids in the adsorption of the mix water into the paste matrix. The AEA inhibits cement flocculation, resulting in improved dispersion of cement grains, while also reducing the surface tension of the mix water, thus providing a quicker adsorption of the water component into the paste matrix than in the non-air-entrained specimens; ultrasonic wave transmission through these specimens may be most dependent on the scattering nature of the solid particles and their interconnectivity within the paste. In contrast, the non-air-entrained specimens still provide strict free-water lines of transmission – liquid percolation phases – as the water is not completely adsorbed into the paste, and the signal transmitted is most influenced by water. Additional evidence of this becomes obvious by comparison of the time-domain waveforms during the first 90 minutes of hydration, as mentioned at the beginning of this section. Thus, it is reasonable to conclude that the non-air-entrained specimens do indeed contain a water-only travel path – in addition to the bulk paste path – and which is most evident and dominant during the first hours of hydration.

When only the "bulk" wave is considered for the non-air-entrained specimens, there

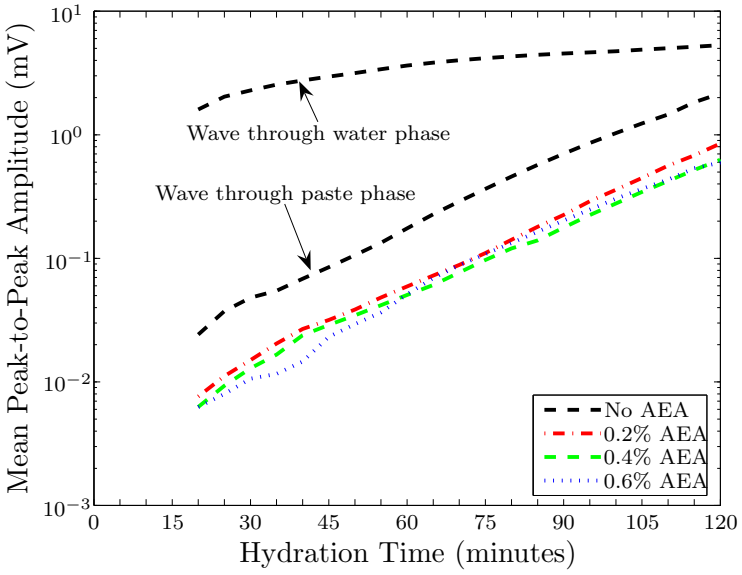

(a)

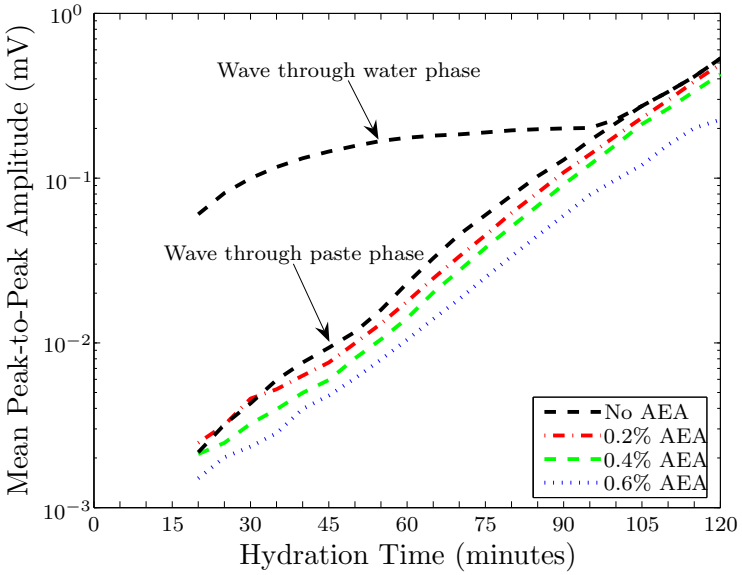

(b)

Figure 5.14: Mean Peak-to-Peak Amplitudes during first 120 minutes of hydration for (a) 12 mm specimens, (b) 16 mm specimens

is a much closer correlation of peak-to-peak magnitudes to those of the air-entrained specimens. Figure 5.14(b) does show some decrease of peak-to-peak signal strength with additional AEA in the 16 mm specimens. After about 40 minutes of hydration, the 0.2% AEA specimens show roughly 10-20% decrease in peak-to-peak magnitude from the non-air-entrained "bulk" wave at a particular time. Also compared to the non-air-entrained specimens, the 0.4% AEA specimens and 0.6% AEA specimens show 30-40% decrease and 50-60% decrease in the peak-to-peak magnitudes, respectively. For now, the comparisons are qualitative at best, and the numerical distinctions carry a high degree of uncertainty given the limited number of specimens. As for the 12 mm specimens as shown in Figure 5.14(a), a similar hierarchy is apparent during the first hour, although less clear than in the 16 mm specimens, and the hierarchy breaks down after about 60 minutes of hydration.

5.2.2 Velocity

There are several possible means of representing travel time – and thus, velocity – of a through-transmission ultrasonic wave through cement. Typically, hardened cement paste specimens offer the advantage of multiple echoes of the pulse signal; Figure 5.15 shows a received waveform including the first echo through an air space. The distance marked "dt_2" in the plot represents the time-delay between corresponding phase points within the initial received disturbance and the following echo. Since this requires the second disturbance to travel through twice the specimen thickness x, the measured velocity is $\frac{2x}{dt_2}$. This method carries further advantages in that the subsequent echoes following the initial pulse inform as to the attenuation through the specimen [51]. A variation of this technique [10] might establish the time-of-travel based on two specimen thicknesses: if the difference in specimen thicknesses is $x_2 - x_1$ and the phase point of interest is delayed $t_2 - t_1$ within the thicker specimen compared to the thinner specimen, then the measured velocity is $\frac{x_2 - x_1}{t_2 - t_1}$. Note that by

using "phase" points within a pulse response, one obtains the *phase velocity*, which is dependent on the reference phase point used.

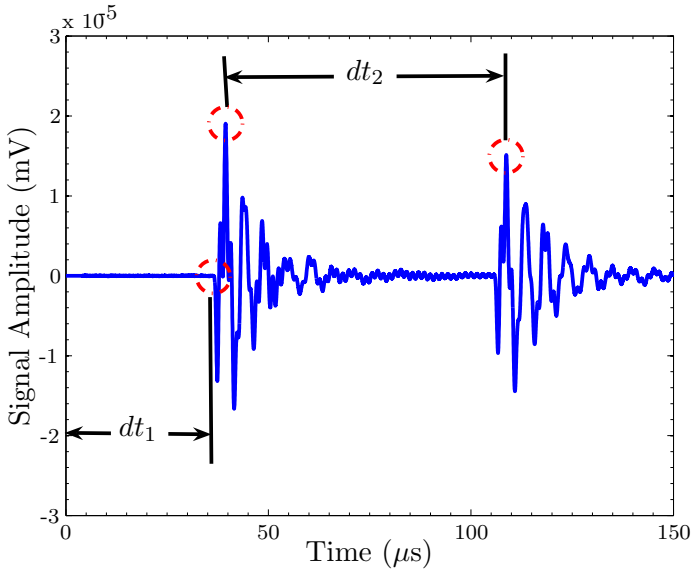

Figure 5.15: Typical waveform in time-domain; time = 0 corresponds to the creation of the initial pulse

Referring to Figure 5.15 again, the time-delay marked "dt_1" represents the *pulse velocity*, or more specifically, the time at which the receiving transducer registers the initial disturbance brought about by the pulse. Given this time of travel through one specimen thickness x, the measured velocity is $\frac{x}{dt_1}$.

For this investigation, both pulse velocity and phase velocity measurements were conducted. However, fresh cement paste is inherently highly attenuative; a considerable amount of amplification is required to merely register the initial pulse disturbance. Unfortunately, using phase velocity methods proved impossible given that there were no detectable echoes received in any of the specimens at any time. Further, part of

the rationale for using two specimen thicknesses was the possibility of phase velocity measurements based on the time-delay through additional thickness. Again, this approach failed to produce reasonable results; often the time-delay appears *negative* when comparing the travel time through additional thickness for equivalent mixes at the same time of hydration. These discrepancies could be due to geometric spreading as well as high-sensitivity to the state of hydration.

Given the elusiveness of phase velocity measurements, a more exhaustive effort was made in obtaining pulse velocity measurements. Time of arrival was determined for each signal through visual inspection of the waveforms. For the signals occuring the latest in the testing, this was not difficult as signal-to-noise is relatively high. The earliest times of hydration were more difficult though as the lower signal-to-noise ratio often obfuscated the discrete point of the initial pulse arrival, and there existed the possibility of the electronic equipment adding their own static artifacts. This last difficulty was mitigated by overlaying consecutive time signals to highlight any static elements from the electronic systems. Once these time of arrival points were established they were corrected for the travel time through the acrylic sheets. The results of the pulse velocity measurements are shown in Figures 5.16(a), 5.17(a), 5.18(a), and 5.19(a). As expected all of the specimens show a continuous increase in pulse velocity as hydration proceeds and additional solid percolation paths emerge. The rate of increase in pulse velocity appears greatest during the first 6 hours of hydration and is probably related to this being the most active period of hydration of the calcium silicates.

There is a clear distinction between the pulse velocities of the non-air-entrained specimens and the air-entrained specimens during the first 6 hours of hydration. Where

the air-entrained specimens show a continuous, roughly linear increase in pulse velocity starting at approximately 200 m/s at 30 minutes of hydration (shown in Figures 5.17(b), 5.18(b), and 5.19(b)), the non-air-entrained specimens show a constant pulse velocity of approximately 1600 m/s through the first 6 hours (shown in Figures 5.16(b)). This latter speed is similar to the speed of sound through liquid water and provides further evidence of a water percolation path unique to the non-air-entrained specimens. Unlike the peak-to-peak magnitude measurements, which allowed for distinction between the early higher-frequency wavelet and the later paste phase wave found in the non-air-entrained specimens, there is no way to objectively determine the pulse velocity of only the paste wave component through the non-air-entrained specimens as the water phase component interferes with the paste component initial disturbance.

Another observation on the non-air-entrained specimens is the divergence of the pulse velocity as measured through the 12 mm and the 16 mm thicknesses from 6 to 12 hours of hydration. This discrepancy increases to as much as 330 m/s difference. This was initially thought to be due to shrinkage effects disproportionally decreasing the thickness of the travel space, but even by taking account of the measured autogenous strain, this correction was minuscule. A similar divergence occurs in the air-entrained specimens: the 12 mm specimens show approximately 100 m/s higher pulse velocities initially; after 4-7 hours the velocity trends cross and the 16 mm specimens show higher pulse velocities onward through 12 hours of hydration. Given the method of containment and the specimen thicknesses,

Figures 5.20 and 5.21 show the comparison of mean pulse velocities through each mix type over the first 12 hours and 4 hours of hydration. Despite the water phase dominating the first 6 hours of hydration in the non-air-entrained specimens, the

mean velocities of each mix type appear to converge by 12 hours of hydration. Plots of the first 4 hours of hydration suggest hierarchy of pulse velocities based on the amount of AEA in each mix with velocities generally decreasing by 100 m/s to 200 m/s with each additional 0.2% AEA by weight of cement at a given time. From another perspective, the hierarchy among the mean pulse velocities for the air-entrained specimens may also be viewed in terms of time-delay of setting. Recalling Figure 5.1, the presence of AEA appears to delay the Vicat Time of Initial Set by approximately 15-20 minutes with each incremental addition of 0.2% AEA by weight of cement. This relationship is most evenly pronounced in Figure 5.21(b) where the pulse velocities of the air-entrained specimens maintain roughly 15-20 minute time-delays for each additional 0.2% increment of AEA during the first 4 hours of hydration. The hierarchy is still evident for the pulse velocities of the 12 mm specimens as well, but the time-delays vary on a range of approximately 5-30 minutes. This last point may be a result of edge effects where the air-entrained voids coalesce as they encounter the mold interfaces; as specimen thickness increases, the contribution of edge effects to scattering and absorption decreases relative to the attenuation effects of the bulk specimen material.

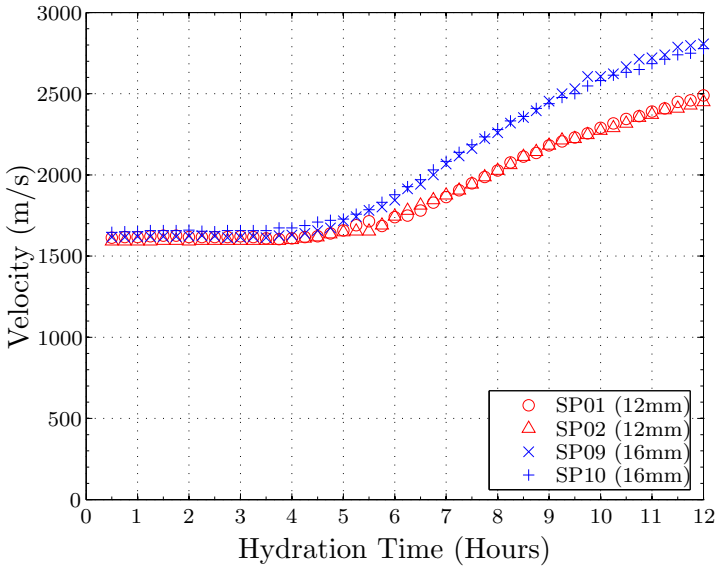

(a)

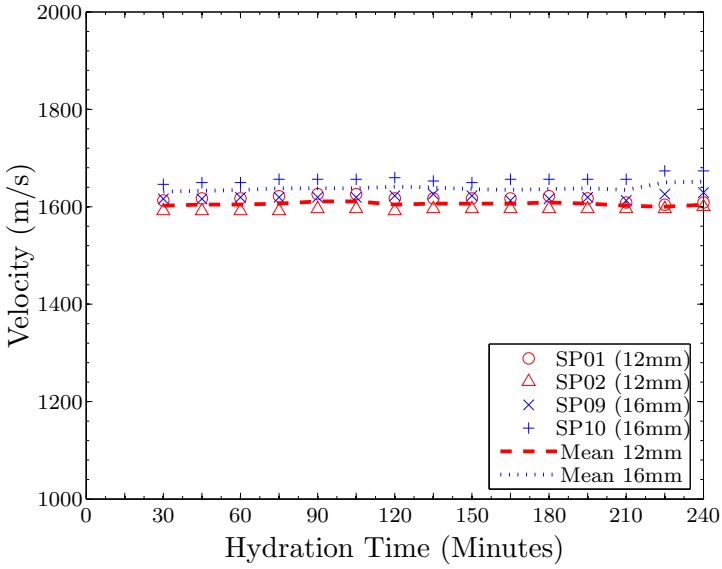

(b)

Figure 5.16: Pulse velocity through 0.0% AEA specimens during first (a) 12 hours, (b) 240 minutes of hydration

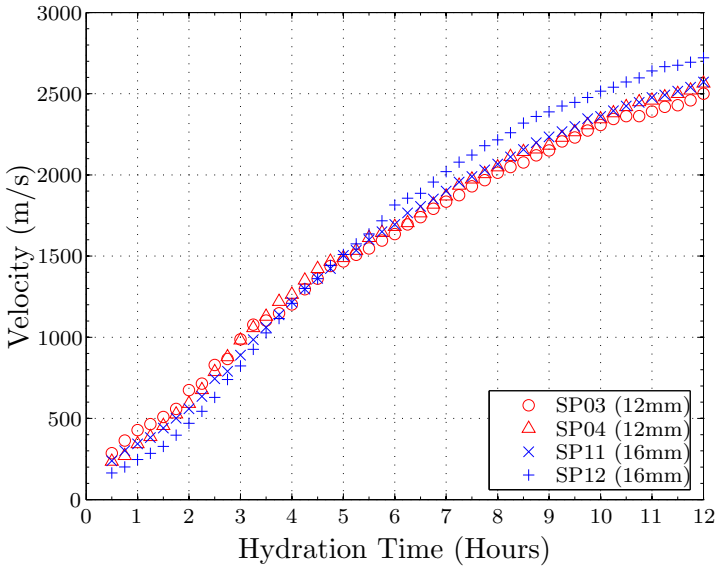

(a)

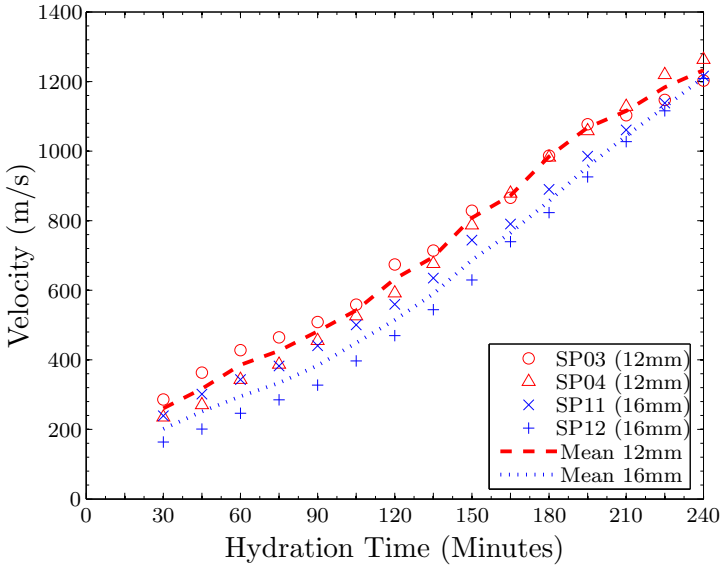

(b)

Figure 5.17: Pulse velocity through 0.2% AEA specimens during first (a) 12 hours, (b) 240 minutes of hydration

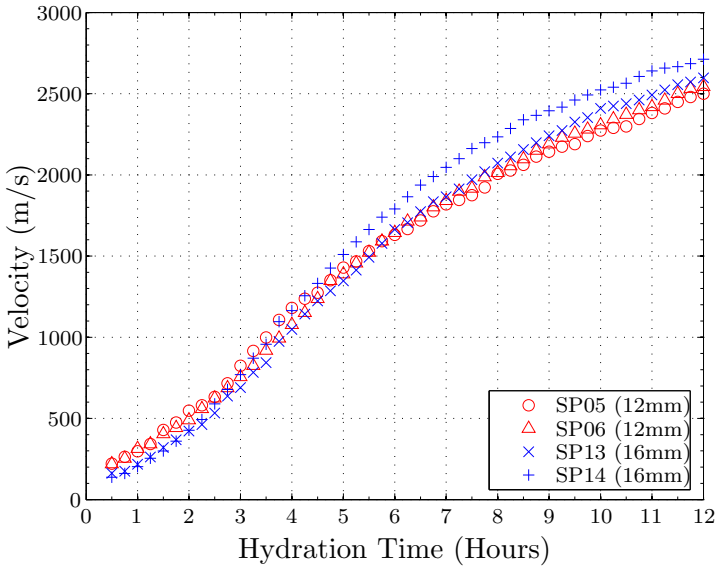

(a)

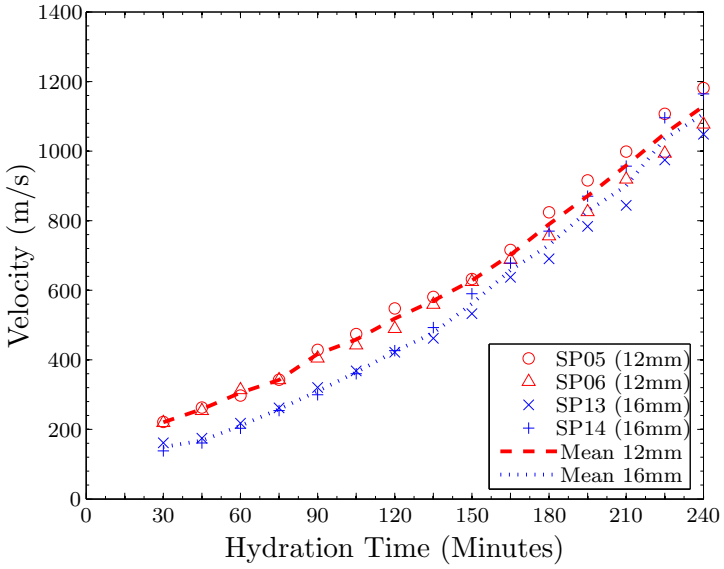

(b)

Figure 5.18: Pulse velocity through 0.4% AEA specimens during first (a) 12 hours, (b) 240 minutes of hydration

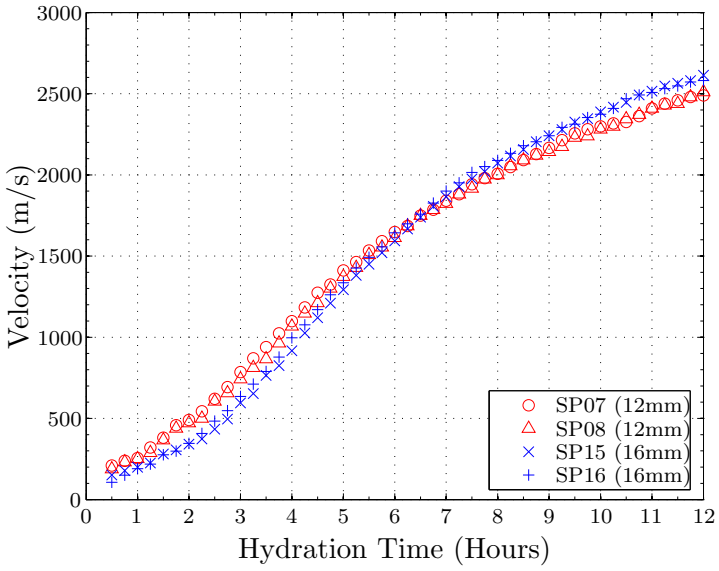

(a)

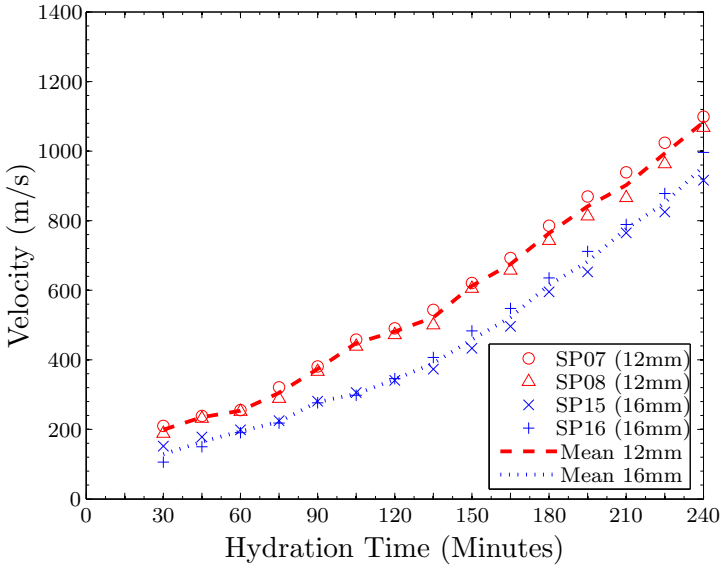

(b)

Figure 5.19: Pulse velocity through 0.6% AEA specimens during first (a) 12 hours, (b) 240 minutes of hydration

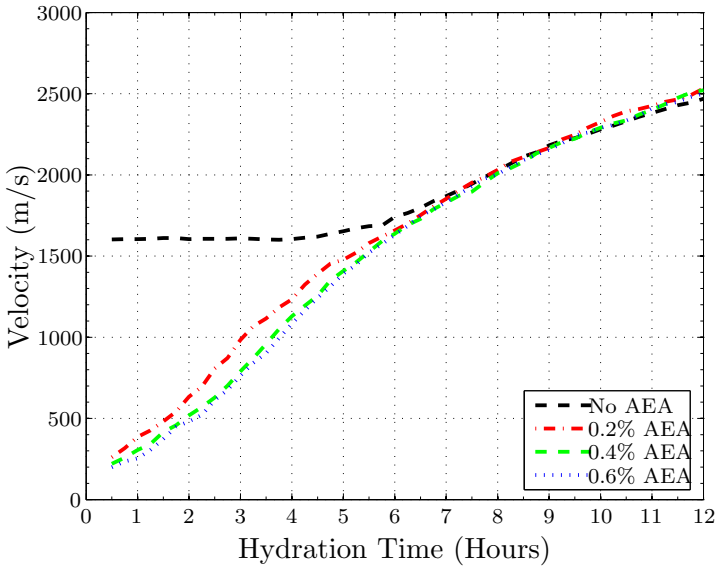

(a)

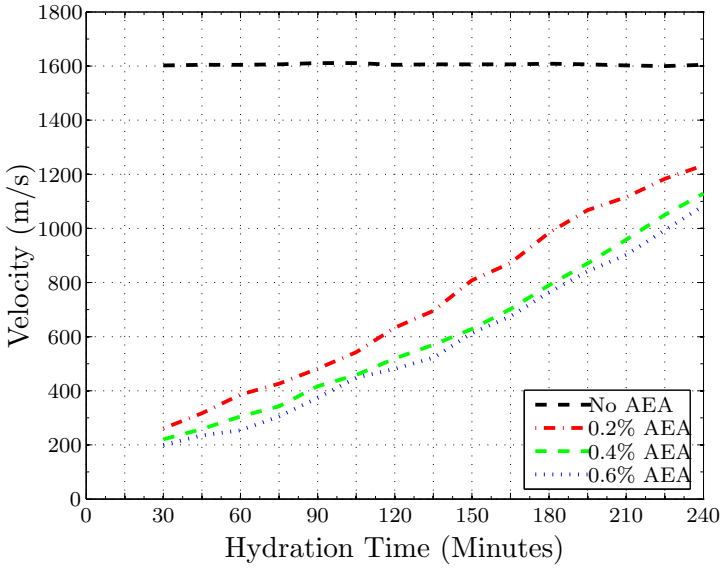

(b)

Figure 5.20: Mean pulse velocity through 12 mm specimens during first (a) 12 hours, (b) 240 minutes of hydration

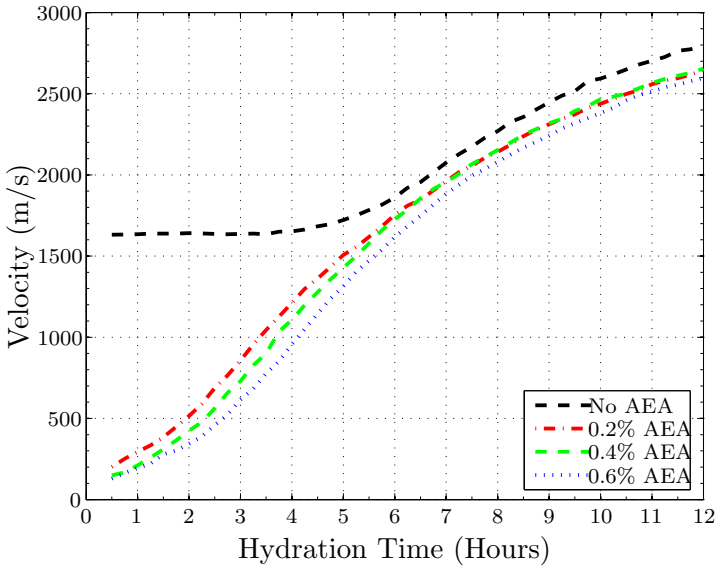

(a)

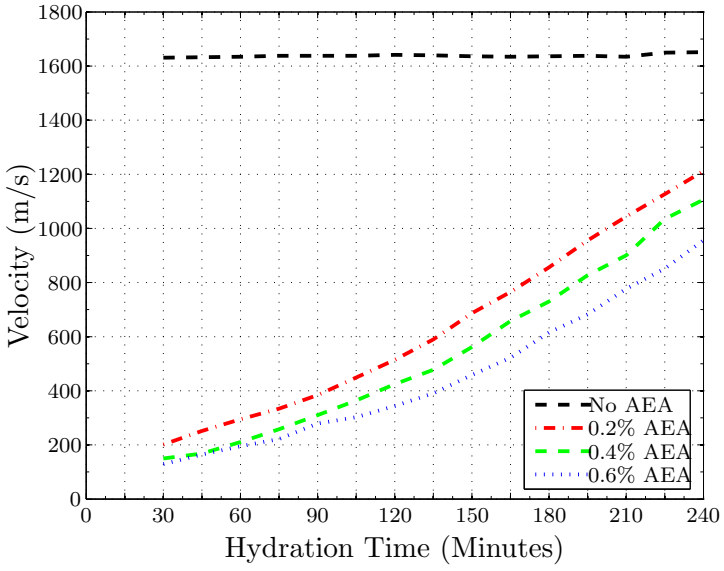

(b)

Figure 5.21: Mean pulse velocity through 16 mm specimens during first (a) 12 hours, (b) 240 minutes of hydration

5.2.3 Frequency

Appendix B shows the frequency spectra for the signals at 60 minute intervals. FFT analysis was performed for each signal using a rectangular window about the first 400 μs of the acquired waveform (blue) as well as using a Hanning window about the "main bang" of each waveform (red). The main bang is the first full cycle of disturbance detected by the receiving transducer; Figure 5.22 illustrates the main bang in a typical time-domain signal. This initial disturbance is the only portion of the waveforms that can be consistently and objectively defined at every time during hydration. That is, when attempting to extract *multiple* cycles for each waveform, difficulty occurs in the middle hours (approximately 4-8 hours) when the character of the waveform undergoes transition from a fluid-influenced wave to a solid-influenced wave. Visual inspection of the waveforms in Appendix A reveals this as a transition from a waveform with multiple peaks during the early hours to a waveform with one main disturbance during the later hours. Figure 5.23 illustrates a typical frequency spectra used in the analysis along with indication of the peak frequency and bandwidth parameters.

Initially, the main bang extracted was windowed on its own as shown in Figure 5.24(a). However, given the nature of the Hanning window, this greatly skewed the latter positive portion of the windowed region and gave considerable bias to the negative portion of the wave, which generally contained less energy than the positive peak. To better emphasize the positive peak, the main bang portion was rotated symmetrically about its endpoint to create a two-cycle wave with rotational symmetry; Figure 5.24(b) shows the resulting composite wave with applied Hanning window. Thus, references to the Hanning window region in Appendix B as well as the following discussion of peak frequency and bandwidth refer to the Hanning window about this composite region.

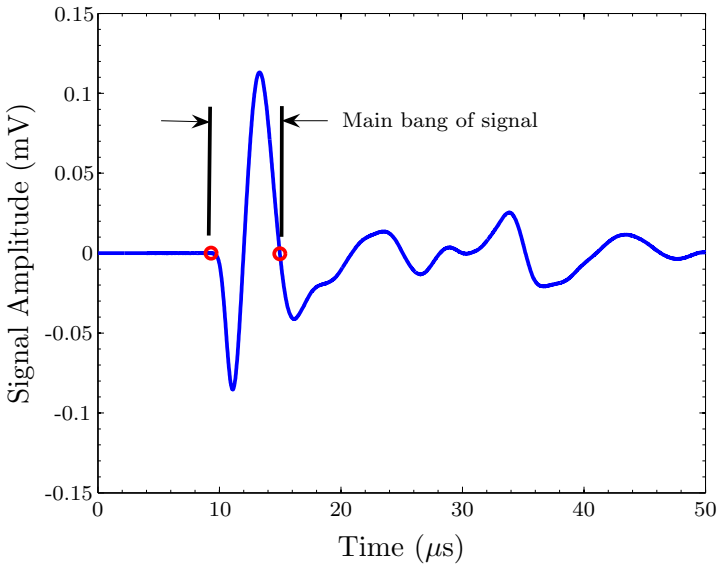

Figure 5.22: Typical time-domain signal with main bang indicated between cirles

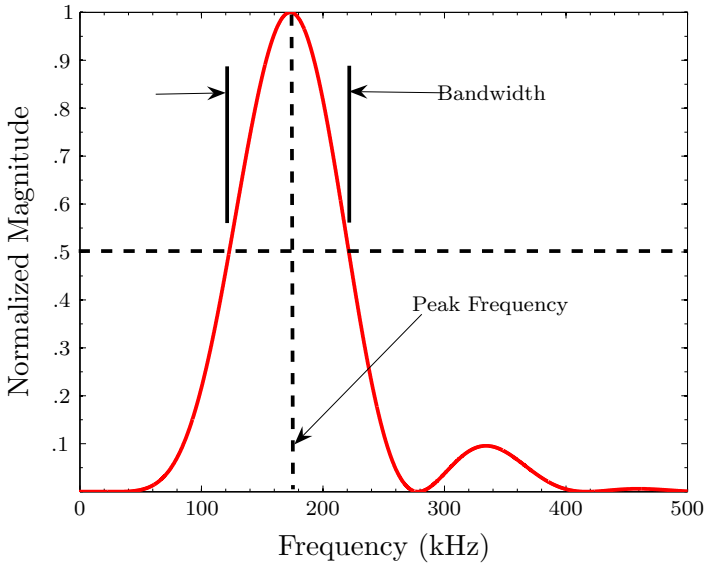

Figure 5.23: Typical normalized frequency spectra acquired using Hanning window; bandwidth is taken at 50% of the maximum magnitude

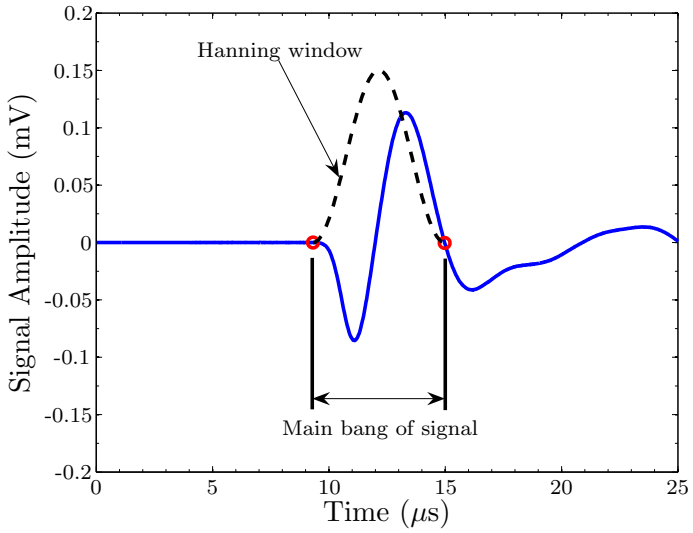

(a)

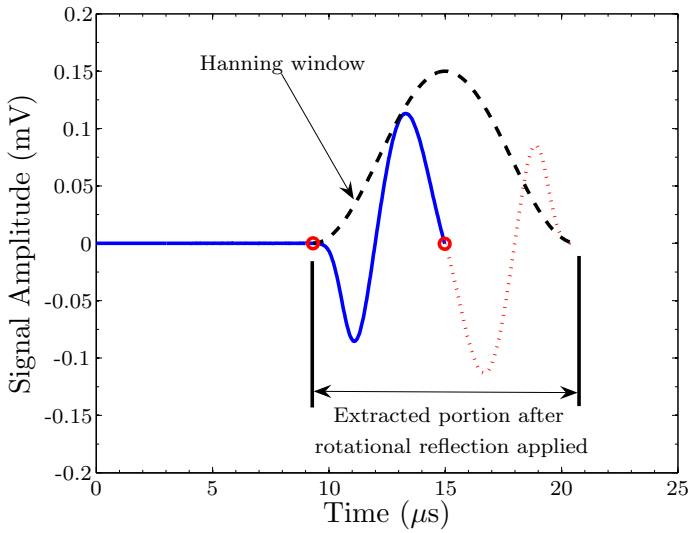

(b)

Figure 5.24: Windowing procedure for frequency analyses (a) main bang of original signal with initially proposed Hanning window, (b) main bang of signal rotationally mirrored with new Hanning window

Figures 5.25, 5.26, 5.27, and 5.28 show the evolution of the peak (central) frequencies for each specimen through the first 12 and 4 hours, respectively. Compared to the evolution of the peak-to-peak amplitudes, interpretation of these plots appears relatively simple. Each plot can be considered in terms of approximate time periods. During the first 2-3 hours of hydration, the paste is dominated by the fluid phase, and the peak frequency response of the system is in the 20-50 kHz range and increasing roughly linearly at 3-4 kHz every 15 minutes. As shown in Figures 5.25(b), 5.26(b), 5.27(b), and 5.28(b) the initial period of peak frequency development is marked by close correlation between the 12 mm and 16 mm thicknesses. After 2-4 hours of hydration, the specimens arrive at a threshold time of hydration at which peak frequency response increases sharply by 8-10 kHz every 15 minutes as the paste enters a period during which the peak frequency response transitions from one dominated by a fluid phase to one dominated by the solid phase. This transition from the relatively dormant first period to the more active second period occurs approximately 1-2 hours longer than the similar transition that occurs in heat of hydration measurements (Figure 5.2 as the cement paste enters its most active period of hydration of the calcium silicates. This 1-2 hour time-delay may reflect the necessary initial degree of hydration of calcium silicates before sufficient solid percolation paths – and thus, higher peak frequency paths – can be established through the paste. In other words, setting and solidification become more apparent during this second period.

Further, the plot of peak frequency response for each specimen displays a distinct pause or dropoff during this transition period. These dropoffs, which occur at times at or within 2 hours after the cement matrix has achieved sufficient rigidity to resist further autogenous shrinkage, suggest distortion of the frequency response as the interface decouples slightly from the paste. In the final period, the frequency response converges to that of the final solid phase and is a full magnitude greater than the

initial frequency response of the fluid phase.

Note that for SP02, the peak frequencies at 30 and 45 minutes of hydration are not visible as these earliest waveforms have dominant frequencies in the 600-800 kHz range; the other non-air-entrained specimens also see significant frequency components in the 600-800 kHz range, though these do not necessary dominate over the 20-60 kHz range. This higher frequency range represents the unique water phase wavelet inherent in all of the non-air-entrained waveforms during the first 90 minutes of hydration while the lower frequency range represents the bulk paste.

Figures 5.29 and 5.30 show the comparison of the mean peak frequencies for each mix type over the first 12 and 4 hours of hydration, respectively. Again, the 12 hour plots show three distinct periods of hydration as the paste transitions from fluid to solid. What is especially interesting is the hierarchy shown during the first 4 hours for the 12 mm and – to a lesser degree – the 16 mm specimens. During the first 2-3 hours, the peak frequency of the non-air-entrained specimen is offset 10-15 additional kHz from that of the other specimens. The air-entrained specimens show close correlation while the paste is in its initial fluid phase. The sharp increase in the slope of the peak frequency plots, as mentioned previously, is delayed for each additional increment of AEA added to the mix. These mean "takeoff" points are probably due to the first instances of solid percolation paths. Although these thresholds lead the Vicat times of setting by 30-40 minutes, this only means that even with available solid paths, sufficient shear resistance for a specimen, as technically measured in the Vicat tests, may still be developing. From another perspective, this suggests that monitoring the rate of increase of the peak frequency provides better evidence of the solid network, and thus a better means of defining initial set.

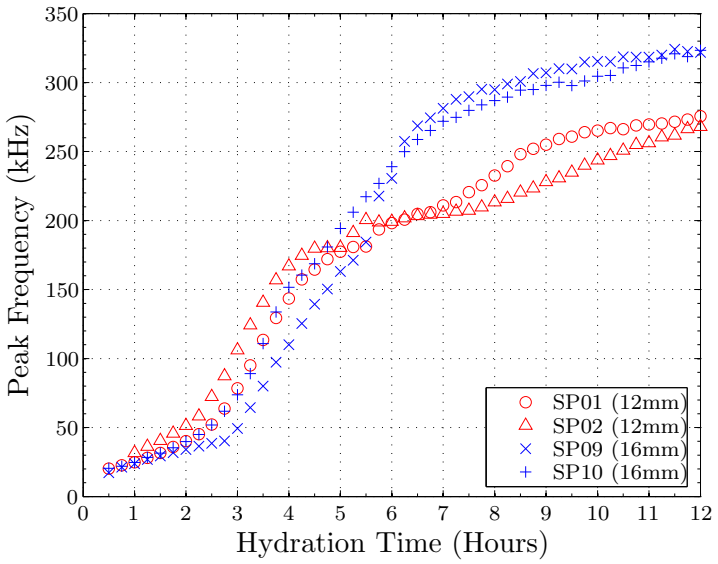

(a)

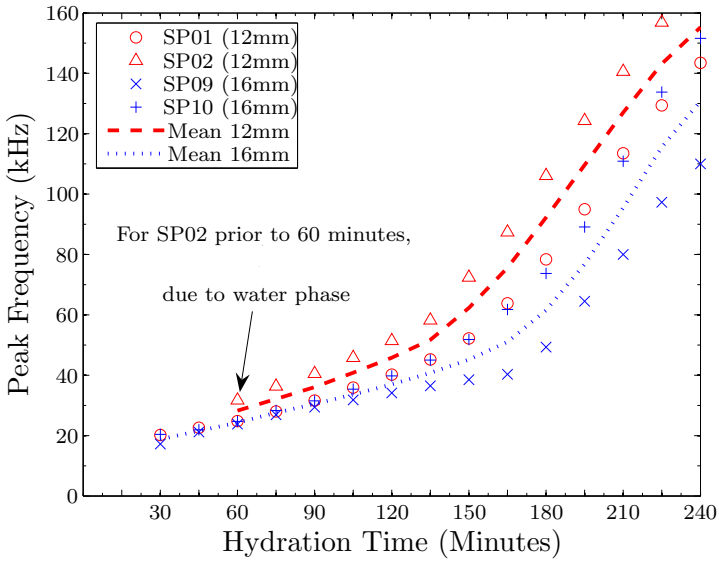

(b)

Figure 5.25: Peak Frequency of initial received pulse through non-air-entrained specimens during first (a) 12 hours, (b) 240 minutes of hydration

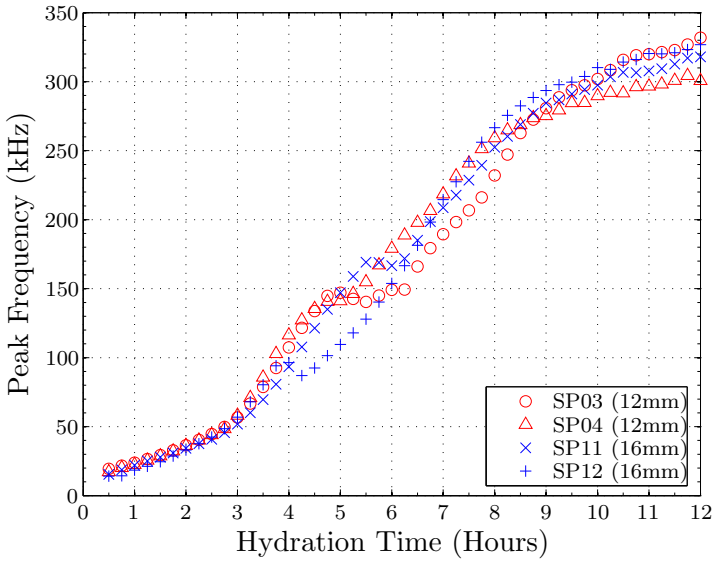

(a)

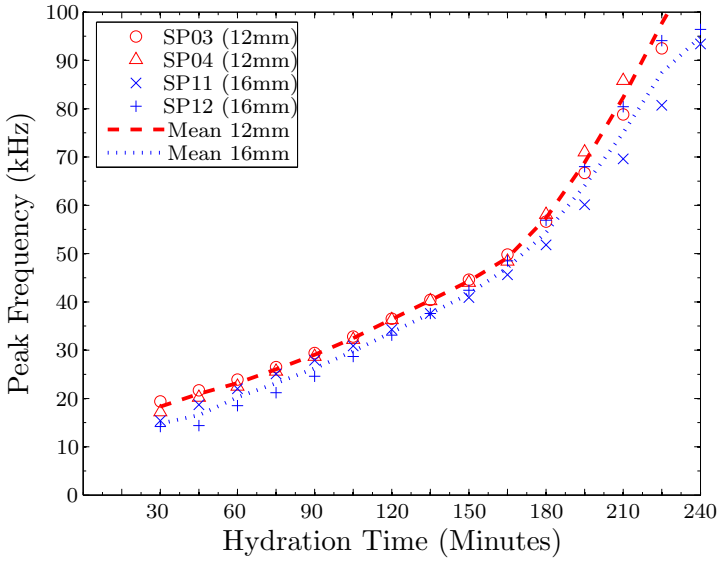

(b)

Figure 5.26: Peak Frequency of initial received pulse through 0.2% AEA specimens during first (a) 12 hours, (b) 240 minutes of hydration

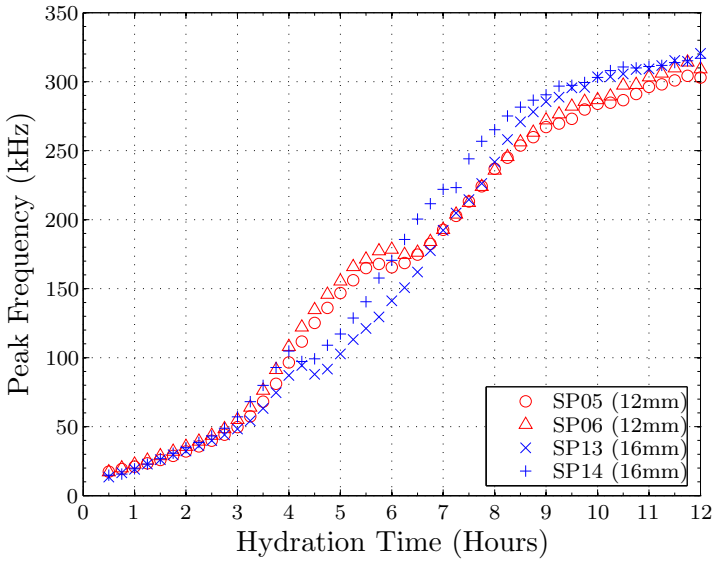

(a)

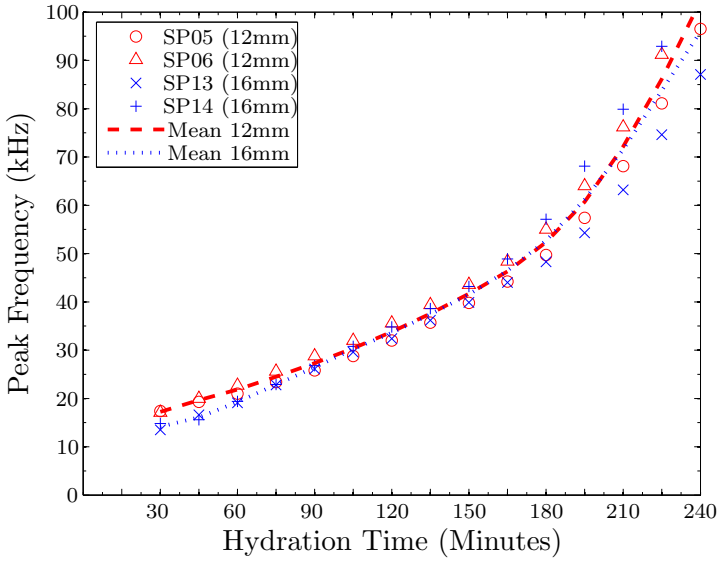

(b)

Figure 5.27: Peak Frequency of initial received pulse through 0.4% AEA specimens during first (a) 12 hours, (b) 240 minutes of hydration

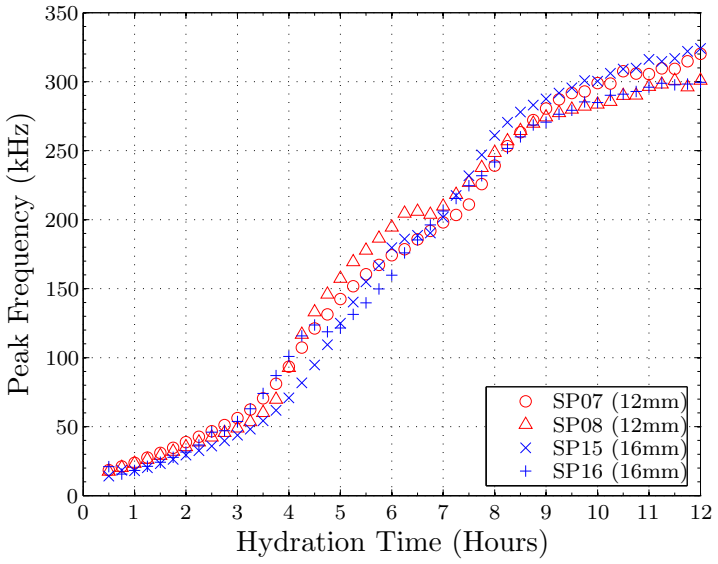

(a)

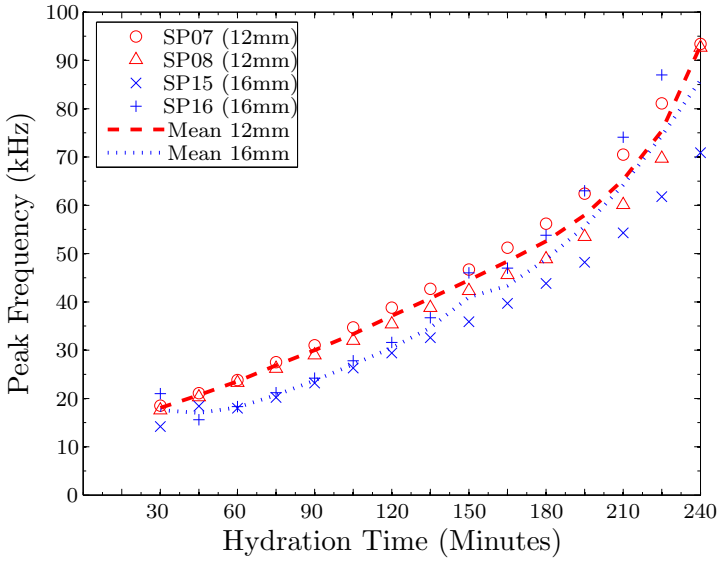

(b)

Figure 5.28: Peak frequency of initial received pulse through 0.6% AEA specimens during first (a) 12 hours, (b) 240 minutes of hydration

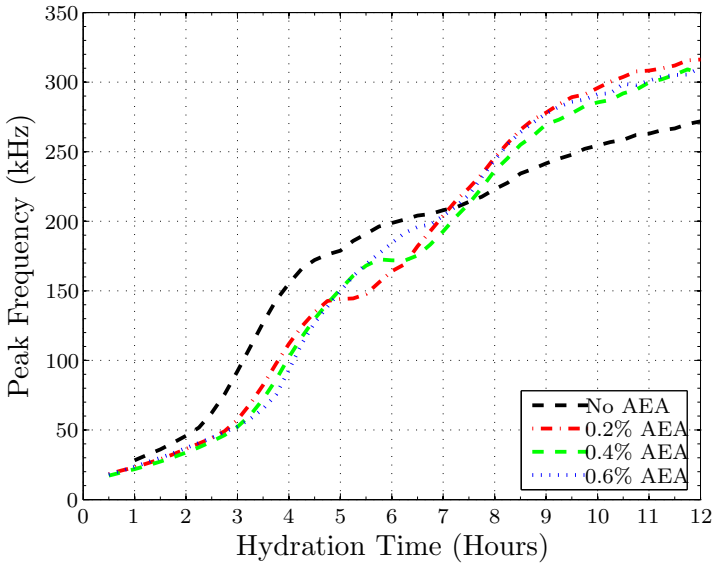

(a)

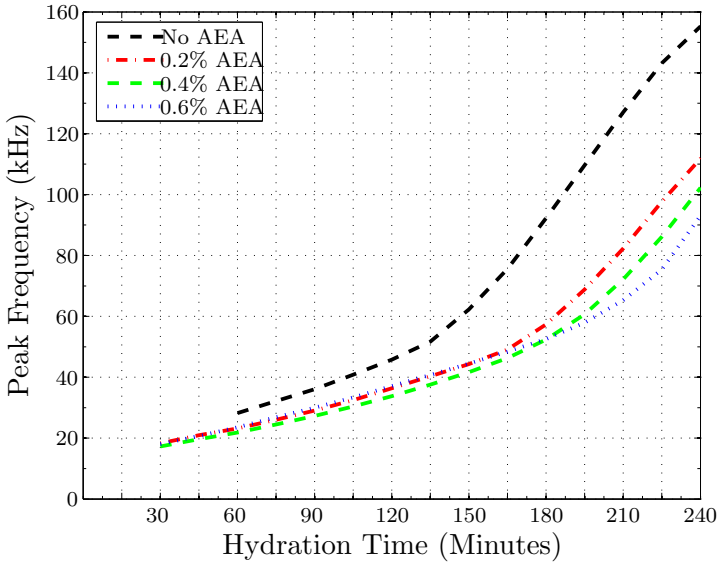

(b)

Figure 5.29: Mean Peak Frequency of initial received pulse (12 mm specimens) during first (a) 12 hours, (b) 240 minutes of hydration

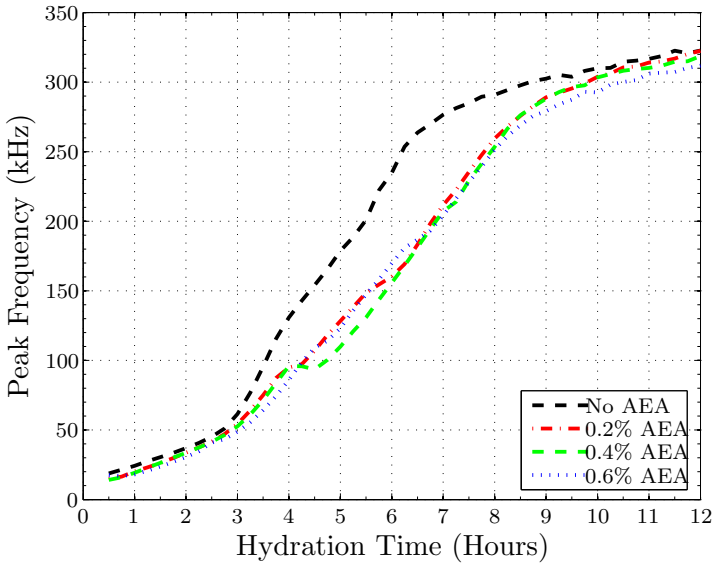

(a)

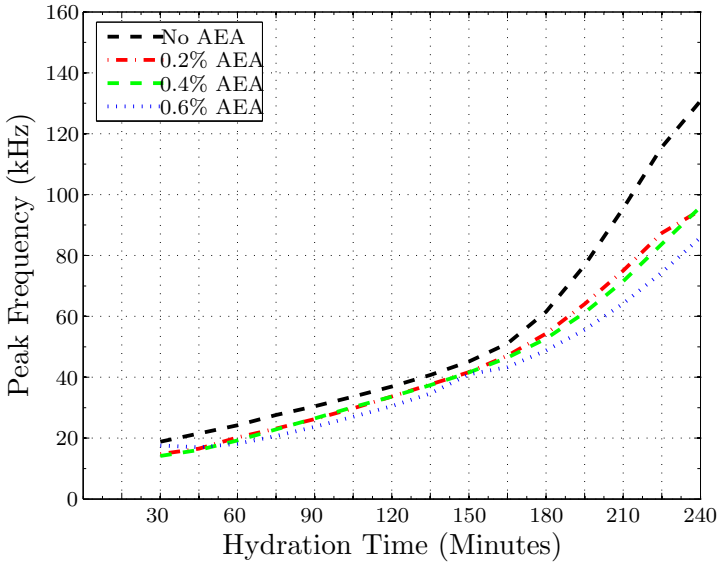

(b)

Figure 5.30: Mean Peak Frequency of initial received pulse (16 mm specimens) during first (a) 12 hours, (b) 240 minutes of hydration

Figures 5.31, 5.32, 5.33, and 5.34 show the evolution of the 50% bandwidth for each specimen through the first 12 and 4 hours, respectively. This essentially indicates the width of the frequency spectra about the peak frequency as indicated by a cutoff frequency, in this case 50% of the magnitude at the peak frequency. The observations made for the peak frequency plots in Figures 5.25, 5.26, 5.27, and 5.28 are the same for the bandwidth measurements. Indeed, the bandwidth measurements track the same unique instances of decoupling within each specimen, and there is a stable peak frequency to bandwidth ratio of 1.1-1.3 throughout the 12 hour hydration period for each of the specimens. Earlier analysis attempts using the windowing style shown in Figure 5.24(a) revealed discrepancies between peak frequency and bandwidth trends; with the improved windowing style of Figure 5.24(b), the peak frequency and bandwidth show close correlation to each other, even during instances of decoupling, suggesting that deviations between mix types are strictly material-based. In other words, the bandwidth measurements provide verification of the observations in the peak frequency measurements.

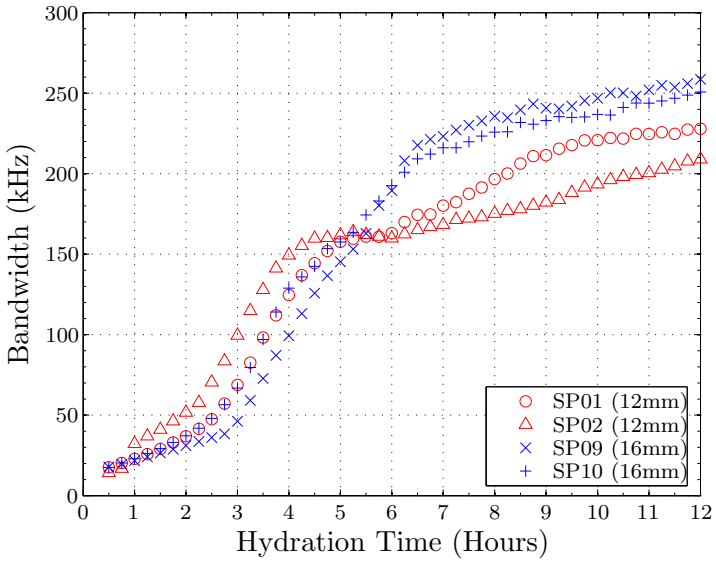

(a)

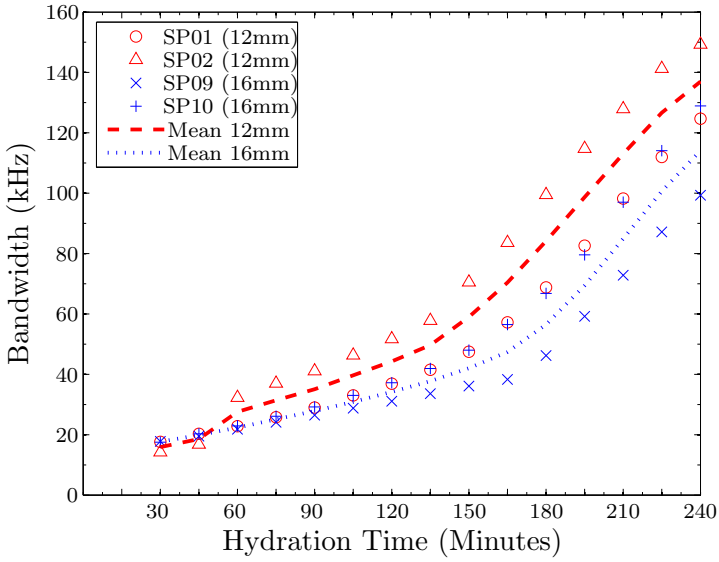

(b)

Figure 5.31: Bandwidth of initial received pulse through 0.0% AEA specimens during first (a) 12 hours, (b) 240 minutes of hydration

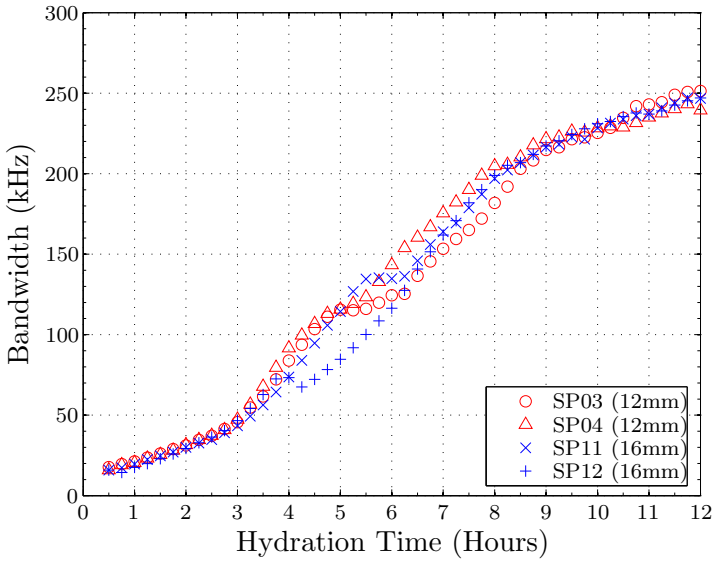

(a)

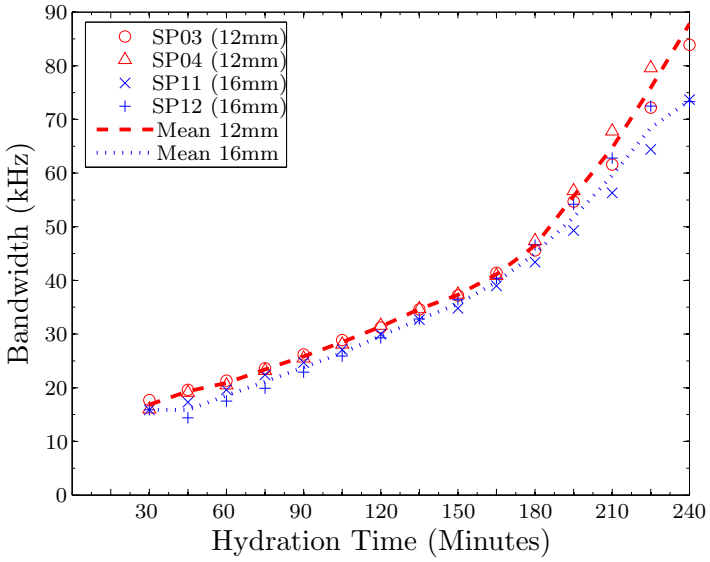

(b)

Figure 5.32: Bandwidth of initial received pulse through 0.2% AEA specimens during first (a) 12 hours, (b) 240 minutes of hydration

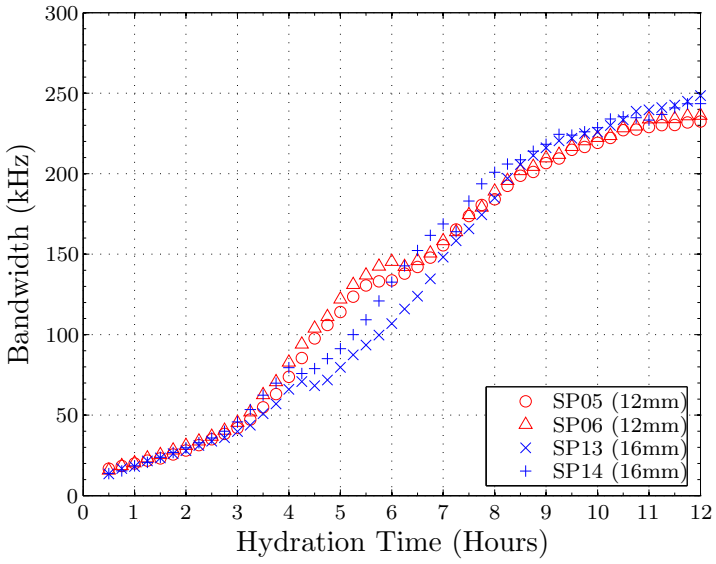

(a)

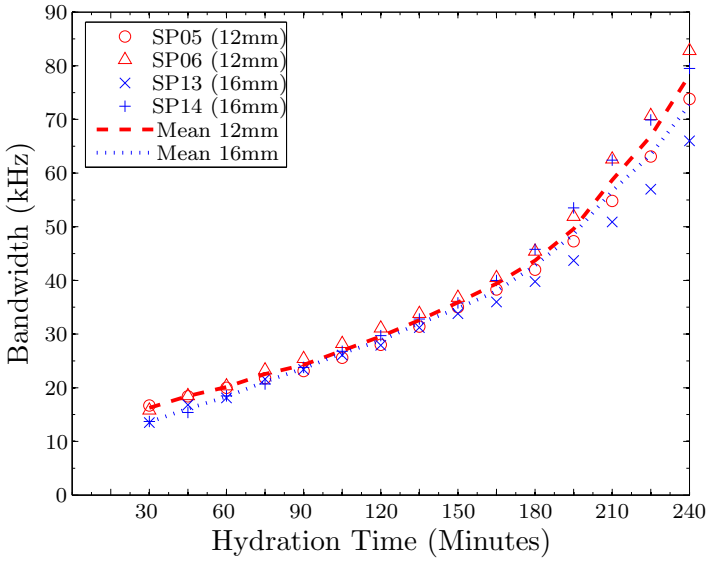

(b)

Figure 5.33: Bandwidth of initial received pulse through 0.4% AEA specimens during first (a) 12 hours, (b) 240 minutes of hydration

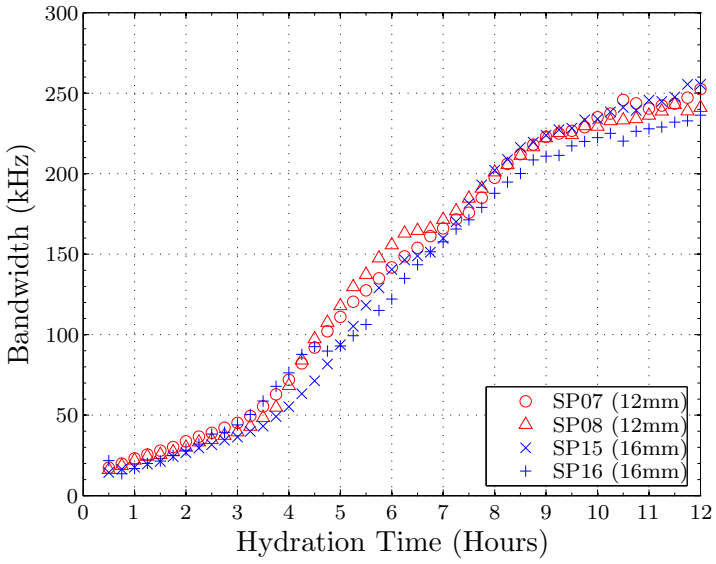

(a)

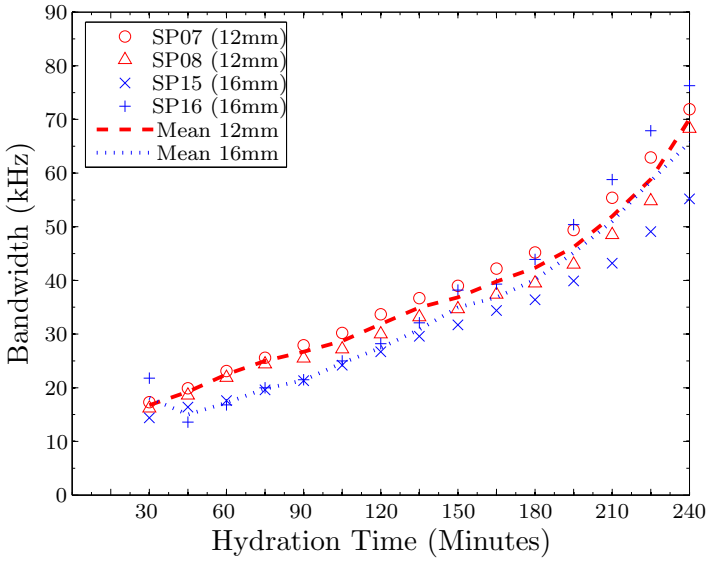

(b)

Figure 5.34: Bandwidth of initial received pulse through 0.6% AEA specimens during first (a) 12 hours, (b) 240 minutes of hydration

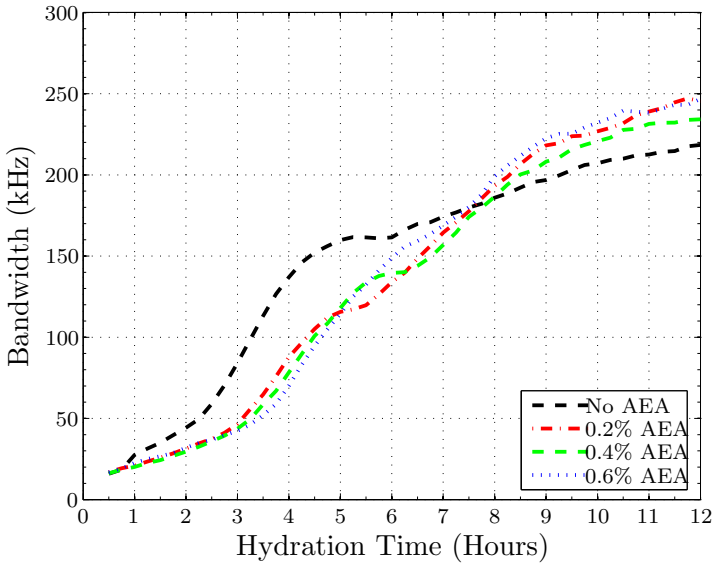

(a)

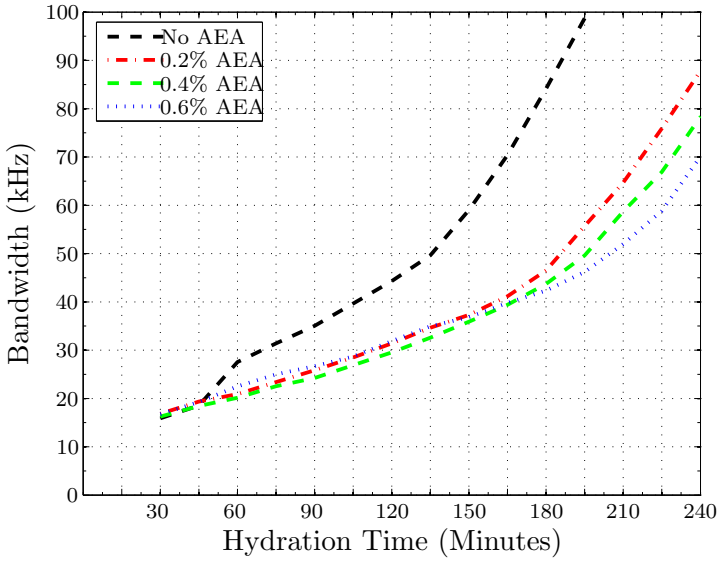

(b)

Figure 5.35: Mean Bandwidth of initial received pulse (12 mm specimens) during first (a) 12 hours, (b) 240 minutes of hydration

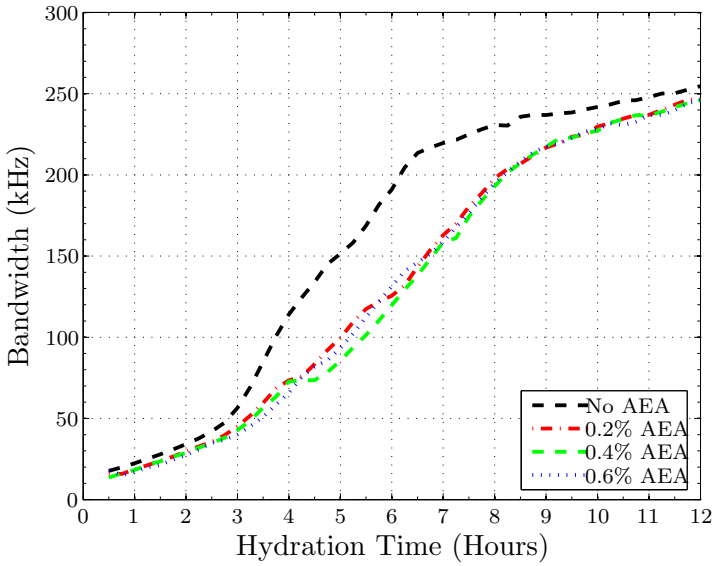

(a)

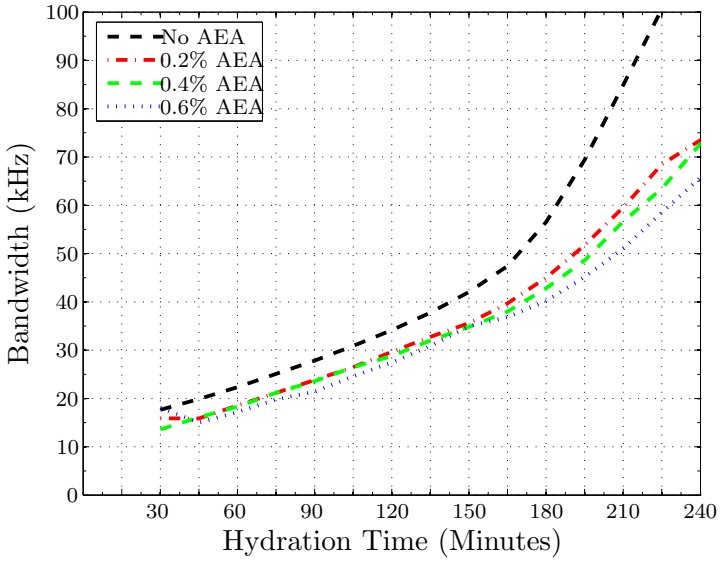

(b)

Figure 5.36: Mean Bandwidth of initial received pulse (16 mm specimens) during first (a) 12 hours, (b) 240 minutes of hydration

CHAPTER 6

Conclusions and Recommendations

This research studied the effects of different degrees of air-entrainment in fresh cement paste on the signature of longitudinal ultrasonic waves with the aim of providing the fundamental base for further development of new methods for measuring the amount of entrained air in cement-based materials at early ages.

6.1 Conclusions

Chapter 5 presents the resulting data from the ultrasonic tests where the ultrasonic signal was characterized by peak-to-peak signal strength, pulse velocity, and frequency spectra. Although specimens were monitored through the first 12 hours of hydration, the data acquired with the current methods appears to be most relevent through the first 2-4 hours of hydration, depending on the metric analyzed.

The most obvious result apparent in the data analysis is the clear distinction between those specimens with and without the air-entraining admixture. As confirmed by the measurements of signal strength (peak-to-peak), pulse velocity, and frequency spectra, the non-air-entrained specimens contain liquid water percolation phases. The non-air-entrained specimens are most distinguishable from the air-entrained specimens through inspection of the peak-to-peak and pulse velocity data. The peak-to-peak strength for the non-air-entrained specimens is significantly higher than that of the

air-entrained specimens during the first two hours of hydration. Likewise, the pulse velocities of the non-air-entrained specimens are also substantially higher than those of the air-entrained specimens – and similar to that of water – through the first four hours of hydration. Inspection of the collected waveforms themselves reveals the unique and universal superposition of a higher-frequency "water phase" wave and a slower, lower-frequency "paste wave" in the non-air-entrained specimens.

The data suggest that, in general, the addition of the AEA suppresses the peak-to-peak signal strength, pulse velocity, and peak frequency in the fresh paste. While an inversion process requires further experimentation, the investigation does highlight the practical challenges inherent in ultrasonic monitoring of fresh cement paste. The 16 mm thickness represents the upper dimensional limit for testing with the laboratory equipment available to this setup; applying the same experimental methods to thicker slabs requires either sample extraction – not ideal for *in-situ* – or equipment, including transducers, capable of more substantial power capabilities. Further, where hardened cement paste specimens offer the advantage of testing at multiple locations on the specimen thickness and using a variety of signals, fresh paste specimen tests are rather limited – the technician cannot assume a chemically stable material over a time scope greater than a few minutes and cannot easily test multiple areas of the specimen using one set of transducers. The former disadvantage prevents testing the same specimen using a range of input signals, i.e., multiple discrete input frequencies, without introducing error due to changes in the paste matrix during a time window. The latter disadvantage requires either a relatively high degree of uncertainty when only testing at one specimen location or several transducer pairs on the same specimen to reduce uncertainty.

6.2 Recommendations

Discrepencies related to changes in specimen thickness, such as pulse velocity and incidence of decoupling, suggest that the experiments are better served by using one thickness for all specimens; this would eliminate variations based on geometric effects. Also, although broadband tranducers were used, repetition of the experimental procedure using transducers of lower center frequencies may be better suited to the spectral response of the paste specimens. Provided the evidence of this investigation, future research can limit experimental monitoring to only the first 4 hours of hydration. This limited scope means that thicker, more rigid acrylic interfaces actually are appropriate; experience suggests that by the time the cement pastes have established sufficient rigidity to decouple from the acrylic, hydration has already proceeded beyond the scope of interest, i.e., longer than 4 hours.

APPENDIX A

Ultrasonic data

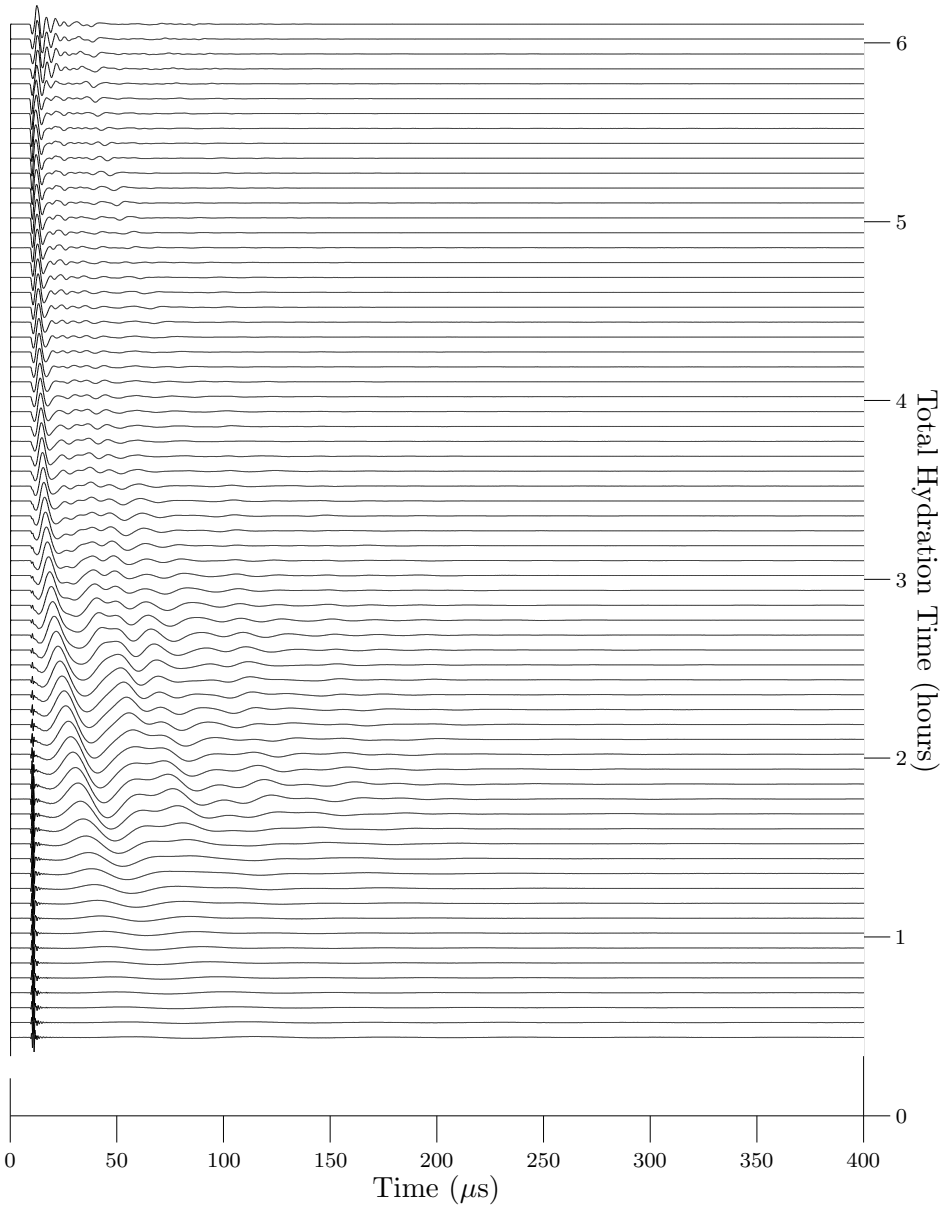

Figure A.1: Specimen 01 (0.0% AEA by weight of cement) normalized signals during the first 6 hours of hydration

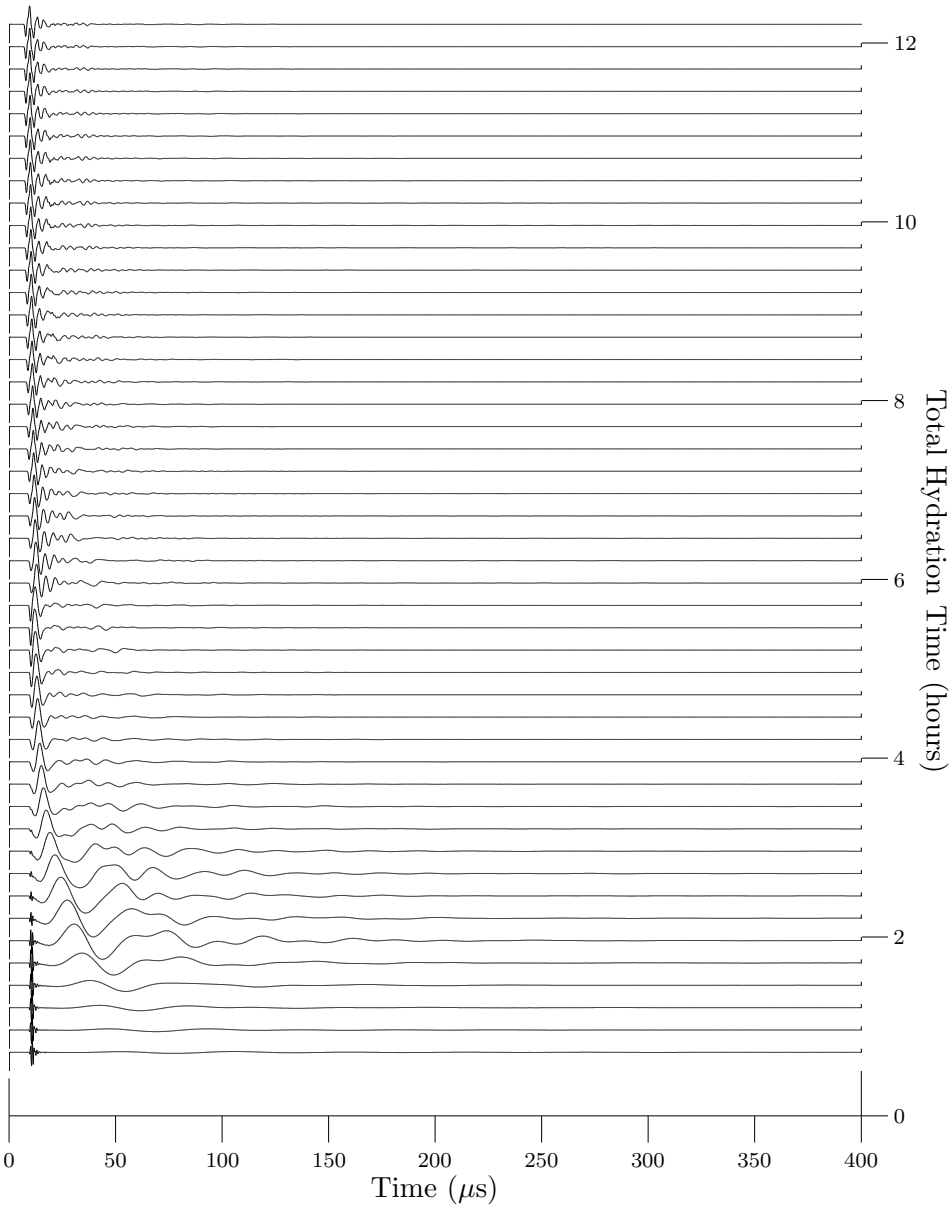

Figure A.2: Specimen 01 (0.0% AEA by weight of cement) normalized signals during the first 12 hours of hydration

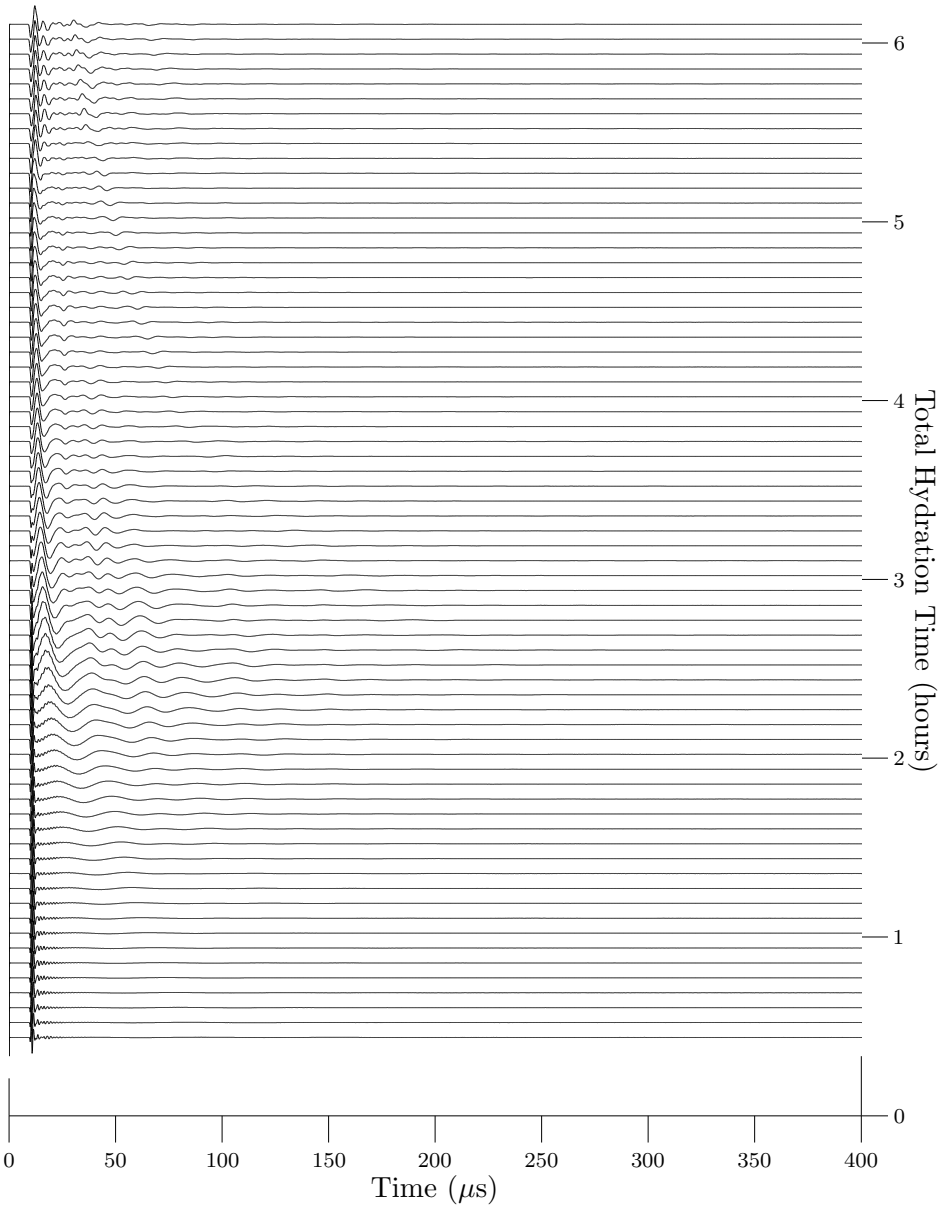

Figure A.3: Specimen 02 (0.0% AEA by weight of cement) normalized signals during the first 6 hours of hydration

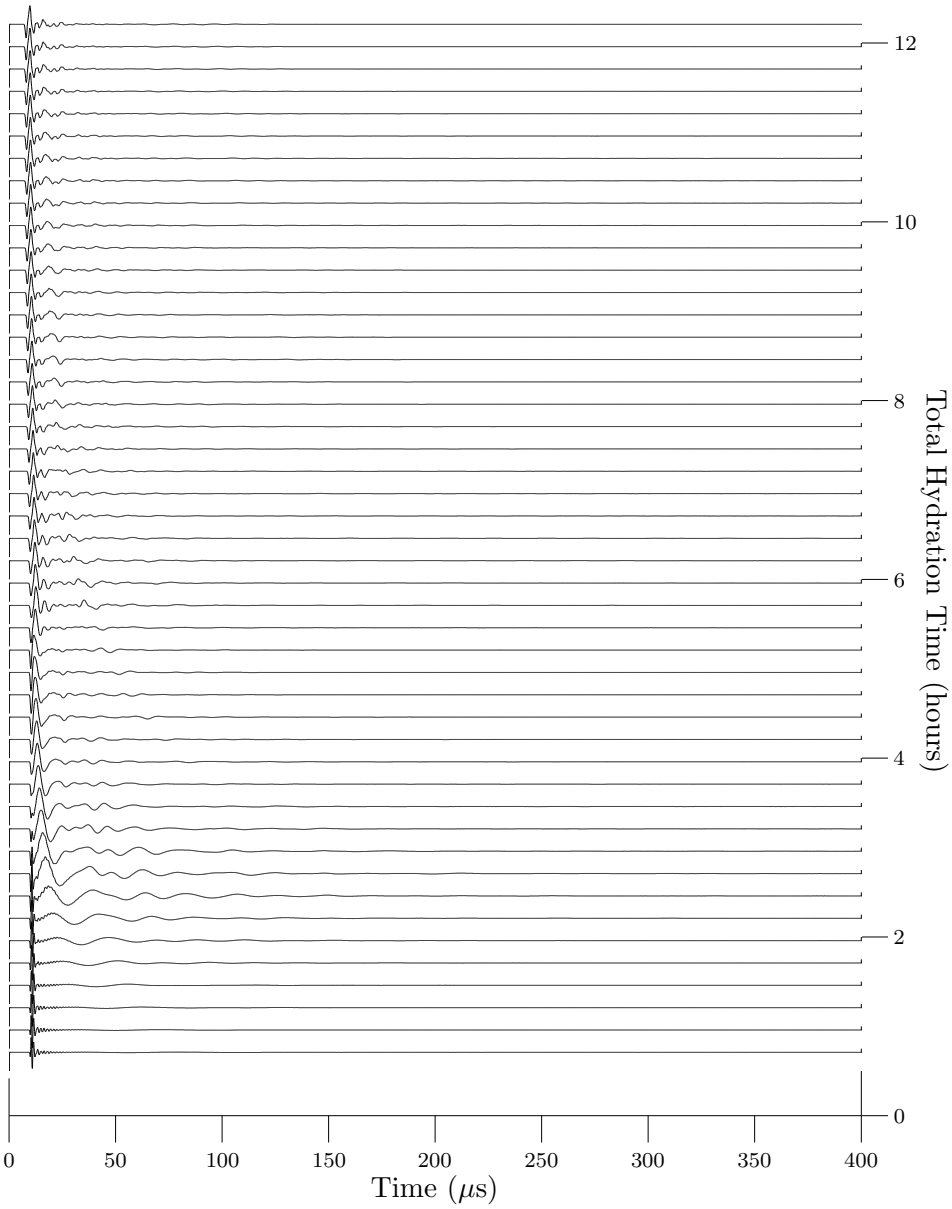

Figure A.4: Specimen 02 (0.0% AEA by weight of cement) normalized signals during the first 12 hours of hydration

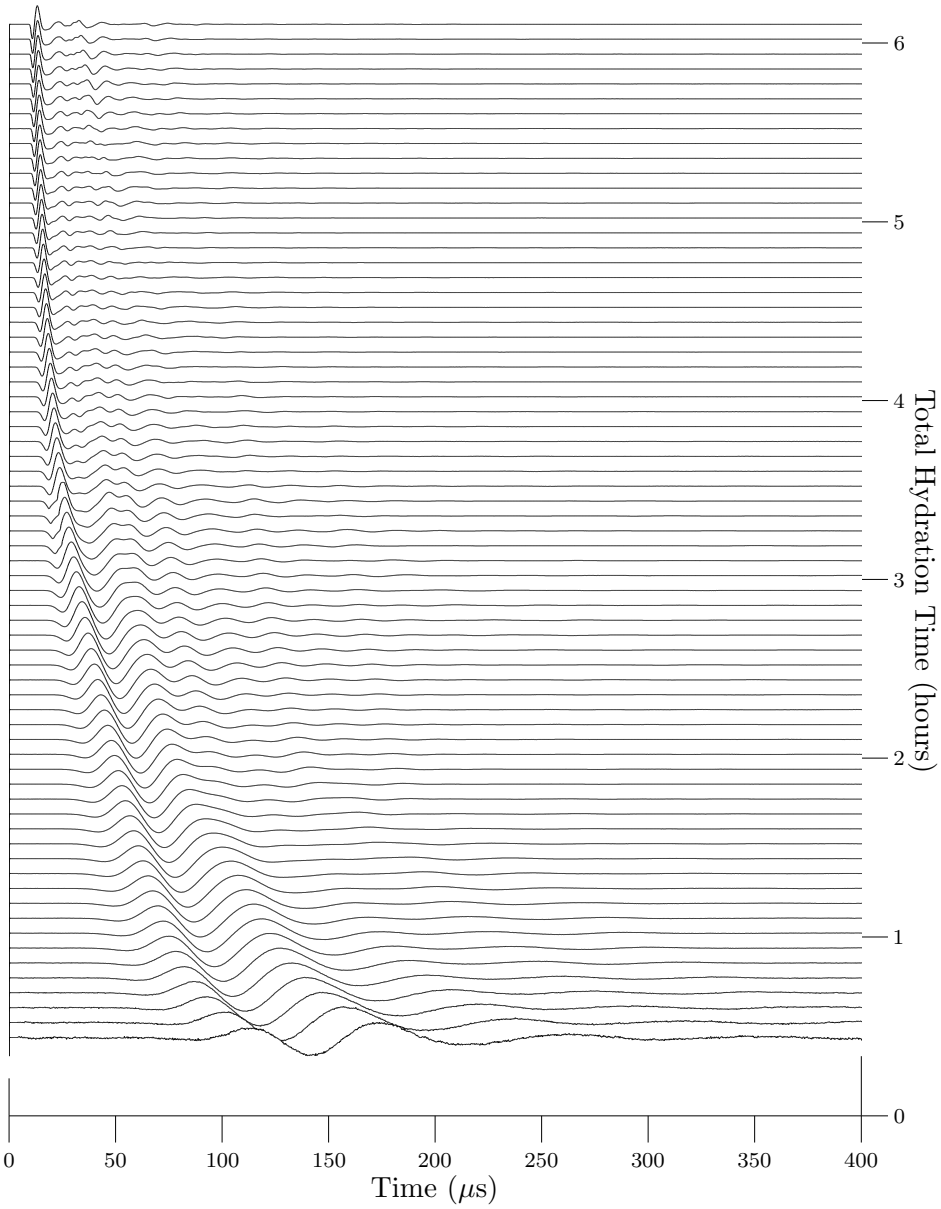

Figure A.5: Specimen 03 (0.2% AEA by weight of cement) normalized signals during the first 6 hours of hydration

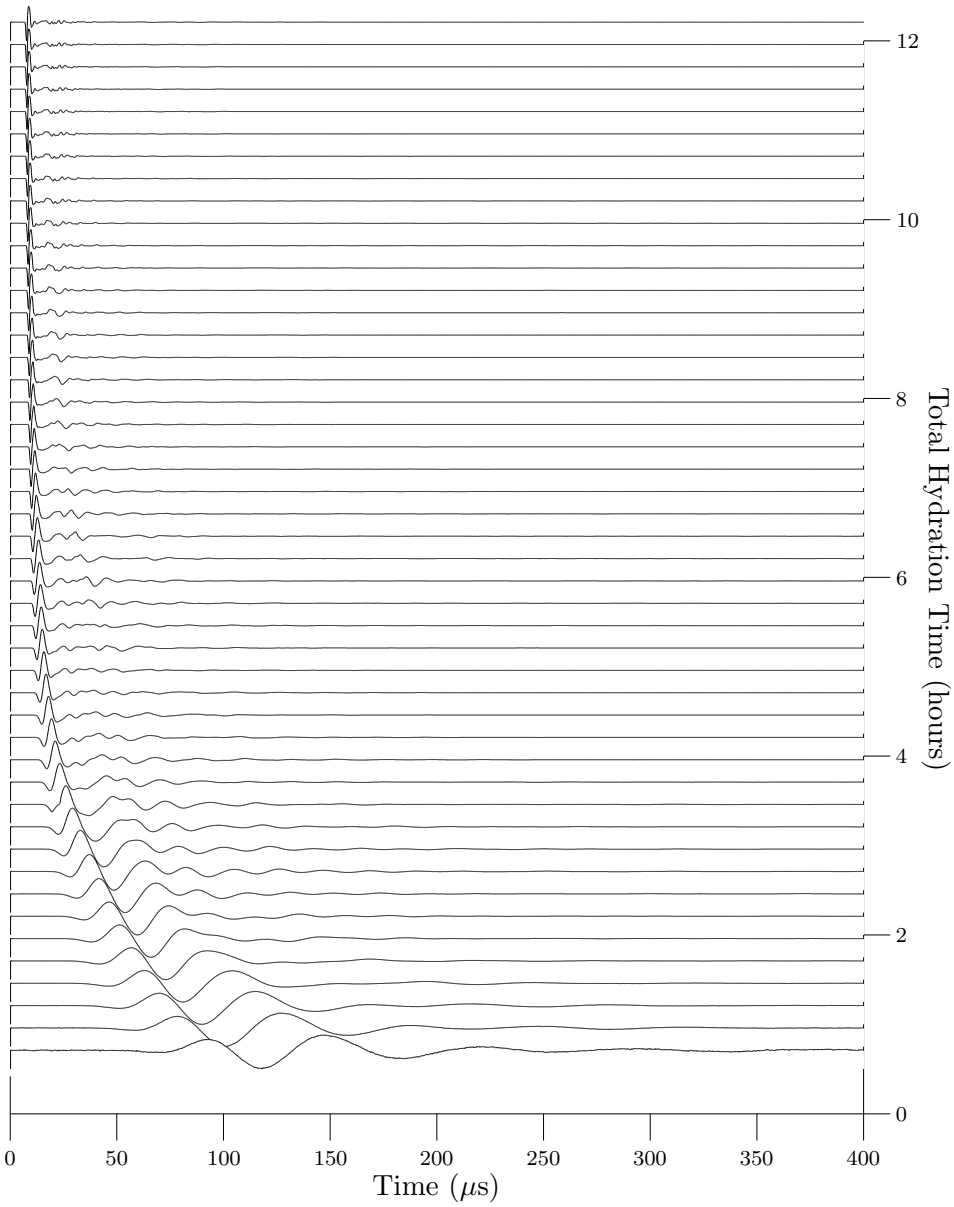

Figure A.6: Specimen 03 (0.2% AEA by weight of cement) normalized signals during the first 12 hours of hydration

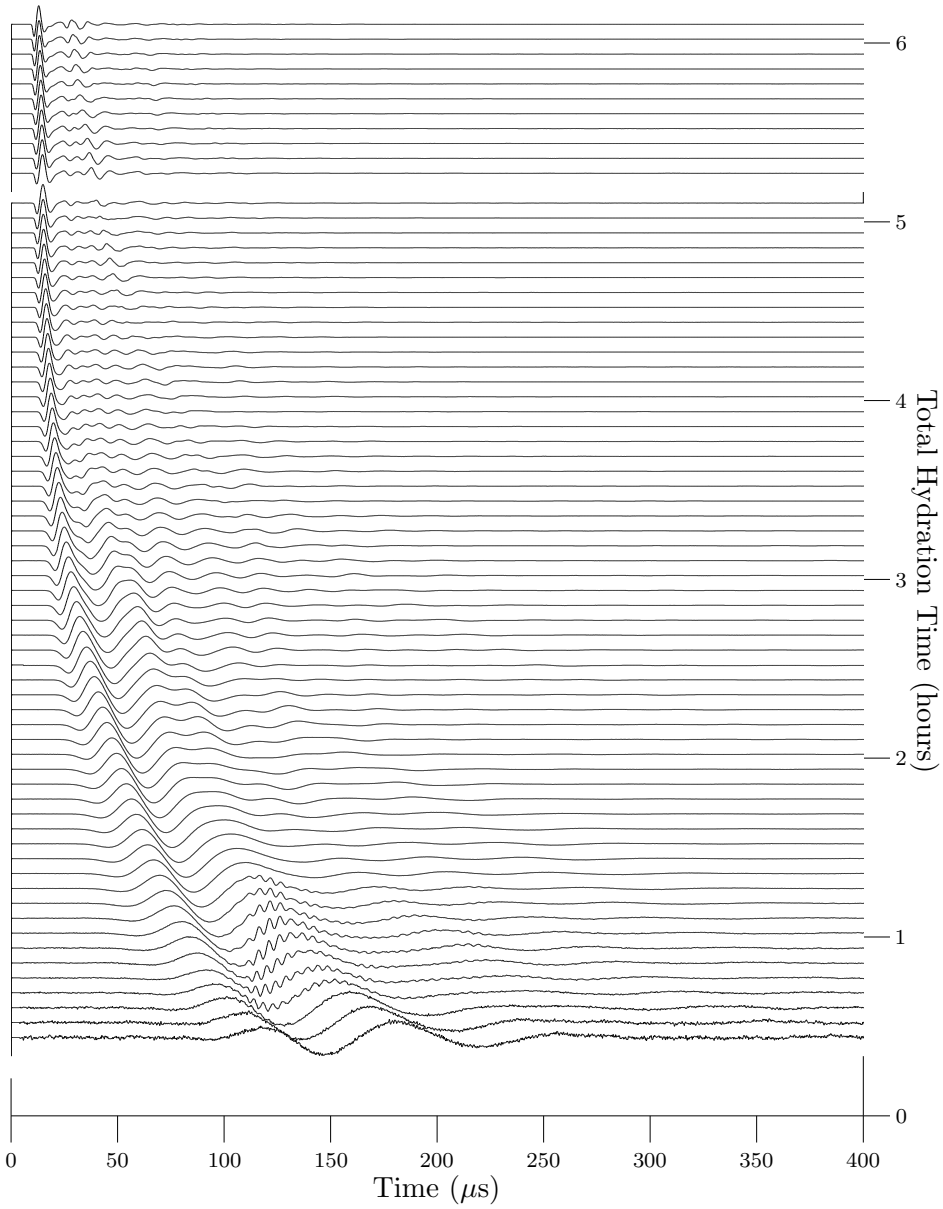

Figure A.7: Specimen 04 (0.2% AEA by weight of cement) normalized signals during the first 6 hours of hydration

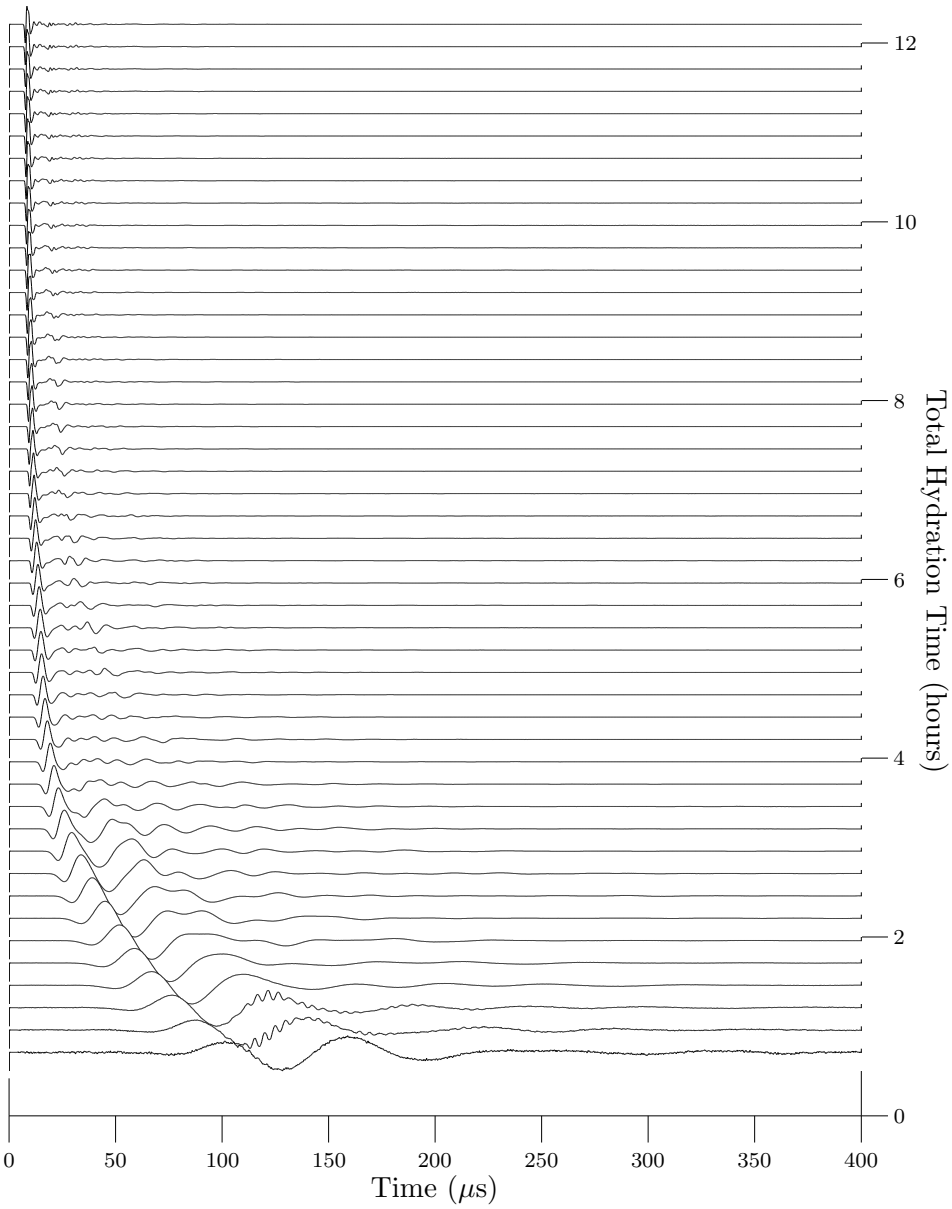

Figure A.8: Specimen 04 (0.2% AEA by weight of cement) normalized signals during the first 12 hours of hydration

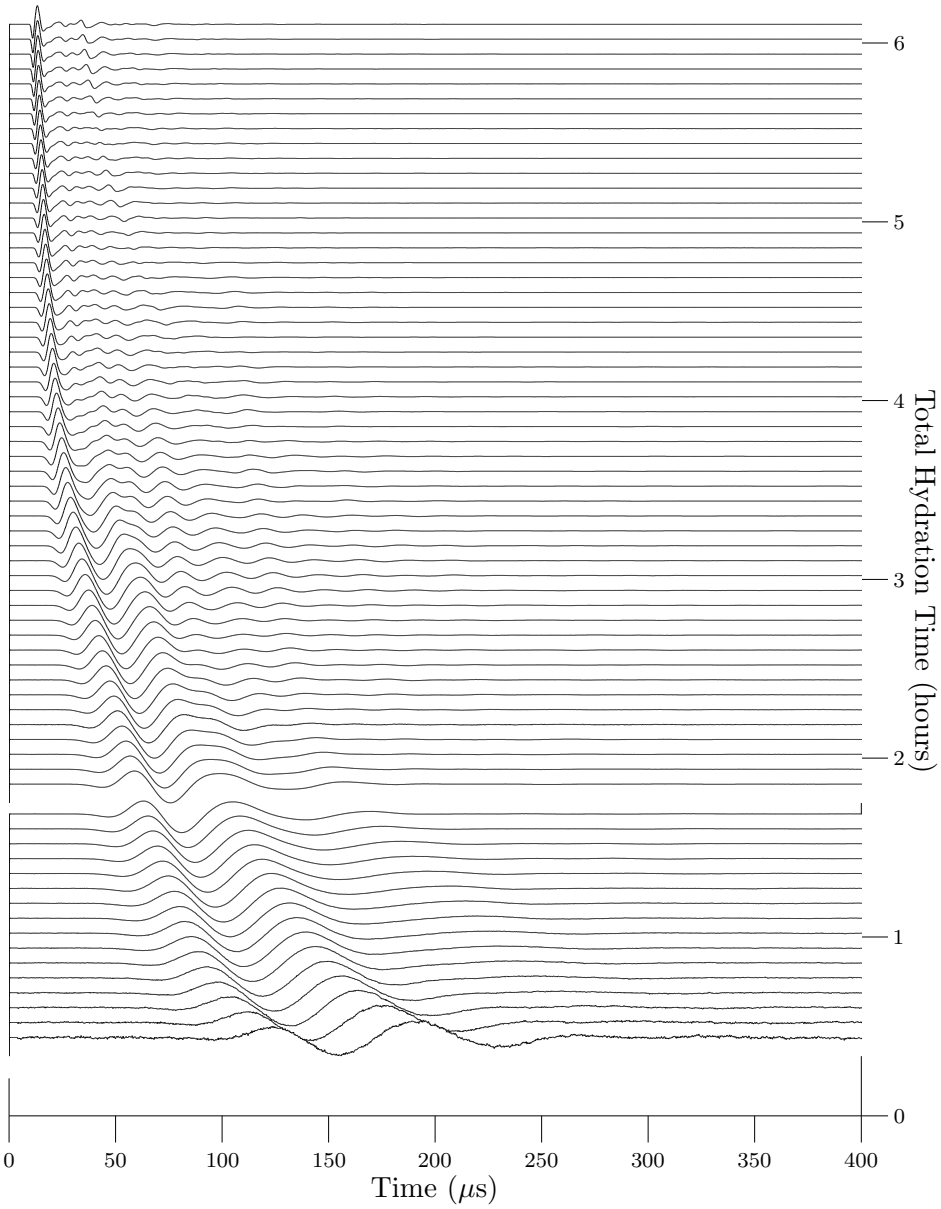

Figure A.9: Specimen 05 (0.4% AEA by weight of cement) normalized signals during the first 6 hours of hydration

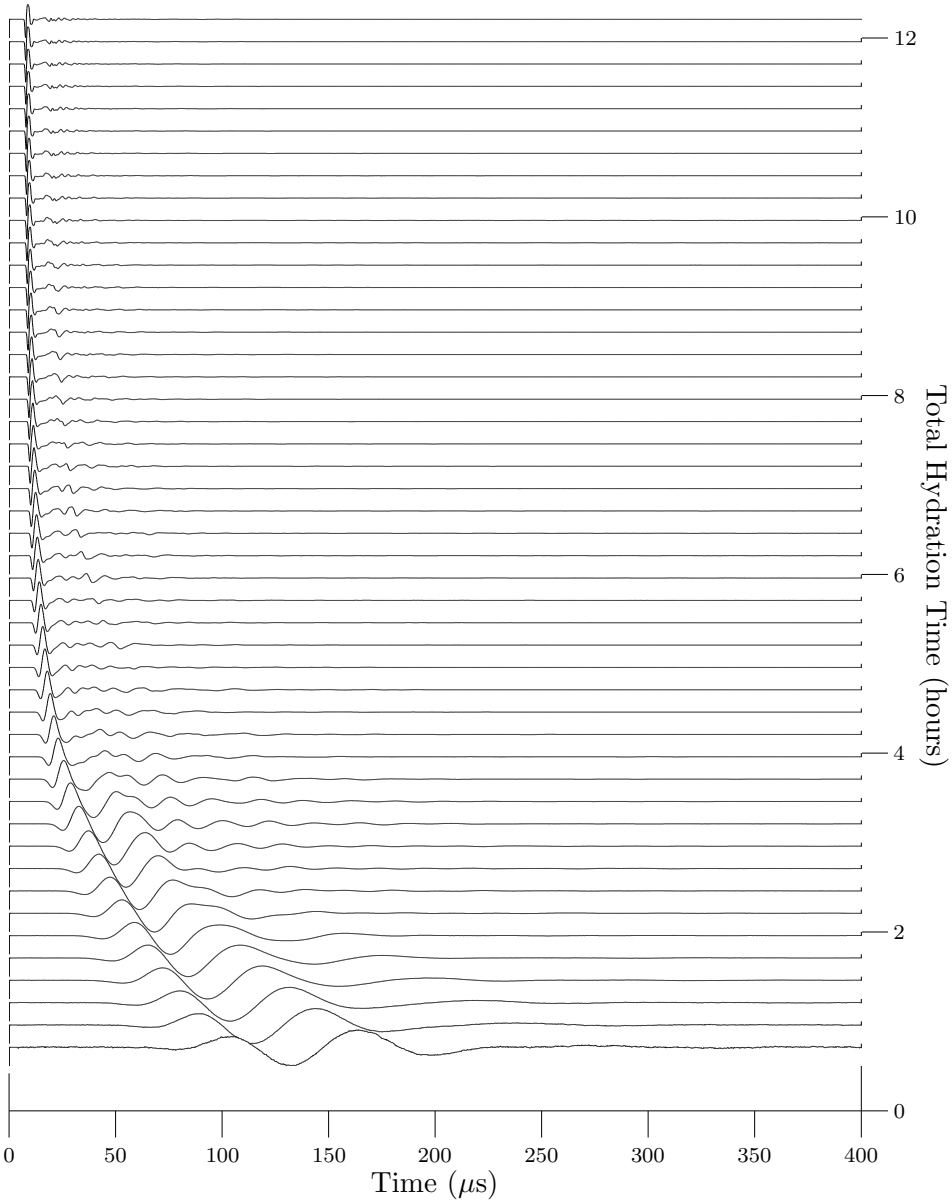

Figure A.10: Specimen 05 (0.4% AEA by weight of cement) normalized signals during the first 12 hours of hydration

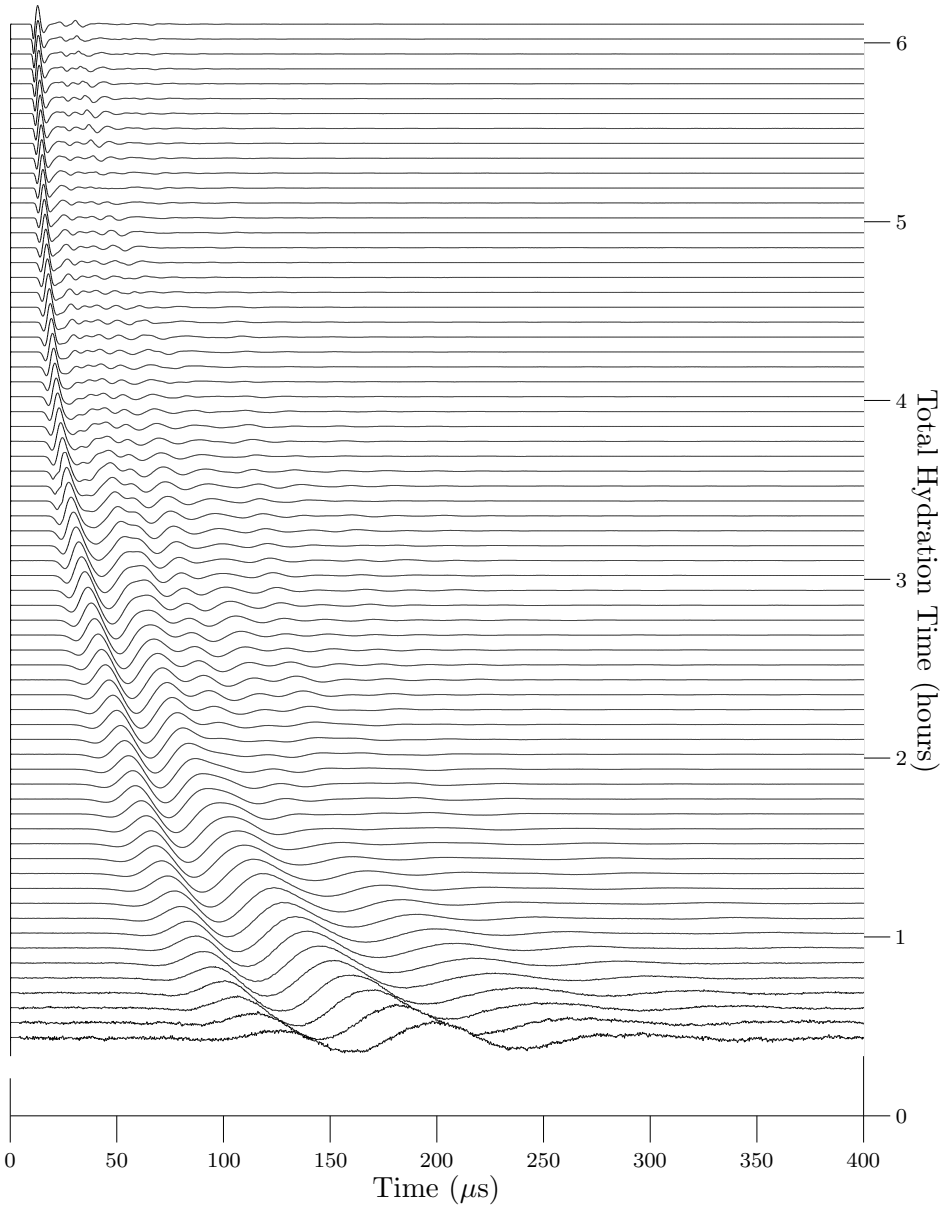

Figure A.11: Specimen 06 (0.4% AEA by weight of cement) normalized signals during the first 6 hours of hydration

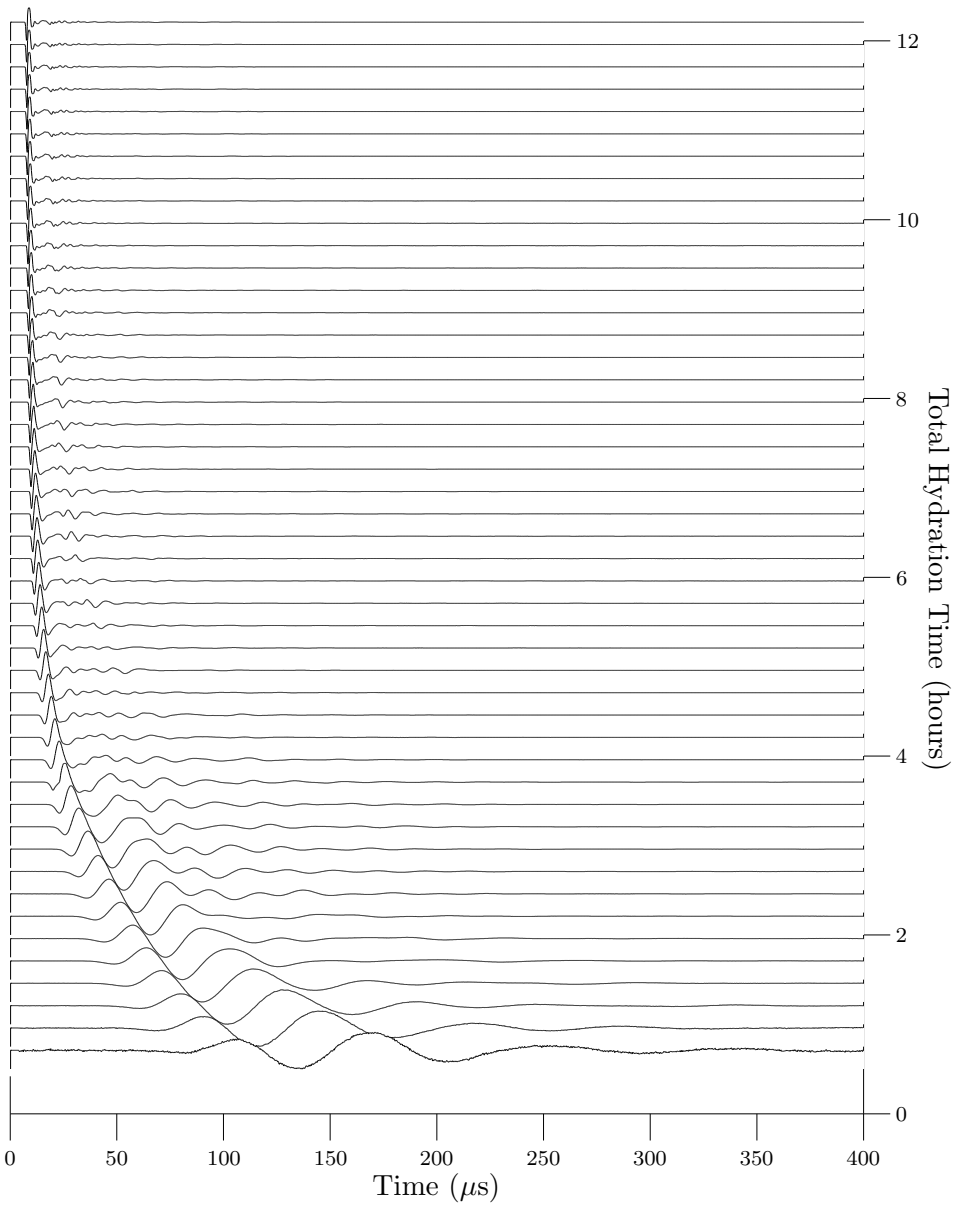

Figure A.12: Specimen 06 (0.4% AEA by weight of cement) normalized signals during the first 12 hours of hydration

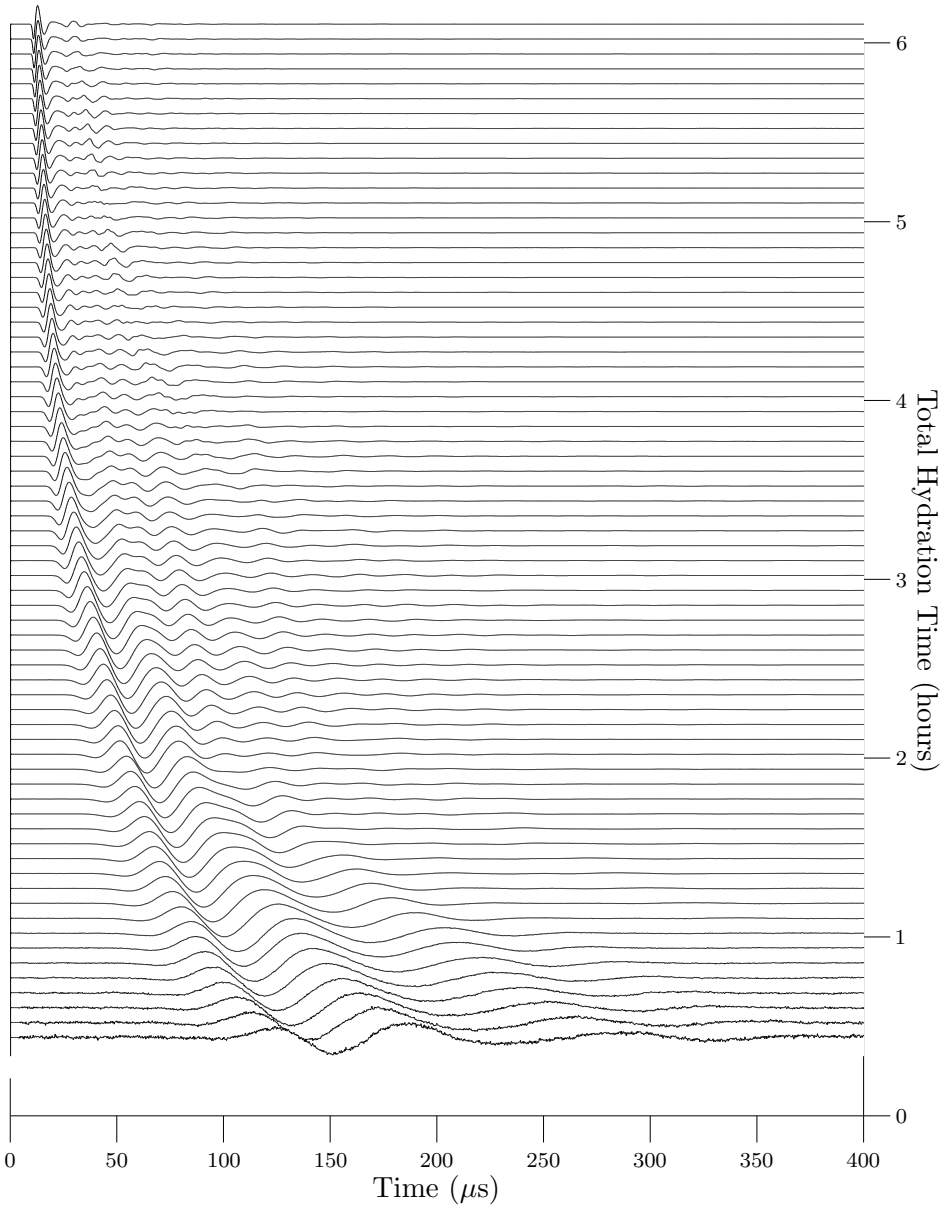

Figure A.13: Specimen 07 (6.0% AEA by weight of cement) normalized signals during the first 6 hours of hydration

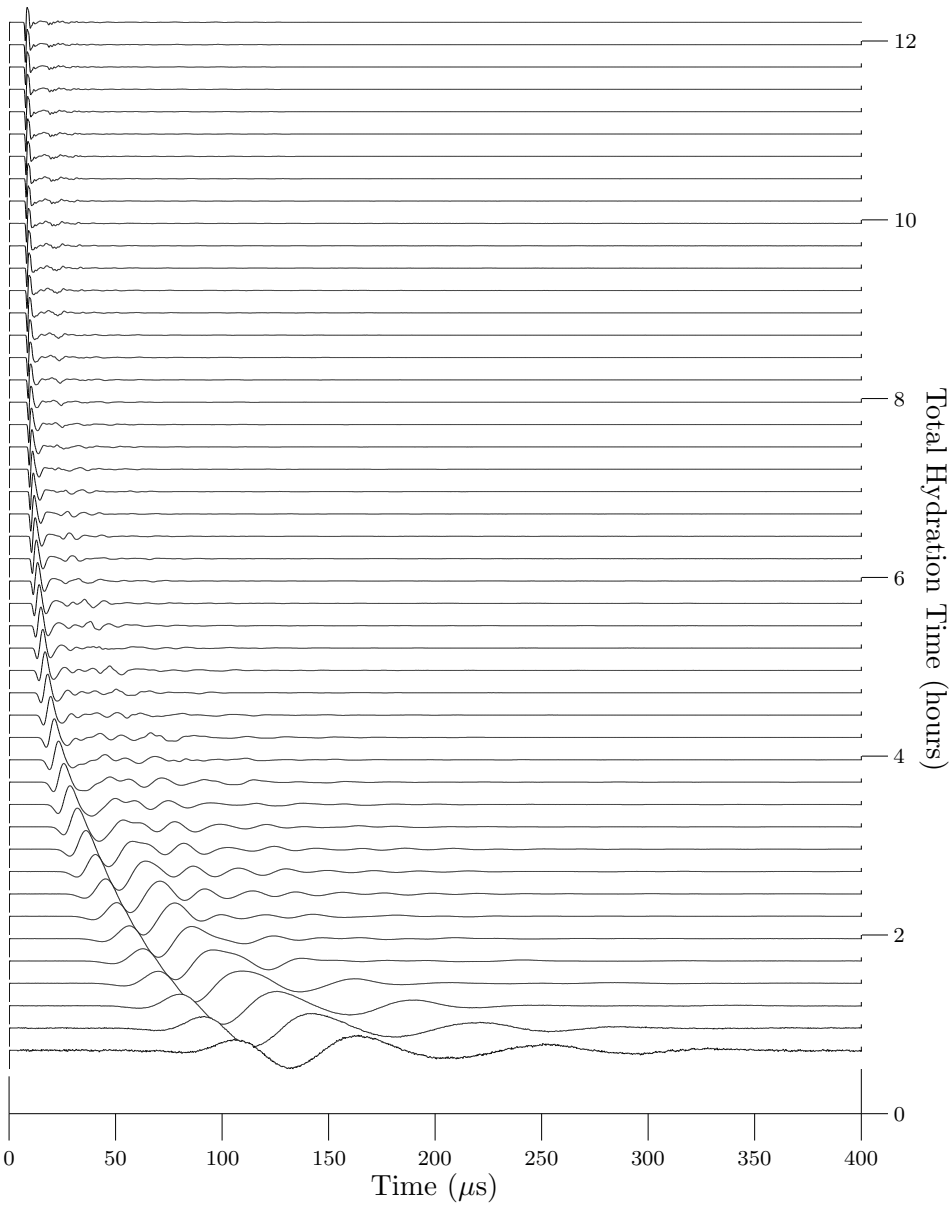

Figure A.14: Specimen 07 (6.0% AEA by weight of cement) normalized signals during the first 12 hours of hydration

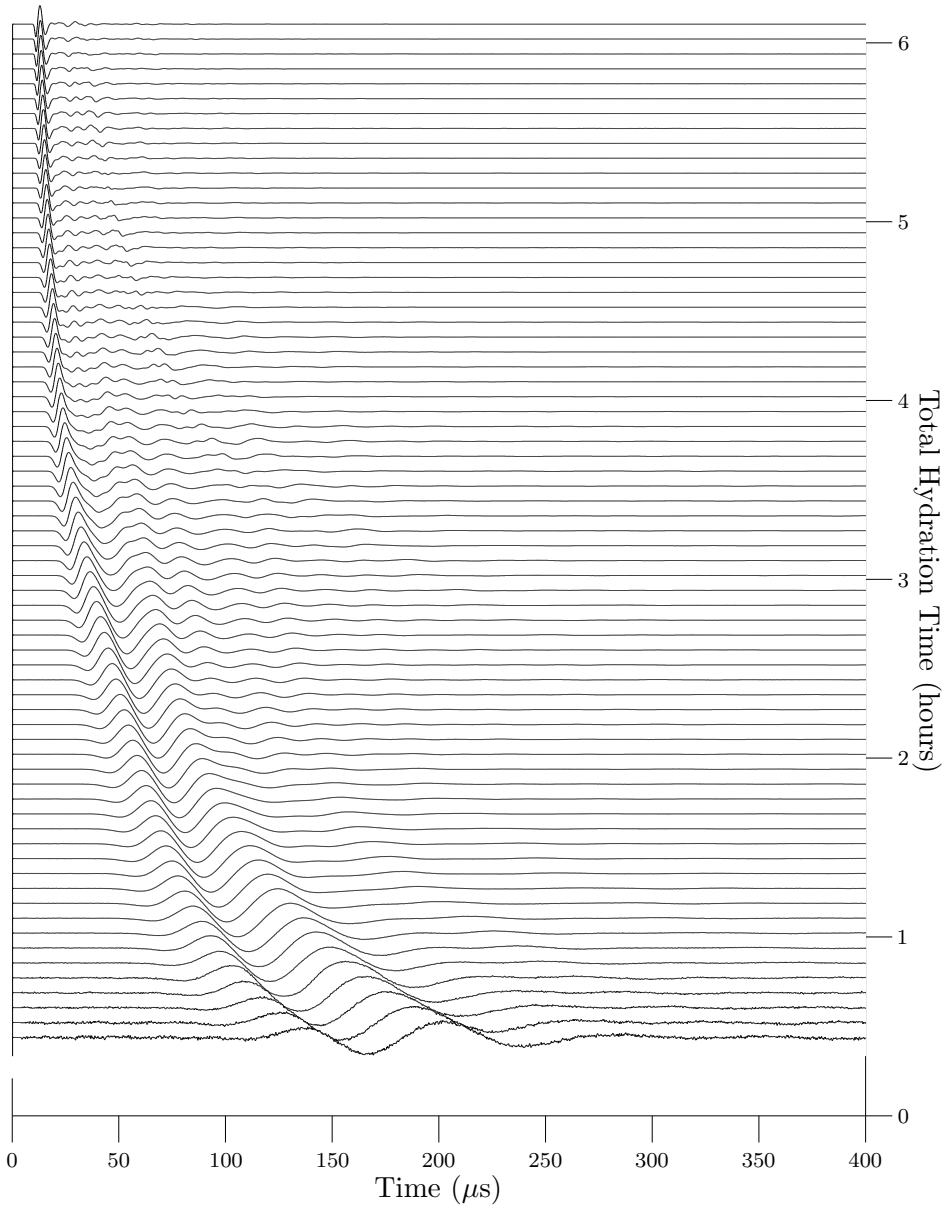

Figure A.15: Specimen 08 (6.0% AEA by weight of cement) normalized signals during the first 6 hours of hydration

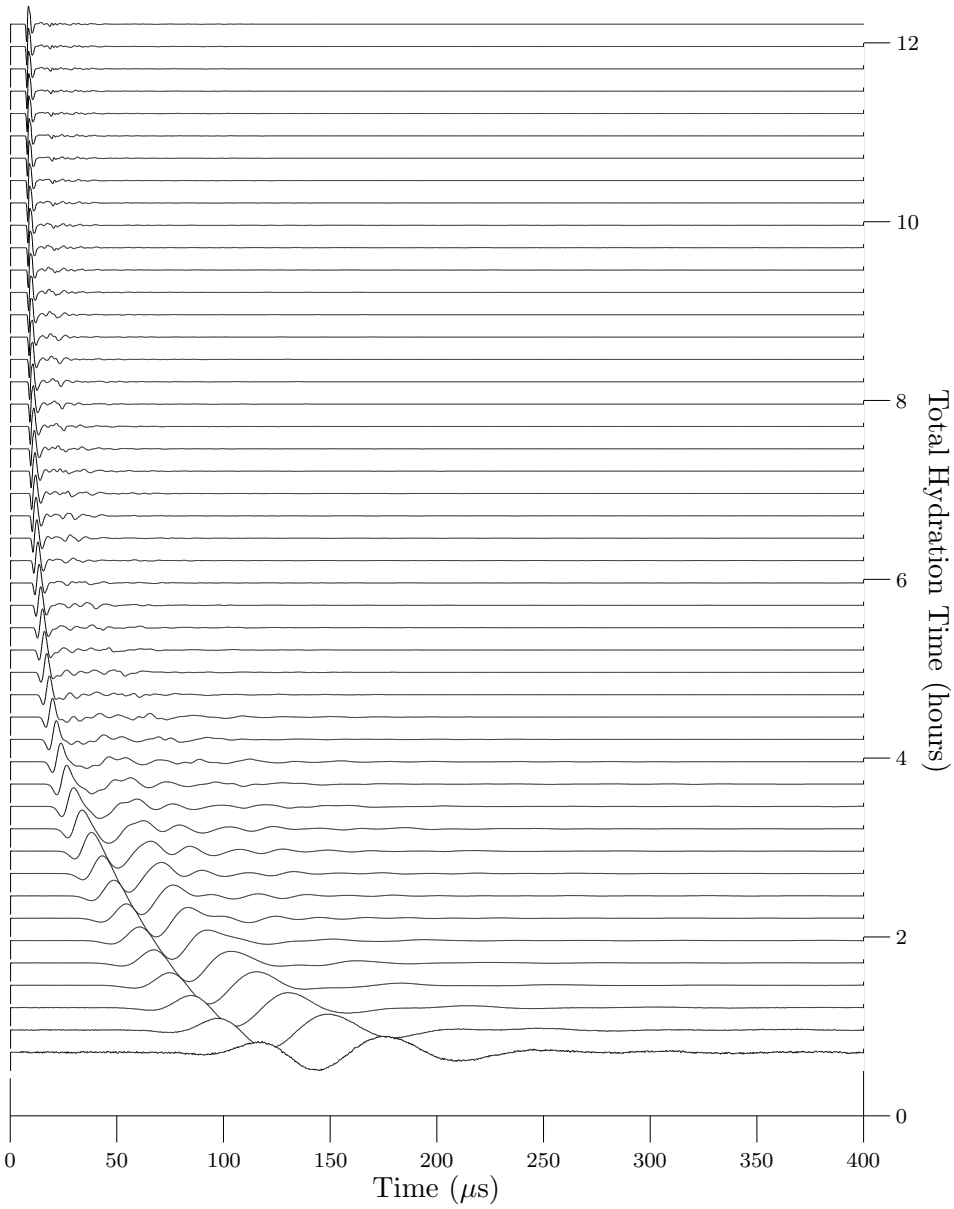

Figure A.16: Specimen 08 (6.0% AEA by weight of cement) normalized signals during the first 12 hours of hydration

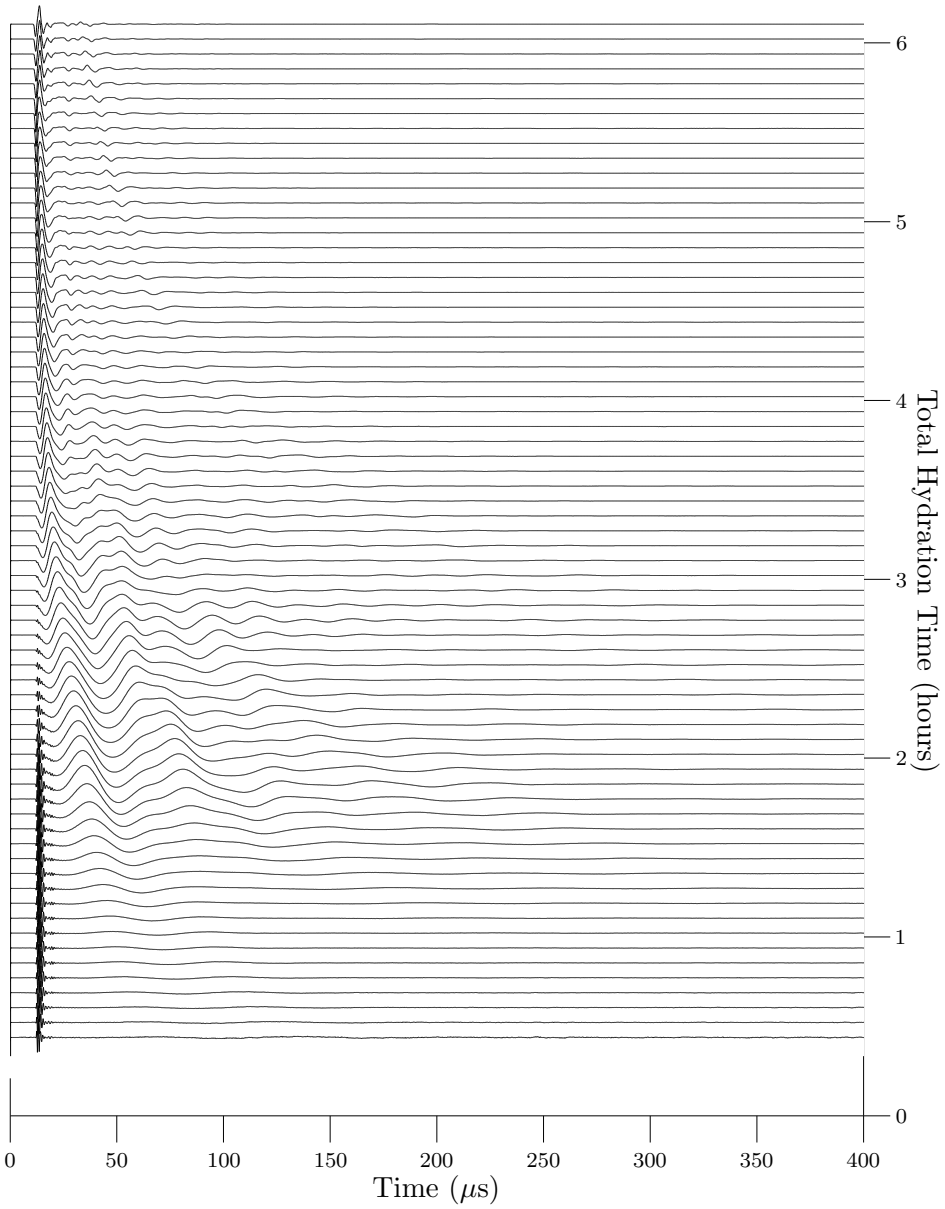

Figure A.17: Specimen 09 (0.0% AEA by weight of cement) normalized signals during the first 6 hours of hydration

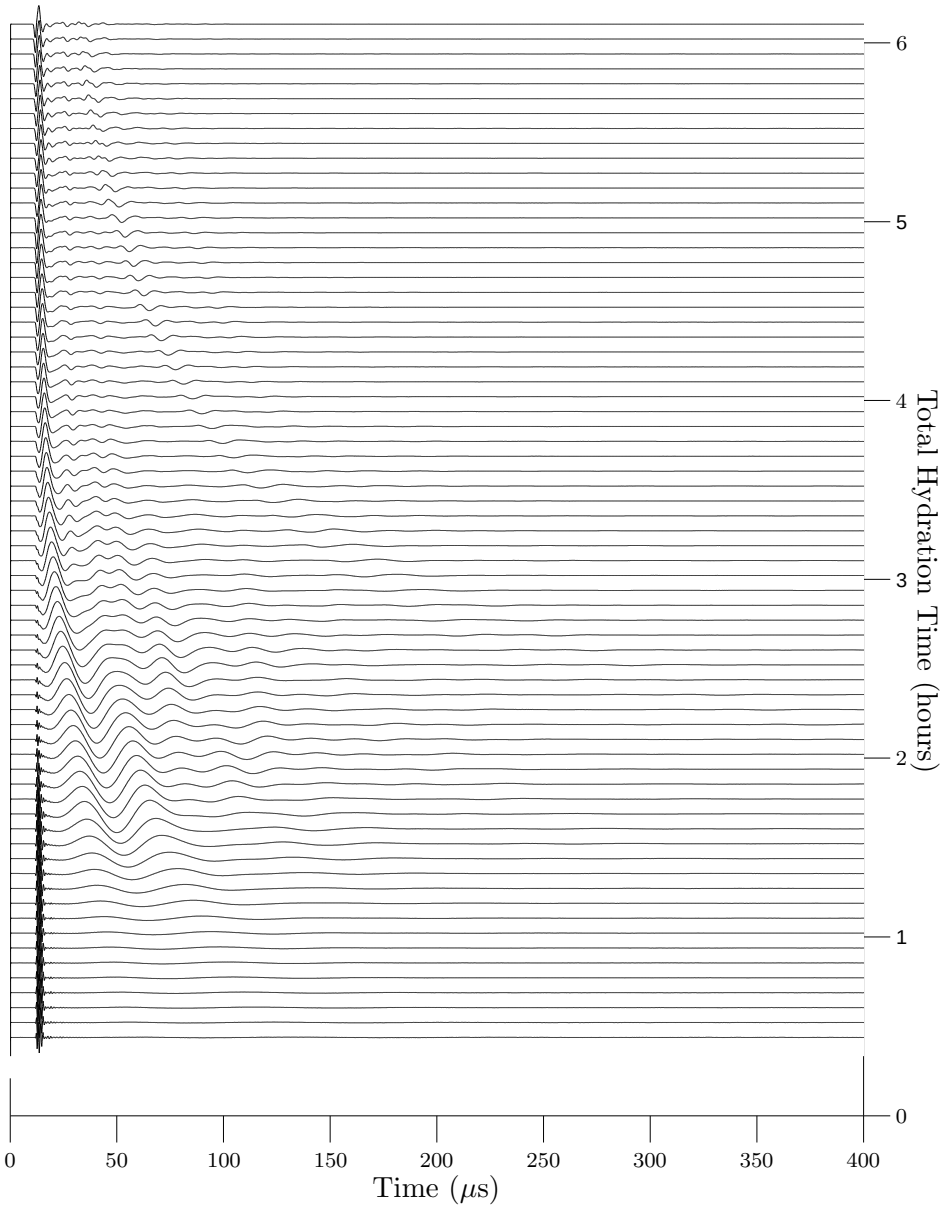

Figure A.18: Specimen 09 (0.0% AEA by weight of cement) normalized signals during the first 12 hours of hydration

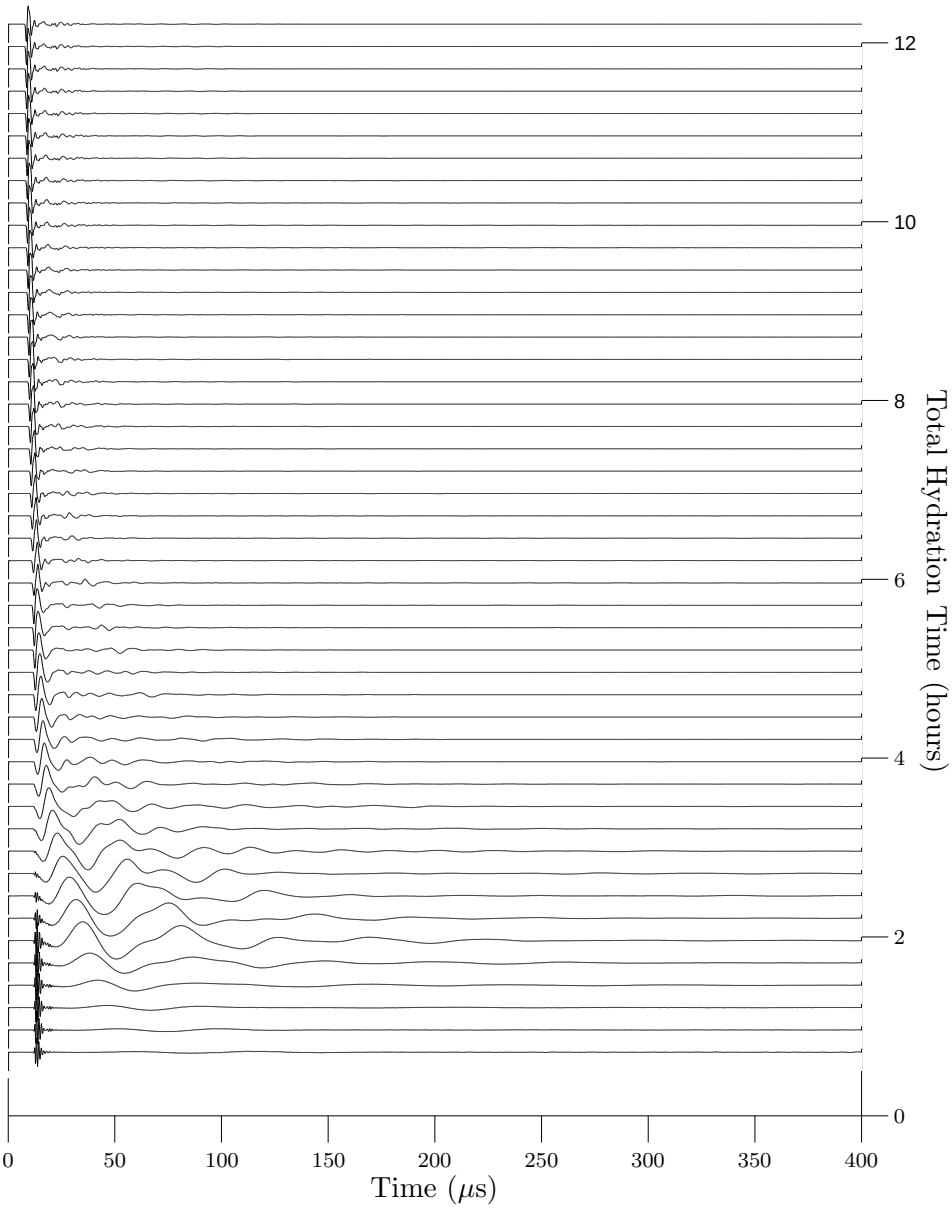

Figure A.19: Specimen 10 (0.0% AEA by weight of cement) normalized signals during the first 6 hours of hydration

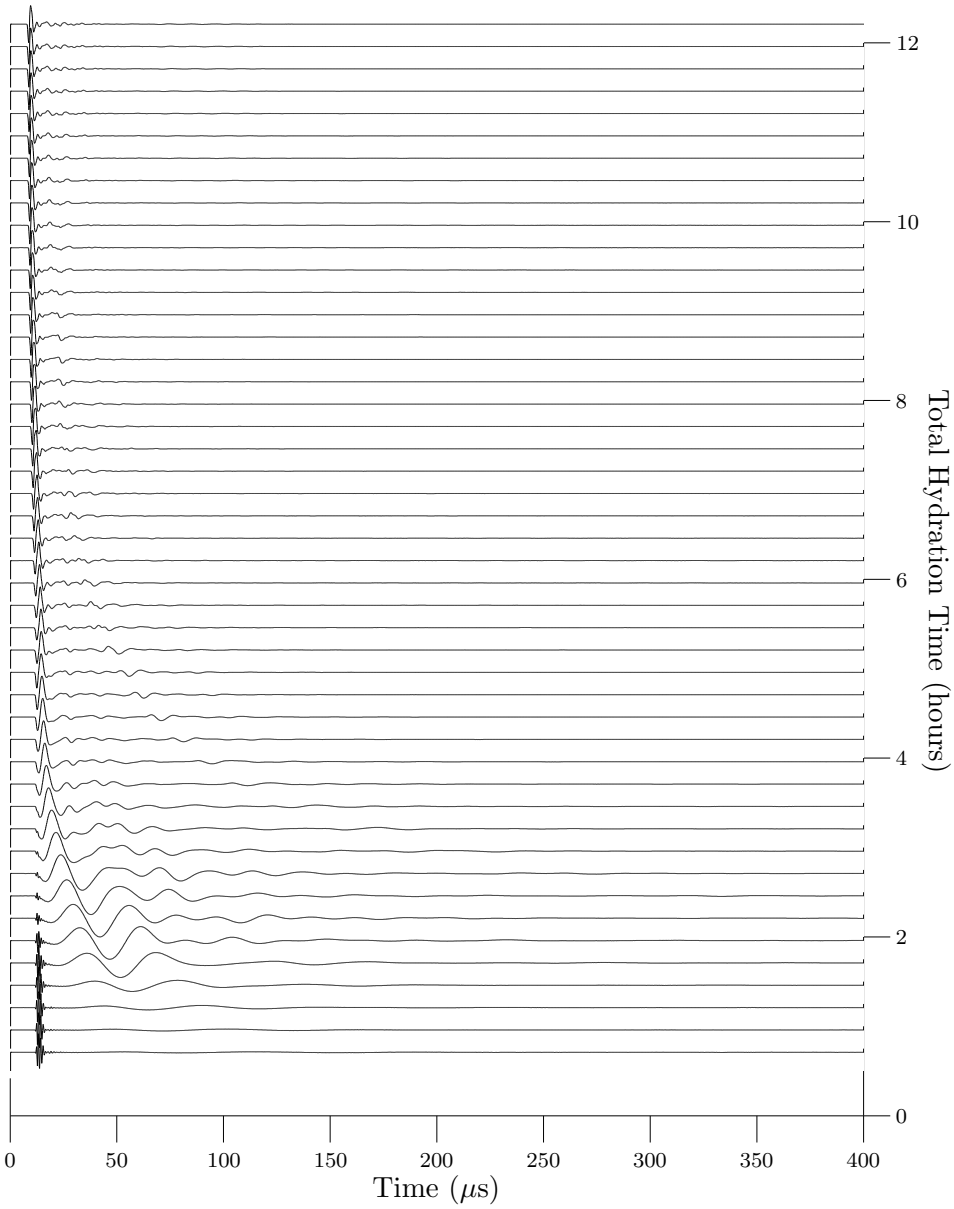

Figure A.20: Specimen 10 (0.0% AEA by weight of cement) normalized signals during the first 12 hours of hydration

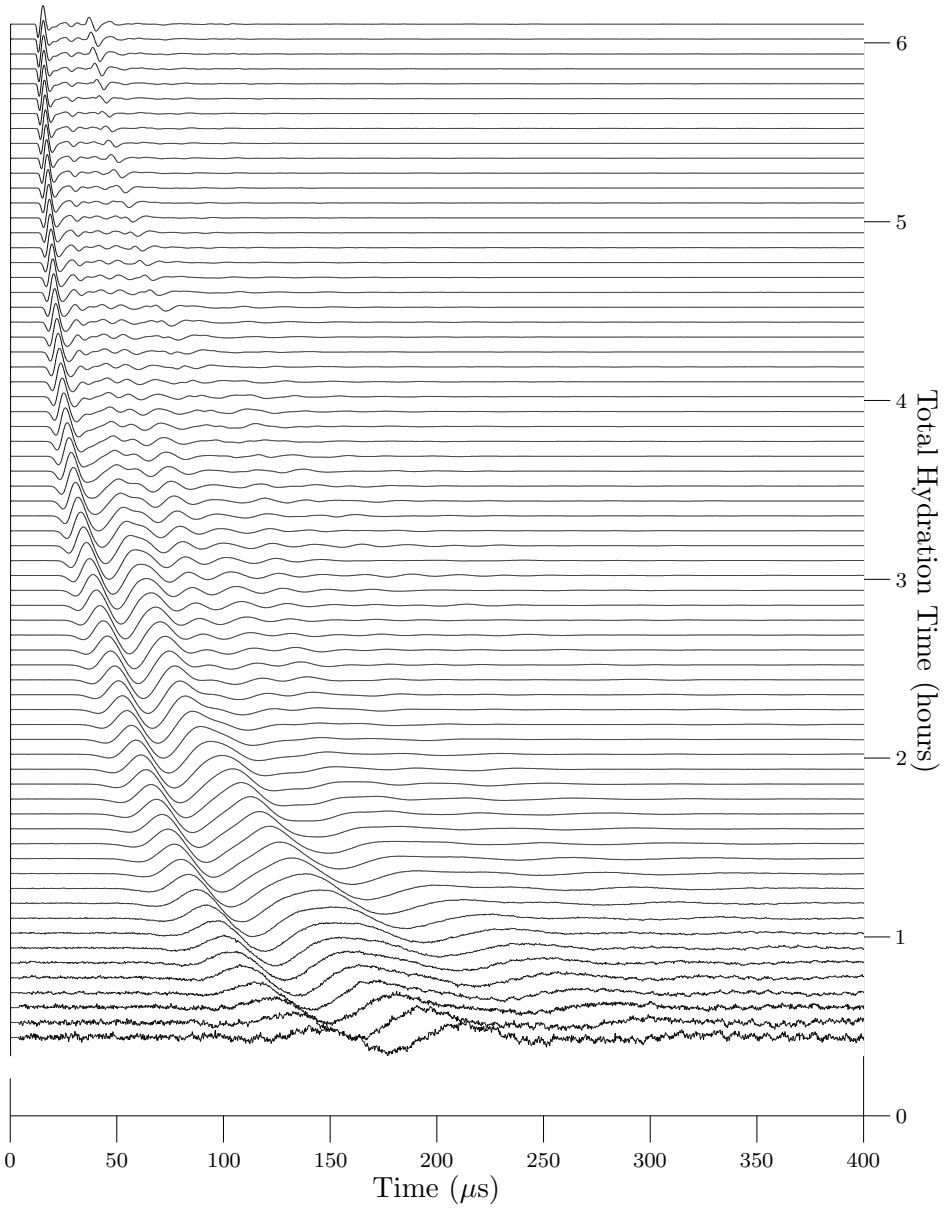

Figure A.21: Specimen 11 (0.2% AEA by weight of cement) normalized signals during the first 6 hours of hydration

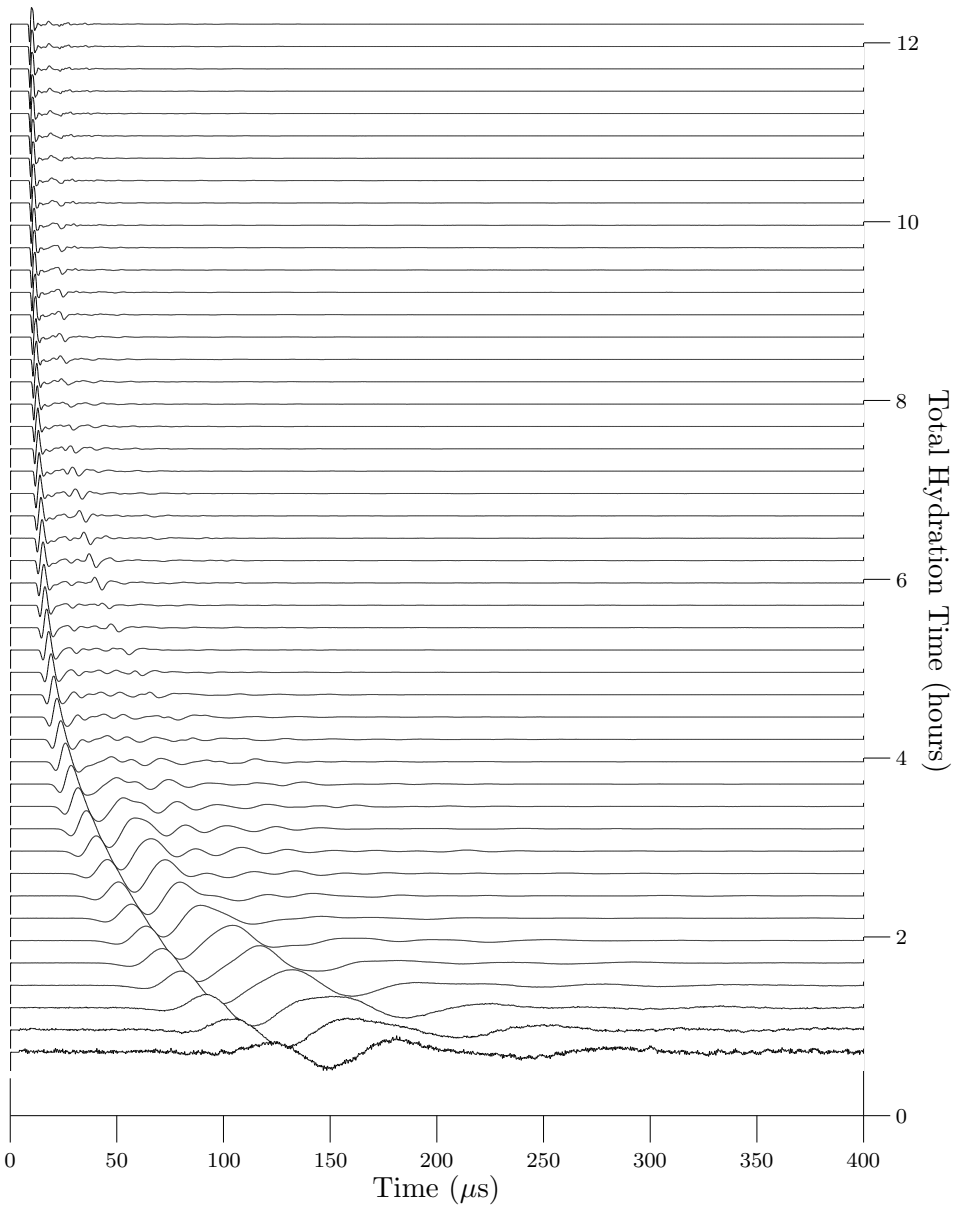

Figure A.22: Specimen 11 (0.2% AEA by weight of cement) normalized signals during the first 12 hours of hydration

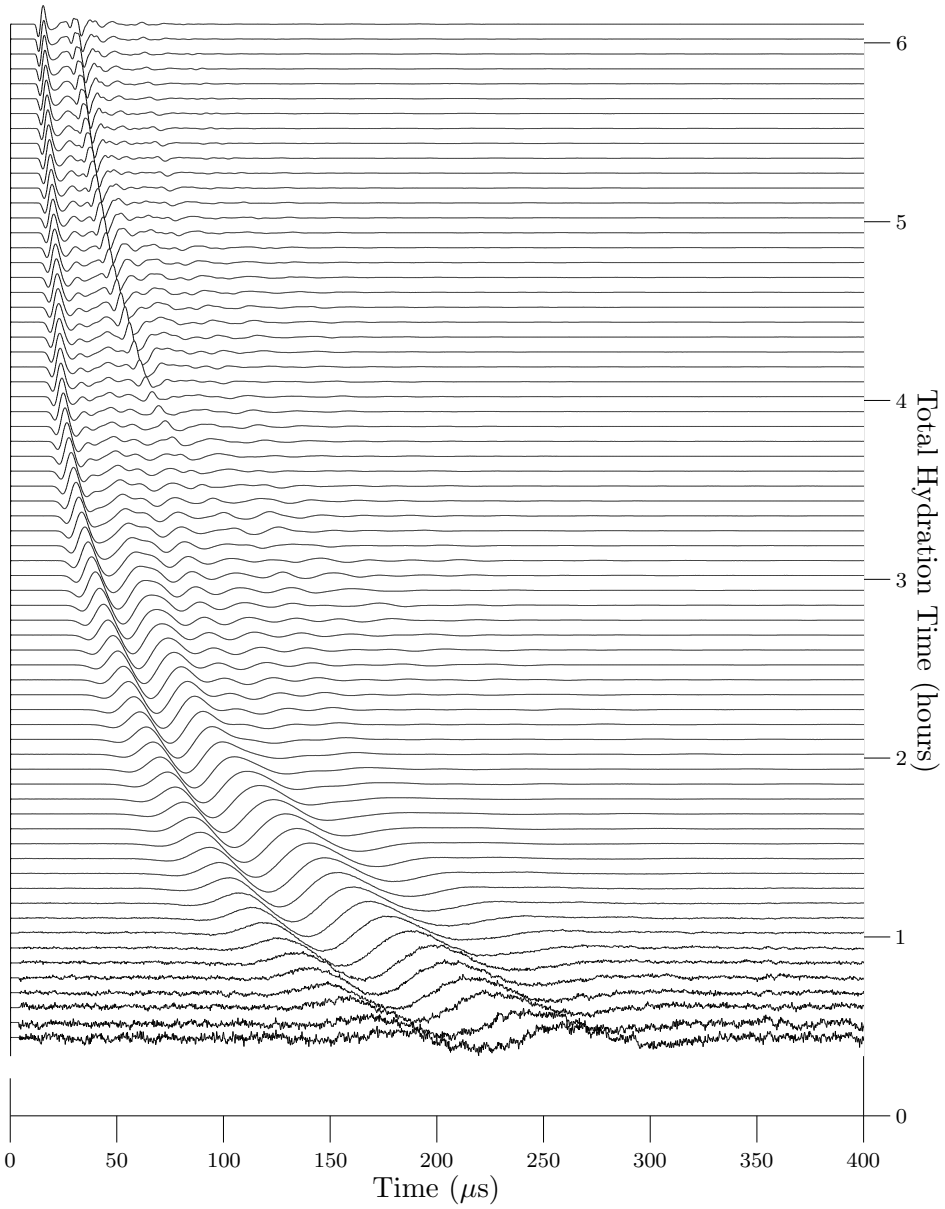

Figure A.23: Specimen 12 (0.2% AEA by weight of cement) normalized signals during the first 6 hours of hydration

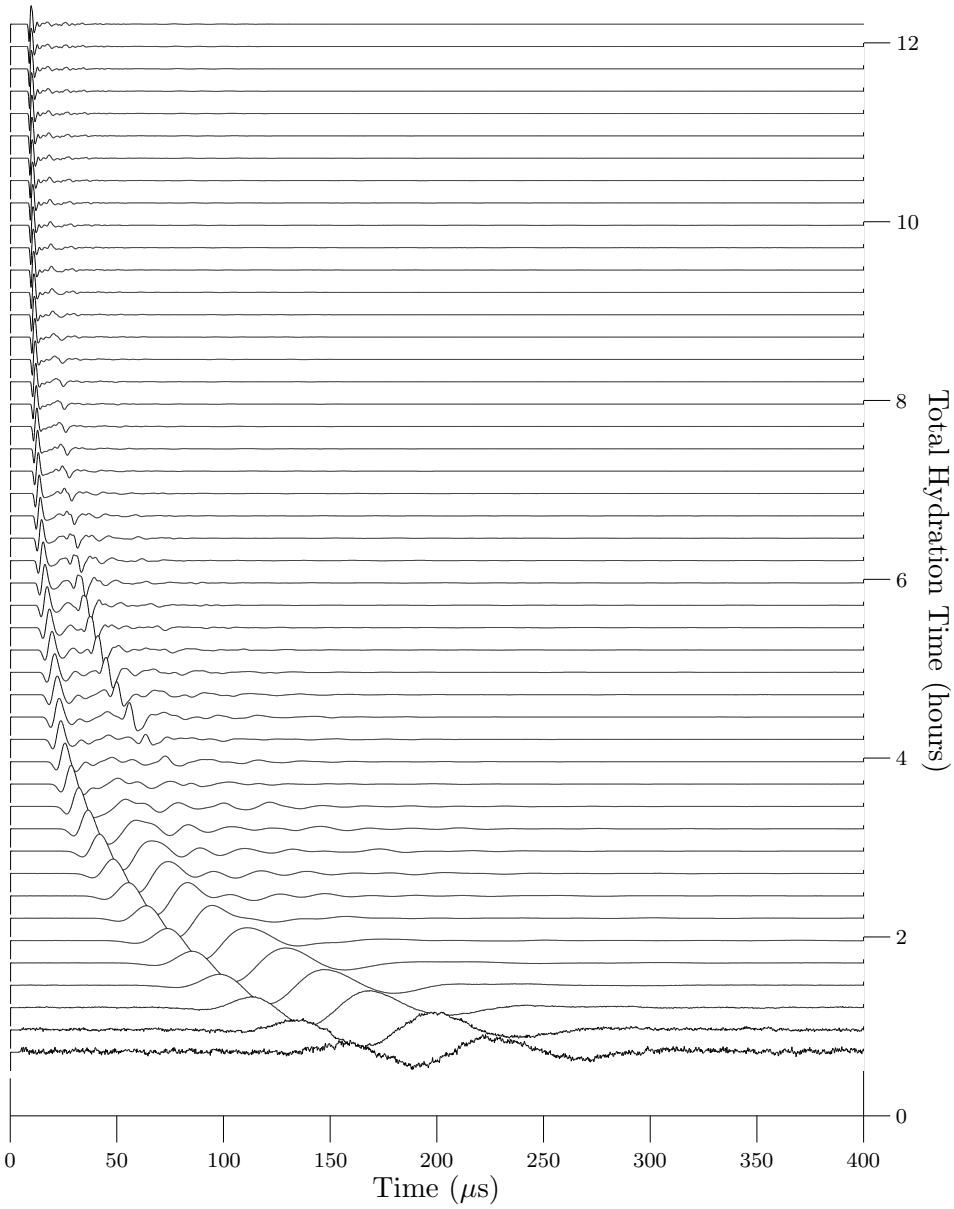

Figure A.24: Specimen 12 (0.2% AEA by weight of cement) normalized signals during the first 12 hours of hydration

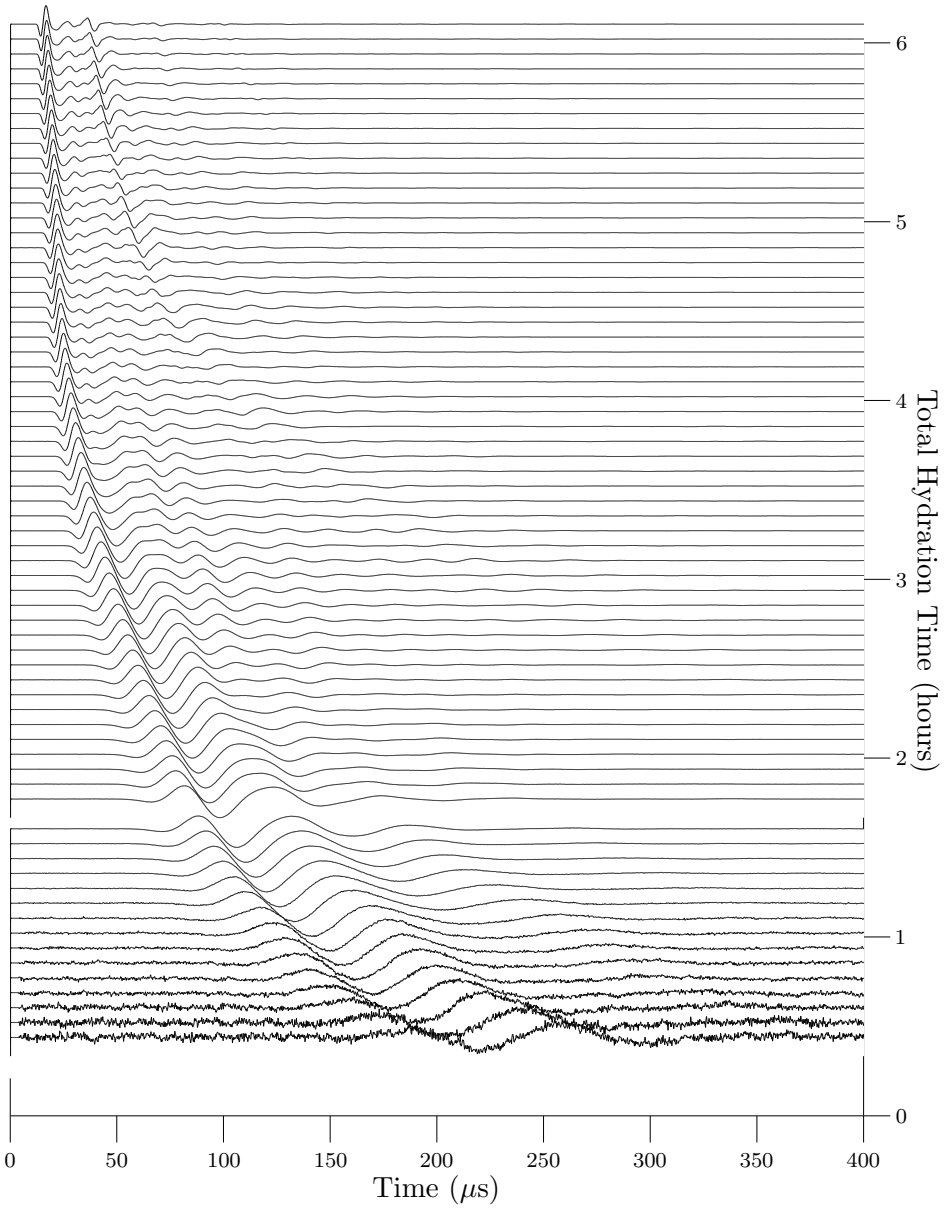

Figure A.25: Specimen 13 (0.4% AEA by weight of cement) normalized signals during the first 6 hours of hydration

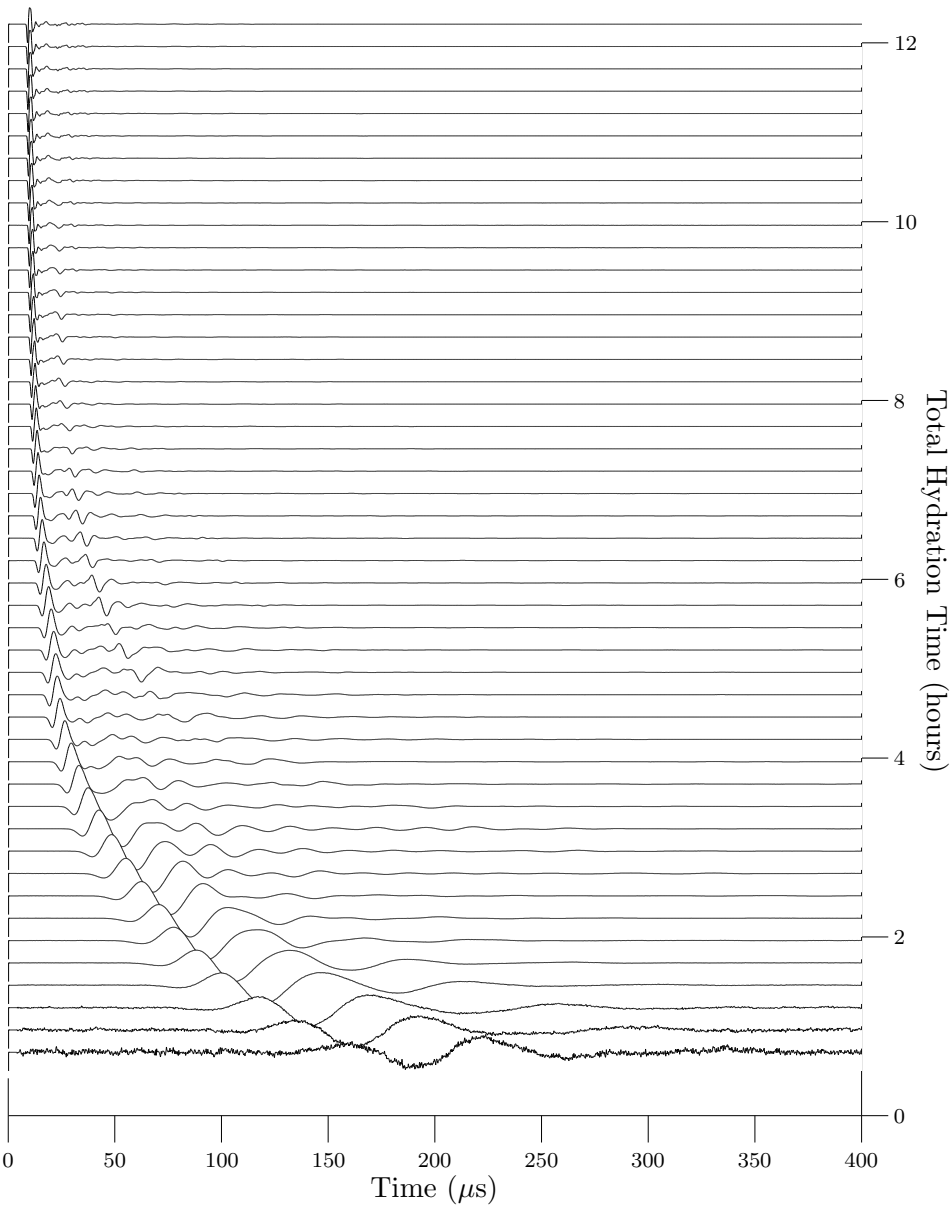

Figure A.26: Specimen 13 (0.4% AEA by weight of cement) normalized signals during the first 12 hours of hydration

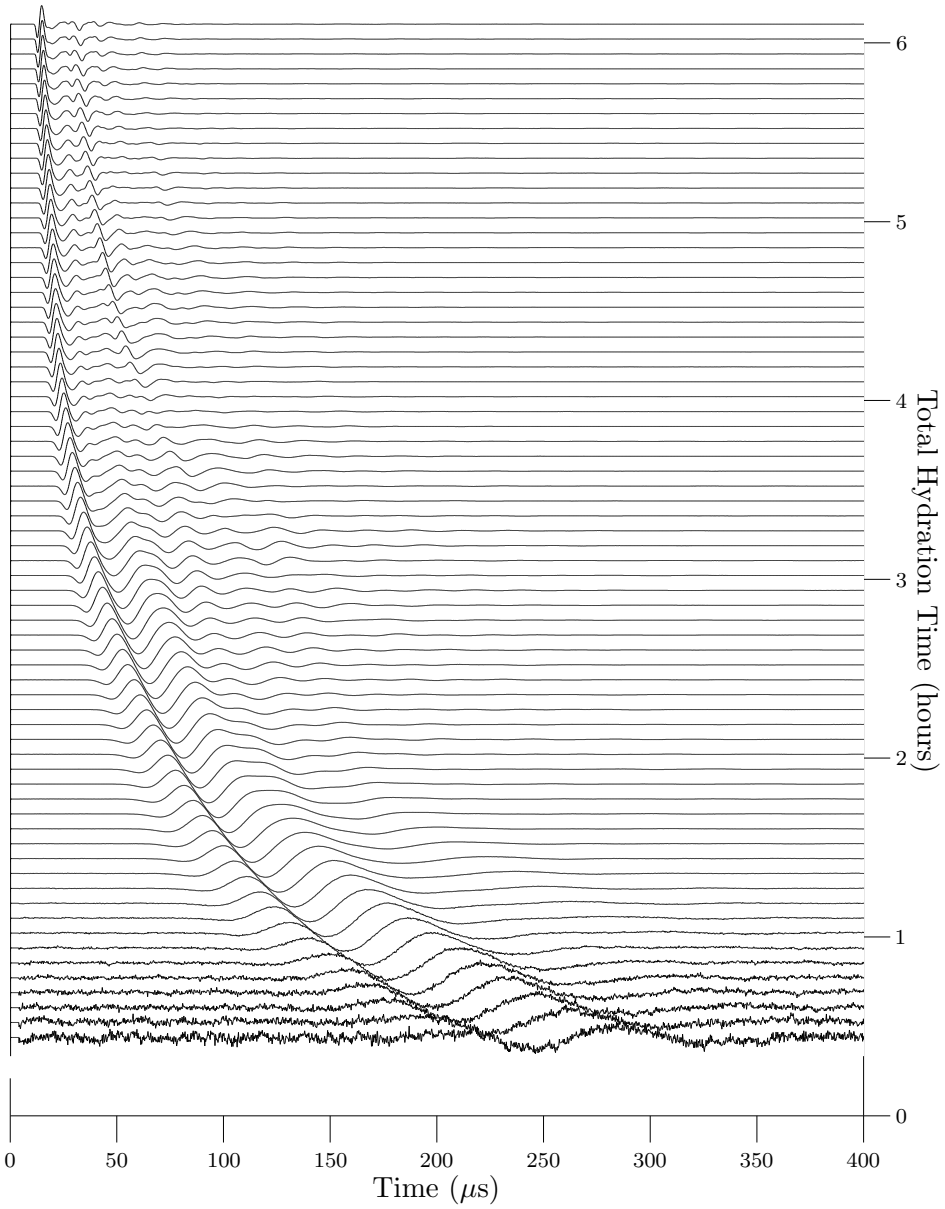

Figure A.27: Specimen 14 (0.4% AEA by weight of cement) normalized signals during the first 6 hours of hydration

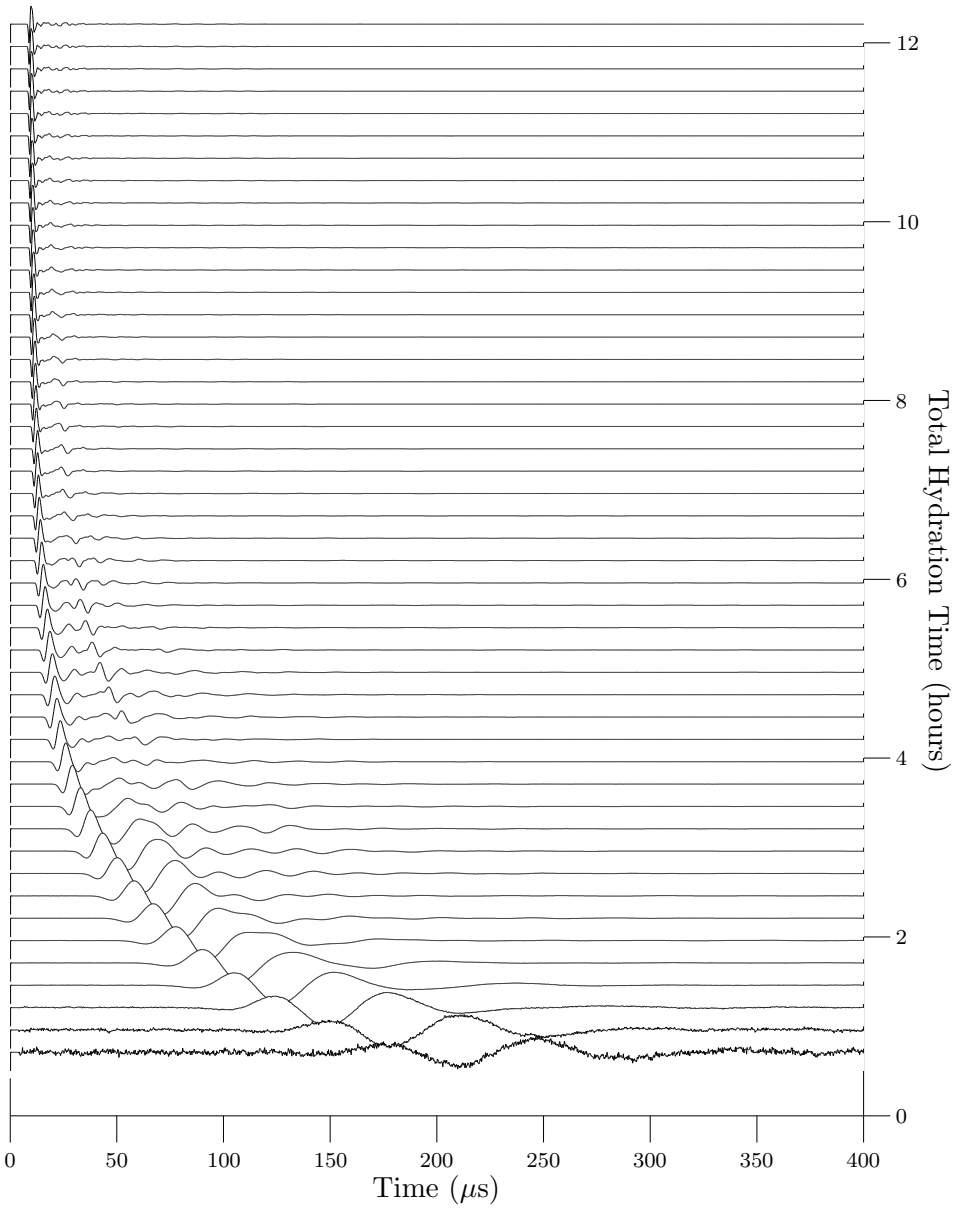

Figure A.28: Specimen 14 (0.4% AEA by weight of cement) normalized signals during the first 12 hours of hydration

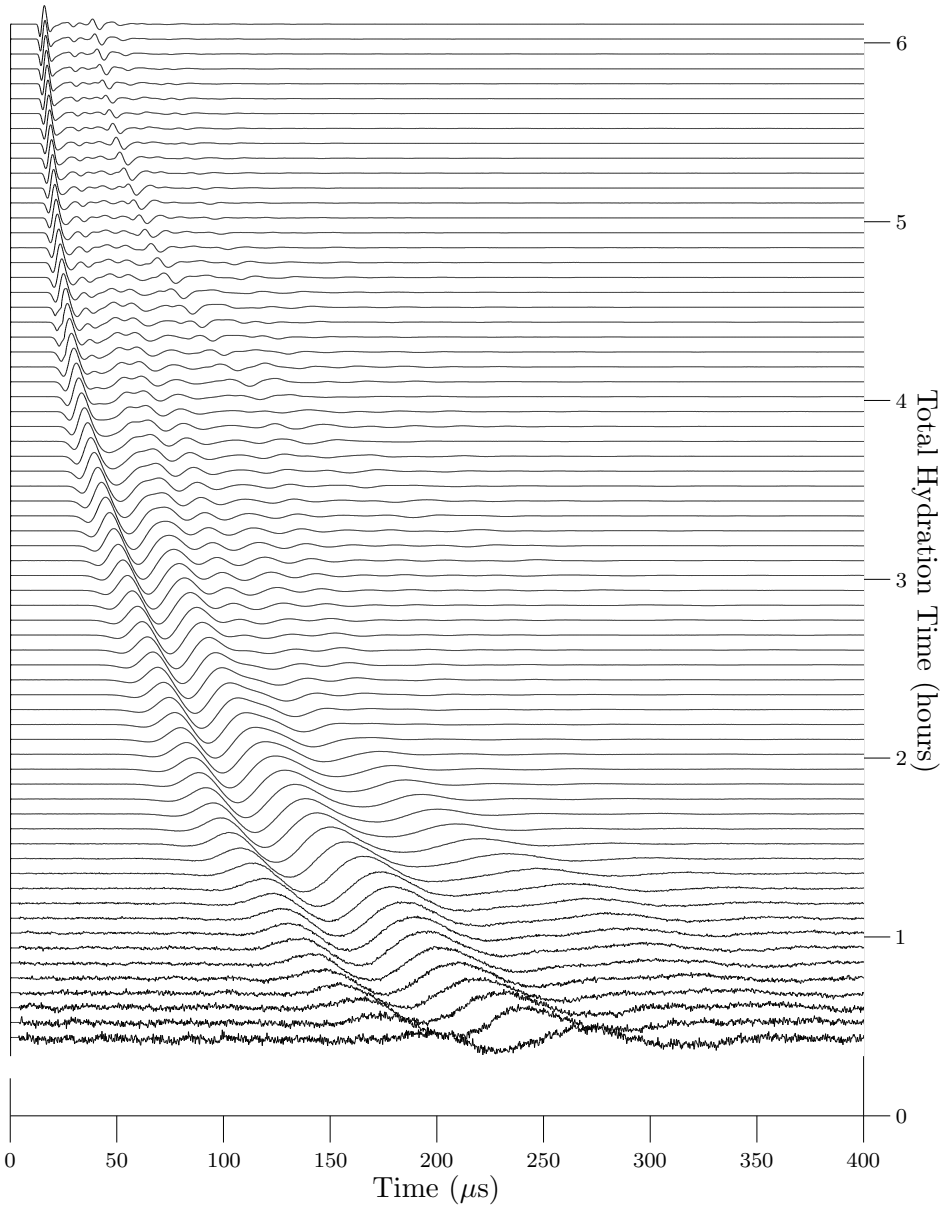

Figure A.29: Specimen 15 (0.6% AEA by weight of cement) normalized signals during the first 6 hours of hydration

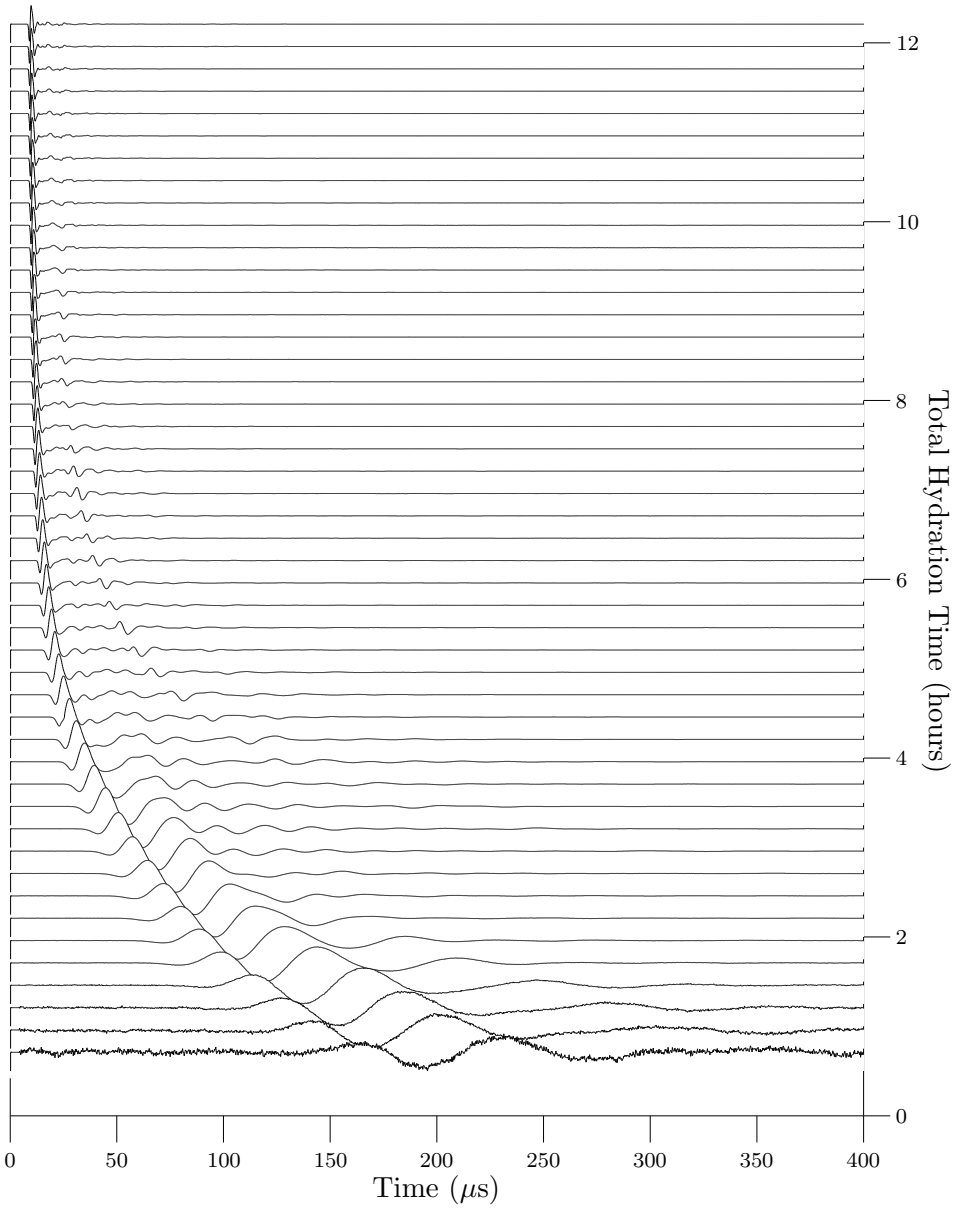

Figure A.30: Specimen 15 (0.6% AEA by weight of cement) normalized signals during the first 12 hours of hydration

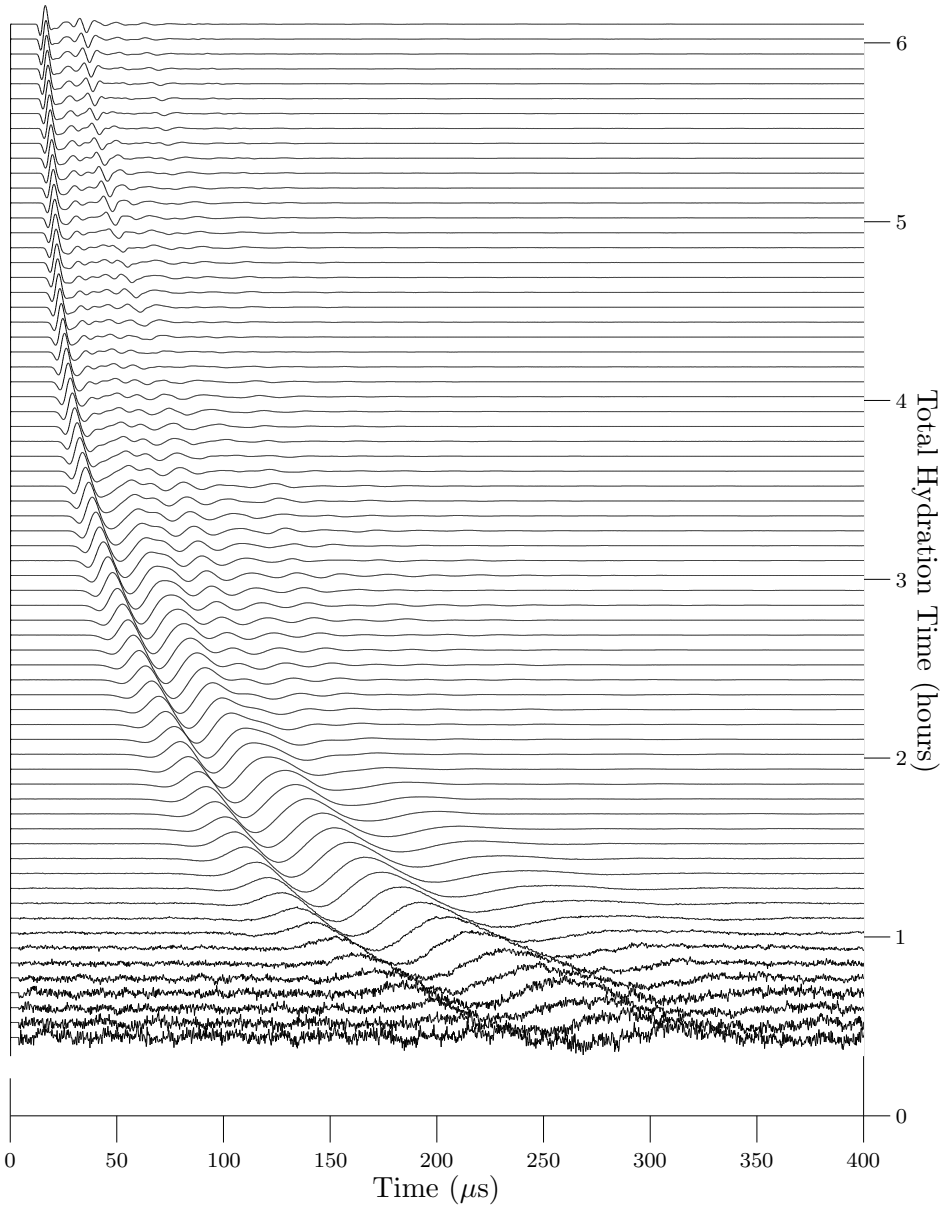

Figure A.31: Specimen 16 (0.6% AEA by weight of cement) normalized signals during the first 6 hours of hydration

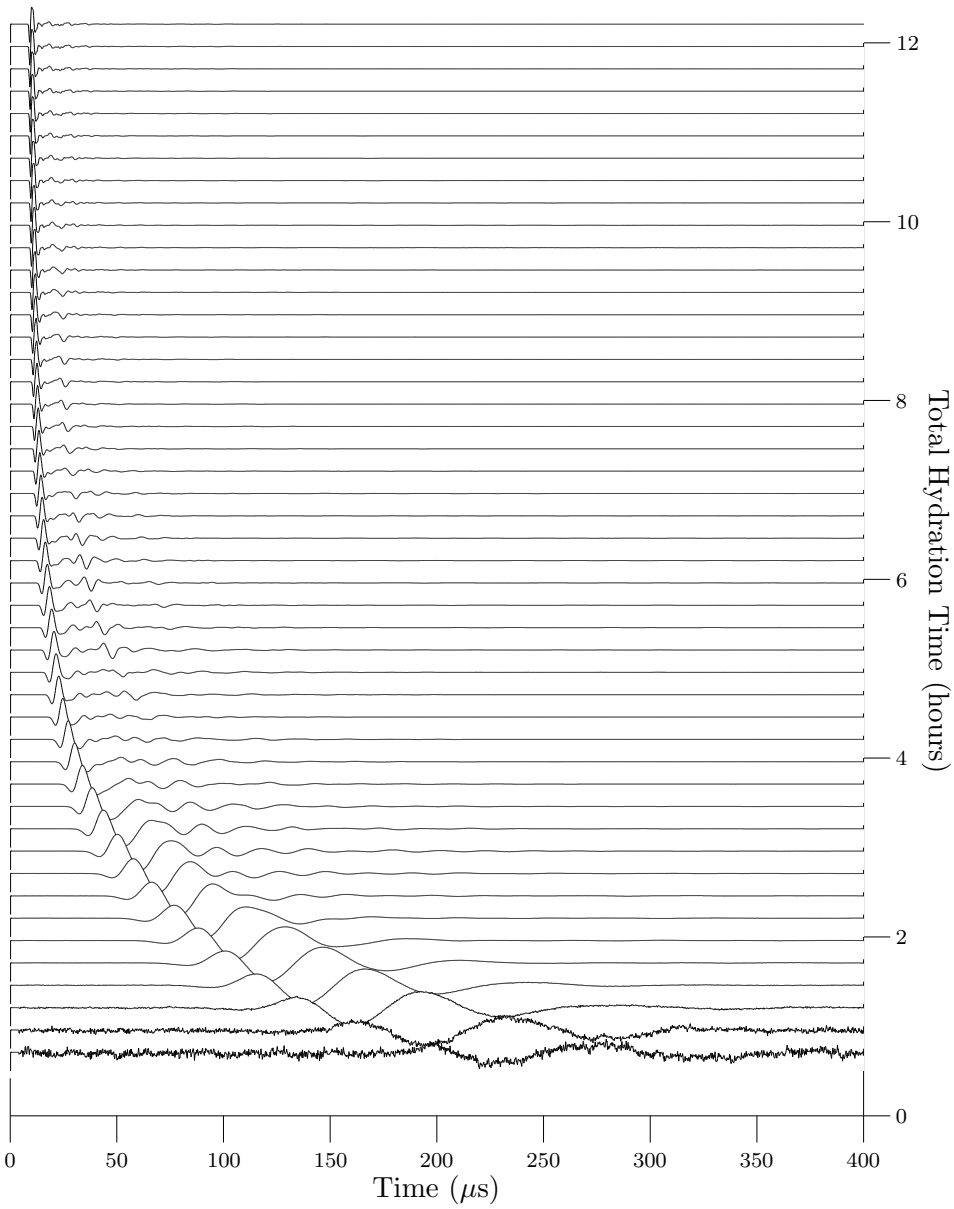

Figure A.32: Specimen 16 (0.6% AEA by weight of cement) normalized signals during the first 12 hours of hydration

APPENDIX B

Frequency Spectra

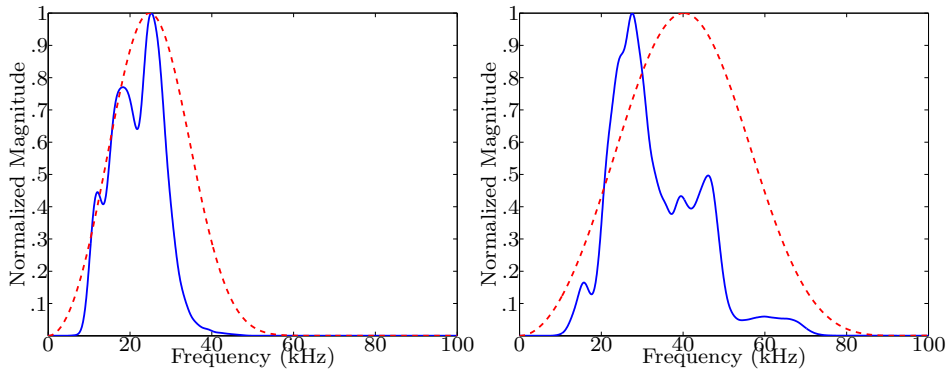

(a) 60 Minutes

(b) 120 Minutes

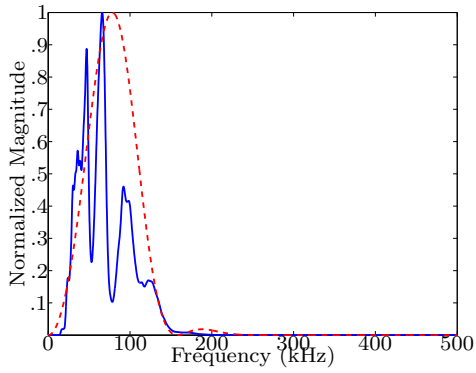

(c) 180 Minutes

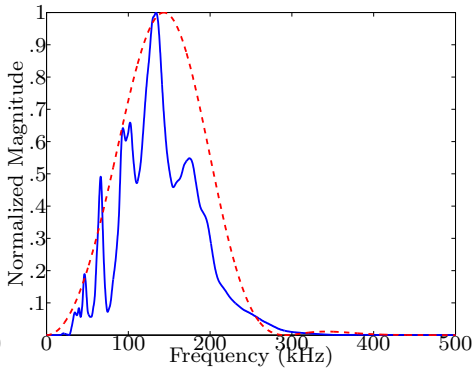

(d) 240 Minutes

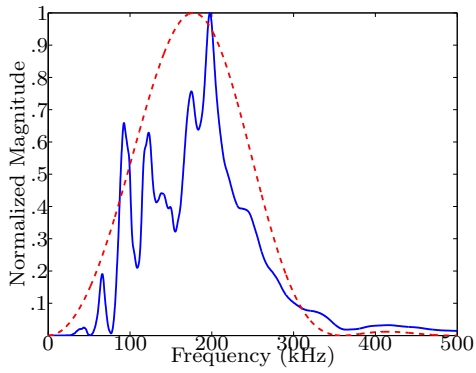

(e) 300 Minutes

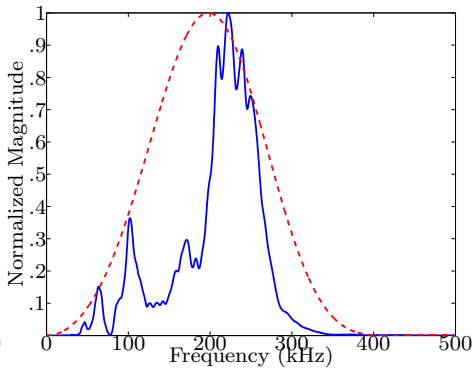

(f) 360 Minutes

Figure B.1: SP01 (0.0% AEA, 12.0 mm) frequency spectra: rectagular window about entire waveform (solid); Hanning window about initial pulse received (dashed)

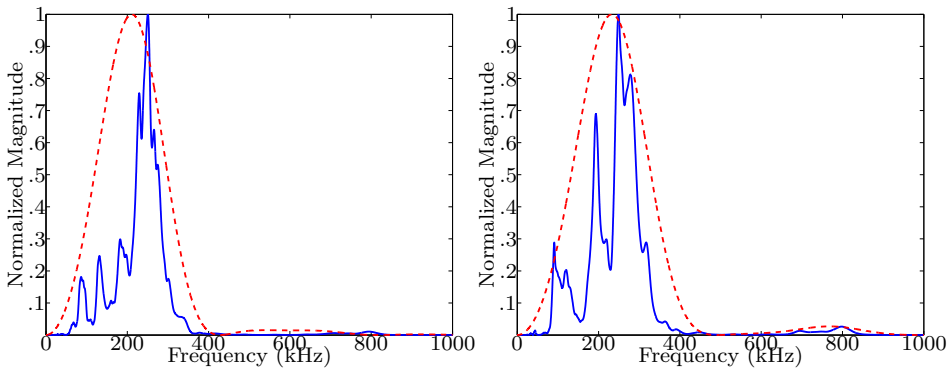

(a) 420 Minutes

(b) 480 Minutes

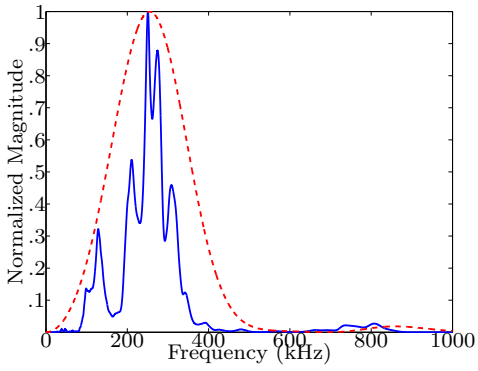

(c) 540 Minutes

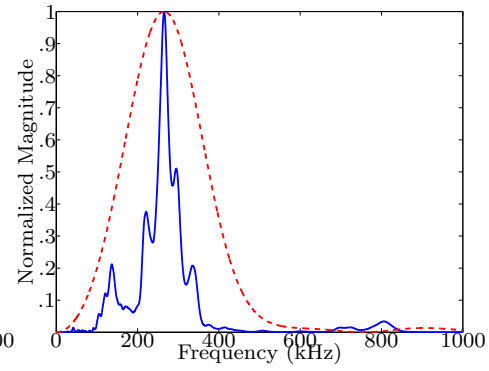

(d) 600 Minutes

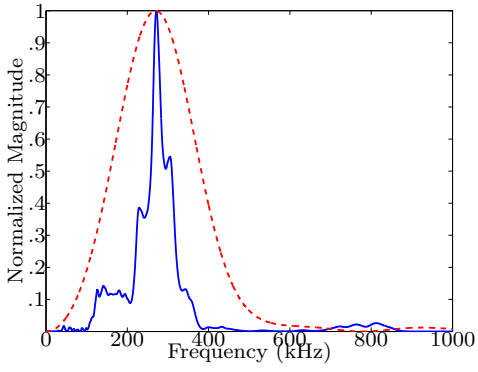

(e) 660 Minutes

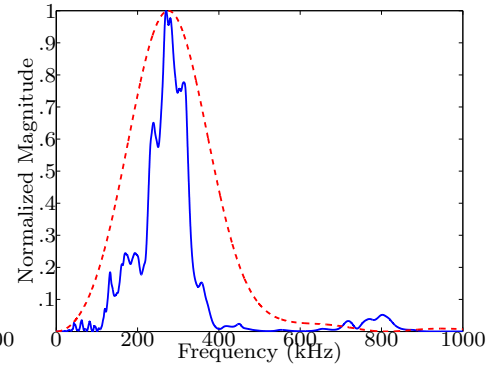

(f) 720 Minutes

Figure B.2: SP01 (0.0% AEA, 12.0 mm) frequency spectra: rectagular window about entire waveform (solid); Hanning window about initial pulse received (dashed)

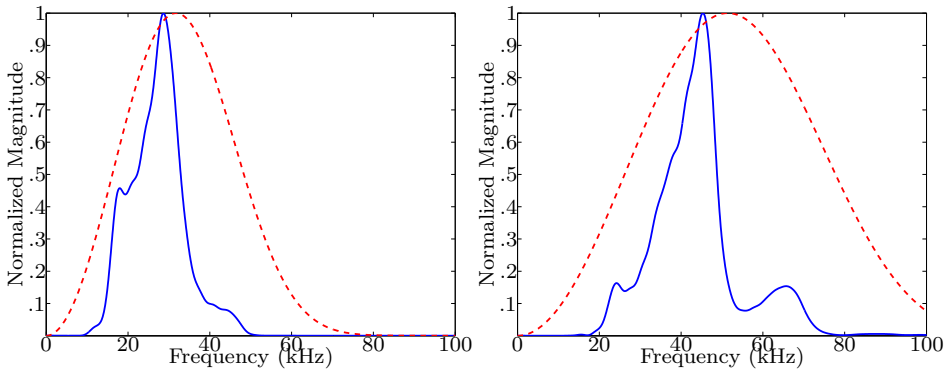

(a) 60 Minutes

(b) 120 Minutes

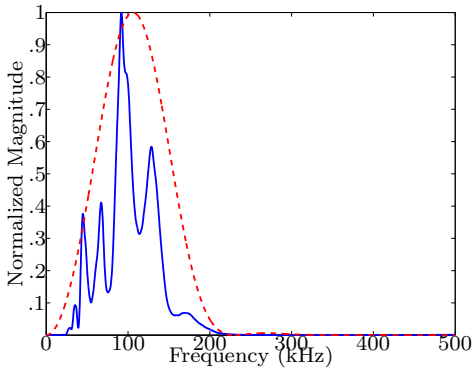

(c) 180 Minutes

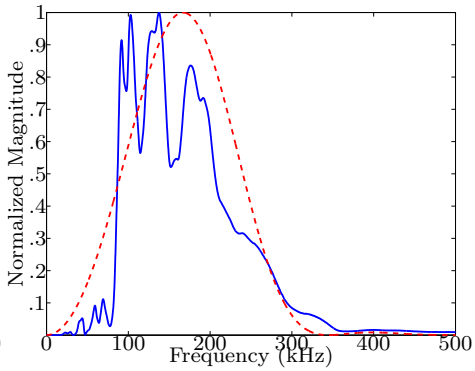

(d) 240 Minutes

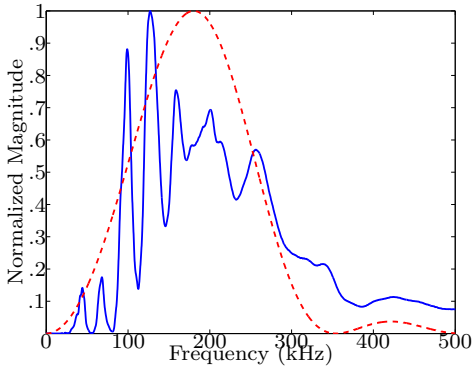

(e) 300 Minutes

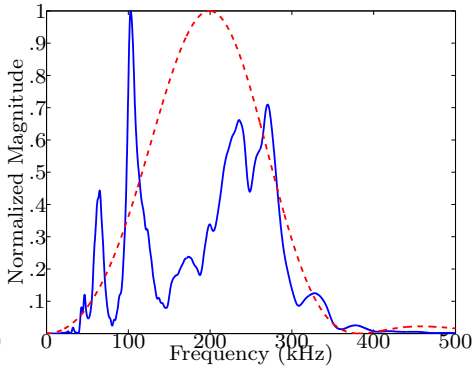

(f) 360 Minutes

Figure B.3: SP02 (0.0% AEA, 12.0 mm) frequency spectra: rectagular window about entire waveform (solid); Hanning window about initial pulse received (dashed)

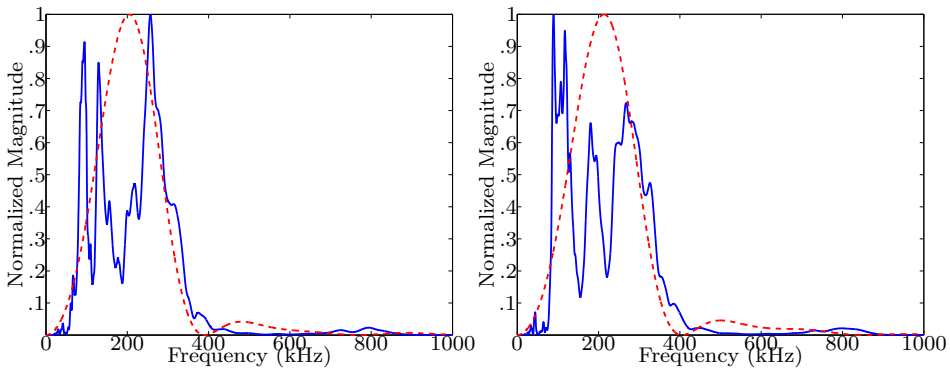

(a) 420 Minutes

(b) 480 Minutes

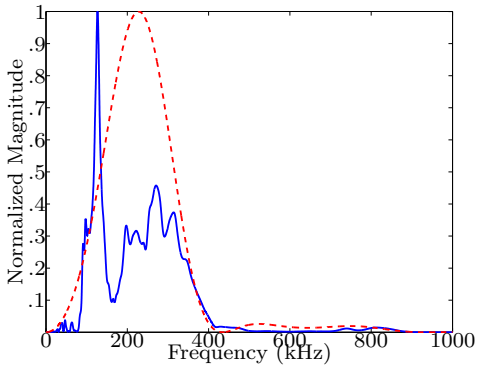

(c) 540 Minutes

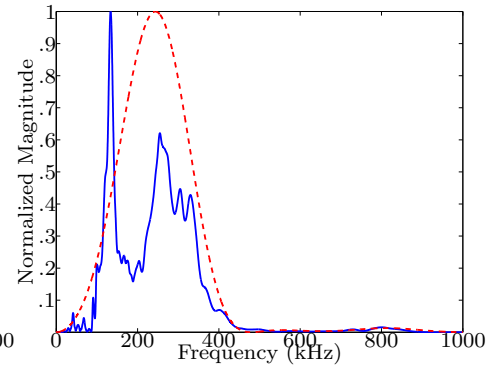

(d) 600 Minutes

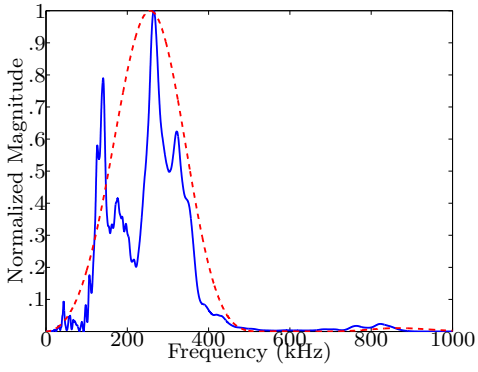

(e) 660 Minutes

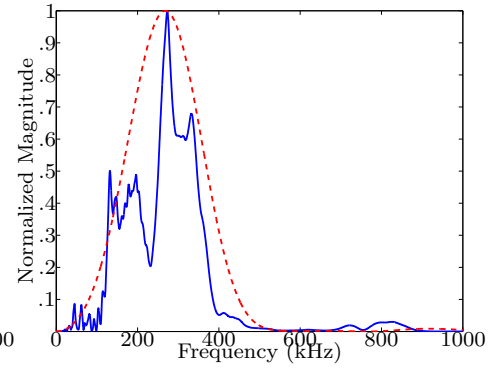

(f) 720 Minutes

Figure B.4: SP02 (0.0% AEA, 12.0 mm) frequency spectra: rectagular window about entire waveform (solid); Hanning window about initial pulse received (dashed)

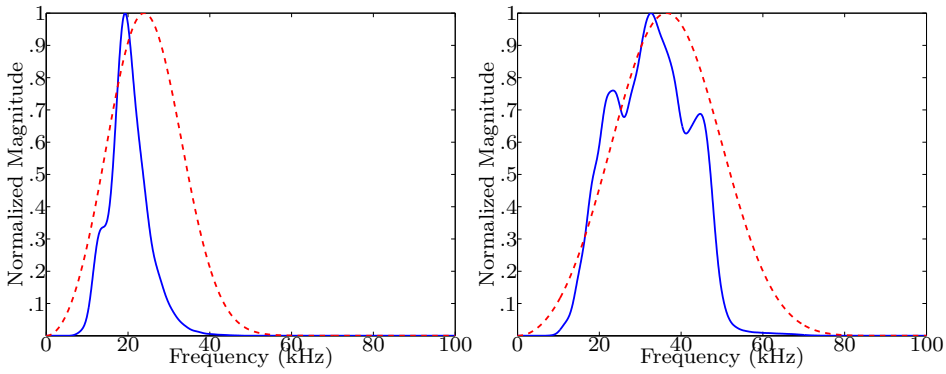

(a) 60 Minutes

(b) 120 Minutes

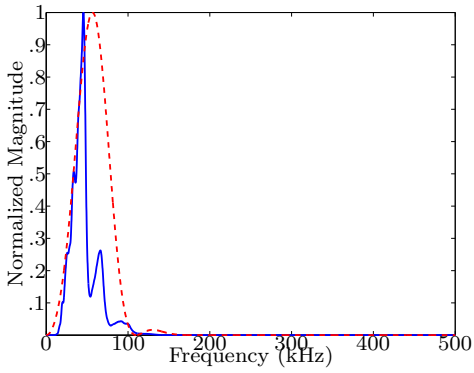

(c) 180 Minutes

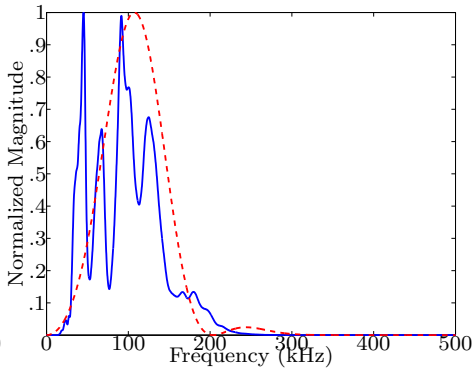

(d) 240 Minutes

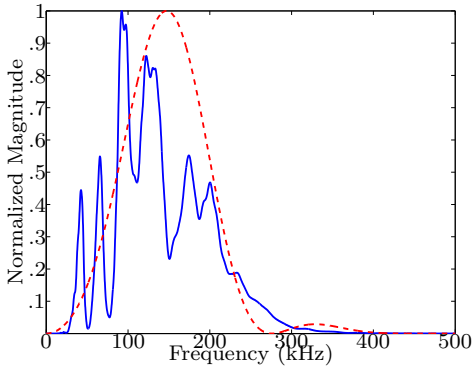

(e) 300 Minutes

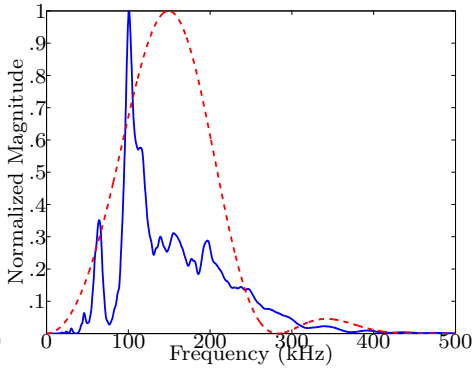

(f) 360 Minutes

Figure B.5: SP03 (0.2% AEA, 12.0 mm) frequency spectra: rectagular window about entire waveform (solid); Hanning window about initial pulse received (dashed)

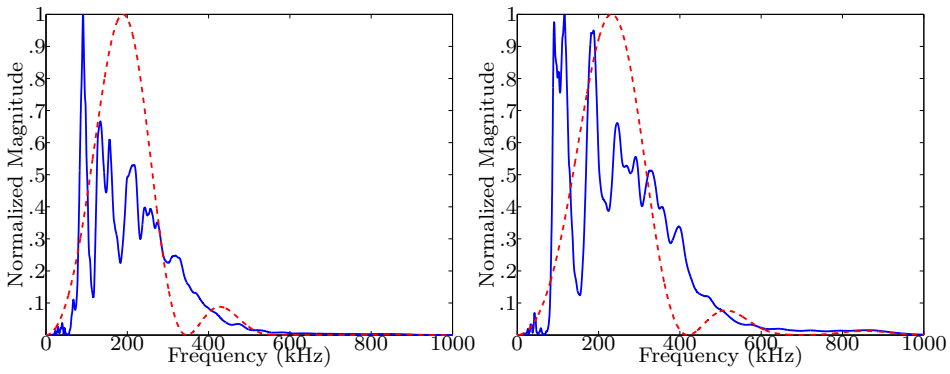

(a) 420 Minutes

(b) 480 Minutes

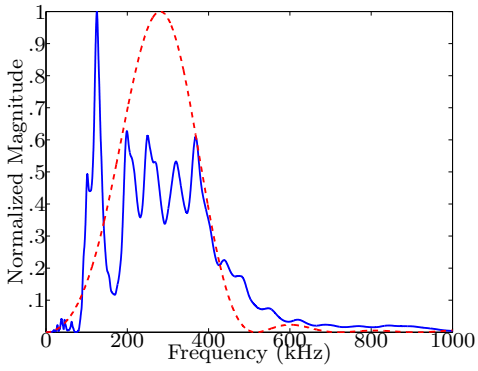

(c) 540 Minutes

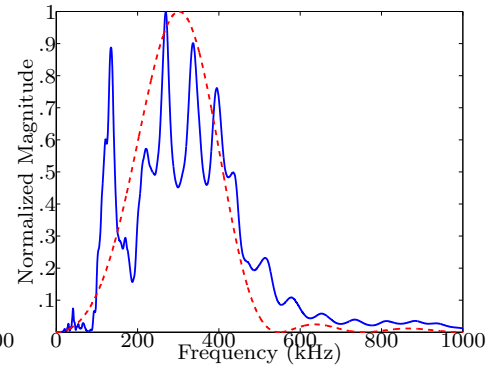

(d) 600 Minutes

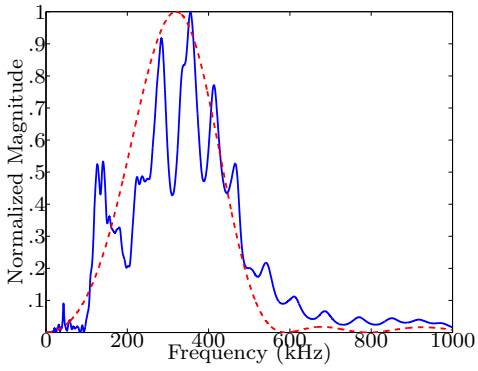

(e) 660 Minutes

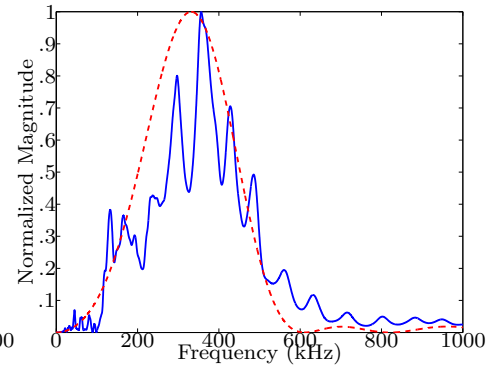

(f) 720 Minutes

Figure B.6: SP03 (0.2% AEA, 12.0 mm) frequency spectra: rectagular window about entire waveform (solid); Hanning window about initial pulse received (dashed)

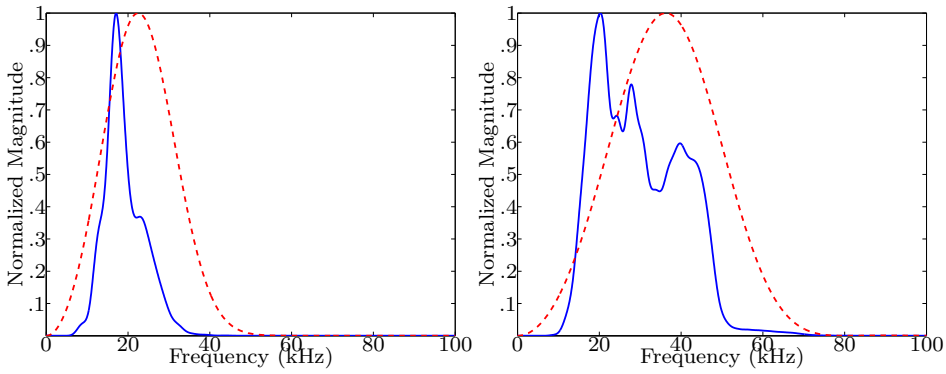

(a) 60 Minutes

(b) 120 Minutes

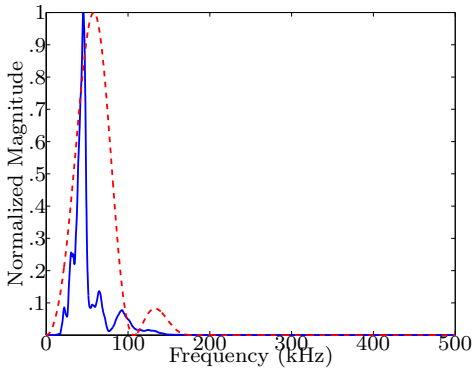

(c) 180 Minutes

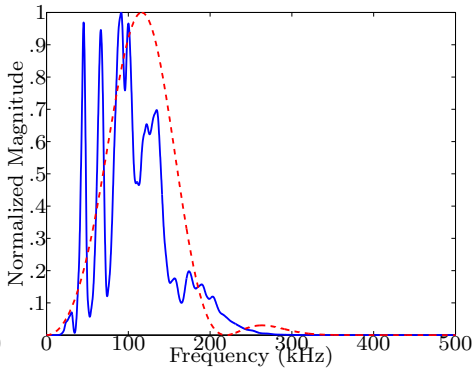

(d) 240 Minutes

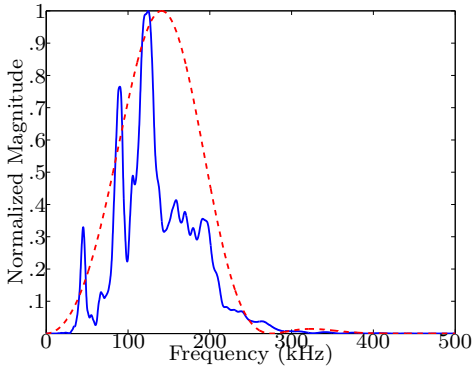

(e) 300 Minutes

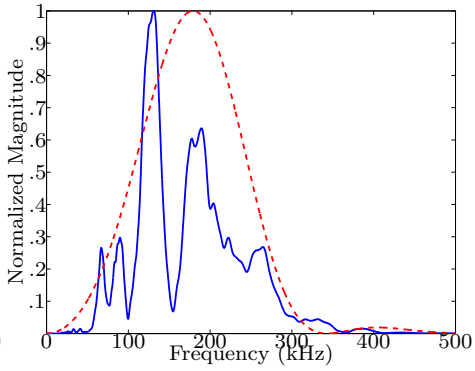

(f) 360 Minutes

Figure B.7: SP04 (0.2% AEA, 12.0 mm) frequency spectra: rectagular window about entire waveform (solid); Hanning window about initial pulse received (dashed)

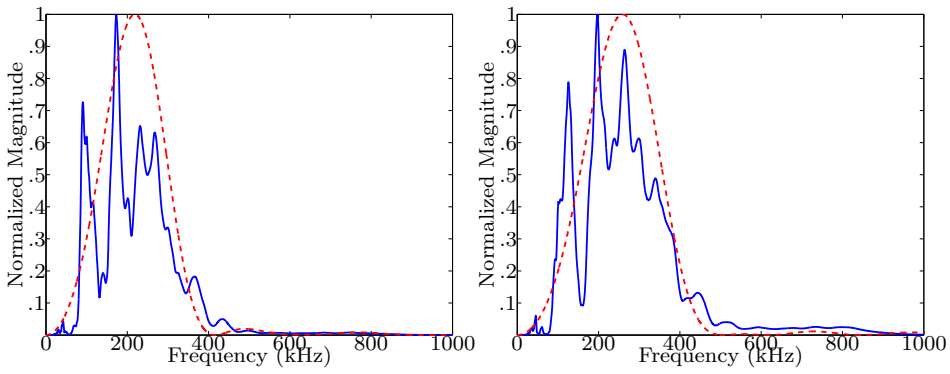

(a) 420 Minutes

(b) 480 Minutes

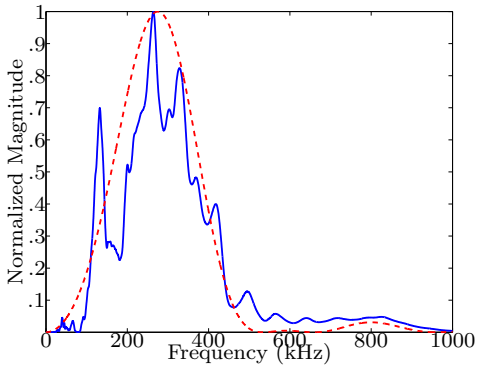

(c) 540 Minutes

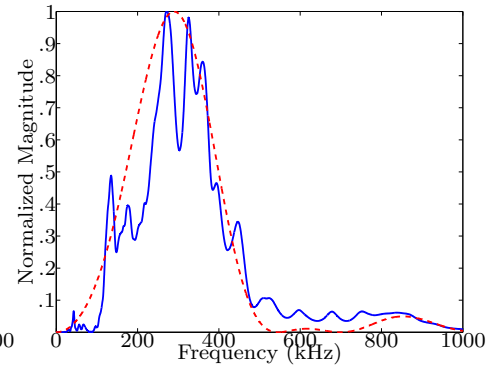

(d) 600 Minutes

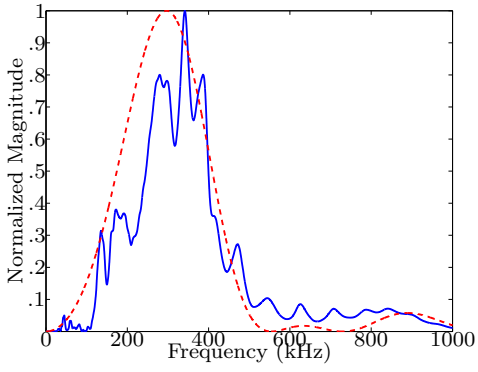

(e) 660 Minutes

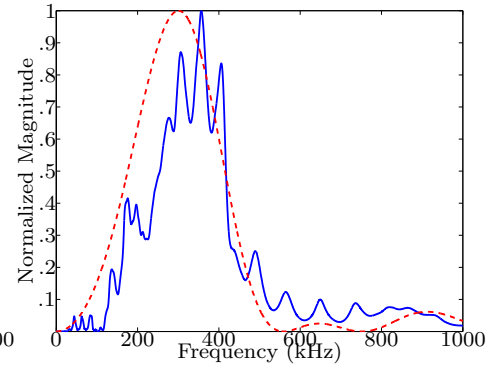

(f) 720 Minutes

Figure B.8: SP04 (0.2% AEA, 12.0 mm) frequency spectra: rectagular window about entire waveform (solid); Hanning window about initial pulse received (dashed)

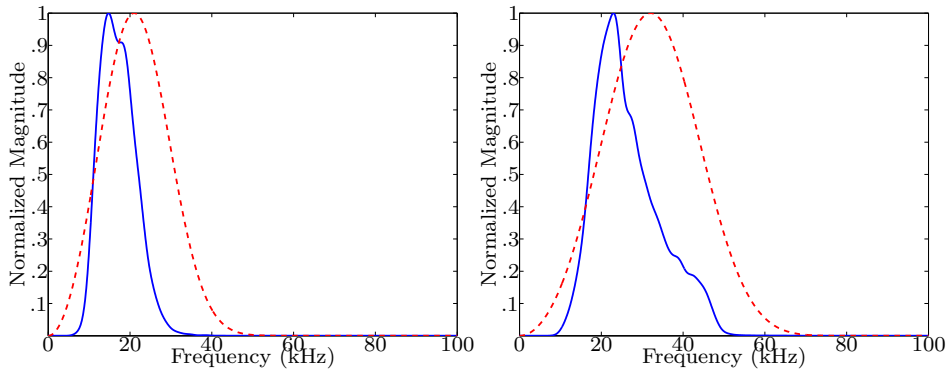

(a) 60 Minutes

(b) 120 Minutes

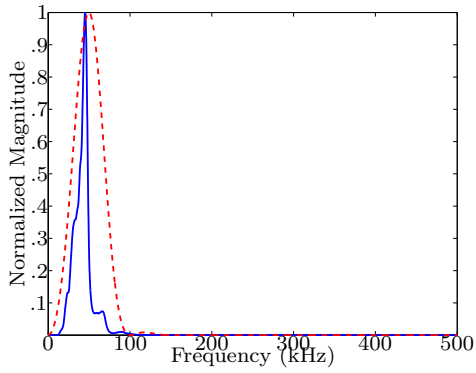

(c) 180 Minutes

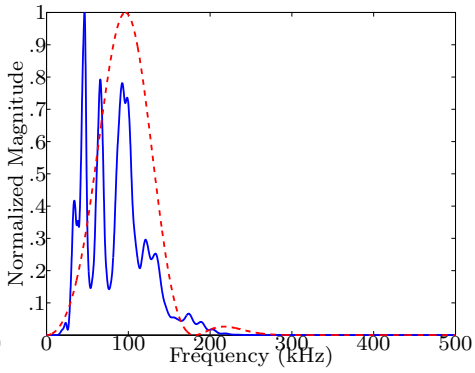

(d) 240 Minutes

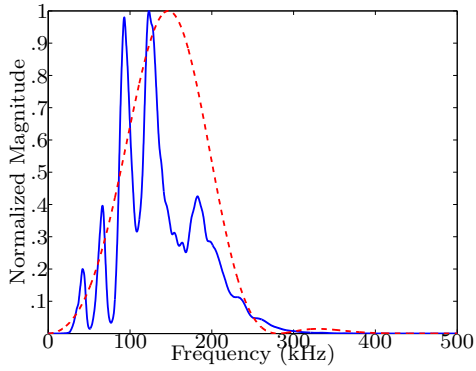

(e) 300 Minutes

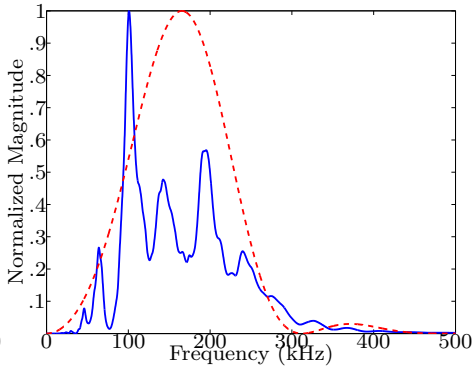

(f) 360 Minutes

Figure B.9: SP05 (0.4% AEA, 12.0 mm) frequency spectra: rectagular window about entire waveform (solid); Hanning window about initial pulse received (dashed)

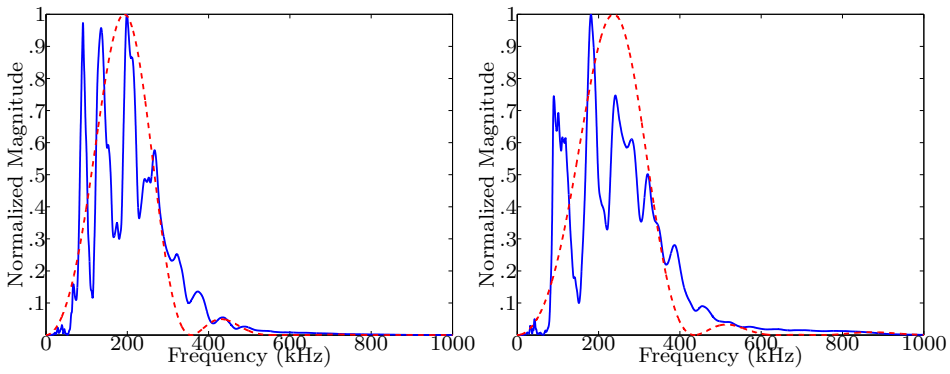

(a) 420 Minutes

(b) 480 Minutes

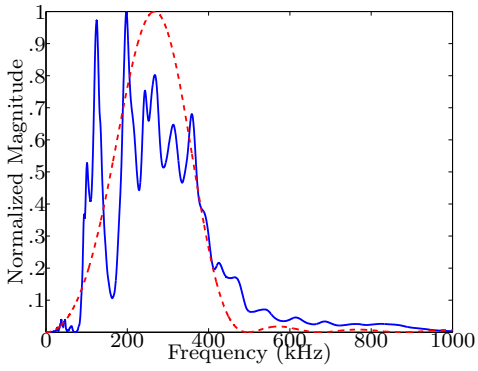

(c) 540 Minutes

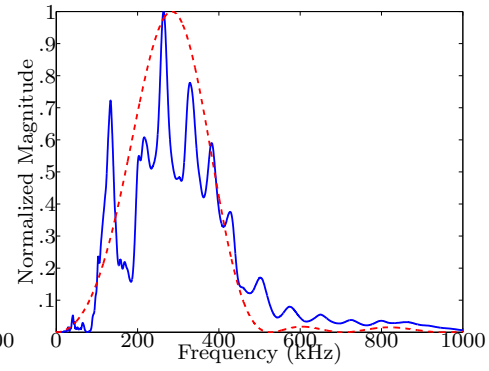

(d) 600 Minutes

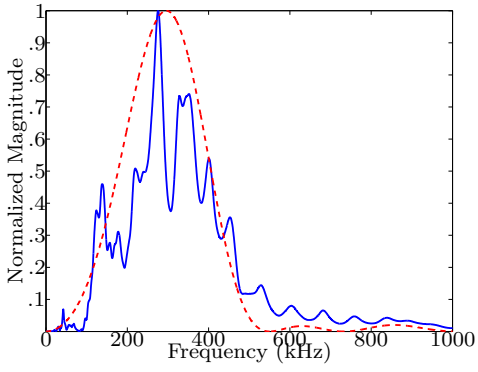

(e) 660 Minutes

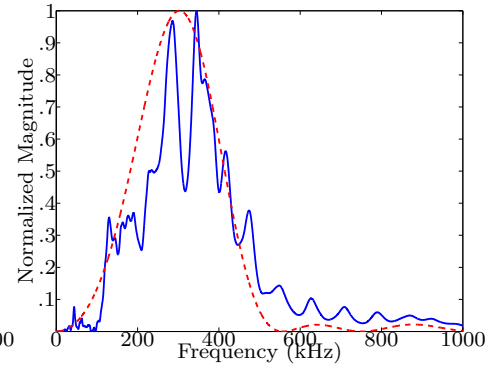

(f) 720 Minutes

Figure B.10: SP05 (0.4% AEA, 12.0 mm) frequency spectra: rectagular window about entire waveform (solid); Hanning window about initial pulse received (dashed)

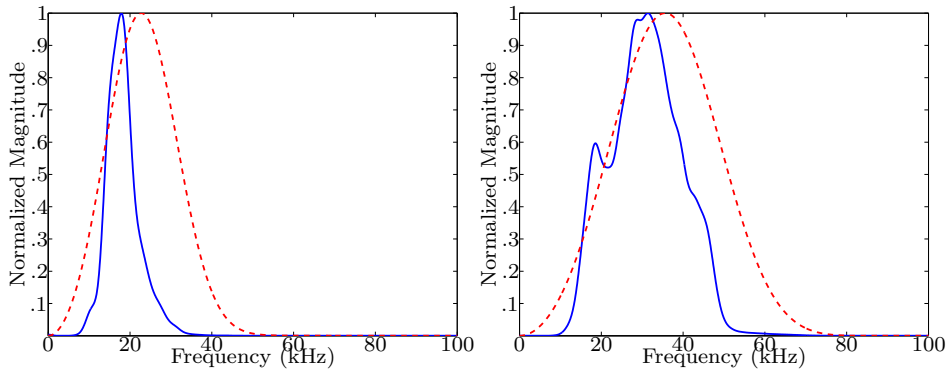

(a) 60 Minutes

(b) 120 Minutes

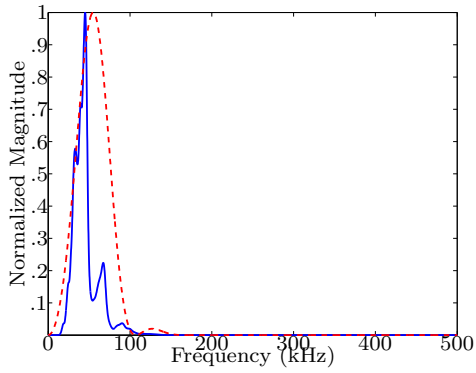

(c) 180 Minutes

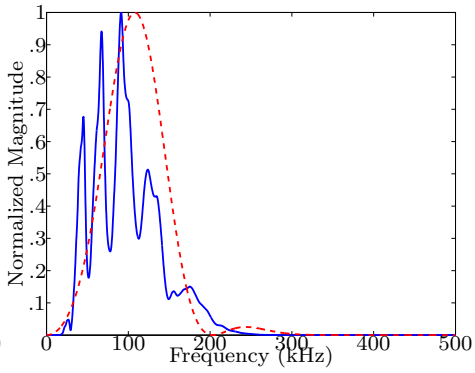

(d) 240 Minutes

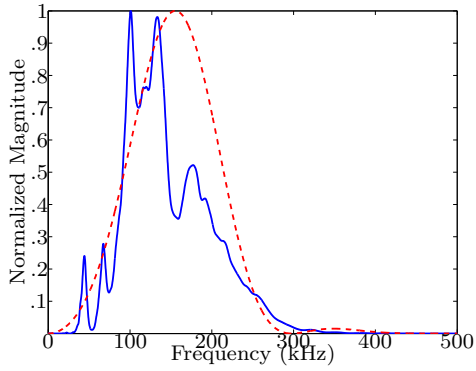

(e) 300 Minutes

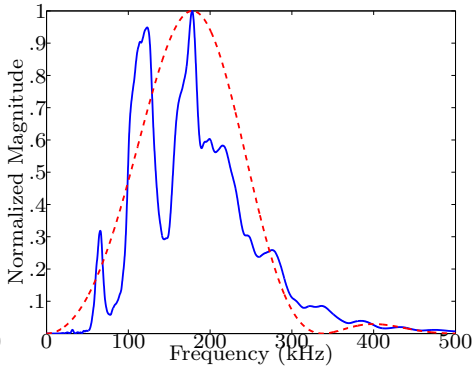

(f) 360 Minutes

Figure B.11: SP06 (0.4% AEA, 12.0 mm) frequency spectra: rectagular window about entire waveform (solid); Hanning window about initial pulse received (dashed)

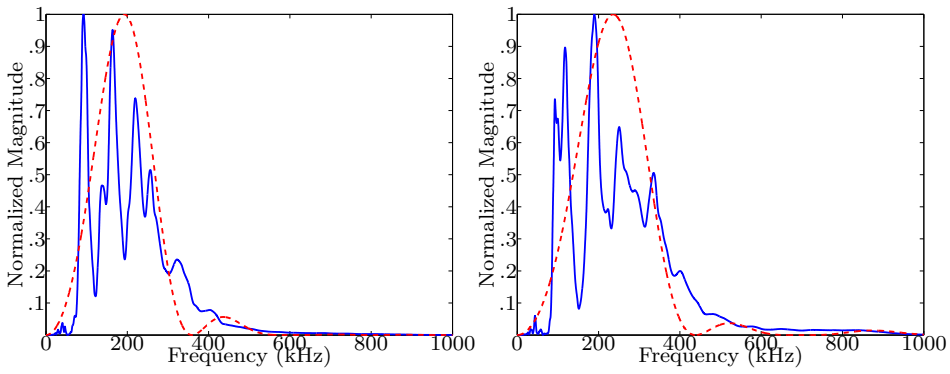

(a) 420 Minutes

(b) 480 Minutes

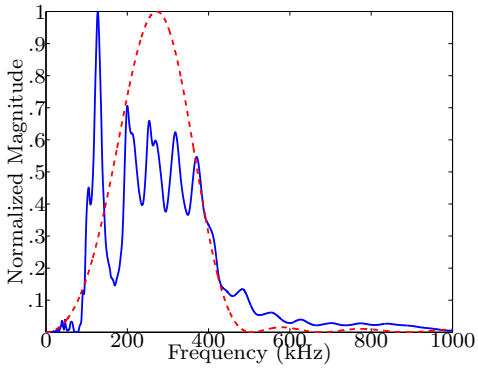

(c) 540 Minutes

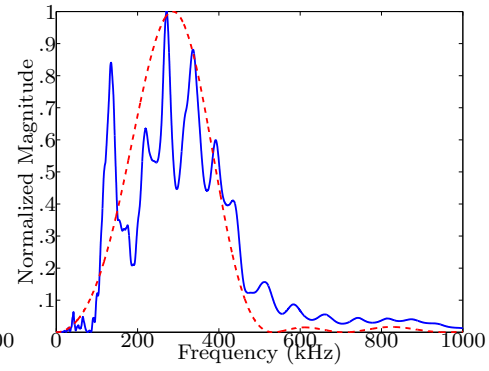

(d) 600 Minutes

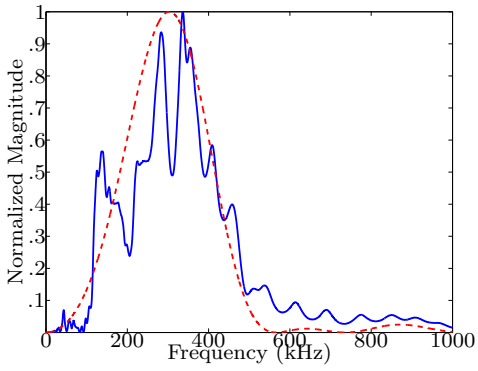

(e) 660 Minutes

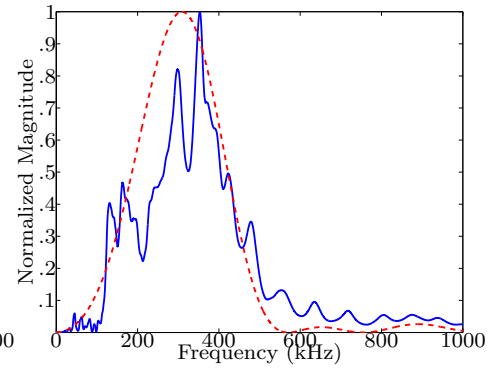

(f) 720 Minutes

Figure B.12: SP06 (0.4% AEA, 12.0 mm) frequency spectra: rectagular window about entire waveform (solid); Hanning window about initial pulse received (dashed)

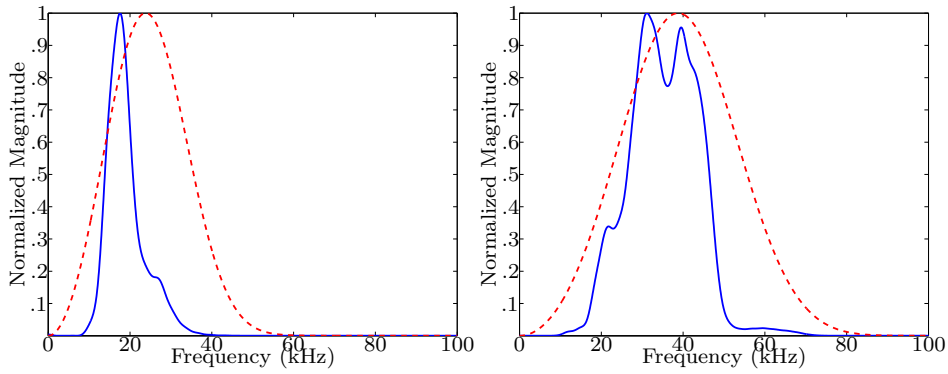

(a) 60 Minutes

(b) 120 Minutes

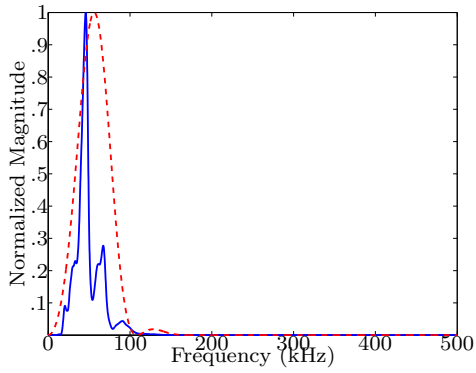

(c) 180 Minutes

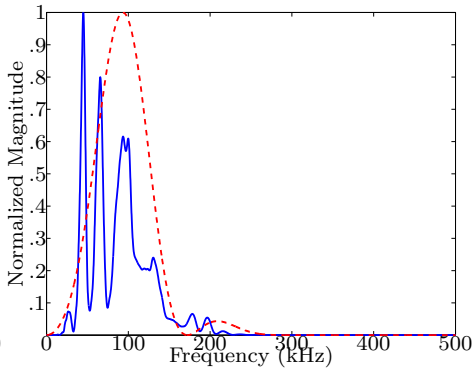

(d) 240 Minutes

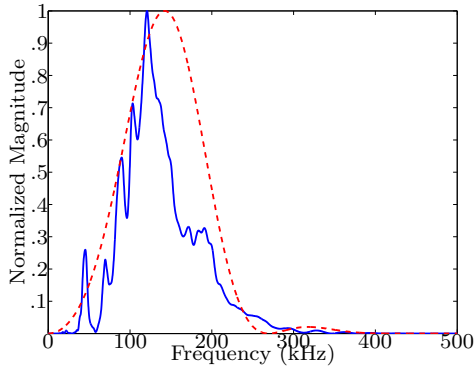

(e) 300 Minutes

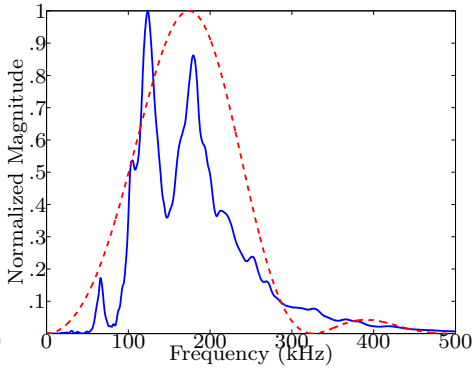

(f) 360 Minutes

Figure B.13: SP07 (0.6% AEA, 12.0 mm) frequency spectra: rectagular window about entire waveform (solid); Hanning window about initial pulse received (dashed)

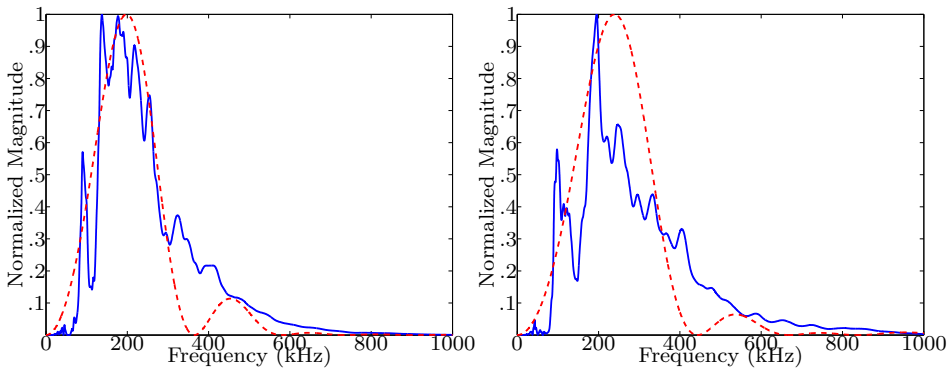

(a) 420 Minutes

(b) 480 Minutes

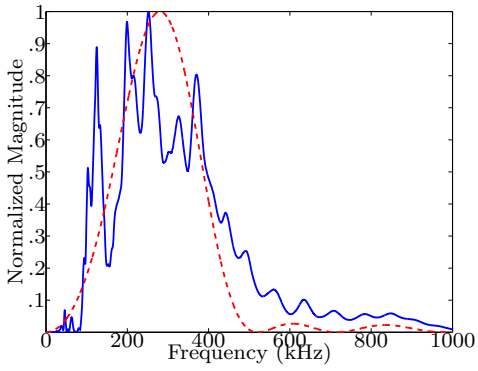

(c) 540 Minutes

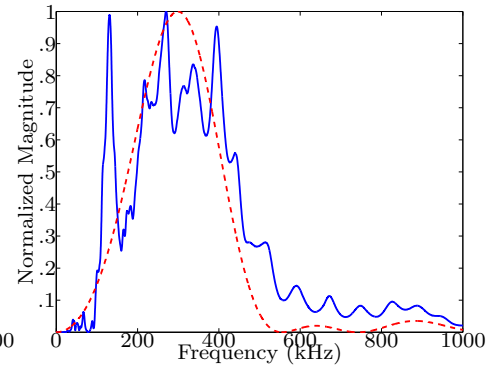

(d) 600 Minutes

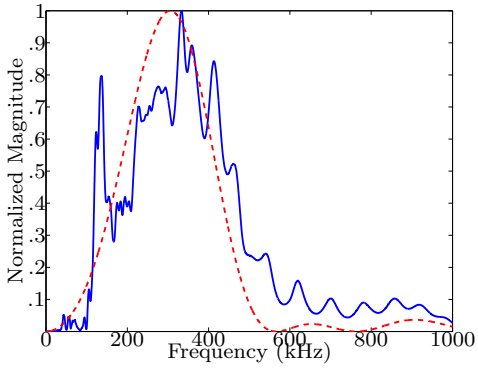

(e) 660 Minutes

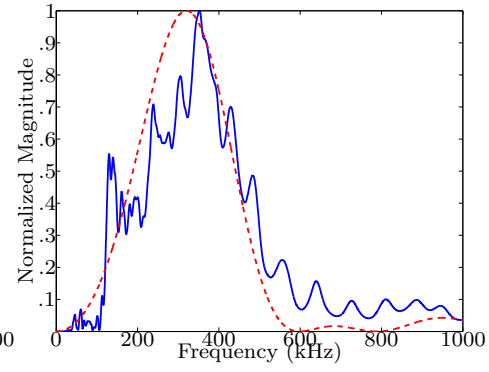

(f) 720 Minutes

Figure B.14: SP07 (0.6% AEA, 12.0 mm) frequency spectra: rectagular window about entire waveform (solid); Hanning window about initial pulse received (dashed)

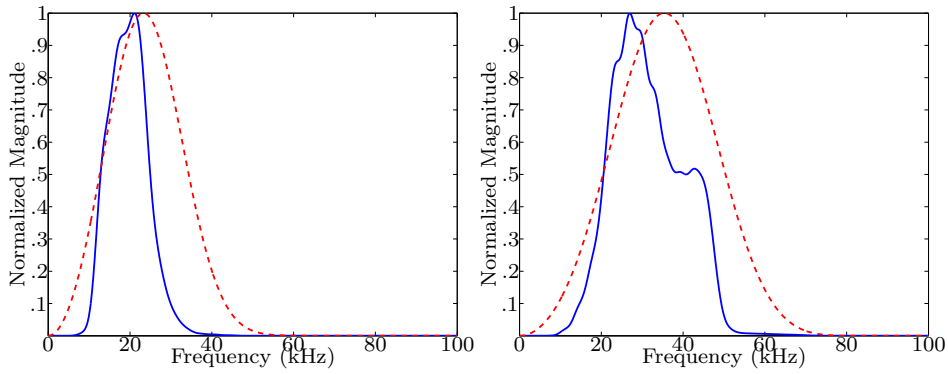

(a) 60 Minutes

(b) 120 Minutes

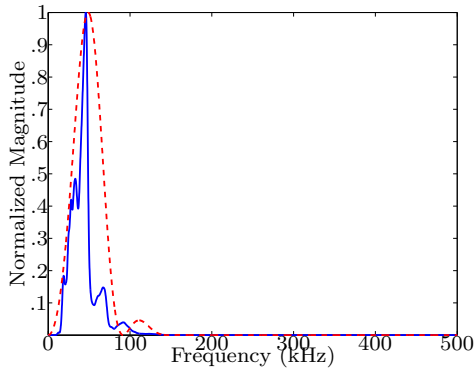

(c) 180 Minutes

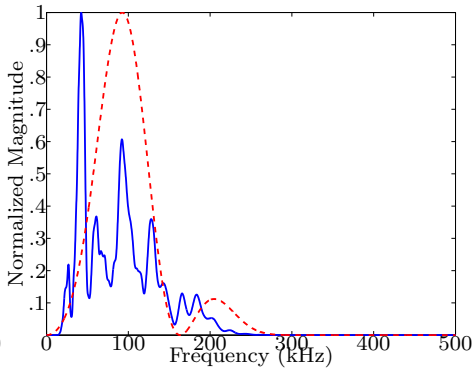

(d) 240 Minutes

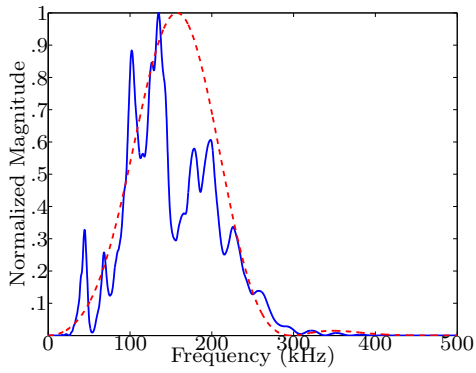

(e) 300 Minutes

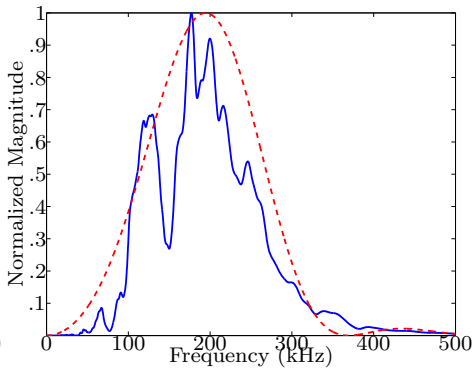

(f) 360 Minutes

Figure B.15: SP08 (0.6% AEA, 12.0 mm) frequency spectra: rectagular window about entire waveform (solid); Hanning window about initial pulse received (dashed)

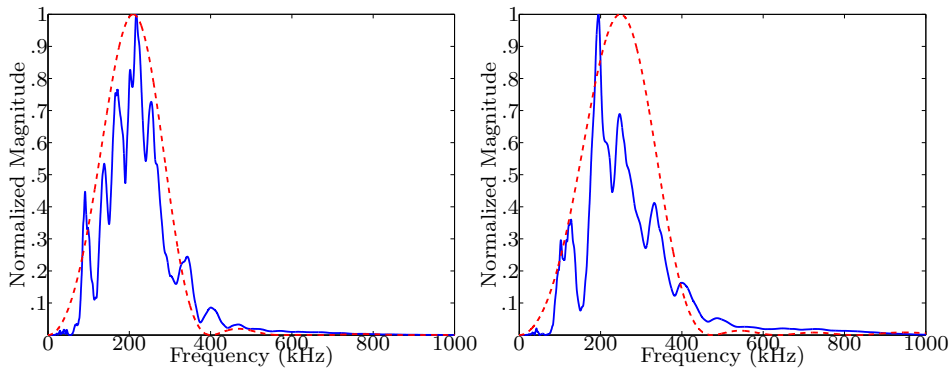

(a) 420 Minutes

(b) 480 Minutes

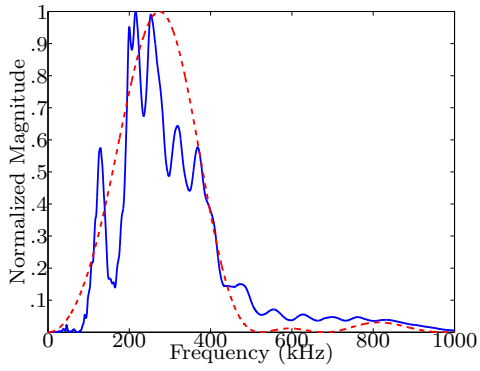

(c) 540 Minutes

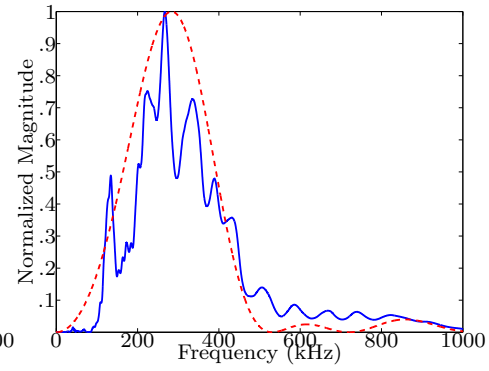

(d) 600 Minutes

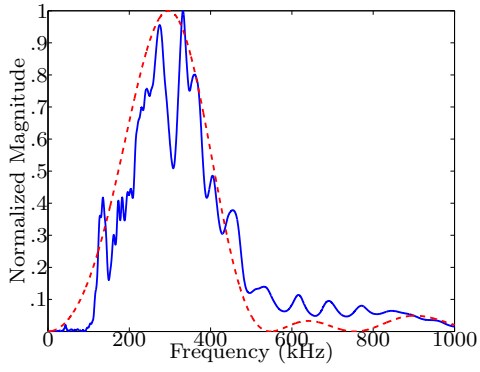

(e) 660 Minutes

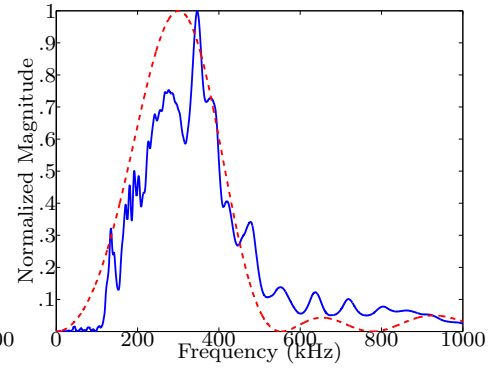

(f) 720 Minutes

Figure B.16: SP08 (0.6% AEA, 12.0 mm) frequency spectra: rectagular window about entire waveform (solid); Hanning window about initial pulse received (dashed)

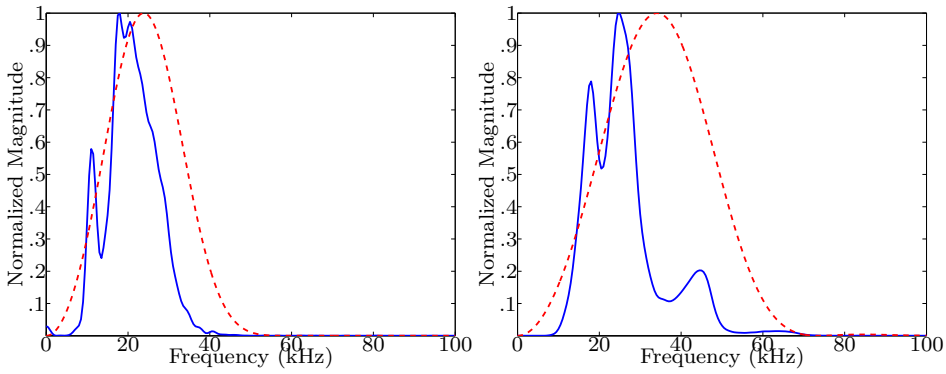

(a) 60 Minutes

(b) 120 Minutes

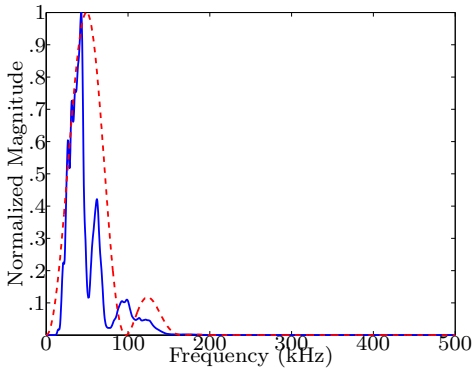

(c) 180 Minutes

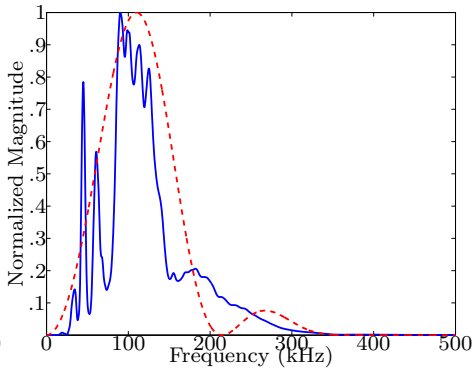

(d) 240 Minutes

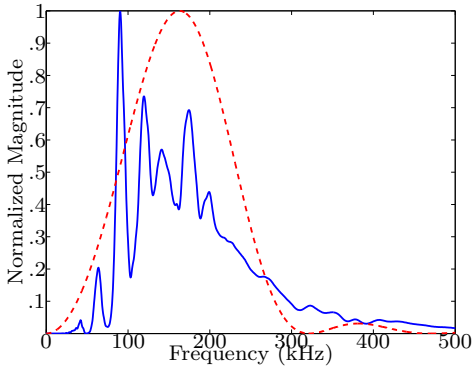

(e) 300 Minutes

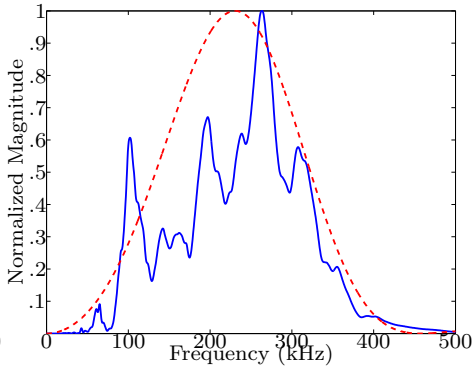

(f) 360 Minutes

Figure B.17: SP09 (0.0% AEA, 16.0 mm) frequency spectra: rectagular window about entire waveform (solid); Hanning window about initial pulse received (dashed)

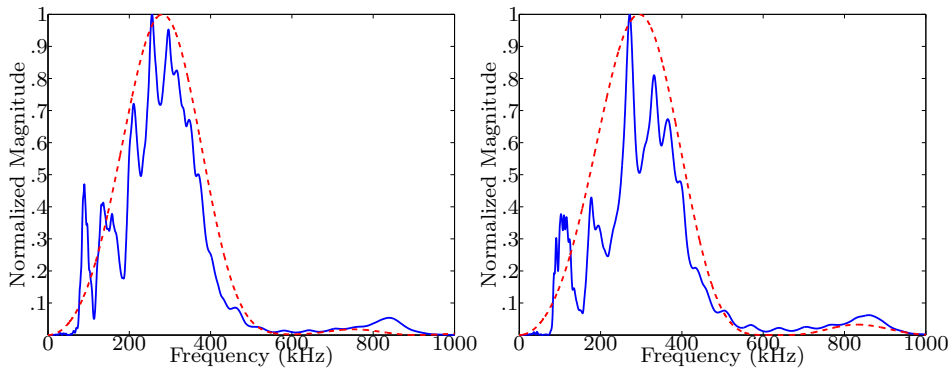

(a) 420 Minutes

(b) 480 Minutes

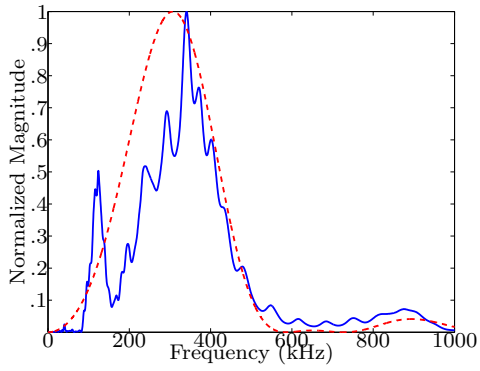

(c) 540 Minutes

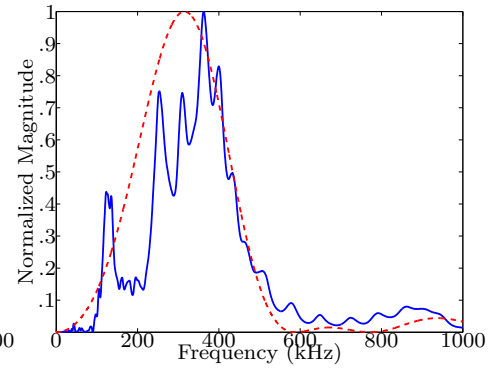

(d) 600 Minutes

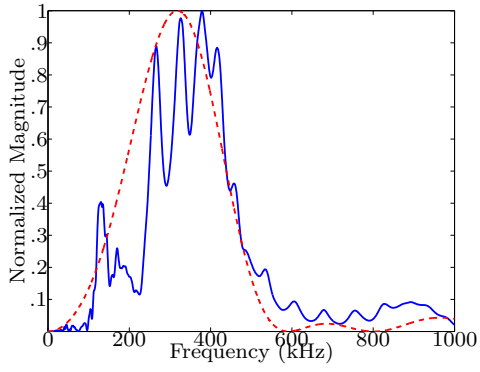

(e) 660 Minutes

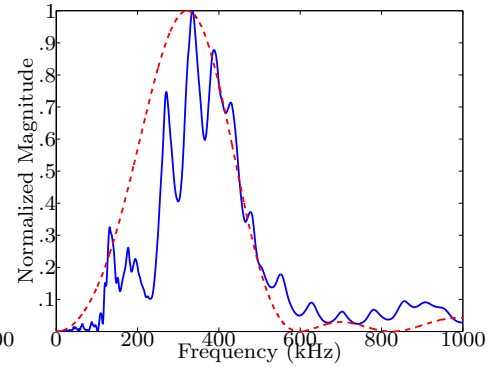

(f) 720 Minutes

Figure B.18: SP09 (0.0% AEA, 16.0 mm) frequency spectra: rectagular window about entire waveform (solid); Hanning window about initial pulse received (dashed)

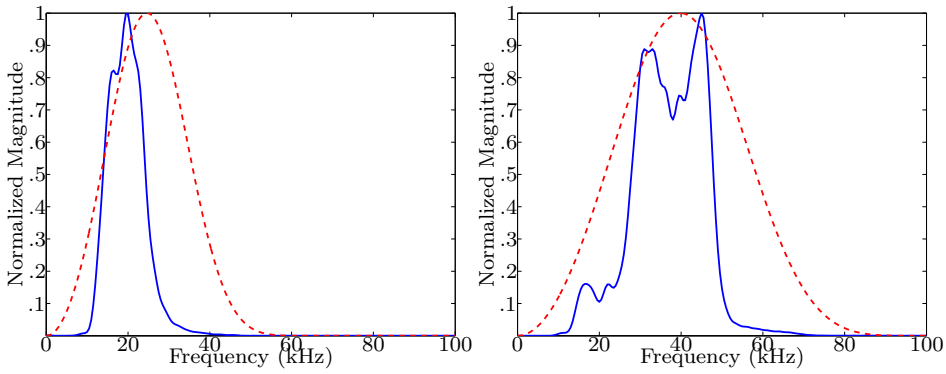

(a) 60 Minutes

(b) 120 Minutes

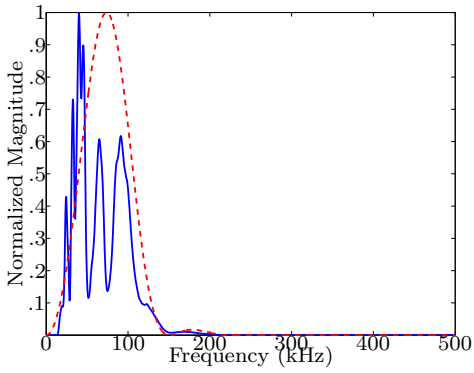

(c) 180 Minutes

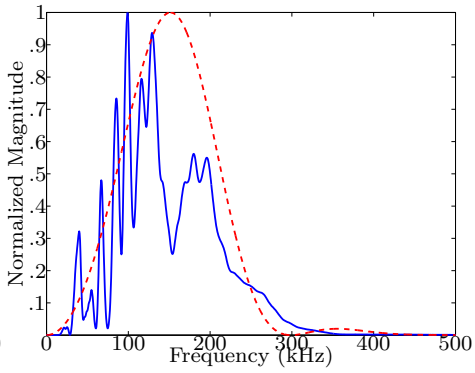

(d) 240 Minutes

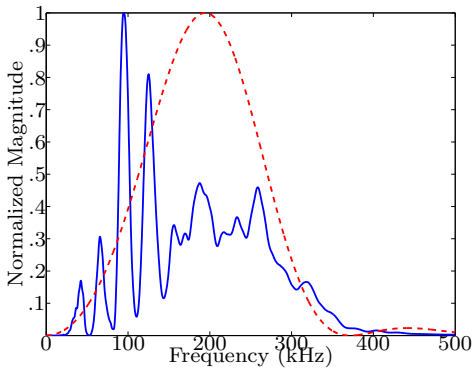

(e) 300 Minutes

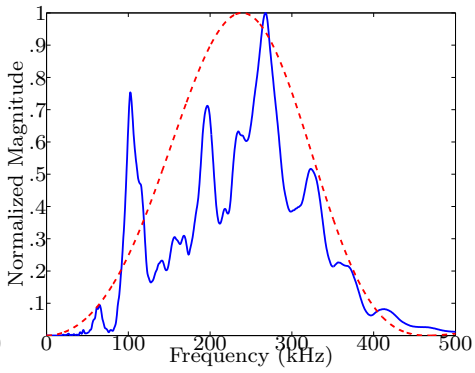

(f) 360 Minutes

Figure B.19: SP10 (0.0% AEA, 16.0 mm) frequency spectra: rectagular window about entire waveform (solid); Hanning window about initial pulse received (dashed)

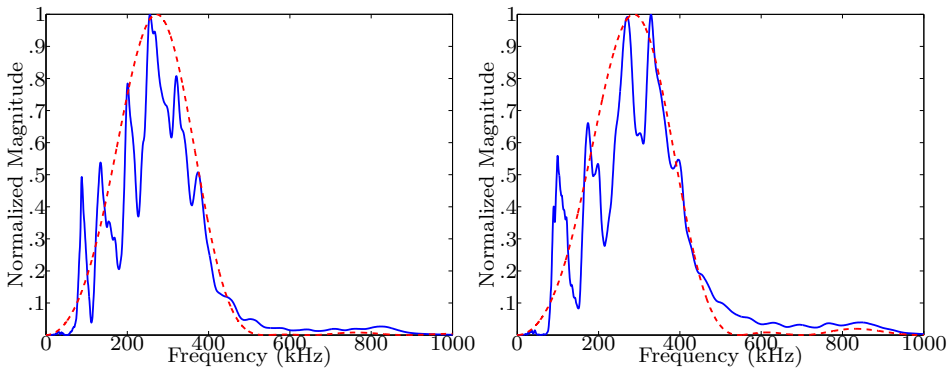

(a) 420 Minutes

(b) 480 Minutes

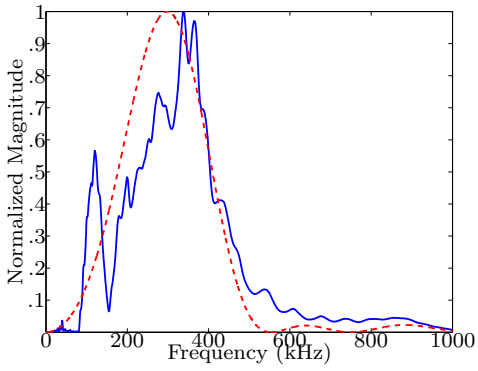

(c) 540 Minutes

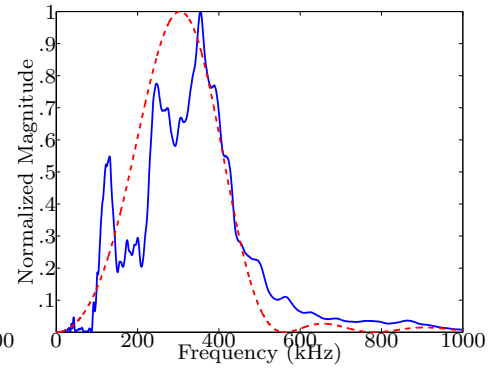

(d) 600 Minutes

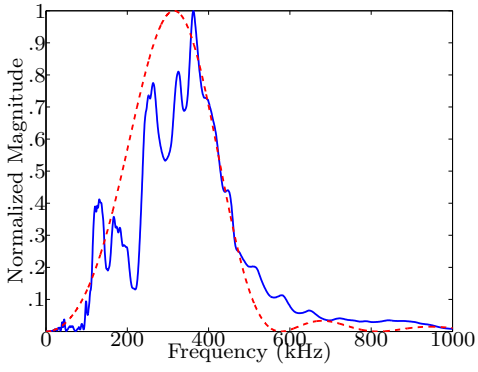

(e) 660 Minutes

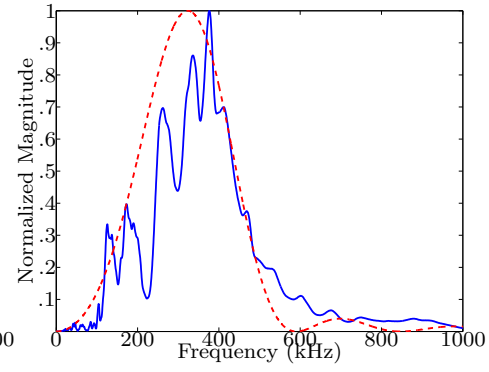

(f) 720 Minutes

Figure B.20: SP10 (0.0% AEA, 16.0 mm) frequency spectra: rectagular window about entire waveform (solid); Hanning window about initial pulse received (dashed)

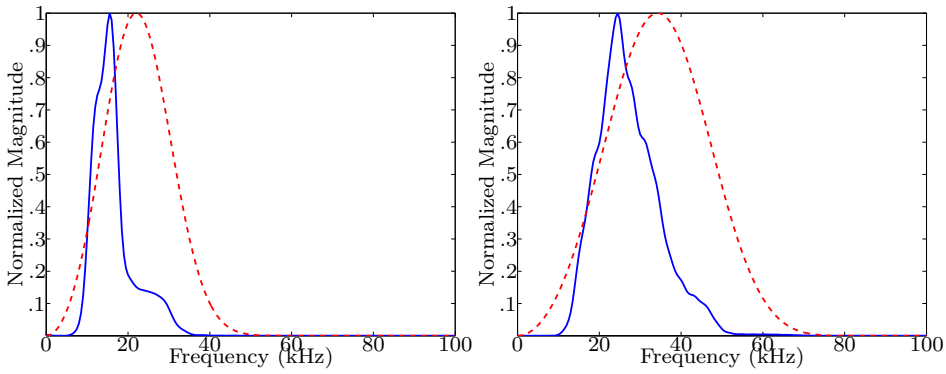

(a) 60 Minutes

(b) 120 Minutes

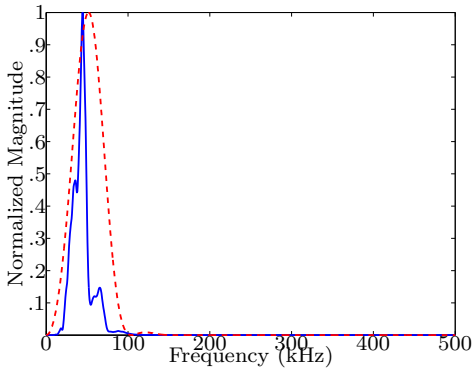

(c) 180 Minutes

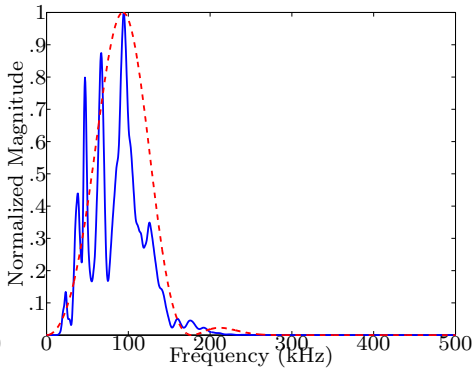

(d) 240 Minutes

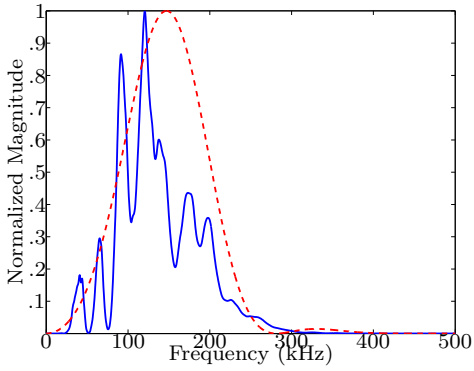

(e) 300 Minutes

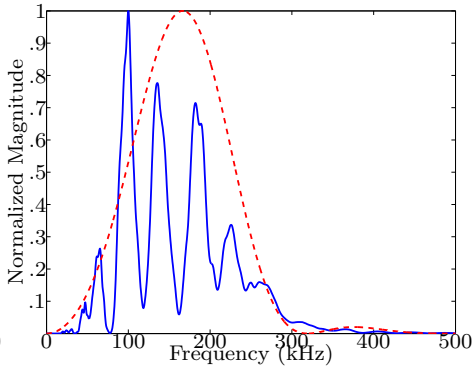

(f) 360 Minutes

Figure B.21: SP11 (0.2% AEA, 16.0 mm) frequency spectra: rectagular window about entire waveform (solid); Hanning window about initial pulse received (dashed)

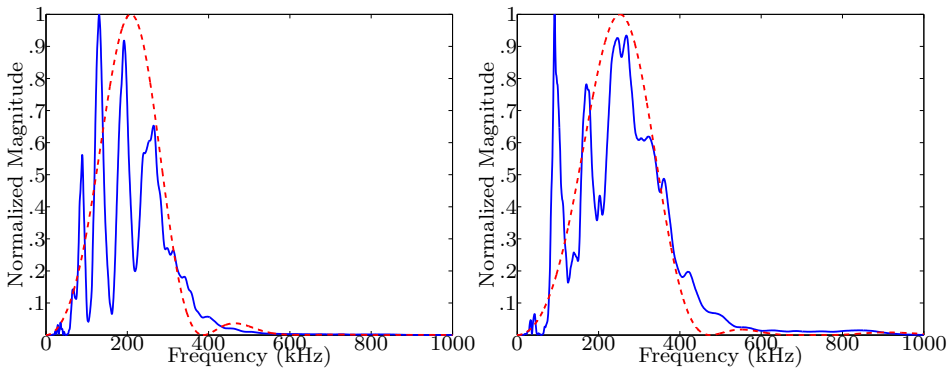

(a) 420 Minutes

(b) 480 Minutes

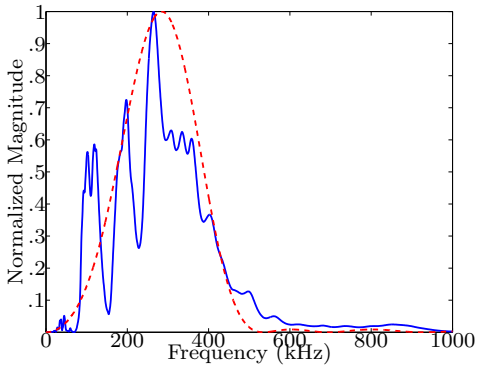

(c) 540 Minutes

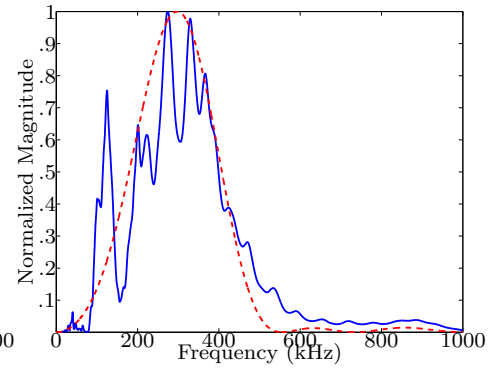

(d) 600 Minutes

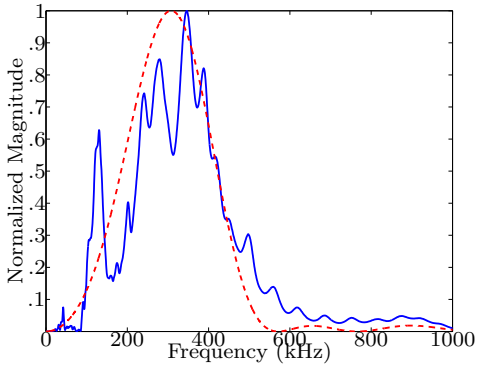

(e) 660 Minutes

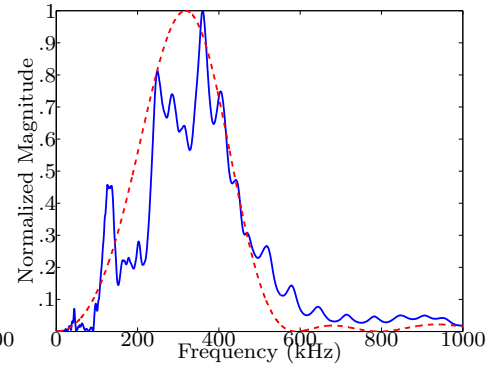

(f) 720 Minutes

Figure B.22: SP11 (0.2% AEA, 16.0 mm) frequency spectra: rectagular window about entire waveform (solid); Hanning window about initial pulse received (dashed)

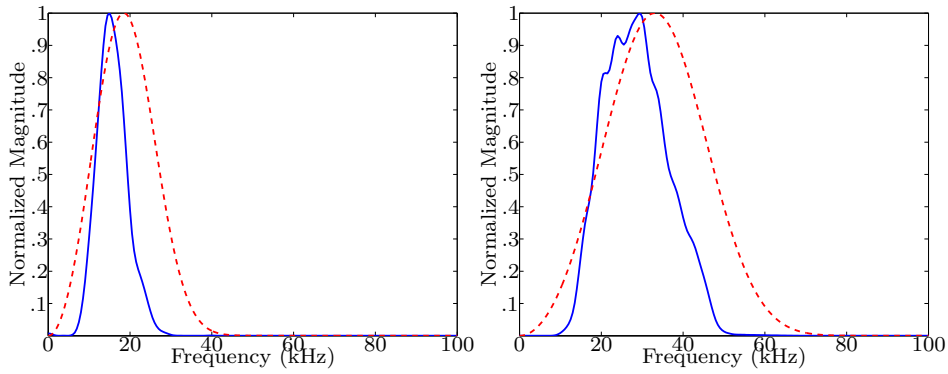

(a) 60 Minutes

(b) 120 Minutes

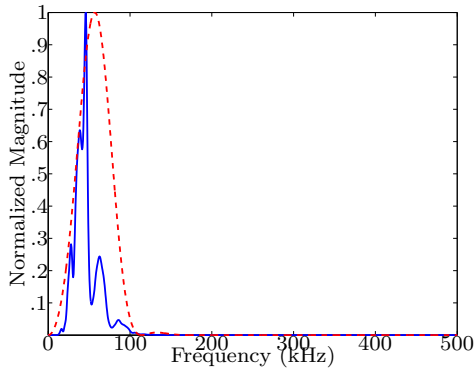

(c) 180 Minutes

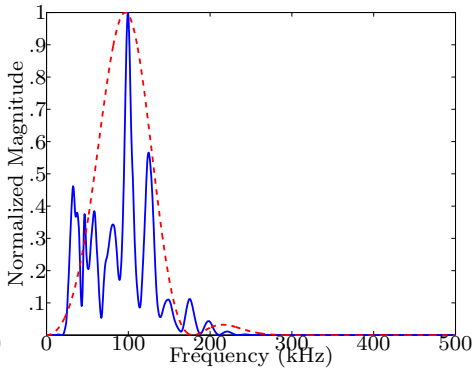

(d) 240 Minutes

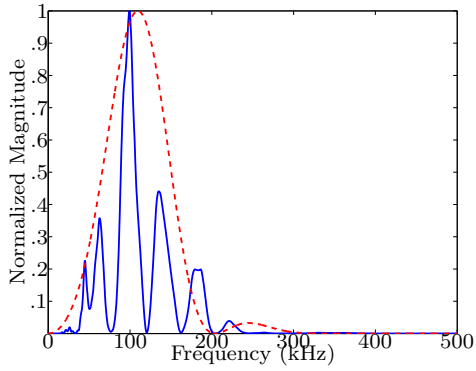

(e) 300 Minutes

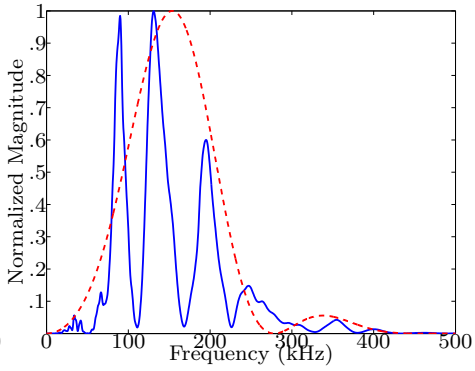

(f) 360 Minutes

Figure B.23: SP12 (0.2% AEA, 16.0 mm) frequency spectra: rectagular window about entire waveform (solid); Hanning window about initial pulse received (dashed)

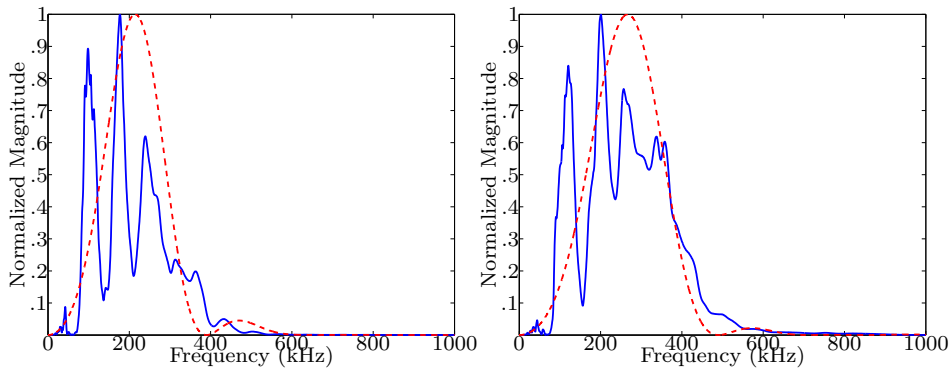

(a) 420 Minutes

(b) 480 Minutes

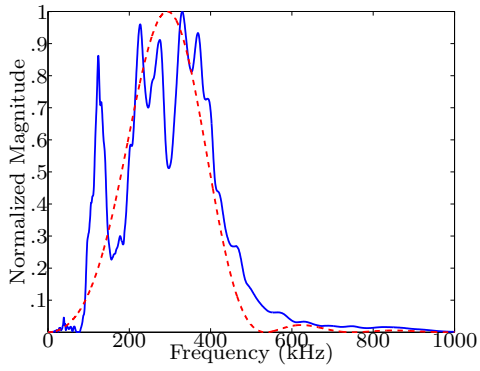

(c) 540 Minutes

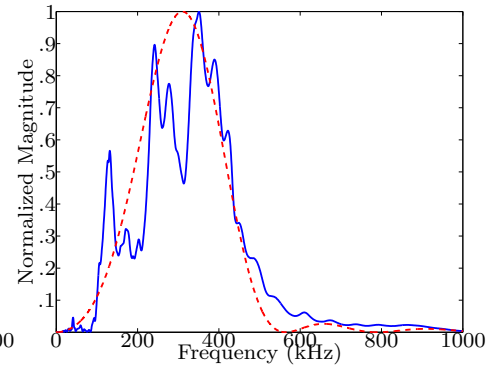

(d) 600 Minutes

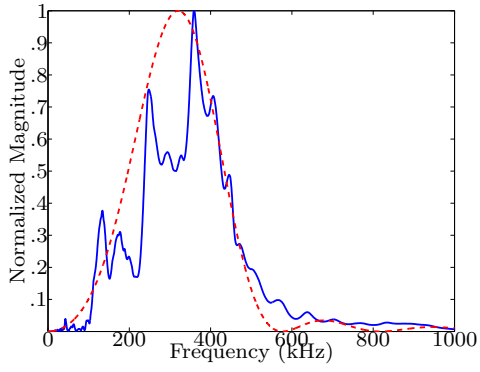

(e) 660 Minutes

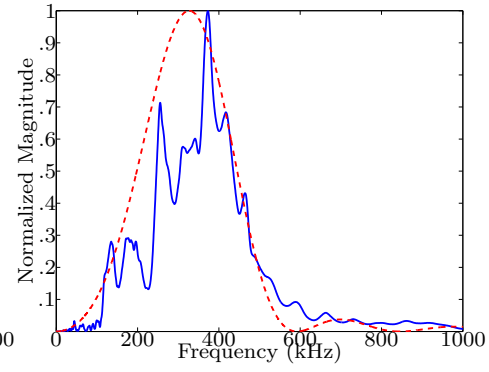

(f) 720 Minutes

Figure B.24: SP12 (0.2% AEA, 16.0 mm) frequency spectra: rectagular window about entire waveform (solid); Hanning window about initial pulse received (dashed)

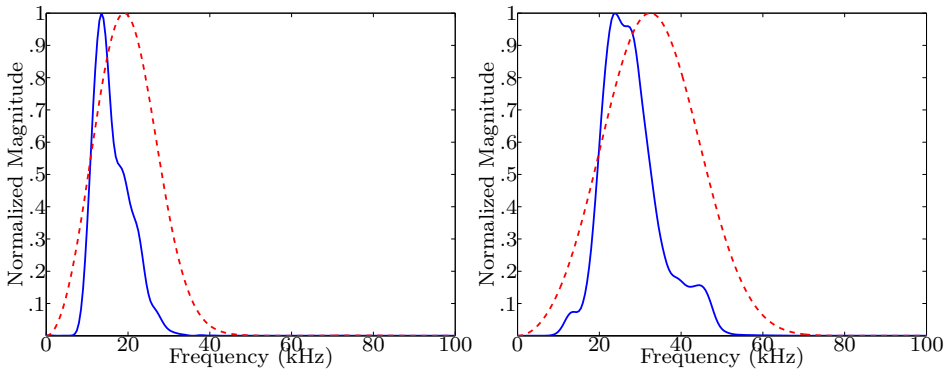

(a) 60 Minutes

(b) 120 Minutes

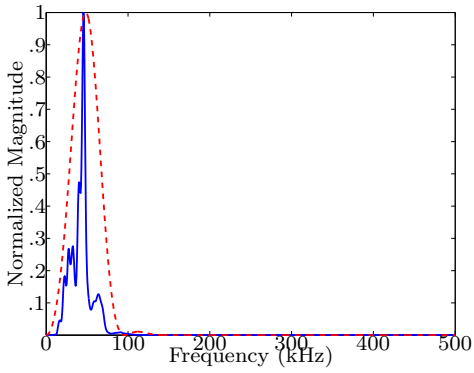

(c) 180 Minutes

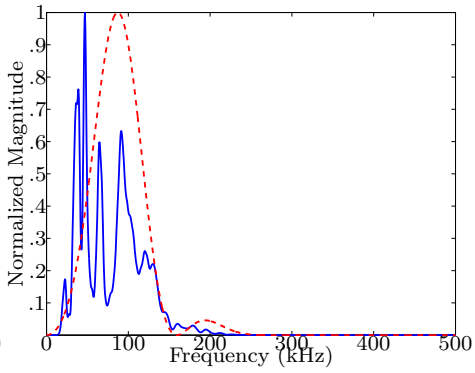

(d) 240 Minutes

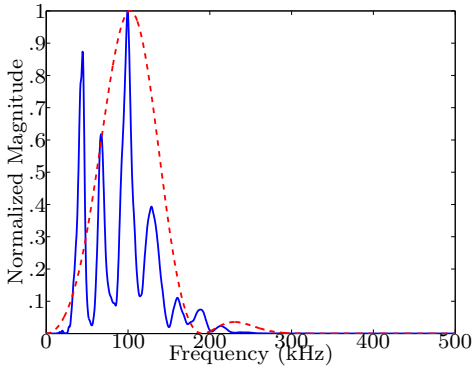

(e) 300 Minutes

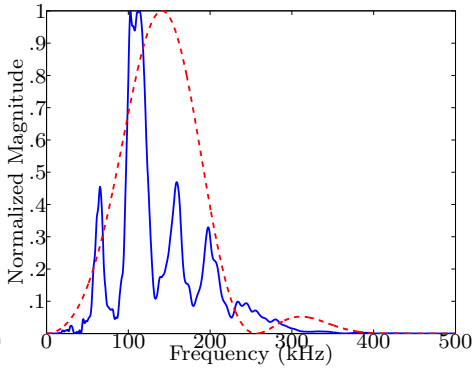

(f) 360 Minutes

Figure B.25: SP13 (0.4% AEA, 16.0 mm) frequency spectra: rectagular window about entire waveform (solid); Hanning window about initial pulse received (dashed)

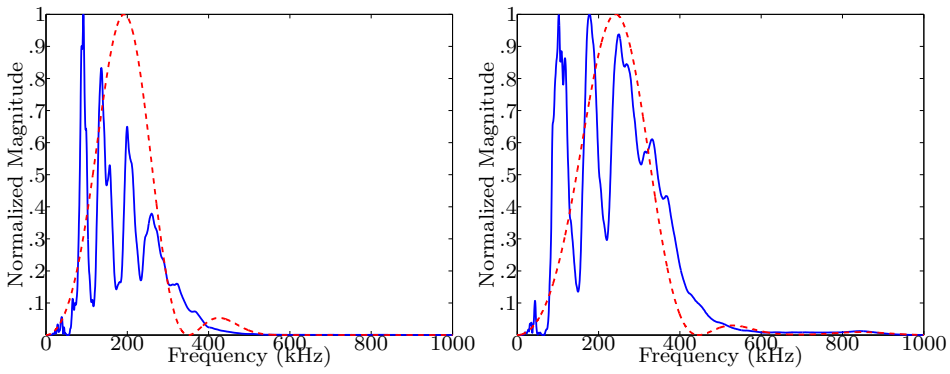

(a) 420 Minutes

(b) 480 Minutes

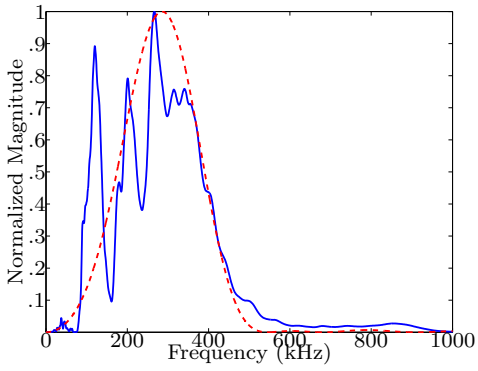

(c) 540 Minutes

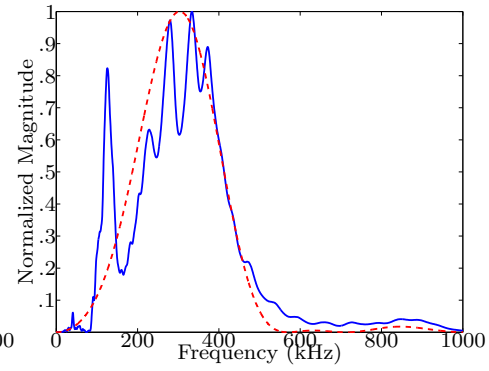

(d) 600 Minutes

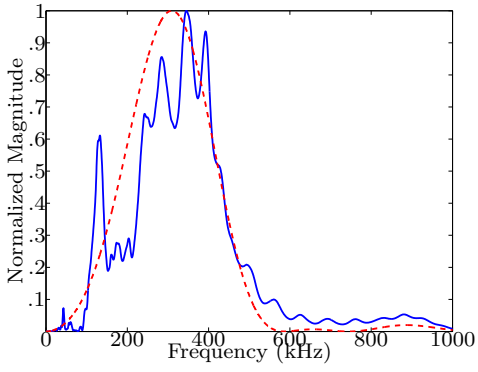

(e) 660 Minutes

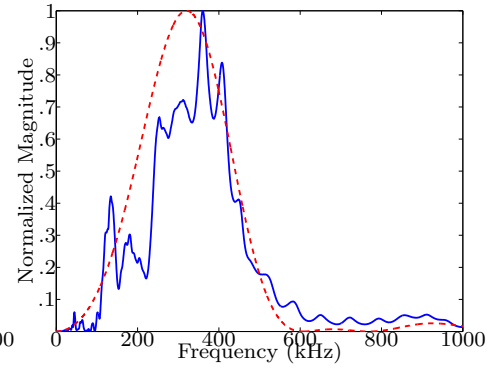

(f) 720 Minutes

Figure B.26: SP13 (0.4% AEA, 16.0 mm) frequency spectra: rectagular window about entire waveform (solid); Hanning window about initial pulse received (dashed)

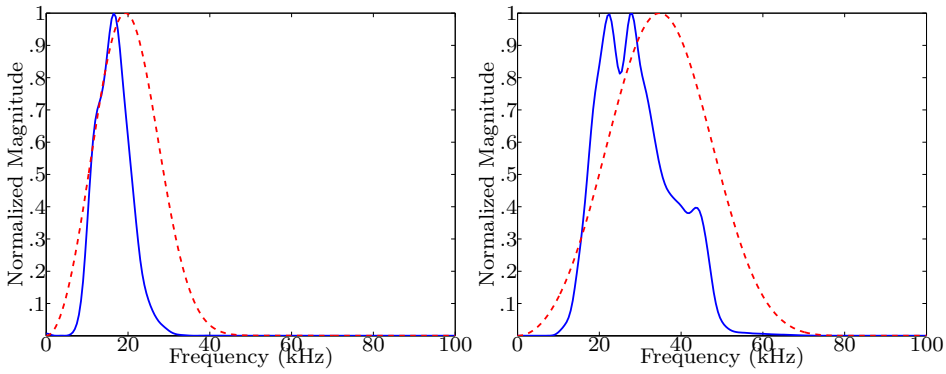

(a) 60 Minutes

(b) 120 Minutes

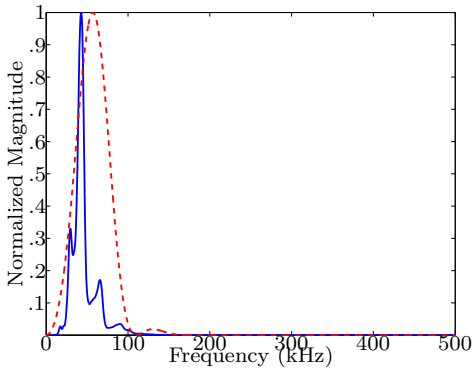

(c) 180 Minutes

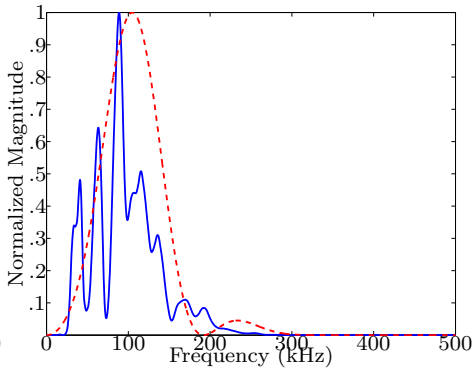

(d) 240 Minutes

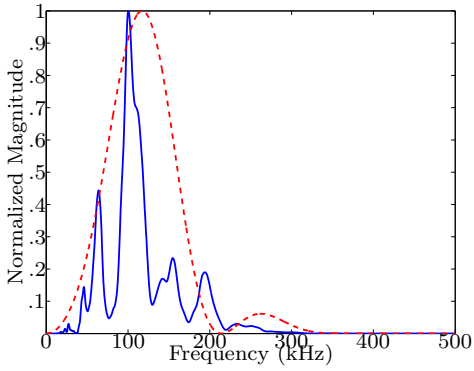

(e) 300 Minutes

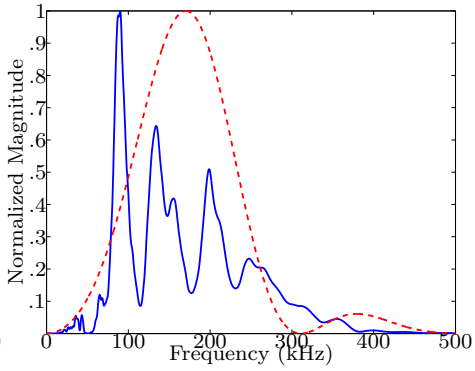

(f) 360 Minutes

Figure B.27: SP14 (0.4% AEA, 16.0 mm) frequency spectra: rectagular window about entire waveform (solid); Hanning window about initial pulse received (dashed)

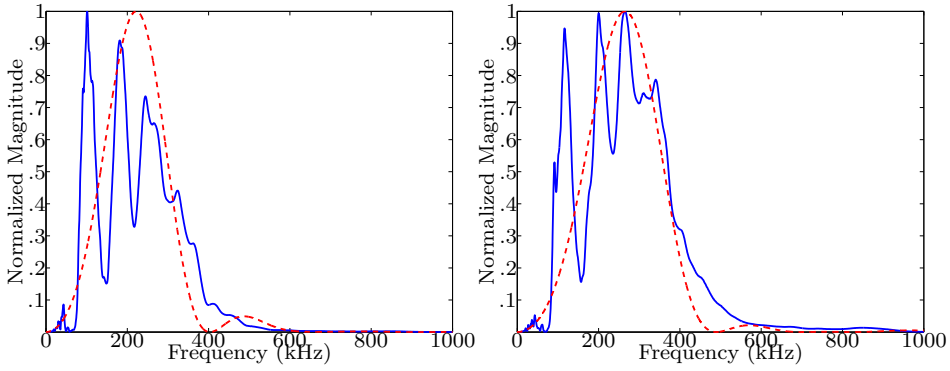

(a) 420 Minutes

(b) 480 Minutes

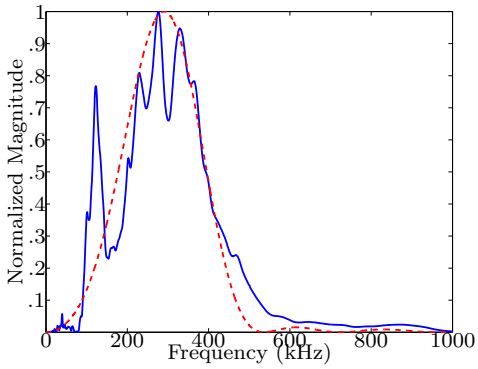

(c) 540 Minutes

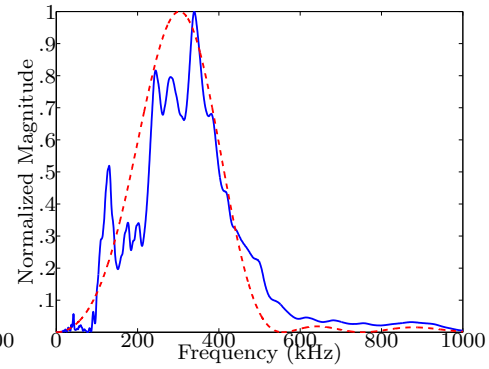

(d) 600 Minutes

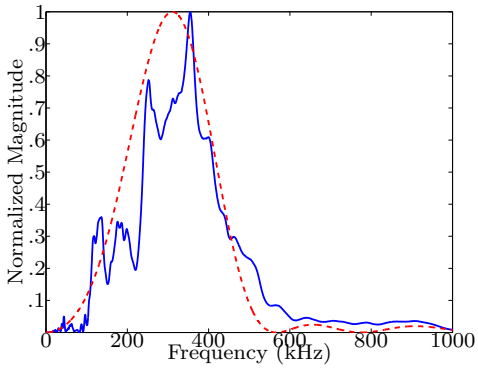

(e) 660 Minutes

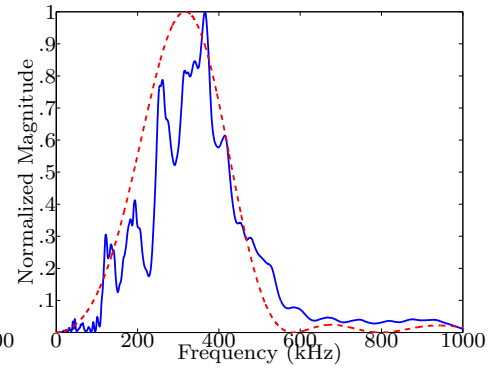

(f) 720 Minutes

Figure B.28: SP14 (0.4% AEA, 16.0 mm) frequency spectra: rectagular window about entire waveform (solid); Hanning window about initial pulse received (dashed)

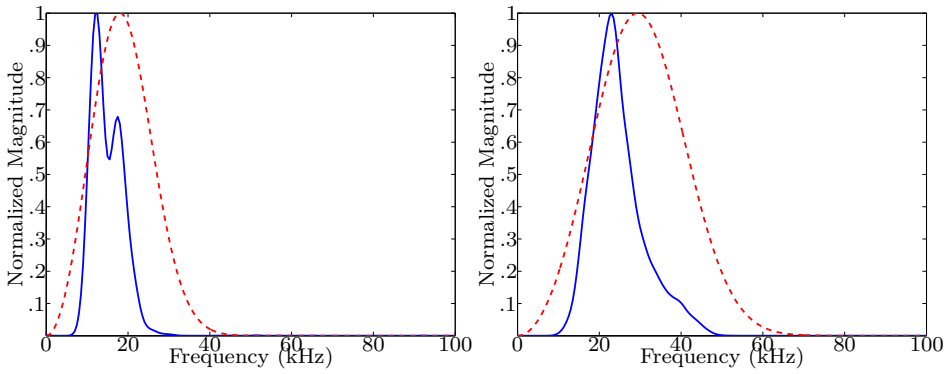

(a) 60 Minutes

(b) 120 Minutes

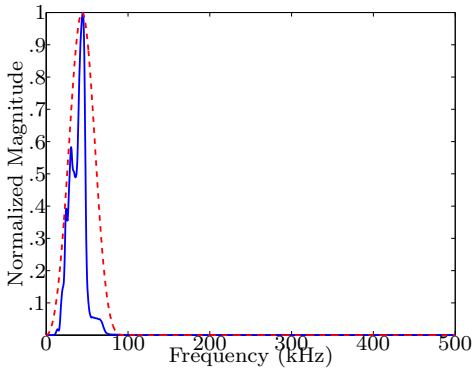

(c) 180 Minutes

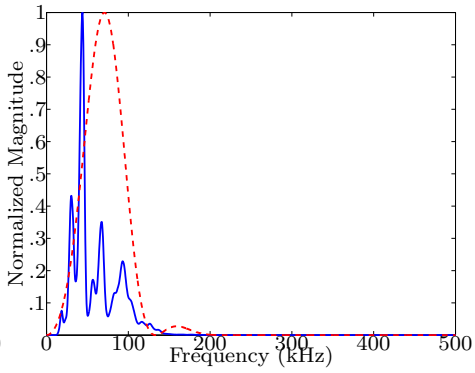

(d) 240 Minutes

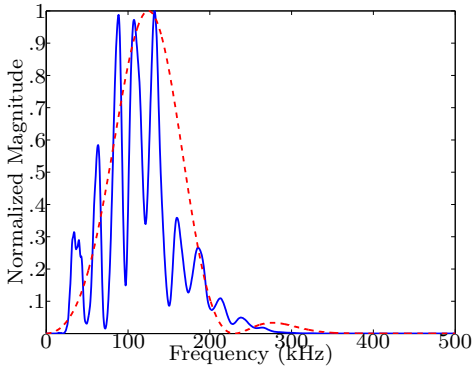

(e) 300 Minutes

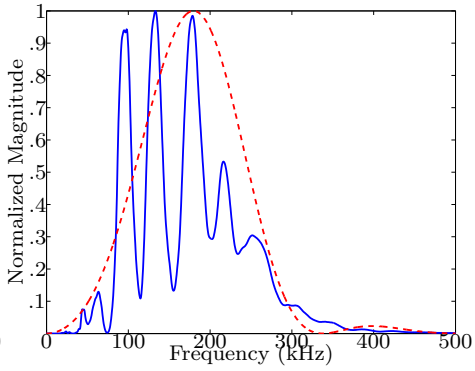

(f) 360 Minutes

Figure B.29: SP15 (0.6% AEA, 16.0 mm) frequency spectra: rectagular window about entire waveform (solid); Hanning window about initial pulse received (dashed)

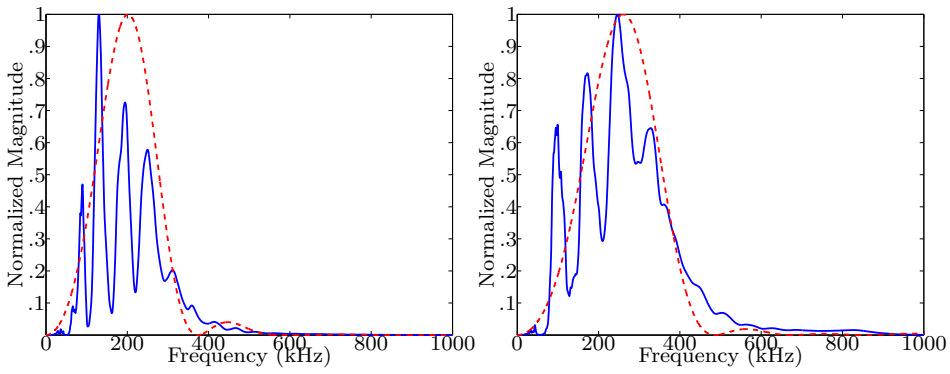

(a) 420 Minutes

(b) 480 Minutes

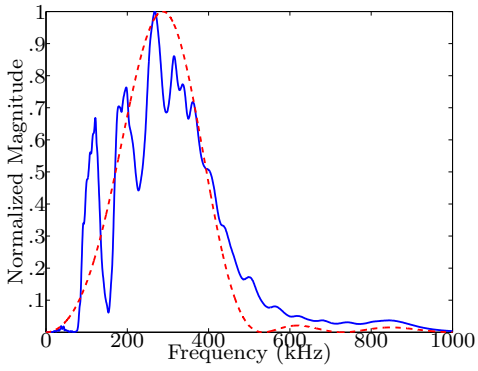

(c) 540 Minutes

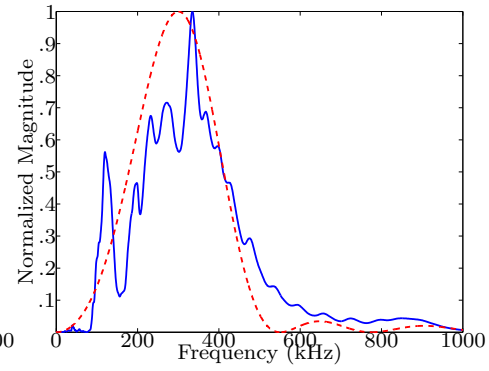

(d) 600 Minutes

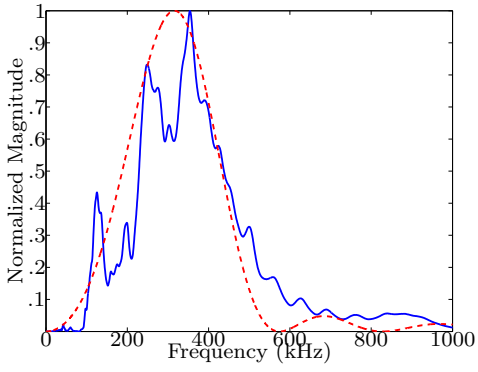

(e) 660 Minutes

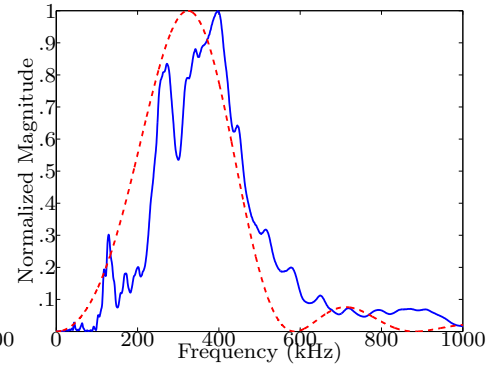

(f) 720 Minutes

Figure B.30: SP15 (0.6% AEA, 16.0 mm) frequency spectra: rectagular window about entire waveform (solid); Hanning window about initial pulse received (dashed)

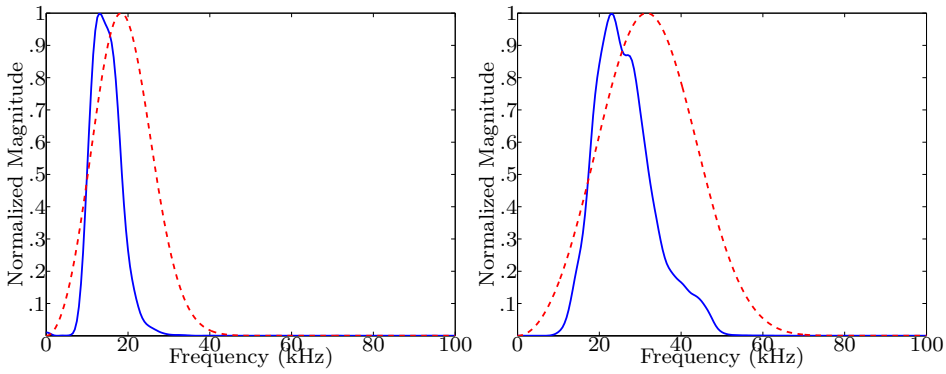

(a) 60 Minutes

(b) 120 Minutes

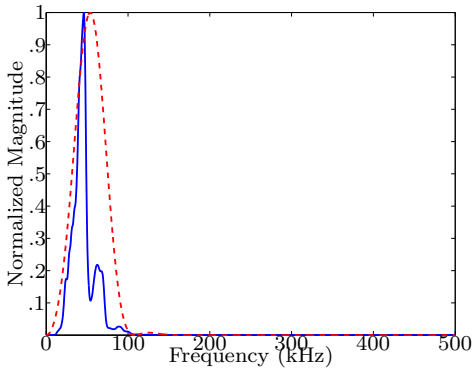

(c) 180 Minutes

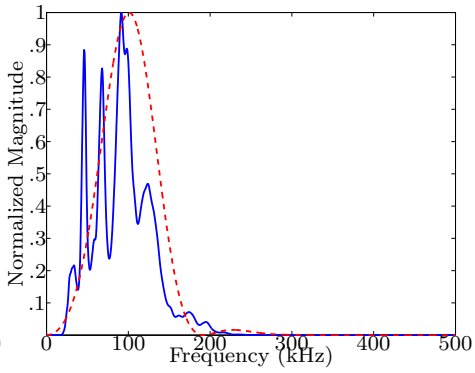

(d) 240 Minutes

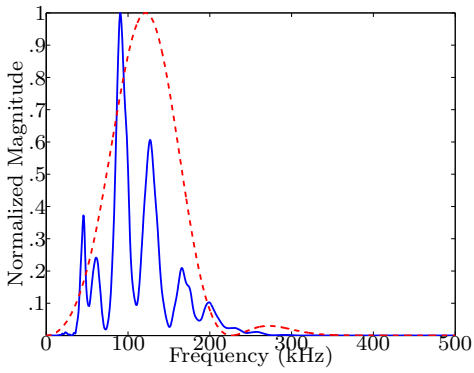

(e) 300 Minutes

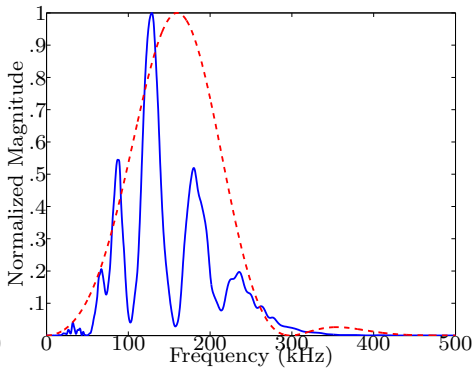

(f) 360 Minutes

Figure B.31: SP16 (0.6% AEA, 16.0 mm) frequency spectra: rectagular window about entire waveform (solid); Hanning window about initial pulse received (dashed)

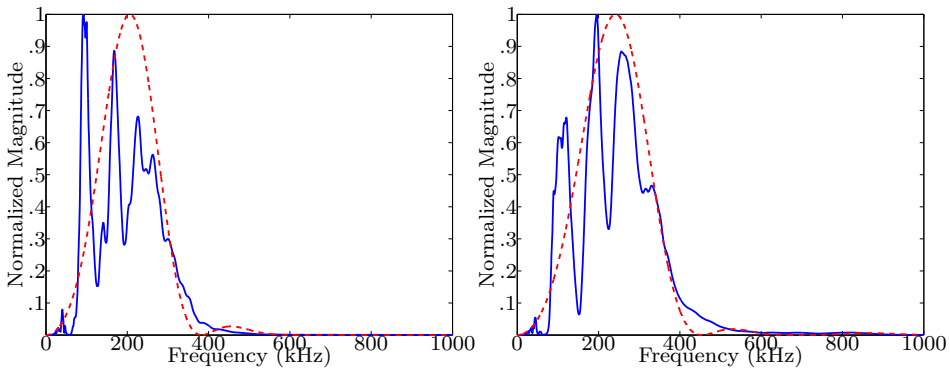

(a) 420 Minutes

(b) 480 Minutes

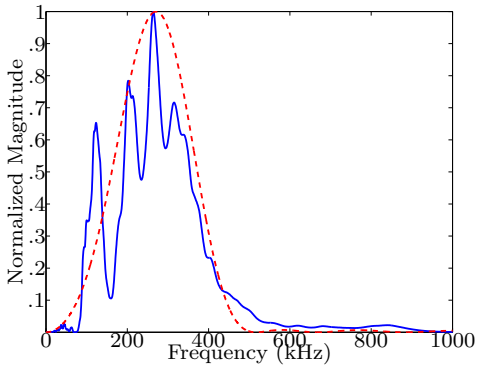

(c) 540 Minutes

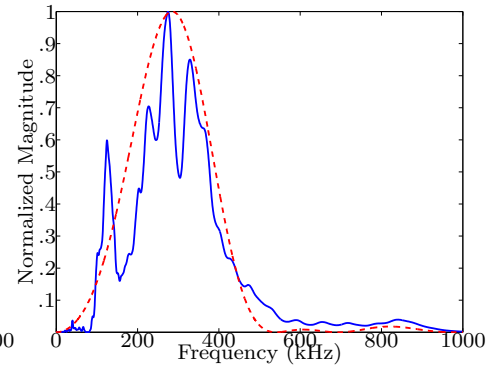

(d) 600 Minutes

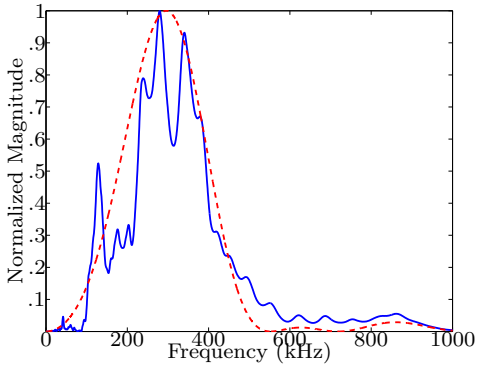

(e) 660 Minutes

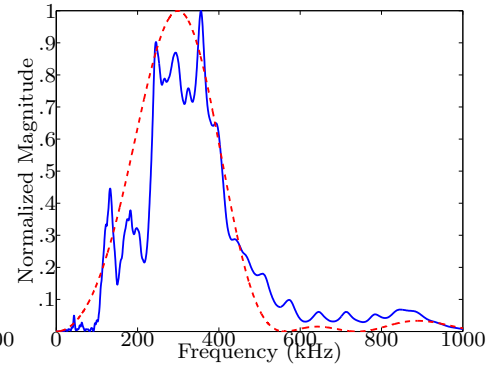

(f) 720 Minutes

Figure B.32: SP16 (0.6% AEA, 16.0 mm) frequency spectra: rectagular window about entire waveform (solid); Hanning window about initial pulse received (dashed)

Bibliography

[1] ACI Committee 201 - Guide to Durable Concrete (ACI 201.2R-08). *American Concrete Institute*. Farmington Hills, Mich., 2008.

[2] Du, L. and Folliard, K.J. Mechanisms of air-entrainment in concrete. *Cement and Concrete Research*, 35:1463–1471, 2005.

[3] Reinhardt, H.W. and Grosse, C.U. Continuous monitoring of setting and hardening of mortar and concrete. *Construction and Building Materials*, 18:145–154, 2004.

[4] Reinhardt, H.W., Grosse, C.U., and Herb, A.T. Ultrasonic monitoring of setting and hardening of cement mortar - a new device. *Materials and Structures*, 33:580–583, 2000.

[5] Öztürk, T., Kroggel, O., Grubl, P. and Popovics, J.S. Improved ultrasonic wave reflection technique to monitor the setting of cement-based materials. *NDT&E International*, 39:258–263, 2006.

[6] Sayers, C.M. and Grenfell, R.L. Ultrasonic propagation through hydrating cements. *Ultrasonics*, 31:147–153, 1993.

[7] Sayers, C.M. and Dahlin, A. Propagation of ultrasound through hydrating cement pastes at early times. *Advanced Cement Based Materials*, 1:12–21, 1993.

[8] Aggelis, D.G. and Philippidis, T.P. Ultrasonic wave dispersion and attenuation in fresh mortar. *NDT&E International*, 37:617–631, 2004.

[9] Aggelis, D.G., Polyzos, D., and Philippidis, T.P. Wave dispersion and attenuation in fresh mortar: theoretical predictions vs. experimental results. *Journal of the Mechanics and Physics of Solids*, 53:857–883, 2005.

[10] Philippidis, T.P. and Aggelis, D.G. Experimental study of wave dispersion and attenuation in concrete. *Ultrasonics*, 43:584–595, 2005.

[11] Kosmatka, S.H., Kerkhoff, B., and Panarese, W.C. *Design and Control of Concrete Mixtures*. Portland Cement Association, Skokie, IL, 2006.

[12] Mehta, P.K. and Monteiro, P.J.M. *Concrete: Microstructure, Properties, and Materials (1st edition)*. McGraw Hall, 1993.

[13] Young, J.F. Mindess, P. and Darwin, D. *Concrete (2nd edition)*. Prentice Hall, 2003.

[14] Taylor, H.F.W. *Cement Chemistry*. Thomas Telford, London, 1997.

[15] ASTM C191 - Standard Test Methods for Time of Setting of Hydraulic Cement by Vicat Needle. *American Society of Testing and Materials*. West Conshohocken, PA, 2007.

[16] Sant, G., Dehadrai, M., Lura, P., Bentz, D., Ferraris, C.F., Bullard, J.W., and Weiss, J. Detecting the fluid-to-solid transition in cement pastes: part i – assessment techniques. In review.

[17] Sant, G., Dehadrai, M., Lura, P., Bentz, D., Ferraris, C.F., Bullard, J.W., and Weiss, J. Detecting the fluid-to-solid transition in cement pastes: part ii – comparison of experimental and numerical techniques. In review.

[18] Bentz, D.P. and Garboczi, E.J. Percolation of phases in a three-dimensional cement paste microstructural model. *Cement and Concrete Research*, 21:325–344, 1991.

[19] Bentz, D.P. Cement hydration: building bridges and dams at the microstructure level. *Materials and Structures*, 40:397–404, 2007.

[20] Chatterji, S. Freezing of air-entrained cement-based materials and specific actions of air-entraining agents. *Cement and Concrete Composites*, 14:757–758, 2003.

[21] Whiting, D.A. and Nagi, M.A. *Manual on control of air content in concrete.* Portland Cement Association, 1998.

[22] Powers, T.C. Structure and physical properties of hardened portland cement paste. *Journal of the American Ceramic Society*, 41:1–6, 1958.

[23] T.C. Powers. *Properties of Fresh Concrete.* John Wiley and Sons Inc., New York, 1968.

[24] Sant, G., Lura, P., and Weiss, J. Measurement of volume changes in cementitious materials at early ages: review of testing protocols and interpretation of results. *Transportation Research Record*, 1979:21–29, 2006.

[25] Bentz, D.P. Influence of water-to-cement ratio on hydration kinetics: Simple models based on spatial considerations. *Cement and Concrete Research*, 36:238–244, 2006.

[26] Powers, T.C. A working hyphothesis for further studies of frost resistance of concrete. *ACI Journal. Proceedings*, 41:245–272, 1945.

[27] Litvan, G.G. Frost action in cement in the presence of de-icers. *Cement and Concrete Research*, 6:351–356, 1976.

[28] Helmuth, R.A. Capillary size restrictions on ice formation in hardened portland cement pastes. *Proceedings of the IV International Symposium on the Chemistry of Cement*, 2:855–869, 1960.

[29] Everett, D.H. The thermodynamics of frost damage to porous solids. *Transactions of the Faraday Society*, 57:1541–1551, 1961.

[30] Litvan, G.G. Phase transitions of adsorbates: Iv, mechanism of frost action in hardened cement paste. *Journal of the American Ceramic Society*, 55:38–42, 1972.

[31] Powers, T.C. and Helmuth, R.A. Theory of volume changes in hardened portland cement paste during freezing. *Proceedings, Highway Research Board*, 32:285–297, 1953.

[32] ACI Committee 201 - Guide for making a condition survey of concrete in service (ACI 201.R-92). *American Concrete Institute*. Farmington Hills, Mich., 1992.

[33] ASTM C173 - Air Content of Freshly Mixed Concrete by the Volumetric Method. *American Society of Testing and Materials*. Philadelphia, PA, 1994.

[34] ASTM C231 - Standard Test Method for Air Content of Freshly Mixed Concrete by the Pressure Method. *American Society of Testing and Materials*. Philadelphia, PA, 1991.

[35] ASTM C138 - Standard Test Method for Density (Unit Weight), Yield, and Air Content (Gravimetric) of Concrete. *American Society of Testing and Materials*. Philadelphia, PA, 2001.

[36] ASTM C457 - Microscopical Determination of Parameters of the Air-Void System in the Hardened Concrete. *American Society of Testing and Materials*. West Conshohocken, PA, 2000.

[37] Achenbach, J.D. *Wave propagation in elastic solids*. North-Holland, 1975.

[38] Graff, K.F. *Wave motion in elastic solids*. Dover publications, 1975.

[39] Ishimaru, A. *Wave Propagation and Scattering in Random Media.* Academic Press, New York, 1978.

[40] Mason, W.P. *Physical acoustics and the properties of solids.* Van Nostrand, Princeton, NJ, 1958.

[41] Hartmann, B. and Jarzynski, J. Ultrasonic hysteresis absorption in polymers. *Journal of Applied Physics*, 43:4304–4312, 1972.

[42] Y.C. Fung. *A First Course in Continuum Mechanics (3rd edition).* Prentice Hall, 1993.

[43] Rose, J.L. *Ultrasonic waves in solid media.* Cambridge University Press, 1999.

[44] Foldy, L.L. The multiple scattering of waves. i. general theory of isotropic scattering by randomly distributed scatterers. *Physical Review*, 67:107–119, 1945.

[45] Waterman, P.C. and Truell, R. Multiple scattering of waves. *Journal of Mathematical Physics*, 2:512–537, 1961.

[46] Dainty, A.M., and Toksoz, M.N. Elastic eave propagation in a highly scattering medium-a diffusion approach. *Journal of Geophysics*, 43:375–388, 1977.

[47] Papadakis, E.P. Ultrasound attenuation caused by scattering in polycrystalline metals. *Journal of the Acoustical Society of America*, 37:711–717, 1965.

[48] Mason, W.P. *Piezoelectric crystals and their application to ultrasonics.* Van Nostrand, New York, 1950.

[49] Jensen, O.M. and Hansen, P.F. A dilatometer for measuring autogenous deformation in hardening portland cement paste. *Materials and Structures*, 28:406–409, 1995.

[50] Santamarina, J.C. and Fratta, D. *Introduction to discrete signals and inverse problems in civil engineering.* ASCE Press, Reston, VA, 1998.

[51] Punurai, W., Jarzynski, J., Qu, J., Kim, J.-Y., Jacobs, L.J. and Kurtis, K. Characterization of multi-scale porosite in cement paste by advanced ultrasonic techniques. *Cement and Concrete Research*, 37:38–46, 2007.